An Investigation of $e^+e^- \rightarrow \pi\pi J/\psi$ Final States produced via Initial State Radiation at Belle

Samuel Thomas M^{c}Onie

A thesis submitted for the degree of
Doctor of Philosophy at the University of Sydney

16th December 2011

Abstract

THE Belle experiment studied e^+e^- collisions produced by the KEKB collider, which was normally tuned to the $\Upsilon(4S)$ resonance for the study of B-mesons. Within the Belle dataset, Initial State Radiation (ISR) events occurred when the initial electron or positron emitted a hard photon. This meant that the e^+ and e^- collided with less energy, allowing states with lower mass than the $\Upsilon(4S)$ resonance to be studied. An investigation of $\pi^+\pi^- J/\psi$ and $\pi^0\pi^0 J/\psi$ combinations with invariant mass near 4260 MeV was conducted using ISR events in Belle data. This was motivated by the discovery of the $Y(4260)$ resonance in $\pi^+\pi^- J/\psi$ events by the *BABAR* collaboration in 2005.

The existence of the $Y(4260)$ was confirmed in the discovery mode: $e^+e^- \rightarrow \gamma_{ISR} Y(4260)$, $Y(4260) \rightarrow \pi^+\pi^- J/\psi$, with $J/\psi \rightarrow e^+e^-$ or $\mu^+\mu^-$. The reconstruction of the ISR photon was not required, however, the $\pi^+\pi^- J/\psi$ combination was required to have four-momentum consistent with ISR production. This analysis was performed using $553.2\,\mathrm{fb}^{-1}$ of data collected at or near the $\Upsilon(4S)$ resonance. The peak at 4260 MeV was confirmed and fitted with a single Breit-Wigner resonance with mass $4295 \pm 10^{+11}_{-5}$ MeV, width $133 \pm 26^{+13}_{-6}$ MeV and $\Gamma_{ee} \cdot \mathcal{B}(Y(4260) \rightarrow \pi^+\pi^- J/\psi) = 8.7 \pm 1.1^{+0.3}_{-0.9}\,\mathrm{eV}$. The properties of the peaking events were also investigated.

A search for events in the experimentally challenging $\pi^0\pi^0 J/\psi$ decay mode was also conducted, with $\pi^0 \rightarrow \gamma\gamma$ and $J/\psi \rightarrow \mu^+\mu^-$ ($e^+e^-\pi^0\pi^0$ events have very low detection efficiency), using $790.9\,\mathrm{fb}^{-1}$ of data. Reconstruction of the ISR photon was required, in addition, the candidate was required to have four-momentum consistent with ISR production. A cluster of events near 4260 MeV was found with low background. These events were fitted with a Breit-Wigner function, with mass and width parameters fixed based on the world average values for the $\pi^+\pi^- J/\psi$ mode. This fit found $\Gamma_{ee} \cdot \mathcal{B}(Y(4260) \rightarrow \pi^0\pi^0 J/\psi) = 3.2^{+1.8+0.6}_{-1.5-0.4}$ eV, consistent with half the production rate of the charged mode; the prediction from isospin. A cross-section as a function of mass was also produced.

Acknowledgements

A lot of work goes into making a thesis. The people listed here all shared their time and effort in helping me produce the work detailed in this document.

I would like to thank my supervisor, A/Prof. Kevin Varvell, for many years of answering my questions and guiding my efforts. Thanks also to my associate supervisor, A/Prof. Lawrence Peak, for supporting me throughout my time in Sydney and editing this thesis. I would especially like to thank my associate supervisor, Dr Bruce Yabsley, for taking care of my first trip to Belle and for the large amount of time and effort he has put into every aspect of this work.

I would like to thank all my Belle colleagues. I thank the Charm conveners who helped me during my study: A/Prof. Boštjan Golob and Drs Jolanta Brodzicka and Anže Zupanc. And I would like to thank the referees of my analyses, who provided many comments and suggestions, A/Prof. Kenkichi Miyabayashi, Profs David Asner and Steve Olsen and especially Dr Pasha Pakhlov who provided so much help while I was starting out. And I thank those who took me out to many lunches and drinks after work, which made my trips to Japan so enjoyable.

While I have been a student with the Sydney Particle Physics group (formerly Falkiner High Energy Physics), I have had the pleasure of getting to know all the staff and students of our research group. From all these people I would like to especially mention Drs Andrew Bakich and Aldo Saavedra for their help and also long term co-students Ms Shoshanna Cole and Drs Anthony Waugh and Jason Lee for their continuing friendship.

I thank the members of the Melbourne EPP group, for their comments and the good times at our common meetings. I especially thank Dr Robin Wedd and Ms T'Mir Julius for putting up with me while we shared an apartment, office and car for months at a time in Japan.

Finally, I would like to thank my family for supporting me throughout this long time. And I thank Rufina, for her love and understanding.

Author's Contribution

The work described in this thesis was performed within the Sydney Particle Physics group at the University of Sydney and the Charm Studies group within the Belle Collaboration. The analyses were conducted on the dataset collected by the Belle detector, operated by the Belle collaboration, using collisions provided by the KEKB electron-positron collider. For the first chapter of this thesis the author prepared a summary of the theoretical and experimental background to this work that has been performed by other groups. The second chapter describes the author's understanding of the construction and operation of the Belle detector and experiment, which was performed by the Belle collaboration. While a member of the Belle collaboration, the author contributed to the running of the experiment by performing on-site shifts in the control room of the Belle detector during data-taking. The data taken during these shifts forms part of the large dataset used in this research.

Chapter 3 describes the first analysis, and Chapters 4 and 5 the second analysis, conducted by the author. The work from Chapter 3 was initially based on a previous internal study by Dr Pasha Pakhlov and also includes a comparison of this work with a later study conducted by Belle researchers: C.Z. Yuan, C.P. Shen and P. Wang. For these chapters, the author performed the great majority of the analysis, which included: initially selecting a reduced dataset; writing a large amount of code to process and reconstruct events; analysing the physical properties of these events, again using self-written code; and giving presentations and writing reports based on these analyses. Both analyses benefited greatly from supervisor guidance and from comments and suggestions provided by both the Charm Studies group and the Sydney Particle Physics group, in addition to the Experimental Particle Physics group within the University of Melbourne. The software written by the author operated within two software frameworks: the Belle Analysis Software Framework, produced by the Belle collaboration; and the ROOT framework, developed by CERN. This work made use of existing MC generated by the Belle collaboration and signal MC generated specifically for this work. The signal MC samples used in Chapters 3 and 4 were generated by Dr Pakhlov and the author, respectively, and processed by the author. The generation step involved code written by Dr Pakhlov to interface between two MC generators. All plots shown in this thesis were produced by the author, except where noted. This document has been proofread and edited by the author; the author's supervision team: A/Prof. Kevin Varvell, Dr Bruce Yabsley and A/Prof. Lawrence Peak; and Ms Rufina Cheung.

Contents

List of Figures

List of Tables

Chapter 1

Theory

THIS thesis describes the confirmation and measurement of the properties of a recently discovered new particle, the $Y(4260)$.[1] The $Y(4260)$ was discovered in the $\pi^+\pi^- J/\psi$ decay mode, produced via Initial State Radiation (ISR) at *BABAR*, a B meson experiment. It has some unusual properties, which have meant that its structure, as yet, has not been conclusively determined.

This work takes place within the current understanding of High Energy Physics as described by the Standard Model of Particle Physics (SM). Detailed descriptions of the SM are available in many textbooks, for example Refs [2, 3]. Briefly, the SM is a field theory in the gauge group $U(1) \times SU(2) \times SU(3)$, with spin-1/2 fermions, the quarks and leptons, interacting via the exchange of force carrying spin-1 gauge bosons. There are six quarks; up (u), down (d), charm (c), strange (s), top (t) and bottom (b), and there are six leptons; the electron (e), muon (μ), and tau (τ), each with its own neutrino; ν_e, ν_μ, ν_τ. All of the quarks and leptons also have a corresponding antiparticle. The forces covered by the SM are Electro-Magnetism (EM), and the weak and the strong forces. There is currently no accepted quantum theory of gravity and it is not included in the SM. Some of the properties of the quarks and leptons are detailed in Table 1.1,[2] including the total angular momentum quantum number, J, parity quantum number, P, and charge conjugation quantum number, C.[3] Some of the properties of the gauge bosons are provided in Table 1.2. In the minimal SM, these particles acquire mass via interaction with the Higgs boson.

[1] Referred to as $X(4260)$ in Ref. [1]

[2] In this thesis, natural units will be used for energy, momentum and mass, with the speed of light in a vacuum is set to 1; which allows these quantities to be compared directly in units of GeV.

[3] The P and C quantum numbers are expressed as either $+$ or $-$ for $+1$ and -1, respectively.

Table 1.1: The quarks and leptons of the SM. They are arranged in generations of increasing mass from left to right, except for neutrinos, whose masses are too small to have been directly measured to date. In this table, q_e is the magnitude of the charge of the electron. The masses are reproduced from Ref. [1]. The quark masses are indicative only, free quarks have never been observed.

Charge (q_e)		Mass (MeV)		Mass (MeV)		Mass (MeV)
			Quarks			
$+2/3$	u	1.7-3.3	c	1250 ± 90	t	$(172 \pm 2) \times 10^3$
$-1/3$	d	4.1-5.8	s	101 ± 29	b	4200 ± 200
			Leptons			
0	ν_e	$< 2 \times 10^{-6}$	ν_μ	< 0.19	ν_τ	< 18.2
-1	e	0.511	μ	105.7	τ	1777
		Generation I		Generation II		Generation III

Table 1.2: The forces of the SM and their mediating gauge bosons. In this table, q_e is the magnitude of the electric charge on the electron. Particle properties have been taken from Ref. [1].

Force	Boson	Charge (q_e)	Mass (GeV)	J^{PC}
EM	γ	0	0	1^{--}
Weak	$W^\pm$	± 1	80.4	1
	Z^0	0	91.2	1
Strong	g	0	0	1^-

There are several competing theoretical models that have been used to attempt to describe the structure of the $Y(4260)$. In this chapter, firstly, theoretical models of meson structure will be discussed in Section 1.1. The $Y(4260)$ is expected to have charm content, because of its decay involving the J/ψ. So, the charmonium system, charmonium particles are mesons with structure $c\bar{c}$, will be discussed in Section 1.2. The $Y(4260)$ has some unusual properties, which have led to speculation that it has a structure proposed by other more exotic models: this will be discussed in Section 1.3. The production mechanism of the $Y(4260)$ in experiment, ISR, will be discussed in Section 1.4, before a review of what is known about this state experimentally will be presented in Section 1.5. Finally in this chapter, the specific models of meson and exotic structure that have been applied in an attempt to understand the observed properties of the $Y(4260)$ and their predictions will be discussed in Section 1.6.

1.1 Models of meson structure

In this section, the theory underlying the structure of hadrons, Quantum Chromo-Dynamics (QCD), will be discussed in Section 1.1.1. The calculations involved in QCD are very difficult to perform at the energy scales involved in hadron binding. One method for doing this is Lattice QCD, which will be discussed in Section 1.1.2. Because of the difficulties in calculating using the full theory of QCD, phenomenological models provide predictions of comparable accuracy to those arising directly from QCD and specific examples will be discussed in Section 1.1.3.

1.1.1 QCD

QCD is the $SU(3)$ component of the SM and is responsible for the binding and structure of hadrons. QCD describes the strong force and introduces three colour charges,[4] *red*, *green* and *blue*, for the quarks, but is not felt by the leptons. These three colours are combined using representations of the $SU(3)$ group, into colour-neutral hadrons. Mesons have a quark and antiquark, carrying colour and anti-colour respectively, and baryons have three quarks each carrying a separate colour. The strong force is mediated by eight massless gluons (g), which also carry colour charge.

[4] Which bear no relationship to visible colours.

Three important related features of QCD are quark confinement, asymptotic freedom and self-interaction amongst the gluons. The strength of the strong force increases with distance, whereas the strengths of EM and the weak forces decrease with distance. This property of QCD leads to quarks being confined with other quarks in colour-neutral hadrons and isolated quarks have never been observed. Similarly, because the strength of the strong force decreases as quarks approach each other, at distances small compared to the size of hadrons quarks essentially interact freely, a property known as asymptotic freedom. Lastly, as the gluons which mediate the strong force also carry their own colour charge, gluons can interact with other gluons. Asymptotic freedom and gluon self-interaction mean that the calculations involved in using the underlying theory of QCD are very difficult to perform for low energy systems.

1.1.2 Lattice QCD

The coupling strength in QCD decreases with energy transfer, therefore the coupling is strong at low energy scales, such as in bound states of hadrons. In addition to this, the self-interaction of gluons means that the theory of QCD is non-perturbative when describing hadron structure. In order to make predictions directly from QCD in this energy range, Lattice QCD is used. For a review of the Lattice QCD method, see Ref. [4]. In Lattice QCD, spacetime is discretised into points on a lattice. The fermion fields representing the quarks are placed on these lattice points and these points are connected by gauge fields. The desired observables are then calculated for a range of volumes and lattice spacings, to extrapolate the limits as the volume goes to infinity and the lattice spacing goes to zero. Lattice QCD calculations will typically involve a large number of points, which makes them computationally expensive to perform. Lattice QCD predictions have only in recent years started having accuracy comparable to the predictions from phenomenological models of hadron structure.

1.1.3 The Quark Model

The quark model is a phenomenological model for the classification of hadrons which predates the full theory of QCD. In this model, each hadron is classified according to its valence quarks, the properties of the quarks are summarised in Table 1.1. This model provides a unified framework for describing all of the observed mesons and baryons. In the quark model, each quark has a baryon number of $+1/3$, so baryons with three valence quarks, qqq, have baryon number $+1$, while mesons, $q\bar{q}$, have baryon number 0. With the development of QCD, the quark model was enhanced with features inspired by QCD and used to calculate the spectrum of both mesons and baryons. In quark and potential models, hadrons are described as quarks in a confining potential, where the form of the potential was developed based on QCD.

The fluxtube model [5] is one of the quark and potential models. In this model, the self-interaction of the gluons is seen as compressing the colour-field between the valence quark and antiquark into a flux tube, which can be modelled as a one dimensional object. This gives a simple linearly rising form to the confining potential at large distances:

$$V(r) = \sigma r,$$

where r is the distance between the quarks and σ is some constant, which has the correct confining behaviour required by QCD. At short distances, compared to the size of the meson, the potential at lowest order is modelled as a Coulomb-like single gluon exchange potential:

$$V_0(r) = -\frac{4}{3}\frac{\alpha_s(r)}{r},$$

where $\alpha_s(r)$ is the running coupling constant from QCD. These models can then be extended by adding in corrections for relativistic and spin dependent effects. These potential models were developed in the charmonium system, where the charm quark is heavy enough to treat the relativistic effects as a correction term, before being successfully applied to the whole meson [5] and baryon [6] spectrum.

1.2 Charmonium

The $Y(4260)$ is expected to have charm content, because of its decay involving the J/ψ. Charmonium was the first experimentally discovered system containing the relatively heavy charm quark and antiquark. The heaviness of the charm quark, relative to the typical energy scales in QCD bound states, allows relativistic effects to be neglected in the simplest models of charmonium. This simplifies the calculations involved and studies of charmonium provide insight into hadron structure and the underlying QCD interactions.

The first charmonium state was discovered independently by two laboratories, Brookhaven National Laboratory [7] and the Stanford Linear Accelerator Center [8], in 1974. A detailed review of both experimental and theoretical studies of the charmonium system can be found in Ref. [9]. This particle was named the J/ψ, which was found to be the lowest mass state in the ψ series of $J^{PC} = 1^{--}$ $c\bar{c}$ resonances. The first excited state in the ψ series, the $\psi(2S)$, alternatively called the ψ', was found soon afterwards [10]. Since then a whole spectrum of charmonium states has been observed. The resonances of the charmonium spectrum are given a name based on their J^{PC} quantum numbers, summarised in Table 1.3, with excited states denoted by either a prime, their mass in brackets or a spectroscopic label. The spectroscopic labels used are the radial quantum number followed by a letter for the orbital angular momentum of the state. These letters include S, P and D, corresponding to $L = 0, 1$ and 2 respectively, where L is the orbital angular momentum quantum number. The parity and charge conjugation quantum numbers, P and C, can be derived from the angular momentum quantum numbers by: $P = (-1)^{L+1}$ and $C = (-1)^{L+S}$, where S is the spin angular momentum quantum number. Charmonium is often referred to as hidden charm, because the c and $\bar{c}$ balance each other, while D mesons, which have either an unbalanced c or a $\bar{c}$, are referred to as open charm. Charmonium generally favours decays to open charm if this is allowed by energy and momentum conservation and other relevant conservation laws. The charmonium spectrum and some of the open charm thresholds are shown in Figure 1.1. Within a year of discovery, descriptions of the charmonium system using potential models had been produced which were able to successfully predict some of its features [11].

Table 1.3: The naming scheme for charmonium particles.

J^{PC}	0^{-+}	1^{+-}	1^{--}	0^{++}	1^{++}	2^{++}
Name	η_c	h_c	ψ	χ_{c0}	χ_{c1}	χ_{c2}

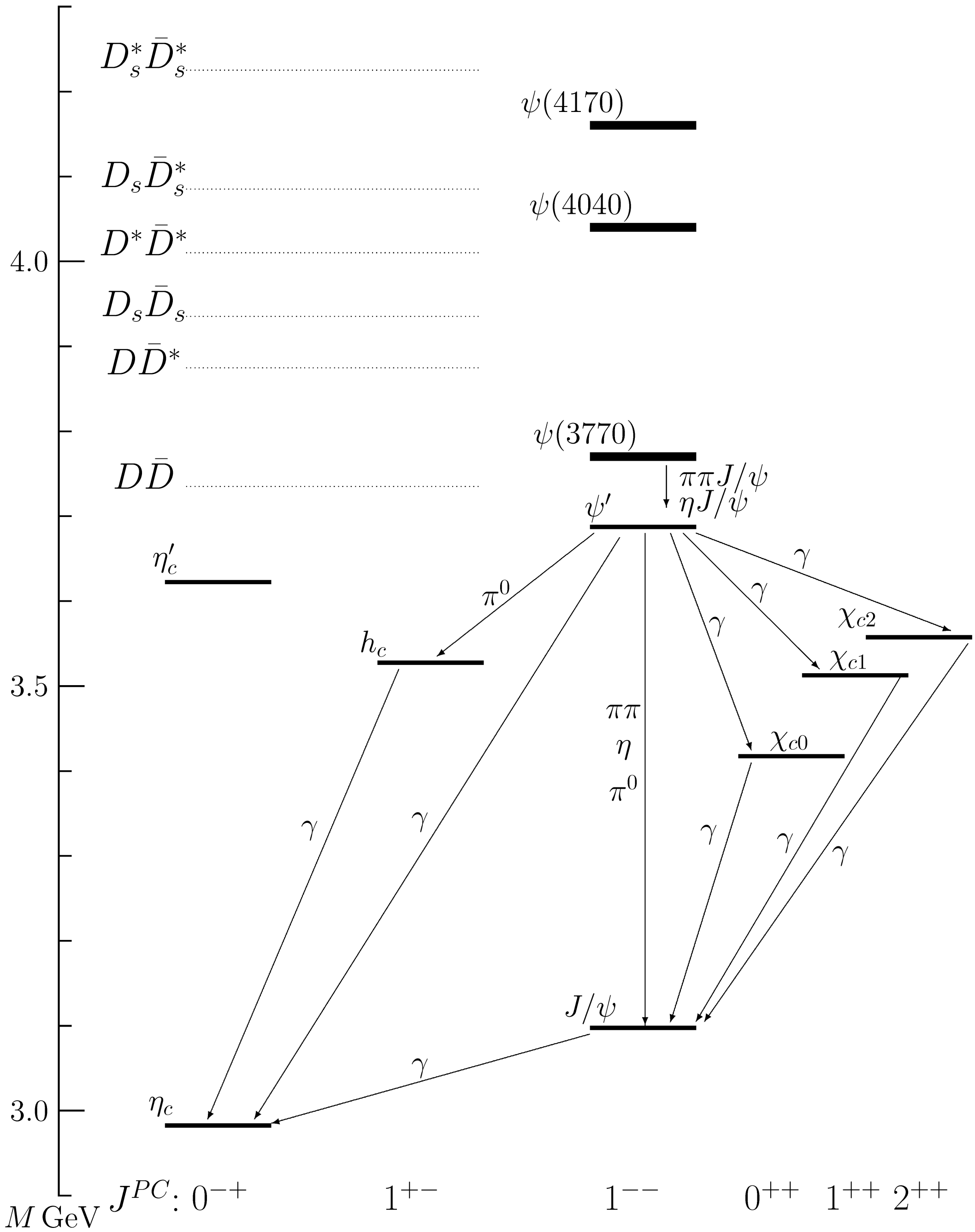

Figure 1.1: The charmonium spectrum, shown with some transitions between states and the open charm thresholds. States are named for their J^{PC} quantum numbers. Adapted from Ref. [9].

1.3 Predicted meson-like states

Some of the properties of the $Y(4260)$ make it difficult to assign it to a place in the standard meson spectrum. In this section we will discuss models for states that, like the standard mesons and baryons, are colour-neutral, which however, contain extra constituents. The application of these models to the $Y(4260)$ will be discussed in Section 1.6.

In QCD at low energies quarks and gluons are bound in colour-neutral mesons, $q\bar{q}$ and baryons, qqq. However, there is nothing in the theory to prevent colour-neutral combinations with a higher number of constituent quarks, such as meson-like tetraquarks, $qq\bar{q}\bar{q}$; molecules of two hadrons which are lightly bound, with structure $([q\bar{q}][q\bar{q}])$ or $(qqq[\bar{q}\bar{q}\bar{q}])$, or baryon-like states, such as pentaquarks with structure $qqqq\bar{q}$.[5] In addition to these states, since gluons can self-interact, there are predictions for meson-like quark-gluon hybrids with a gluon excited into a valence state, which would be written as $q\bar{q}g$, and colour-neutral states composed entirely of gluons named glueballs. The following sub-sections will discuss some of the history and predictions of these meson-like models; an example of a review with more theoretical detail of meson-like states can be found in Ref. [13].

1.3.1 Tetraquarks

One possible structure for states that have more constituents than the basic meson or baryon structures, $q\bar{q}$ or qqq, would be $qq\bar{q}\bar{q}$, where each quark interacts essentially freely with the other quarks in the state. Particles with this structure would be referred to as tetraquarks. In this case the state will be bound if $M(qq\bar{q}\bar{q}) < 2M(q\bar{q})$. It was pointed out that the potentials used in quark and potential models would confine a $QQ\bar{q}\bar{q}$ system, where Q is a heavy quark and q a light quark, when the ratio of the masses of the two quarks, $M(Q)/M(q)$, is large enough [14]. From results using this method, it was found that a $bb\bar{q}\bar{q}$ state would be bound by of order 100 MeV, while the charm quark equivalent, $cc\bar{q}\bar{q}$, would be unbound [15].

[5] For a review of pentaquarks, see Ref. [12].

1.3.2 Molecules

There are models for bound states of multiple hadrons into molecules of mesons or baryons, with structure $([q\bar{q}][q\bar{q}])$ and $([qqq][\bar{q}\bar{q}\bar{q}])$ respectively. These states are predicted to be loosely bound via pion, or other light meson, exchange. Specifically there have been predictions for bound states of D mesons to contribute to the spectrum near the various $D\overline{D}$ thresholds [16, 17]. The masses of the molecular states are expected to be close to the relevant threshold, in the cases where binding occurs.

1.3.3 Quark-gluon hybrids

A quark-gluon hybrid is a predicted state that has gluonic excitation of quarkonium ($q\bar{q}$ states such as charmonium). A predicted quark-gluon hybrid state would have structure: $q\bar{q}g$, where g is a gluon. In the fluxtube model, where mesons are modelled as quarks bound by a tube of flux, see Section 1.1.3, the excitations of the quark sector lead to the standard meson spectrum. In this same model, it is also possible to excite the gluons in the flux tube, which is predicted to lead to a new spectrum of quark-gluon hybrid states. Very soon after the discovery of the first charmonium states and the early successes of the quark and potential models [11], predictions were made using these models that the first $c\bar{c}g$ state should exist within 2 GeV of the mass of the J/ψ [18]. There are specific predictions for the first charmonium-gluon hybrids to exist with mass approximately between 4.1 and 4.2 GeV [19]. Additionally, it is predicted that quark-gluon hybrids will not decay to a pair of S-wave mesons, but instead will favour decays to a combination of S and P-wave mesons [20]. In the specific case of a $c\bar{c}g$ hybrid, the decays to $D^{(*)}\overline{D}^{*}$ will be suppressed and the first open charm decay mode for a $c\bar{c}g$ hybrid will be $D^0\overline{D}_1(2422)^0$, with threshold 4287 MeV [1].

1.3.4 Glueballs

From the fact in QCD that gluons are able to self-couple, bound states consisting of mainly gluons, with no valence quarks, have been predicted. For a review of the predictions and theory of glueballs, see Ref. [21]. Two main properties are ascribed to glueballs: Firstly, as glueballs contain no constituent quarks, their decays are expected to be flavour-blind with regard to the quark content of the decay products. Secondly, as gluons are electrically-neutral, glueballs are not expected to couple to photons [21]. Glueballs have never been conclusively observed, though there have been candidates such as the $\eta(1440)$, see Section 4.2 of Ref. [22]. Current predictions from Lattice QCD suggest that the lowest mass $J^{PC} = 1^{--}$ glueballs may occur at about 3850 MeV [23].

1.4 ISR

In this section, the production mechanism for the $Y(4260)$ in this thesis, Initial State Radiation, or ISR, will be discussed. ISR is a Quantum Electro-Dynamic (QED) process. QED is the $U(1)$ component of the SM, describing the interaction between particles with electric charge, and is mediated by the massless photon. Belle, see Chapter 2, is an e^+e^- collider and the primary interactions studied at Belle are from e^+e^- annihilation, one of the lowest order QED processes. In e^+e^- annihilation, $e^+e^- \rightarrow \gamma^*$, where the virtual photon, γ^*, couples to a vector state, which subsequently decays to a final state measured by the detector. ISR is a higher order QED process that occurs in e^+e^- annihilation, where one of the incident electrons emits a hard photon[6] and the virtual photon formed by the remaining e^+e^- has a lower Centre of Mass (CM) energy. This process is also known as "radiative return"; because if the initial particles have energy higher than the mass of the resonance, the radiated photon "returns" the energy of the event to the resonance. For B-factories, which are e^+e^- colliders that typically operate at a fixed energy, such as that of the $\Upsilon(4S)$ resonance, the ISR process allows the study of states produced over a range of e^+e^- collision energies that would not otherwise be able to be accessed.

At first order, this process is described by two diagrams, as shown in Figure 1.2, with either the initial electron or positron emitting a single photon. Resonances formed in ISR events are produced from the resultant e^+e^- via a virtual photon. This restricts the number of states able to be produced to those with the same quantum numbers as the photon. In the case of states produced via ISR the quantum numbers are $J^{PC} = 1^{--}$. The formulae in the remainder of this section are reproduced from Ref. [24], which discusses ISR in the specific case where e^+e^- colliders are tuned to the $\Upsilon(4S)$ resonance.

The direction of the ISR photon and the fraction of the CM energy that it carries away from the e^+e^- system is important for determining the number of events in

[6] Hard and soft photons refer to high and low energy photons, respectively.

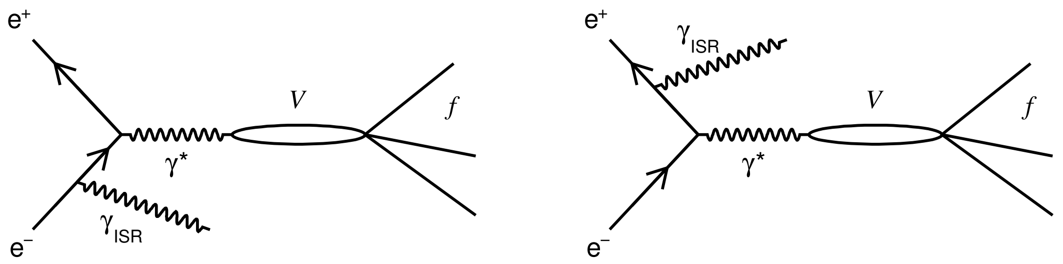

Figure 1.2: The two first order diagrams of the ISR process. Left: the incoming electron emits the ISR photon, γ_{ISR}. Right: the incoming positron emits the ISR photon. The electron and positron then annihilate and the virtual photon, γ^*, couples to a vector state V, before it decays to final state f.

which the decay products will interact with the detector in a given experiment. The Born term for the differential cross-section, $d\sigma$, with respect to the angle of photon emission, θ, and the fraction of the total energy radiated by the photon, x, is given by (Equation (2) of Ref. [24]):

$$\frac{d\sigma(\theta,x)}{dx\,d\cos\theta} = \frac{2\alpha}{\pi x}\cdot\frac{(1-x+\frac{x^2}{2})\sin^2\theta}{(\sin^2\theta+\frac{m_e^2}{E^2}\cos^2\theta)^2}\cdot\sigma_0(s[1-x]),$$

where $x = E_\gamma/E$, E_γ is the energy of the ISR photon, E is the energy of the electron (or positron) beam in the CM frame, $\sqrt{s}$ is the total energy of the collision ($\sqrt{s} = 2E$), m_e is the electron mass, α is the fine structure constant and $\sigma_0(s)$ is the cross-section of hadronic production in e^+e^- annihilation.

For a given x, up to m_e^2/s terms, the angular distribution for the ISR photon to be emitted with respect to the incoming beam is given by (Equation (9) of the reference):

$$\frac{dP}{d\theta} = \frac{\sin^2\theta - \frac{x^2\sin^4\theta}{2(x^2-2x+2)} - \frac{m_e^2}{E^2}\frac{(1-2x)\sin^2\theta - x^2\cos^4\theta}{x^2-2x+2}}{(\sin^2\theta+\frac{m_e^2}{E^2}\cos^2\theta)^2}. \tag{1.1}$$

This distribution was calculated for $\psi(2S)$ events produced via ISR for beams tuned to the $\Upsilon(4S)$ resonance and the results are shown in Figure 1.3. As can be seen in the figure, ISR events are primarily produced along the beam-line $(\cos(\theta) = \pm 1)$. This is relevant when trying to detect ISR photons in e^+e^- colliders as there are usually gaps in the detector coverage near the beam-line, as will be discussed in later chapters.

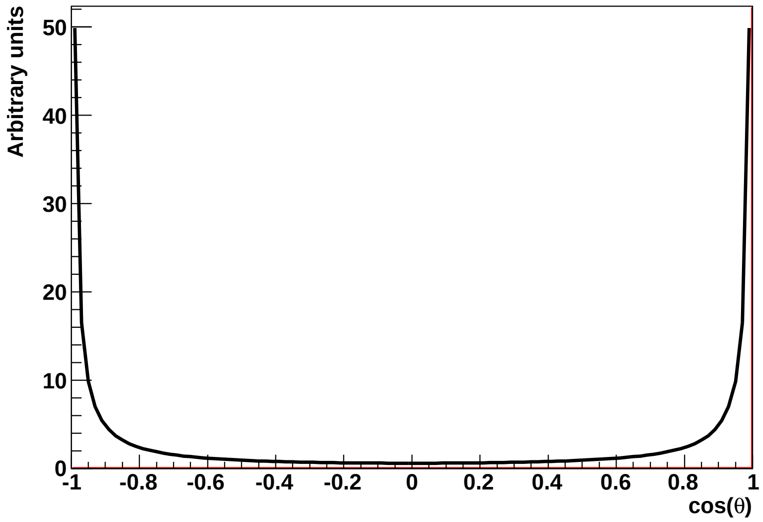

Figure 1.3: The angular distribution for ISR events for angle θ relative to the incoming electron, calculated for radiative return to the $\psi(2S)$ for a beam tuned to the $\Upsilon(4S)$ resonance.

Integrating over θ, at first order in α, the probability function for an ISR photon to be emitted with fraction x, of the total event energy is (Equation (4) of the reference):

$$W(s,x) = \frac{2\alpha}{\pi \cdot x} \cdot (L-1) \cdot (1 - x + \frac{x^2}{2}), \quad L = 2\ln\frac{\sqrt{s}}{m_e}.$$

The leading α^2 corrections are also known, and at α^2 order this becomes (Equation (8) of the reference):

$$\begin{aligned} W(s,x) &= \Delta \cdot \beta x^{\beta-1} - \frac{\beta}{2}(2-x) + \\ & \frac{\beta^2}{8}\left\{(2-x)[3\ln(1-x) - 4\ln x] - 4\frac{\ln(1-x)}{x} - 6 + x\right\}, \end{aligned} \tag{1.2}$$

where:

$$\begin{aligned}
\Delta &= 1 + \frac{\alpha}{\pi}\left(\frac{3}{2}L + \frac{1}{3}\pi^2 - 2\right) + \left(\frac{\alpha}{\pi}\right)^2 \delta_2, \\
\delta_2 &= \left(\frac{9}{8} - 2\zeta_2\right) L^2 - \left(\frac{45}{16} - \frac{11}{2}\zeta_2 - 3\zeta_3\right) L - \\
& \quad \frac{6}{5}\zeta_2^2 - \frac{9}{2}\zeta_3 - 6\zeta_2 \ln 2 + \frac{3}{8}\zeta_2 + \frac{57}{12}, \\
\beta &= \frac{2\alpha}{\pi}(L-1), \quad \zeta_2 = 1.64493407, \quad \zeta_3 = 1.2020569.
\end{aligned}$$

Figure 1.4 plots this probability function, as a function of the energy of the resultant e^+e^- system, which corresponds to the mass of the state that can be produced after the emission of the ISR photon. This was done for a beam tuned to the $\Upsilon(4S)$ resonance. The probability function for an ISR photon is slowly varying in the $\psi(2S)$ and $Y(4260)$ mass region, which is important for this study.

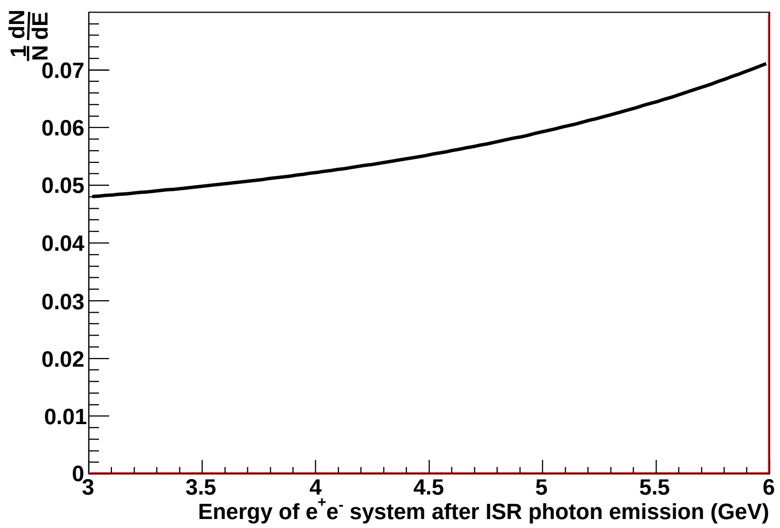

Figure 1.4: The probability function for an ISR event to occur as a function of the energy of the resultant e^+e^- system, for beams which are tuned to the $\Upsilon(4S)$ resonance. Here N is the number of events and E is the energy of the e^+e^- system after ISR photon emission.

1.5 The discovery of the $Y(4260)$

In 2005, the *BABAR* collaboration announced the discovery of a new state, which they called the $Y(4260)$ [25]. The $Y(4260)$ showed up as an enhancement in the $\pi^+\pi^- J/\psi$ invariant mass spectrum produced via ISR events. The *BABAR* experiment, see Ref. [26], has a similar design and purpose to the Belle experiment, which will be discussed in Chapter 2.

BABAR first noticed the enhancement while conducting a search for the $X(3872)$ in ISR events in a subsample of their data. They then conducted a blind search using the remainder of their data. For the blind search, they optimised their selection criteria using the $\psi(2S)$ control sample events in the regions adjacent to the observed peak. Once unblinded, *BABAR* found a peak with large significance, which they fitted using an unbinned maximum likelihood fit with a Breit-Wigner signal function and second order polynomial background, reproduced in Figure 1.5. The results of this fit can be seen in the top row of Table 1.4. Additionally, the observed $M(\pi^+\pi^-)$ distribution for these events was found to be inconsistent with phase space.

Table 1.4: The results of fitting a non-relativistic Breit-Wigner to the $\pi^+\pi^- J/\psi$ invariant mass spectrum produced via ISR in various experiments. The results in Belle (2006) were superseded by the results in Belle (2007). In Belle (2007), the fit involving a single non-relativistic Breit-Wigner was not the primary fit used in the analysis; for the results of the main fit, see Table 1.5. The results of *BABAR* (2005) were updated in *BABAR* (2008). Here the first errors are statistical and the second, where available, are systematic.

	Yield	Mass (MeV)	Width (MeV)	$\Gamma_{ee} \cdot \mathcal{B}$ (eV)
BABAR (2005) [25]	125 ± 23	$4259 \pm 8\ ^{+2}_{-6}$	$88 \pm 23\ ^{+6}_{-4}$	$5.5 \pm 1.0\ ^{+0.8}_{-0.7}$
CLEO (2006) [27]	$13.6\ ^{+4.7}_{-3.9}$	$4284\ ^{+17}_{-16} \pm 4$	$73\ ^{+39}_{-25} \pm 5$	$8.9\ ^{+3.9}_{-3.1} \pm 1.8$
Belle (2006) [28]	165 ± 24	$4295 \pm 10\ ^{+10}_{-3}$	$133 \pm 26\ ^{+13}_{-6}$	$8.7 \pm 1.1\ ^{+0.3}_{-0.9}$
Belle (2007) [29]	–	4263 ± 6	126 ± 18	9.7 ± 1.1
BABAR (2008) [30]	344 ± 39	$4252 \pm 6\ ^{+2}_{-3}$	$105 \pm 18\ ^{+4}_{-6}$	$7.5 \pm 0.9 \pm 0.8$

The $Y(4260)$ signal has since been confirmed in ISR by both CLEO in 2006 [27] and Belle, initially at the International Conference on High Energy Physics, ICHEP, in 2006 (Moscow) [28], which was superseded by a journal publication in 2007 [29]. The CLEO detector is described in Refs [31, 32, 33]. Since then *BABAR* have produced an updated result which was presented at the ICHEP in 2008 (Philadelphia) [30]. In all of these searches, the $\pi^+\pi^- J/\psi$ invariant mass spectrum was fitted with a Breit-Wigner signal function over a polynomial background; the results of these fits can be seen in Table 1.4. The production rate in these modes was measured as a product of the width to two electrons, Γ_{ee}, and the branching fraction to the observed decay mode, $\mathcal{B}(Y(4260) \to \pi^+\pi^- J/\psi)$. This will be shortened to $\Gamma_{ee} \cdot \mathcal{B}$. The central mass, width and production rate measured by each experiment are consistent with each other, though with large errors on the width. However the single Breit-Wigner with polynomial background function was not the primary fit function used in the Belle 2007 result. The Belle 2007 paper, in addition to the above fit function, also used a fit where the background function was fixed using the results of a fit to the $M(\pi^+\pi^- J/\psi)$ distribution from the J/ψ

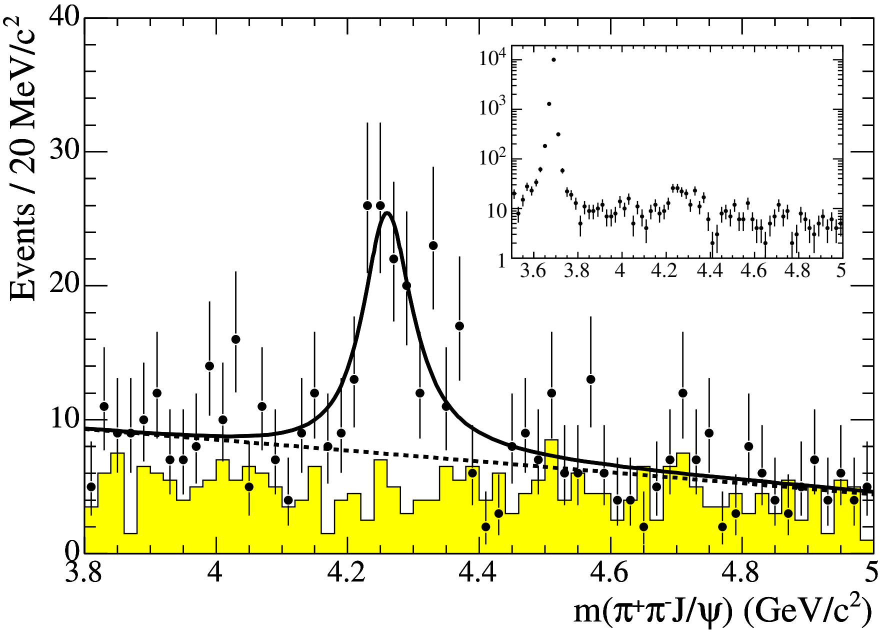

Figure 1.5: The $\pi^+\pi^- J/\psi$ invariant mass spectrum produced via ISR measured by *BABAR*. Reproduced from Ref. [25]. The data points are events from the J/ψ signal region and the solid yellow histogram are the results from the J/ψ sidebands, described in the reference. The solid line shows the fit used in the reference to measure the properties of the $Y(4260)$ and the inset is the $\pi^+\pi^- J/\psi$ invariant mass spectrum on a log scale including the $\psi(2S)$ mass region.

sidebands, and all the events above this attributed to two interfering Breit-Wigner signal functions. There are two solutions for this fit function, one with constructive and the other with destructive interference. The results of this fit can be see in Table 1.5, where the $Y(4260)$ signal is the second resonance, $R2$. The Belle 2007 and *BABAR* 2008 $\pi^+\pi^- J/\psi$ invariant mass spectra produced via ISR are reproduced in Figure 1.6.

Table 1.5: Results of the primary fit to the $\pi^+\pi^- J/\psi$ invariant mass spectrum produced via ISR measured by Belle in 2007. The fit was composed of two interfering signal resonances, with background component fixed using the J/ψ sidebands. Resonance $R2$ corresponds to the $Y(4260)$. Solutions I and II are the results of the fit with constructive and destructive interference, with the interference parameter, ϕ, for Solutions I and II shown in the bottom row. Here the first errors are statistical and the second errors are systematic.

Parameters			Solution I	Solution II
Mass	(MeV)	$R1$	$4008 \pm 40^{+114}_{-28}$	
Width	(MeV)	$R1$	$226 \pm 44 \pm 87$	
$\Gamma_{ee} \cdot \mathcal{B}$	(eV)	$R1$	$5.0 \pm 1.4^{+6.1}_{-0.9}$	$12.4 \pm 2.4^{+14.8}_{-1.1}$
Mass	(MeV)	$R2$	$4247 \pm 12^{+17}_{-32}$	
Width	(MeV)	$R2$	$108 \pm 19 \pm 10$	
$\Gamma_{ee} \cdot \mathcal{B}$	(eV)	$R2$	$6.0 \pm 1.2^{+4.7}_{-0.5}$	$20.6 \pm 2.3^{+9.1}_{-1.7}$
ϕ	(degrees)		$12 \pm 29^{+7}_{-98}$	$-111 \pm 7^{+28}_{-31}$

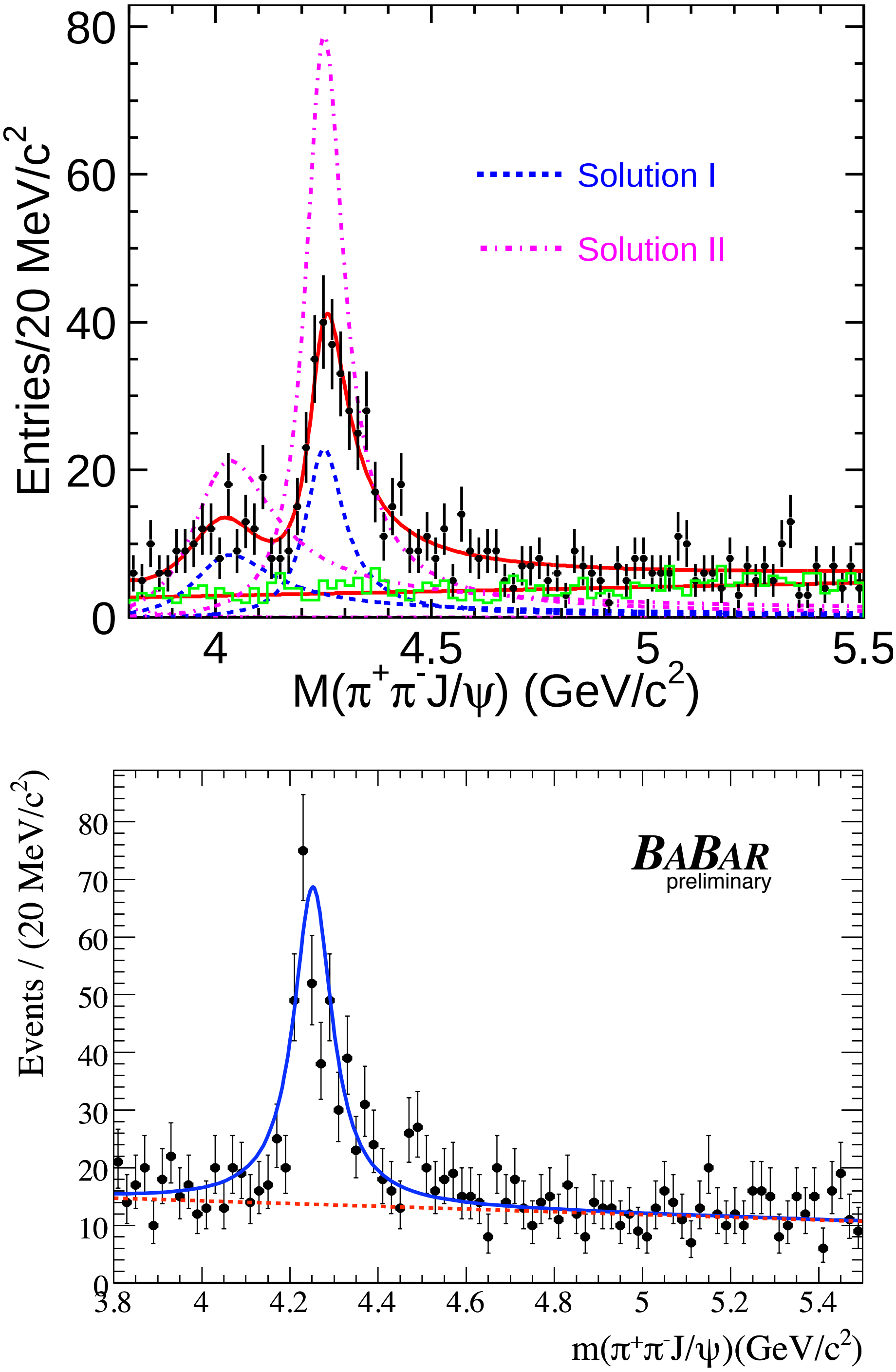

Figure 1.6: The fits to the most recent Belle and *BABAR* $\pi^+\pi^- J/\psi$ invariant mass distributions. These plots are reproduced from Belle (2007) [29] and *BABAR* (2008) [30], for the top and bottom plots respectively, where the details of the fits and selection are described. In both plots, the data is represented by points with error bars and in the top plot, the data from the J/ψ sidebands is shown as a histogram with a solid green line. The solid and dashed lines represent the fits to data, described in the respective reference for each plot.

1.5.1 Related results

Separate to the results in the $\pi^+\pi^- J/\psi$ mode produced via ISR, there are several other decay modes which shed light on what is happening in this mass region. The following results will be discussed in this section: *BABAR* saw an enhancement at a similar mass to the $Y(4260)$ in $B \to K\pi^+\pi^- J/\psi$ decays in 2006. In addition to the $\pi^+\pi^- J/\psi$ mode produced via ISR, CLEO also measured several other decay modes produced in direct e^+e^- annihilation at 4260 MeV, including the $K^+K^- J/\psi$ mode. The $K^+K^- J/\psi$ mode has also been measured by Belle in ISR. Belle and *BABAR* have also measured $\pi^+\pi^-\psi(2S)$ as well as various $D\overline{D}$ decay modes produced via ISR. The total width for $e^+e^- \to hadrons$ has also been measured for this mass range, which has led to limits on the branching ratio for $Y(4260) \to \pi^+\pi^- J/\psi$.

After *BABAR*'s initial discovery, they attempted to identify the $Y(4260)$ in the decays of B mesons [34]. *BABAR* searched for the decay $B^- \to K^- Y(4260)$, $Y(4260) \to \pi^+\pi^- J/\psi$.[7] They saw a small enhancement at 4.26 GeV over a large combinatorial background. Fixing the mass and width to the values observed in their ISR study, they fitted the enhancement and found a yield of 128 ± 42 signal events. This provided a statistical significance, calculated from $\sqrt{-2\ln\mathcal{L}_0/\mathcal{L}}$, of 3.1σ, where $\mathcal{L}$ ($\mathcal{L}_0$) are the likelihoods of the signal (null) fits. They found the 95% confidence level, C.L., upper limit on the branching fraction to be $\mathcal{B}(B^- \to K^- Y(4260),\ Y(4260) \to \pi^+\pi^- J/\psi) < 2.9 \times 10^{-5}$.

CLEO measured the cross-section of various final states in direct e^+e^- annihilation at $\sqrt{s} = 4.26$ GeV, shown in Table 1.6. Whilst they could not measure a line shape, they were able to measure the production rate in many modes. Specifically, they found in the $\pi^0\pi^0 J/\psi$ mode, approximately half the production rate of the $\pi^+\pi^- J/\psi$ mode and then for the $K^+K^- J/\psi$ mode, approximately half the production rate again. Belle measured the $K^+K^- J/\psi$ mode produced via ISR [35]. In the $Y(4260)$ mass region they found very few events and produced a cross-section with production rate consistent with the CLEO result within large errors. In the $\pi^+\pi^-\psi(2S)$ channel in direct production, CLEO saw zero events. In this mode produced via ISR, both *BABAR* and Belle have the cross-section in this mass region, in Refs [36] and [37], respectively. Neither experiment found evidence for $Y(4260) \to \pi^+\pi^-\psi(2S)$.

[7] Charge conjugate modes are implied throughout this thesis.

Table 1.6: Results in various reconstruction channels in CLEO from direct e^+e^- annihilation at 4.26 GeV. For each mode $e^+e^- \to X$, the detection efficiency, ϵ; the number of signal (background) events in data, $N_{\rm s}$ ($N_{\rm b}$)] and the cross-section $\sigma(e^+e^- \to X)$ are shown. Upper limits are at 90% C.L. Table extracted from Ref. [38], with the ratio of branching fractions: $\frac{\mathcal{B}(Y\to X)}{\mathcal{B}(Y\to\pi^+\pi^- J/\psi)}$, calculated in Ref. [39] based on the measurements in this table.

Channel	ϵ (%)	$N_{\rm s}$	$N_{\rm b}$	σ (pb)	$\frac{\mathcal{B}(Y\to X)}{\mathcal{B}(Y\to\pi^+\pi^- J/\psi)}$
$\pi^+\pi^- J/\psi$	38	37	2.4	$58^{+12}_{-10}\pm4$	1
$\pi^0\pi^0 J/\psi$	22	8	0.3	$23^{+12}_{-8}\pm1$	$0.39^{+0.20}_{-0.15}\pm0.02$
$K^+K^- J/\psi$	21	3	0.07	$9^{+9}_{-5}\pm1$	$0.15^{+0.10}_{-0.08}\pm0.02$
$\eta J/\psi$	16	5	2.7	<32	<0.6
$\pi^0 J/\psi$	22	1		<12	<0.2
$\eta' J/\psi$	11	0	1.5	<19	<0.3
$\pi^+\pi^-\pi^0 J/\psi$	22	0		<7	<0.1
$\eta\eta J/\psi$	6	1		<44	<0.8
$\pi^+\pi^-\psi(2S)$	19	0		<20	<0.3
$\eta\psi(2S)$	15	0		<25	<0.4
$\omega\chi_{c0}$	9	11	11.5	<234	<4.0
$\gamma\chi_{c1}$	26	1	3.3	<30	<0.5
$\gamma\chi_{c2}$	27	4	3.3	<90	<1.6
$\pi^+\pi^-\pi^0\chi_{c1}$	9	0		<46	<0.8
$\pi^+\pi^-\pi^0\chi_{c2}$	9	0		<96	<1.7
$\pi^+\pi^-\phi$	18	7	5.5	<5	<0.1

Belle, CLEO and *BABAR* have all measured various $D\overline{D}$ decay modes produced via ISR, or direct e^+e^- annihilation, and none of these measurements have provided any evidence for $Y(4260) \to D\overline{D}$. Here D stands for charged or neutral mesons containing a single charm quark in the ground or excited state. The list of $D\overline{D}$ decay modes studied by these experiments is summarised, with references, in Table 1.7. Specifically, Refs [40, 41, 42] noted a minimum in the $D\overline{D}$ cross-section near the mass of the $Y(4260)$. Some references produced a ratio for the production rate of selected $D\overline{D}$ decay modes and the rate of $\pi^+\pi^- J/\psi$ production; these are summarised in Table 1.8.

Table 1.7: $D\overline{D}$ decay modes studied by Belle and *BABAR* in ISR and CLEO in direct e^+e^- annihilation, with references.

	Studied by: (Ref.)		
Decay mode	Belle	*BABAR*	CLEO
$D^0\overline{D}^0$	[43]	[44, 41]	[45]
$D^{*0}\overline{D}^{*0}$		[41]	[45]
$D^{0*}\overline{D}^0$		[41]	[45]
D^+D^-	[43]	[44, 41]	[45]
D^+D^{*-}	[40]	[41]	[45]
$D^{*+}D^{*-}$	[40]	[41]	[45]
$D_s^+D_s^-$	[42]	[46]	[45]
$D_s^+\overline{D}_s^{*-}$	[42]	[46]	[45]
$D_s^{*+}\overline{D}_s^{*-}$	[42]	[46]	[45]
$D^0D^-\pi^+$	[47]		
$D^0D^{*-}\pi^+$	[48]		

Table 1.8: Ratio of branching fractions for $Y(4260)$ to selected $D\overline{D}$ decay modes and $\pi^+\pi^- J/\psi$ in Belle, *BABAR* and CLEO at 90% C.L., except where noted.

Final state (X)	Belle $\frac{\mathcal{B}(Y \to X)}{\mathcal{B}(Y \to \pi^+\pi^- J/\psi)}$	*BABAR* $\frac{\mathcal{B}(Y \to X)}{\mathcal{B}(Y \to \pi^+\pi^- J/\psi)}$	CLEO $\frac{\sigma(Y \to X)}{\sigma(Y \to \pi^+\pi^- J/\psi)}$
$D\overline{D}$		< 1.0 [44]	< 4.0 [45]
$D^*\overline{D}$		< 34 [41]	< 45 [45]
$D^*\overline{D}^*$		< 40 [41]	< 11 [45]
$D^0 D^{*-}\pi^+$	< 9 [48]		< 15 [45]
$D^{*0} D^{*-}\pi^+$			< 8.2 [45]
$D_s^+ D_s^-$		< 0.7 at 95% C.L. [46]	< 1.3 [45]
$D_s^+ \overline{D}_s^{*-}$		< 44 at 95% C.L. [46]	< 0.8 [45]
$D_s^{*+} \overline{D}_s^{*-}$		< 30 at 95% C.L. [46]	< 9.5 [45]

The observed $Y(4260)$ signal occurs at a local minimum for the total hadronic cross-section, $e^+e^- \to hadrons$. This can be seen in the R values, the ratio $R = \sigma(e^+e^- \to hadrons)/\sigma(e^+e^- \to \mu^+\mu^-)$, measured by the BES collaboration in Ref. [49] and reproduced in Figure 1.7. By comparing the R values to the production rate for $Y(4260) \to \pi^+\pi^- J/\psi$ measured by *BABAR* [25], the authors of Ref. [50] calculated that $\Gamma(Y(4260) \to e^+e^-) < 580$ eV at 90% C.L. From this they also calculated that $\mathcal{B}(Y(4260) \to \pi^+\pi^- J/\psi) > 0.58\%$ at 90% C.L.

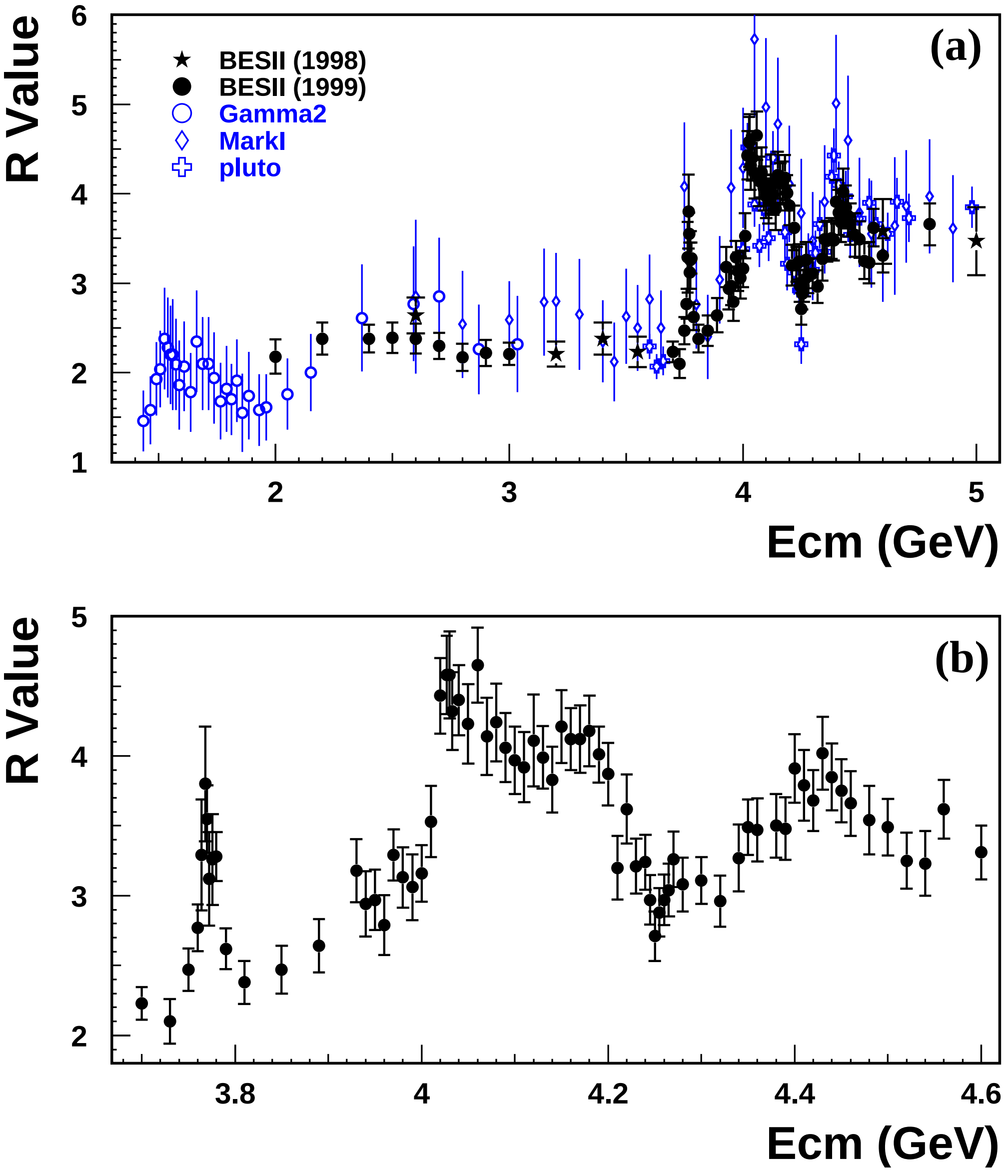

Figure 1.7: Top: values of ratio $R = \sigma(e^+e^- \to hadrons)/\sigma(e^+e^- \to \mu^+\mu^-)$ measured by various experiments with respect to the CM energy, E_{CM}. Bottom: R values measured in the $Y(4260)$ mass region by the BES collaboration. Reproduced from Ref. [49].

1.6 Theoretical interpretations

When considering possible theoretical models for the structure of the $Y(4260)$, it was noted that this particle has several features that make it difficult to assign it as a conventional meson. Firstly, the $Y(4260)$ has a prominent decay to a J/ψ and light hadrons, therefore it is expected to have $c\bar{c}$ content. From the production mechanism, ISR, it is known to have $J^{PC} = 1^{--}$ quantum numbers. These two features would normally place it as a ψ state in the charmonium spectrum. However, the radial excitations of the ψ states are already well established in this mass region and line up well with predictions [51, 52]. So the $Y(4260)$ would appear to be an overpopulation of the ψ states. Additionally, the $Y(4260)$ does not behave like other ψ states in this mass region, for example, the width for the decay to e^+e^-, Γ_{ee}, is smaller than that of the other $J^{PC} = 1^{--}$ charmonia and the decay to $\pi^+\pi^- J/\psi$ is larger than that of the other charmonia in this mass range [53]. Also, as would be unusual for a $c\bar{c}$ state above the $D\overline{D}$ threshold, decays to open charm have not been observed. For these reasons, several models have been proposed for the structure of the $Y(4260)$; these models and their predictions for the $Y(4260)$ will be discussed in this section.

Conventional charmonium assignments for the $Y(4260)$, which involve the reassignment of other observed ψ states, have been attempted; these will be discussed in Section 1.6.1. There have also been proposals that the $Y(4260)$ is not a true resonance at all, but instead the result of the opening of the $D_s^*\overline{D}_s^*$ threshold combined with the depletion of the $\pi^+\pi^- J/\psi$ spectrum around 4.26 GeV, which will be discussed in Section 1.6.2. If the $Y(4260)$ is indeed resonant and not a conventional charmonium meson, then it is a candidate to have a structure proposed by other more exotic hypotheses. These include the possibility that the $Y(4260)$ is a quark-gluon hybrid, discussed in Section 1.6.3, a molecular state, discussed in Section 1.6.4, or, that the $Y(4260)$ is a tetraquark or glueball state, discussed in Section 1.6.5.

1.6.1 The $Y(4260)$ as a conventional meson

In order to accommodate the $Y(4260)$ as a conventional charmonium state, Refs [54, 55] have suggested adjusted models of the charmonium system. For the $Y(4260)$ to be produced via ISR it must be a $J^{PC} = 1^{--}$ S-wave or D-wave state, where S and D are the orbital angular momentum quantum numbers [56]. The models proposed in Refs [54, 55] predict lower masses for the ψ states, such that they assign the $Y(4260)$ to the $\psi(4S)$ state. The authors of Ref. [54] then assign the $\psi(4415)$, which is currently favoured as the $\psi(4S)$ state, to the $\psi(5S)$ resonance. The authors note that the branching fraction to $\pi^+\pi^-J/\psi$ is still too large in their models, but they hypothesise that this could be due to final state interactions between charmed mesons. The author of Ref. [55] proposes that the large branching fraction to $\pi^+\pi^-J/\psi$ could be due to the $Y(4260)$ being an admixture with a small four-quark component of $J/\psi f_j$, $j = 0, 1, 2,$ etc. In this model, the non-observation in the K^+K^-J/ψ mode could be due to a phase space effect enhanced by other possible features and the lack of decays to $D\overline{D}$ modes could be due to $S - D$ wave interference. Reference [56] specifically excludes the possibility of the $Y(4260)$ being interpreted as a D wave state, as the expected decay width for these states to $D\overline{D}$ pairs is 125 MeV, which is larger than the total observed width.

1.6.2 The $Y(4260)$ as non-resonant $\pi^+\pi^-J/\psi$ production

There is also the possibility that the $Y(4260)$ is not a true resonance, but an enhancement due to a different phenomenon. An interesting feature of the $Y(4260)$ is the line shape observed by both *BABAR* and Belle, see Figure 1.6. Specifically there is a sharp turn on of the signal at approximately 4.2 GeV. The authors of Ref. [57], noting that the $Y(4260)$ signal is between the resonances $\psi(4160)$ and $\psi(4415)$, attempted to see whether the interference between these two charmonium states could affect the shape of non-resonant $\pi^+\pi^-J/\psi$ production and were able to reproduce the observed line shape. The separate possibility that the $Y(4260)$ is a phenomenon connected with the opening of the $D_s^*\overline{D}_s^*$ threshold with a coupling to the $f_0(980)J/\psi$ channel, is discussed in a series of papers by the authors of Refs [58, 59, 60, 61]. They point out that the $Y(4260)$ peak observed by both Belle and *BABAR* has a line shape that does not fit well to a Breit-Wigner and may be better described by a sharp rise at threshold and a flatter fall off. The sharp rise coincides with the $D_s^*\overline{D}_s^*$ threshold at 4424 ± 1 MeV [1], where strange quarks are able to be produced with $c\bar{c}$ near rest. These strange quarks would then couple to the $f_0(980)$. However, they conclude that the $Y(4260)$ signal arises not only from the threshold effect. They point out that the known charmonium $J^{PC} = 1^{--}$ states are not seen in the $\pi^+\pi^-J/\psi$ channel and propose that decays by these states to $D\overline{D}$ are depleting the $\pi^+\pi^-J/\psi$ signal, leaving what remains to show up as the $Y(4260)$ peak.

The possible interpretations of the structure of the $Y(4260)$, assuming that the $Y(4260)$ is both resonant and not a conventional charmonium state, will now be discussed.

1.6.3 The $Y(4260)$ as a quarkonium-gluon hybrid

One of the more exotic proposals for the structure of the $Y(4260)$ is that it may be the first observation of a quarkonium-gluon hybrid, with structure $c\bar{c}g$. Prior to the discovery by *BABAR*, the authors of Ref. [53] had predicted a $c\bar{c}g$ state using the fluxtube model with mass of ≈ 4200 MeV and with width, production rate and decays consistent with the observed $Y(4260)$. References [53, 62] provide details of the models and selection rules which prevent hybrids from decaying to a pair of D mesons, consistent with the non-observation in open charm modes and the large branching for the decay to $\pi^+\pi^- J/\psi$. Both these papers note that the lowest two-body decay to open charm available for quarkonium-gluon hybrids is the $D^{**}\overline{D}$ channel and the $Y(4260)$ is below threshold. References [53, 63] note that the mass of the $Y(4260)$ may be attracted to the $D_1(2420)D$, $D_1'\overline{D}$ and $D^*\overline{D}_0$ thresholds, thus allowing the mass be higher than that predicted by theory. However, the authors of Ref. [55] suggest, using similar selection rules to those that forbid a $c\bar{c}g$ hybrid decaying to $D\overline{D}$, that the decay to a J/ψ final state is unlikely and that hybrids would prefer to decay to a P-wave meson, such as a χ_c meson. They also suggest that it is unlikely for a $c\bar{c}g$ hybrid to couple to a photon due to the separation of the charm quarks in the fluxtube model, stopping production via ISR.

In other decay modes, if the $Y(4260)$ is a ccg hybrid, then Ref. [52] predicts that the state should decay to $\pi^0\pi^0 J/\psi$ with half the rate of the $\pi^+\pi^- J/\psi$ mode and also to $\eta\eta J/\psi$, though that mode may be suppressed due to phase space. Reference [53] notes that the mass of the pair of pions in the Belle and *BABAR* data is consistent with peaks at the mass of the σ and the mass of the $f_0(980)$ and $a_0(980)$ mesons. Therefore, they expect that the decay to $K^+K^- J/\psi$ should be important and Ref. [64] expects this mode to have comparable branching fraction. The authors of Ref. [62] expect the dominant decay for the $Y(4260)$ to be to $D^{(*)}D^{(*)}n\pi$, where n is an integer, which they suggest may explain the large observed width and the authors of Ref. [53] predict decays to $D^{(*)}D\pi$ and D_sD_s.

1.6.4 The $Y(4260)$ as a molecular state

Another proposal with exotic structure is the possibility that the $Y(4260)$ is a molecular state of two or more other particles that are normally distinct. Several combinations have been proposed in the literature which have about the right mass and may or may not match the other observed features of the $Y(4260)$. References [64] and [65] both considered states where the expected charm anticharm component of the $Y(4260)$ is bound in a charmonium particle, which is lightly bound to a meson made from light quarks. The $(\chi_{c1}\rho^0)$ and $(\chi_{c1}\omega)$ molecules were proposed in Ref. [64] and Ref. [65], respectively. In both these models they suggest that decays to $D\overline{D}$ would be suppressed. If the $Y(4260)$ were a $(\chi_{c1}\rho^0)$ state then the mass of the pions in the decay to $\pi^+\pi^- J/\psi$ should peak at the ρ^0 mass. Additionally, the decay to $K^+K^- J/\psi$ should be suppressed and there should be partner states: $(\chi_{c0}\rho^0)$, $(\chi_{c2}\rho^0)$ and $(\chi_{c1}\rho^\pm)$ [64]. As the ρ^0 decays to $\pi^+\pi^-$ and does not decay to $\pi^0\pi^0$ [1], decays to $\pi^0\pi^0 J/\psi$ should be suppressed relative to the $\pi^+\pi^- J/\psi$ decay mode [64]. If the $Y(4260)$ were a $(\chi_{c1}\omega)$ state, then it should decay to $\pi^+\pi^-\pi^0\chi_{c1}$ at a similar rate to $\pi^+\pi^- J/\psi$ and to $\pi^0\pi^0 J/\psi$ at half that rate; it also should have no partners [65].

The other possibility for molecular states made from a pair of mesons is that the expected charm and anticharm quarks are instead each bound with a light quark in their own D meson. Reference [52] mentions that the width of the $Y(4260)$ disfavours combinations of ground state $(D\overline{D})$ molecules. $(D_1\overline{D})$ and $(D_0\overline{D}^*)$ molecules were studied in Ref. [66] and found to be possible. In their model the molecules could be bound via pion or η exchange. However, the authors of Refs [67] point out that parity conservation forbids pion exchange other than between the two states $(D_1\overline{D}) \to (D_0\overline{D}^*)$, and therefore pion exchange would not play the leading role in the binding of these molecules. They propose instead a molecule composed of the heavier $(D_1(2420)D^*(2010))$ combination, where the binding from the pion exchange is of order 100 MeV. They follow up this discussion in Ref. [68] and predict that the $Y(4260)$ would have a large branching to $D\overline{D}3\pi$, in comparison to a $(D_1\overline{D})$ or $(D_0\overline{D}^*)$ molecule which would decay to $D\overline{D}2\pi$. Reference [69] believes that if the $Y(4260)$ is a $(D\overline{D}_1)$ molecule, it may be visible in $D\overline{D}^*\pi$. They also predict, in this case, that there should be an excited state which decays to $\pi^+\pi^-\psi(2S)$.

Distinct from the models of meson molecules discussed so far, the authors of Ref. [70] propose that the $Y(4260)$ may be a baryonium state, with structure

$(\lambda_c^+\lambda_c^-)$. This baryonium state would be a combination of baryons similar to helium. In this model they note that two-body decays, and decays to $D\overline{D}$, would be suppressed and three-body decays favoured. In their model the $Y(4260)$ should decay to $D^*\overline{D}^*\pi$, but not decay to $D\overline{D}\pi$ due to conservation laws. The λ_c particles in their model are not required to have neutral colour charge, which they suggest could explain the large energy difference between the $Y(4260)$ mass and the $\lambda_c^+\lambda_c^-$ threshold at 4572.9 ± 0.3 MeV [1]. They propose that a molecular $(\lambda_c^+\lambda_c^-)$ state would have a low branching to $p\bar{p}$ and predict that the it should decay to $\pi^+\pi^-\psi(2S)$ with branching $\approx 0.08 \times \mathcal{B}(Y(4260) \to \pi^+\pi^- J/\psi)$. This state should also decay to $\pi^0\pi^0 J/\psi$ with half the rate of the $\pi^+\pi^- J/\psi$ mode, while decays to $K^+K^- J/\psi$ should be suppressed.

Lastly among the the molecular interpretations of the $Y(4260)$, Ref. [71] considers the possibility that the $Y(4260)$ is not a two-body bound state, but a three-body $(K\overline{K}J/\psi)$ state. In their model they find a three-body state with similar mass and width to the $Y(4260)$, which would decay to $\pi^+\pi^- J/\psi$. However in this model the decay to $K^+K^- J/\psi$ should be larger than the decay to $\pi^+\pi^- J/\psi$, which is inconsistent with the experimental observations, see Section 1.5.1.

1.6.5 Other possible structures for the $Y(4260)$

The last two non-standard meson-like structures that have been proposed in the literature are that the $Y(4260)$ may be a non-molecular tetraquark, or a glueball, without constituent quark content at all. The mass of the $Y(4260)$ is about right for it to be considered as the first orbital excitation of a $cs\bar{c}\bar{s}$ tetraquark [72], though some studies suggest that this combination should be unbound, see Section 1.3.1. If this structure were correct, the decays to $K^+K^- J/\psi$ and $D_s\overline{D}_s$ should be larger that the decay to $\pi^+\pi^- J/\psi$, however these decays have not been observed. Specifically, CLEO finds that the production rate of $K^+K^- J/\psi$ is much lower than the production rate of $\pi^+\pi^- J/\psi$, in direct e^+e^- annihilation at 4.26 GeV [38] and the Belle results in ISR agree [35]. Also both CLEO and BABAR place upper limits on the production rate of $D_s^+D_s^-$ from $Y(4260)$ at around the production rate of the $\pi^+\pi^- J/\psi$ mode, see Table 1.8. The $Y(4260)$ could also have separate tetraquark structure: $(\frac{1}{\sqrt{2}}[u\bar{u}+d\bar{d}]+c\bar{c})$, however, this structure should decay to $D\overline{D}$ with large width [52, 73, 74], which is not observed. Lastly, if the $Y(4260)$ were a tetraquark, then it should exist as part of a flavour nonet [52, 72], with partners in a similar mass range. One of these partners would also have $J^{PC} = 1^{--}$ and may be visible in the $\pi^+\pi^-\pi^0 J/\psi$ channel.

Finally, the glueball structure is considered unlikely, see Section 1.3.4, as gluons would not couple to the ISR photon, making the production unlikely. Also, the decays of glueballs are expected to be flavour-blind, so if the $Y(4260)$ were a glueball it should decay to multiple light mesons with large phase space. This would mean that the decay to $\pi^+\pi^- J/\psi$ would not be dominant [52]. If this model were correct, then Ref. [55] predicts the decay to $\pi^+\pi^-\phi$ should be measurable in the $\pi^+\pi^- K^+K^-$ channel.

1.7 Conclusion

The $Y(4260)$ is a newly observed state with expected charm anticharm content, that does not fit easily within the known charmonium spectrum and is thus a candidate for a being a particle with a more exotic structure. In this chapter, an outline of the theory of QCD was presented and used to discuss the current theoretical understanding of the structure of mesons, and in particular the charmonium system. From there, an overview of models with exotic, meson-like structures was presented. The interactions at colliders that can produce these states was discussed, before the discovery of the $Y(4260)$ and its properties was presented. Finally, because some of the observed properties of the $Y(4260)$ make its structure difficult to determine, the competing theoretical interpretations of this state were presented. There are multiple incompatible models for the structure of the $Y(4260)$ that have been proposed; these include adjustments to the models of charmonium that allow the $Y(4260)$ to be assigned to the $\psi(4S)$ state, and the suggestion that the $Y(4260)$ may be non-resonant resonant $\pi^+\pi^- J/\psi$ production that is being influenced by thresholds or interference with surrounding states. In addition to these two conventional possibilities, the $Y(4260)$ is a candidate for a more exotic structure, such as being the first observation of a quarkonium-gluon hybrid, a molecular state, or a tetraquark state.

In order to understand the $Y(4260)$, more experimental information is required and forms the basis for the searches performed in this thesis. In the next chapter, the Belle experiment, including detector, collider and organisation, will be described. The work presented in this thesis was begun in late 2005 after *BABAR*'s initial discovery. The first step undertaken was to confirm the existence of the $Y(4260)$ in the discovery mode in Belle data, in Chapter 3. From there, the more difficult to measure experimentally $\pi^0\pi^0 J/\psi$ mode was investigated as a blind analysis, with the development of reconstruction techniques discussed in Chapter 4 and the results from the unblinded data region discussed in Chapter 5. The investigation of this mode will complement the data in the $K^+K^- J/\psi$ and various $D\overline{D}$ modes, produced via ISR, studied at Belle and by other experiments in this mass region and hopefully contribute to the understanding of the $Y(4260)$.

Chapter 2

The Belle Experiment

The Belle detector, located in Tsukuba, Japan, was used to acquire the data used in this thesis. It is described in this chapter along with the Belle collaboration, which built and maintained it, and the KEKB accelerator at the KEK complex, which provided the collisions studied here and by other Belle analyses.

THE Belle collaboration, described in Section 2.1, analyses collisions produced with the KEKB asymmetric energy e^+e^- collider, described in Section 2.2. The collisions are measured using the Belle detector; which is formed from several subdetectors detailed in Section 2.3. Particle identification is performed by combining the output from the various subdetectors; this is discussed in Section 2.4. The dataflow, from the electronic readout to user analysis, is described in Section 2.5. This analysis makes heavy use of the software designed and maintained by the Belle collaboration and other organisations, which will be detailed in Section 2.6.

2.1 Belle collaboration

The Belle collaboration consists of approximately 400 people from 55 institutes in 14 countries. It built, runs and maintains the Belle detector while analysing the large datasets measured with this detector. See Figure 2.1 for a photo of the collaboration from the completion of the detector. The collaboration was formed with the primary purpose of studying CP violation in B decays and now studies many types of B decay. Additionally, other processes, such as τ pair and two-photon interactions, as well as charm mesons produced in the continuum and via higher order QED processes, are studied. Recently, partly as the result of interest in new states, several studies into ISR production have been undertaken. The collaboration is divided into groups and subgroups based on analysis topics. The analyses presented in this thesis were performed within the Charm physics group, which studies decays involving the c quark.

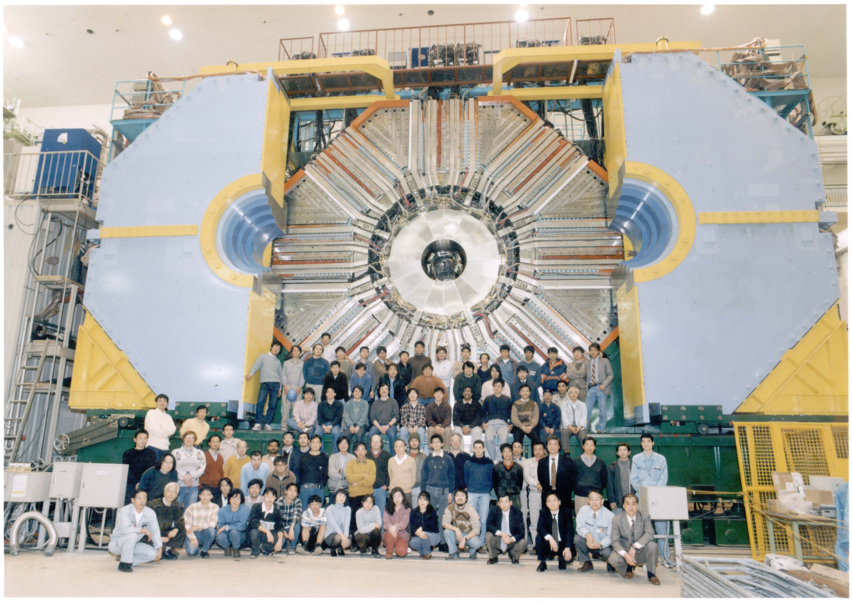

Figure 2.1: A photo of Belle from the completion of the detector. Produced by the Belle collaboration.

2.2 KEKB asymmetric energy e^+e^- collider

The Belle detector is situated at the interaction point of the KEKB e^+e^- collider at KEK in Tsukuba, Japan. An aerial photo and diagram of the KEKB ring is reproduced in Figure 2.2. KEK stands for *Kou Enerugi Kasokuki kenkyuu kikou* or High Energy Accelerator Research Organisation. The “B” at the end of KEKB refers to its primary goal, the production of B mesons. The collider is normally tuned to the $\Upsilon(4S)$ resonance, which decays to $B\bar{B}$ more than 96% of the time. The electron and positron beams are produced at asymmetric energies. The electrons, which are produced at higher energies, are stored in the High Energy Ring, HER, and the positrons stored in the Low Energy Ring, LER. Asymmetric energy collisions are chosen in order to boost the resulting Centre of Mass (CM) frame relative to the laboratory frame. This boost translates the lifetime difference between B and $\bar{B}$ mesons to a difference in the positions of their decay vertices in the z direction, which is measurable using the innermost subdetector of Belle, the Silicon Vertex Detector (SVD), described in Section 2.3. The parameters of the KEKB collider are summarised in Table 2.1.

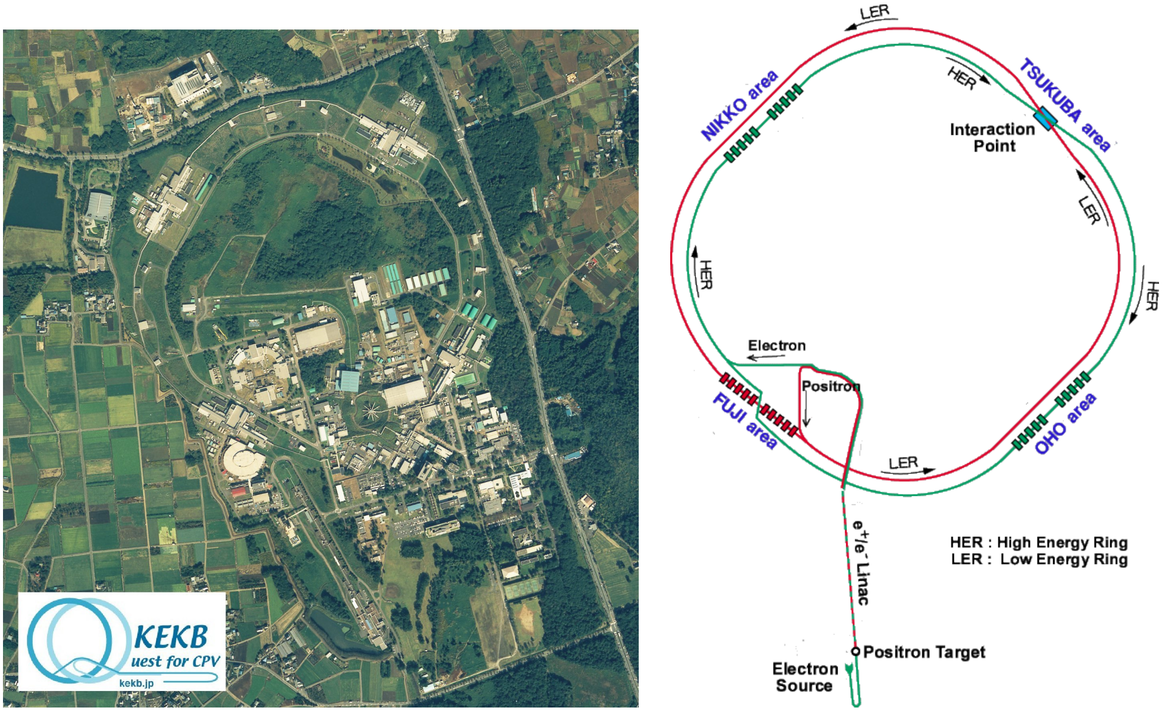

Figure 2.2: Photo, left, and diagram, right, of the KEKB ring.

In addition to $B\bar{B}$ events, KEKB produces other particles. Other interactions that occur include quark jets from $q\bar{q}$ ($q = u,\ d,\ s$ or c), τ pair events, as well as two-photon interactions and other higher order QED processes. When not operating at the $\Upsilon(4S)$ resonance, KEKB also takes data 60 MeV below the $\Upsilon(4S)$ resonance, which is called off-resonance data. Off-resonance data is used to measure the continuum under the $\Upsilon(4S)$ peak, primarily in analyses of B decays. Energy scans and on-resonance runs at the $\Upsilon(3S)$ and $\Upsilon(5S)$ energies have also taken place; henceforth runs taken at the energy of the $\Upsilon(4S)$ resonance will be referred to

Table 2.1: KEKB collider parameters.

Electron beam energy	8.0 GeV
Positron beam energy	3.5 GeV
Crossing Angle	22 milliradians
Boost relative to lab frame	$\beta\gamma = 0.425$

as on-resonance data, and runs taken 60 MeV below the $\Upsilon(4S)$ resonance will be referred to as off-resonance data, while all other runs will be specified. The analysis described in this thesis, which is of particles produced via ISR, uses both the on- and off-resonance datasets. Detailed descriptions of the KEKB accelerators can be found in Refs [75, 76].

Since 2003 KEKB has been operating in continuous top-up mode, where the beams are topped up while the detector is running. This has contributed to KEKB being able to achieve world record luminosity. These factors have contributed to KEKB currently holding the records for peak luminosity: 2.11×10^{34} cm^{-2}s^{-1} and one day integrated luminosity of 1.479 fb^{-1}, both achieved in 2009. Figure 2.3 reproduces a diagram of the interaction region and the integrated luminosity achieved over time by KEKB.

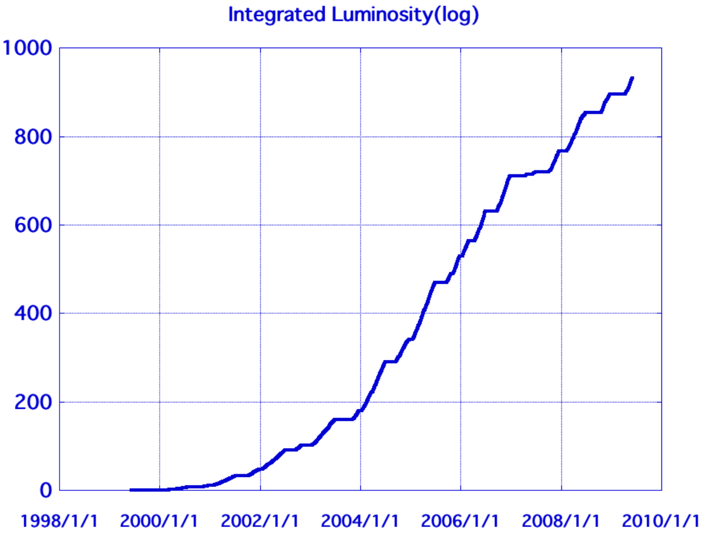

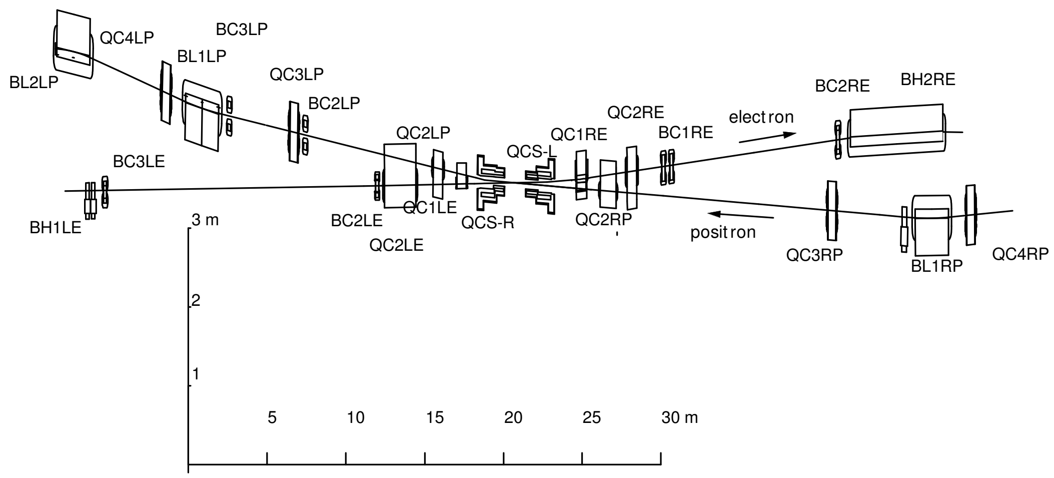

Figure 2.3: Top: the log of the total integrated luminosity of KEKB over time in fb^{-1}, from Ref. [77]. Bottom: a diagram of the beam interaction region, with beams and magnets indicated and separate horizontal and vertical scales, from Ref. [78]

2.3 The Belle Detector

The Belle detector began operation in 1999 and is described in detail in the Belle detector book [78]. The Belle detector is a barrel-shaped detector with several subdetectors arranged in layers around the interaction point. The subdetectors, from innermost to outermost are:

SVD Silicon Vertex Detector: The SVD is used to measure the decay vertices of charged particles. (Section 2.3.1.)

CDC Central Drift Chamber: The CDC is primarily used for charged particle tracking and low momentum particle identification. (Section 2.3.2.)

ACC Aerogel Čerenkov Counters: The ACC is used for particle identification, specifically to distinguish between charged pions and kaons in the momentum region around 1 to 2 GeV. (Section 2.3.3.)

TOF Time Of Flight: The TOF provides measurement of the time of flight. TOF information for a particle with a given momentum over the known distance from the interaction point, provides information about the mass of the particle in the region below 1.2 GeV. (Section 2.3.4.)

ECL Electromagnetic Calorimeter: The ECL is used to identify electrons, detect photons and measure the energy of both electrons and photons. (Section 2.3.5.)

MAGNET 1.5 T superconducting solenoid magnet: The magnet encompasses the inner detectors and the magnetic field bends charged tracks. The curvature of the tracks is used in the CDC to measure their momentum.

KLM K_L and Muon: The KLM is interleaved with the iron flux return for the superconducting solenoid. It provides location and time information for long lived particles that make it through the inner detector. (Section 2.3.6.)

EFC Extreme Forward Calorimeter: The EFC comprises two detectors built forward and backward to extend the angular coverage of the calorimetry, it is discussed in Ref. [78]. This subdetector was not used for the physics analysis in this thesis, and will not be discussed further.

The information from the tracks in these subdetectors is combined to produce likelihoods for a track to be each of five particles: $e^{\pm}$, $\mu^{\pm}$, $\pi^{\pm}$, $K^{\pm}$ and p or $\bar{p}$;

the particle identification algorithms are described in Section 2.4. At Belle two coordinate systems are used: Cartesian (x, y, z) and spherical (radius r, polar angle θ, and azimuth angle ϕ), with $\theta = 0$ corresponding to the z axis. The z axis of the detector and the magnetic field is aligned to the Low Energy Ring (LER) beam, with the positive direction, $+z$, being opposite to the direction of the positrons. The LER has a slight crossing angle with the High Energy Ring (HER) beam in the z-y plane. A photo of the Belle detector is reproduced in Figure 2.4 and a schematic diagram of the Belle detector is reproduced in Figure 2.5.

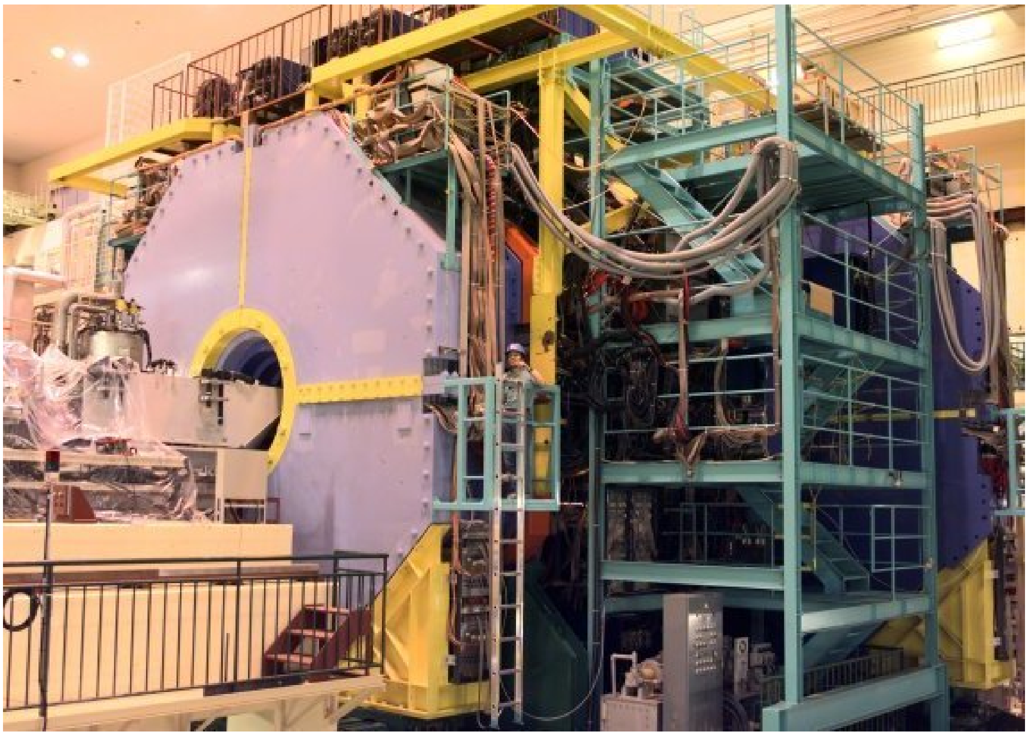

Figure 2.4: Photo of the Belle detector, provided by the Belle collaboration.

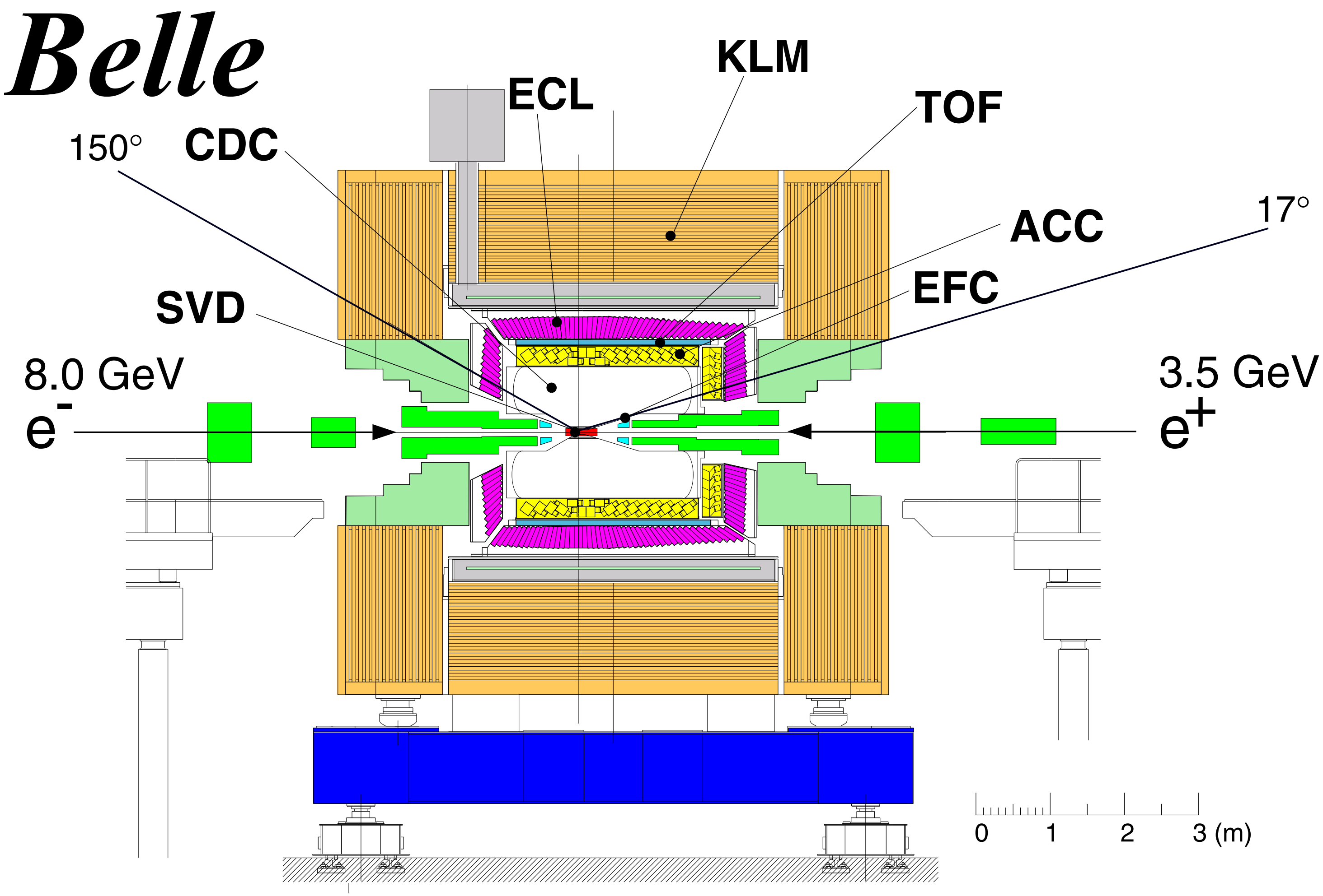

Figure 2.5: Schematic diagram of the Belle detector adapted from Ref. [78]. The SVD, CDC, ACC, TOF, ECL, KLM and EFC subdetectors are indicated; the initial energies of the colliding electron and positron are also shown.

2.3.1 Silicon Vertex Detector (SVD)

The SVD aims to precisely determine the decay vertex of B and $\overline{B}$ mesons in order to observe asymmetries in their decay times. This lifetime asymmetry is evidence for CP violation, and measuring this was one of the primary goals of the Belle experiment. The CM frame is boosted with respect to the laboratory frame, so the asymmetry in the lifetime of the B and $\overline{B}$ mesons in the CM frame, corresponds to an asymmetry in decay position in the laboratory frame. The SVD is constructed out of Double-sided Silicon Strip Detectors (DSSD, plural DSSDs). When a particle travels through the detector, it leaves hits on both sides of the DSSDs, which are oriented cylindrically around the beampipe, made from Beryllium (Be). One side of the DSSDs measures z position and the other measures ϕ position. As this detector is the closest to the beam it experiences the largest radiation dose and all of its components need to be radiation-hard. Belle has used two SVD configurations, referred to as SVD1 and SVD2. The differences between each configuration are reproduced in Table 2.2.

Table 2.2: Characteristics of SVD1 and SVD2, from Ref. [79].

	SVD1	SVD2
Beampipe radius (mm)	20	15
Number of layers	3	4
Radii of layers 1/2/3/4 (mm)	30.0/45.5/60.5	20.0/43.5/70.0/88.8
Ladders per layer	8/10/14	6/12/18/18
DSSDs per ladder	2/3/4	2/3/5/6
Angular coverage (acceptance)	$23 < \theta < 140^\circ$ (0.86)	$17 < \theta < 150^\circ$ (0.92)
Strip pitch (μm) for z	84	75 (73 for layer 4)
Strip pitch (μm) for $r\phi$	25 (50 for readout)	50 (65 for layer 4)
Radiation tolerance (MRad)	~ 1	> 20

SVD1

The original Belle SVD configuration (schematic reproduced in Figure 2.6) was used from the beginning of data taking in 1999 until it was replaced by SVD2 in October 2003. SVD1 had several problems including limited radiation tolerance and non-negligible dead time. These problems of SVD1 led to its eventual replacement by SVD2. Further information relating to the performance of SVD1 and issues leading to its replacement can be found in Ref. [80]. The impact parameter resolution of SVD1 was angle and momentum dependent, the resolution of the xy and z parameters are summarised by the following formulae:

$$\sigma_{xy} = 19 \oplus 50/[p\beta\sin(\theta)^{3/2}]\,\mu\text{m},$$
$$\sigma_{z} = 36 \oplus 42/[p\beta\sin(\theta)^{5/2}]\,\mu\text{m}.$$

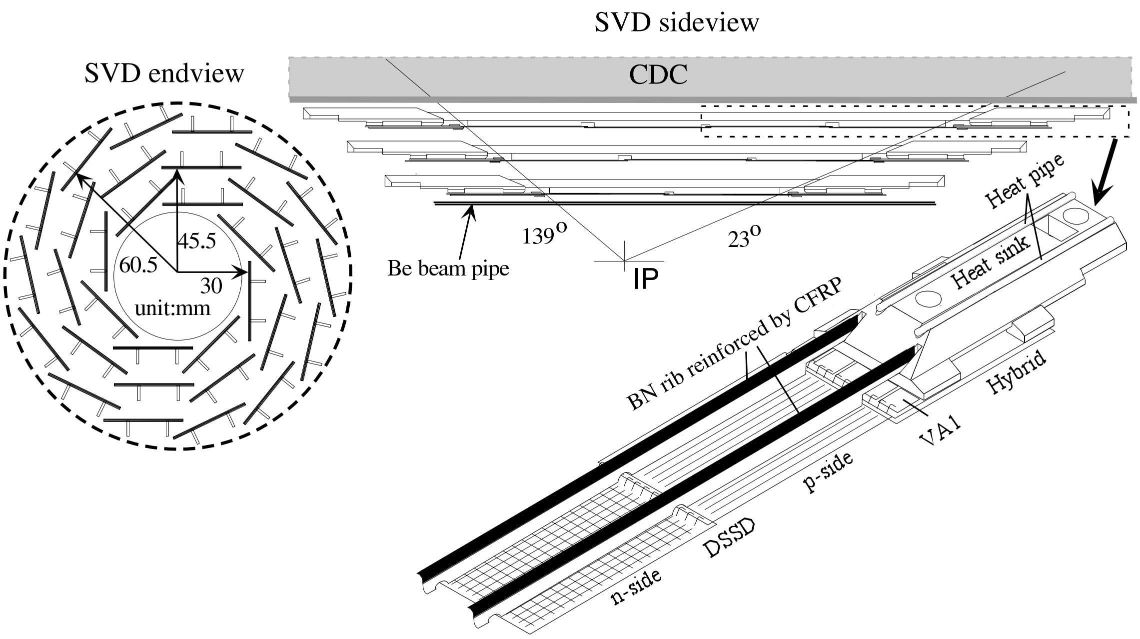

Figure 2.6: Diagram of SVD1 end and side views. An example DSSD, showing the location of the readout chip (VA1), the reinforced boron-nitride support ribs and heat sink, is also shown. Reproduced from Ref. [78].

SVD2

A schematic of SVD2 is reproduced in Figure 2.7. Further information about the performance of SVD2 can be found in Ref. [81]. When the new SVD was installed, the radius of the beampipe was reduced to accommodate the inner layers of SVD2 and to improve vertex resolution; this is described in Ref. [82]. The resolution of the $r\phi$ and z impact parameters for SVD2 are summarised by the following formulae:

$$\sigma_{d(r\phi)} = 22 \oplus 36/[p\beta \sin(\theta)^{3/2}]\,\mu\mathrm{m},$$
$$\sigma_{dz} = 28 \oplus 32/[p\beta \sin(\theta)^{5/2}]\,\mu\mathrm{m}.$$

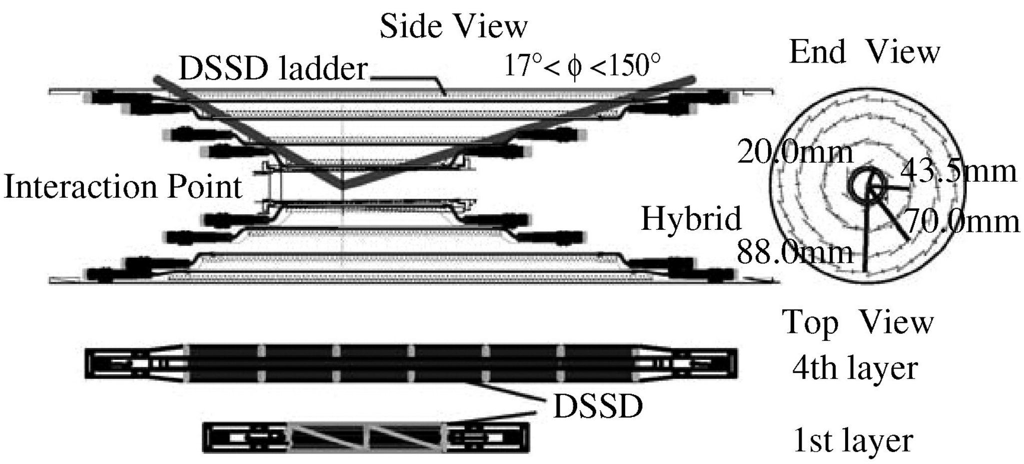

Figure 2.7: Diagram of SVD2 side and end views, indicating positions of the DSSDs. Reproduced from Ref. [81].

2.3.2 Central Drift Chamber (CDC)

The main purpose of the CDC in Belle is to provide tracking for charged particles. The momentum of charged particles can be measured from the curvature of the tracks in the magnetic field provided by the 1.5 T superconducting solenoid. Drift chambers in High Energy Physics are filled with a low-Z gas, which minimises the effect of multiple scatterings on particles with low momentum. While traversing a drift chamber, charged particles interact with the gas by ionising it. Wires are strung throughout the volume with a voltage applied to them to provide an electric field. The ions then drift in this field into the wires where the charge is measured. Drift time information is then converted into position information within each cell along the track to improve the position measurement. The path of the particle through the chamber is then extrapolated from the position measurements. In addition to tracking, the energy that a particle of given momentum loses as it passes through the gas in the chamber (dE/dr) exhibits a well known β^{-2} dependence, which provides a measure of the mass and is used in particle identification (see Section 2.4).

The Belle CDC is composed of 50 cylindrical layers of sense wires each with 3-6 layers (either axial or small angle stereo) and three cathode strip layers; which make up a total of 8400 nearly-square drift cells. The inner three layers are smaller than the rest. The CDC is filled with a mixture of 50% helium and 50% ethane (C_2H_6). An overview of the CDC shape can be seen in the top of Figure 2.8, while in the bottom of the figure the cell structure and cathode strip layout can be seen. This configuration was shown with test beam data to have a spatial resolution of between 120 and 150 μm depending on layer and the dE/dr measurement was found to have a resolution of 5.2% for 3.5 GeV pions. The CDC covers a polar angle of $17.0^\circ \leq \theta \leq 150.0^\circ$.

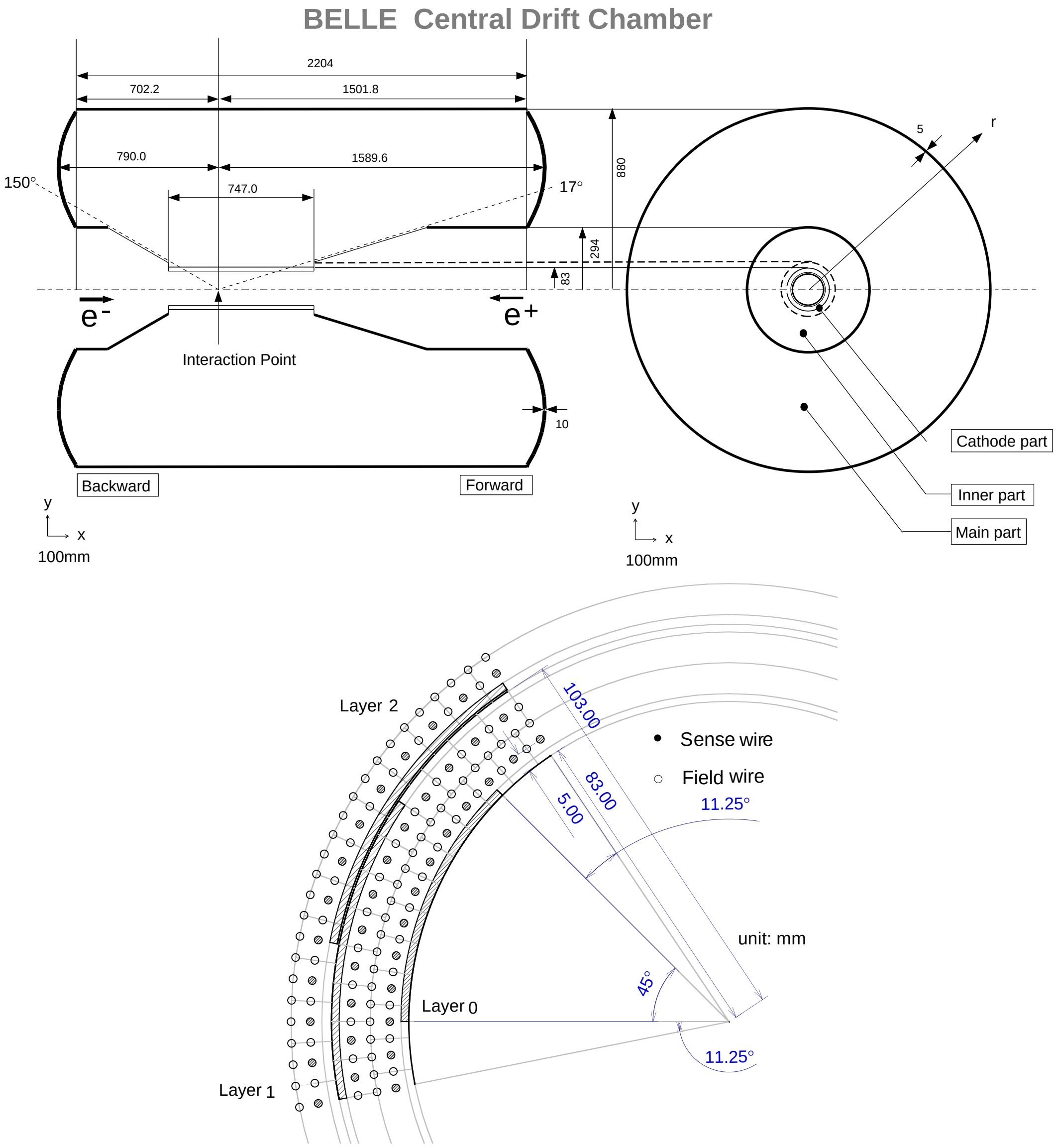

Figure 2.8: Top: overview of the CDC structure (lengths are in mm). Bottom: cell structure of the CDC sense wires, with the layout of the three cathode strips layers indicated. Reproduced from Ref. [78].

2.3.3 Aerogel Čerenkov Counters (ACC)

The ACC is designed to provide discrimination between charged pions and kaons in the momentum region not covered by dE/dx measurements from the CDC or time of flight measurements from the TOF. For a particle travelling through a medium with speed ($\beta = v/c$) greater than the speed of light in that medium (c/n, where n is the refractive index of the medium), the particle will produce light, called Čerenkov radiation, at a distinct angle (θ), given by:

$$\cos(\theta) = 1/\beta n \ \ [83].$$

The medium selected by the ACC was chosen such that, in the momentum range of interest, pions (which are light) and kaons (which are relatively heavy) would have velocities above and below the threshold for producing Čerenkov radiation, respectively.

The medium chosen for the ACC was silica aerogel with a refractive index between 1.01 and 1.03, depending on the angle in the detector, which corresponds to the boost of the particle relative to the CM frame. In the barrel region 960 counter cells are segmented into 60 cells in the ϕ direction, while in the forward end-cap 228 modules are arranged in 5 concentric layers, all pointing towards the interaction point, see Figure 2.9. Each module contains 5 aerogel tiles stacked inside an aluminium box with one or two fine-mesh photomultiplier tubes (FM-PMTs) attached. The number of photoelectrons measured by the FM-PMTs is then used to determine whether the traversing particle was above or below threshold. The detected light yields measured for light particles ranges from ≈ 10 photoelectrons to ≈ 26 photoelectrons, depending on the type of module.

2.3.4 Time Of Flight counters (TOF)

The purpose of the TOF counters is to distinguish between charged pions and kaons with momentum below 1.2 GeV by measuring the travel time from the interaction point. For a particle travelling length L over a time T with momentum P, the mass m is given by ($c = 1$):

$$m^2 = (\frac{T^2}{L^2} - 1)P^2.$$

The TOF also has a secondary purpose; to provide event timing to the Belle trigger system. The event timing from the TOF is synchronised to a radio frequency reference clock in time with the beam collisions.

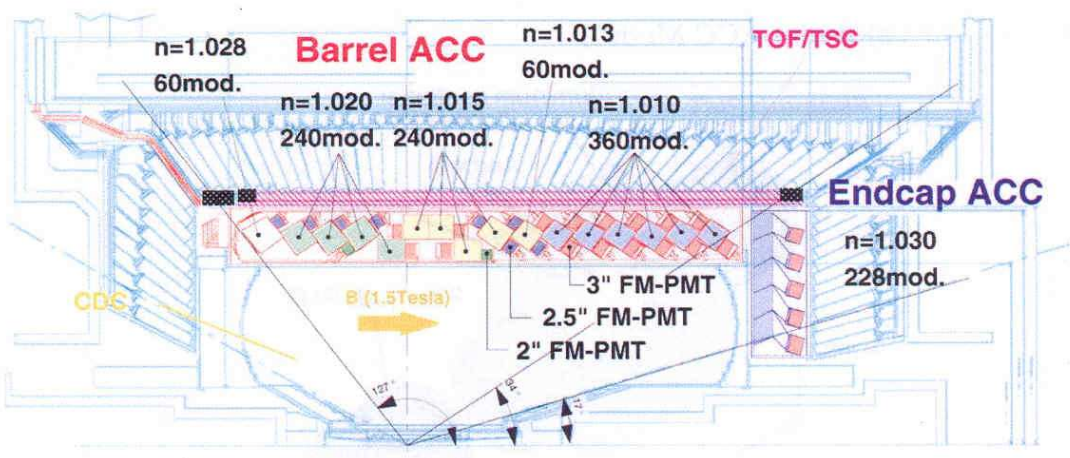

Figure 2.9: Schematic of ACC with surrounding subdetectors. The refractive index (n) of the silica aerogel in different detector regions, the number of modules (mod.) and the location of the photomultiplier tubes (FM-PMT) are indicated. Reproduced from Ref. [78].

The TOF was constructed using plastic scintillation counters, 1.2 m from the interaction point. The TOF is constructed from 64 modules, each of which contain two TOF plastic scintillation counters and one Trigger Scintillation Counter (TSC) placed radially outwards 1.5 cm. Coincidences between the TSC and TOF counters are used to reduce the photon conversion background. (The 1.5 cm gap prevents electrons and positrons created in the TOF layer from reaching the TSC layer.) The TOF covers the polar angle range of $34° < \theta < 120°$. The TOF has a time resolution of 100 ps for minimum ionising particles, which provides for a 3σ separation of pions and kaons, for particles with momentum less than 1.2 GeV.

2.3.5 Electromagnetic Calorimeter (ECL)

The ECL is designed to measure the energy of electromagnetic particles, those with electric charge and photons. At Belle there are a large number of photons with low energy, so the ECL was required to have good performance at energies below 0.5 GeV, while having high resolution up to 4 GeV, needed to measure high energy photons from certain decays. Additionally high momentum π^0 reconstruction requires the separation of nearby photons and a precise determination of their opening angle.

The ECL at Belle was made from CsI(Tl) crystals. The crystals were arranged in a highly segmented array with silicon photodiode readouts covering a polar angle of $17.0° < \theta < 150.0°$. The crystals were arranged in a barrel configuration, 3 m in length, with forward and backward end-caps at $z = +2, -1$ m, where $z = 0$ is the interaction point. Each crystal was pointed almost directly at the interaction point: in order to avoid having gaps between crystals, a tilt of $1.3°$ was applied to the crystals in the barrel, a tilt of $1.5°$ in the forward end-cap and a tilt of $4.0°$ applied in the backward end-cap. The parameters of the ECL design are summarised in Table 2.3.

Table 2.3: ECL parameters. Reproduced from the Belle Detector Book [78].

Section	θ coverage	θ segments	ϕ segments	Crystals
Forward end-cap	$12.4° - 31.4°$	13	$48 - 144$	1152
Barrel	$32.2° - 128.7°$	46	144	6624
Backward end-cap	$130.7° - 155.1°$	10	$64 - 144$	960

Photons and other particles with high energy entering a crystal will interact with the material via pair production and bremsstrahlung recursively, in a cascade that produces an electromagnetic shower. The shower shape and the energy deposition in the crystals help identify the type of incident particle, whether photons, electrons or hadrons. When reconstructing a shower, the first step is to select the seed crystal which has the highest energy amongst its neighbours. Then the energy from a 5×5 matrix of crystals around the seed is collected and the energy and position of this cluster is recorded. The energy resolution achieved was measured with Bhabha scattering and $e^+e^- \to \gamma\gamma$ events and found to be 1.70% for the barrel and 1.74% and 2.85% for the forward and backward end-caps, respectively. For π^0 events an energy resolution of 4.8 MeV has been achieved, with an energy resolution of 12.1 MeV for η events. Further details of ECL performance can be found in Ref. [84].

2.3.6 K_L and Muon detector (KLM)

The KLM was built to identify long lived particles which make it through the inner detectors. Long-lived neutral K_L particles will hardly interact in the inner detector. Muons are long-lived and, though charged, penetrate further through the detector than charged pions and kaons which undergo strong interactions.

The KLM consists of a barrel region with a polar angle coverage of $45^\circ < \theta < 125^\circ$ and two endcaps which extend the total angular coverage to $20^\circ < \theta < 155^\circ$. The KLM is built into the iron flux return for the superconducting solenoid magnet. 15 detector layers are interleaved with 14 iron flux return layers of thickness 4.7 cm, which are arranged in an octagon around the inner detectors. Glass resistive plate counters are used to measure charged tracks in the KLM. An ionising track passing between 2 plates in these counters will provide a discharge, from which the time and location are measured. In each KLM module, 2 resistive plate counters are layered with readout electronics.

For K_L particles the ECL provides 0.8 interaction lengths for the particle to interact and the KLM with its layers of iron provides a further 3.9 interaction lengths. When they interact, K_L particles produce a shower which can be used to identify the direction of the particle. However, variations in the resulting showers do not allow for effective measurement of the energy of the K_L particles. Muons can be identified, as charged tracks that can be matched to hits in the KLM are unlikely to be pions or kaons. A muon requires > 0.5 GeV to reach the KLM. These detectors have a maximum rate of ≈ 0.2 s^{-1}cm^{-2}, but because of the low flux of particles reaching the KLM this is sufficient to measure particles with high efficiency. Details of the performance of the KLM's glass resistive plate counters can be found in Ref. [85] and further information about the KLM can be found in Ref. [86].

2.4 Particle Identification (PID)

In order to identify the type of particle that makes each charged track in the detector, the response of each subdetector is combined to produce likelihoods for each of five mass hypotheses. The five final state particles that are measured as charged tracks in Belle are: $e^\pm$, $\mu^\pm$, $\pi^\pm$, $K^\pm$ and p or $\bar{p}$. Separate groups inside the Belle collaboration have studied the detector response and developed specific particle identification likelihoods to identify electrons, muons and to discriminate between pions, kaons and protons. An overview of the information used is given below.

Electron Identification

Electron Identification at Belle is performed using a ratio of likelihoods produced from the responses of the CDC, ACC and ECL sub-detectors. The five quantities used to discriminate between the electron and other mass hypotheses are:

- The light yield in the ACC.
- The transverse shower shape in the ECL, as electro-magnetic and hadronic showers have different shapes.
- The matching between the track extrapolated from the CDC to the ECL and the ECL cluster position and energy.
- The energy in the ECL and the momentum measured by the CDC, $E^2 = m^2 + p^2 \simeq p^2$ and therefore $E/p = 1$ within measurement errors.
- And lastly, the rate of energy loss (dE/dr) as it travels through the gas in the CDC, which exhibits a well known β^{-2} dependence.

The electron Identification at Belle has achieved an efficiency for $e^{\pm}$ $(92.4 \pm 0.4)\%$, with a $\pi^{\pm}$ fake rate of $(0.25 \pm 0.02)\%$. The ratio of the likelihoods for a particular track to be an electron or one of the other four mass hypotheses is provided to the user via the EID package in the Belle Analysis Software Framework (BASF). Further information can be found in Ref. [87].

Muon Identification

Muons are identified using a ratio of likelihoods for each track to be a muon or a hadron. The likelihoods are produced using two quantities: ΔR, the difference between the expected range for the track extrapolated from the CDC and the range measured in the KLM. And, χ^2_r, the goodness of fit of the transverse deviations associated with the track. The ratio of likelihoods for a track being a muon compared with a hadron is then provided to the user via the MuID package in the BASF. Between 1.0 and 3.0 GeV the identification efficiency for $\mu^{\pm}$ was found to be 89%, and the $\pi^{\pm}$ fake rate per track was found to be 1.4% [88].

Kaon-pion discrimination

The likelihoods for a track to be a kaon or a pion are generated and the ratio of these two likelihoods is used to identify the track as either a pion or a kaon. These likelihoods are formed using information from energy loss measurements in the CDC, dE/dr, Čerenkov light yields in the ACC, and time of flight measurements from the TOF. Collaboration studies on the kaon-pion discrimination, using kinematically tagged pions and kaons from D decays in data, show a kaon identification efficiency higher than 80% with a pion fake rate below 10%. The ratio of likelihoods for a track being either a kaon or a pion is provided via the atc_pid (from ACC-TOF-CDC_PID) package in the BASF. Further information can be found in Ref. [89].

2.5 Dataflow

Interactions that occur during a bunch crossing inside Belle are referred to as events. Not all events are of interest to the physics programme at Belle. Events that are not of interest form a background to the processes being studied. The data rate is too high for every event to be stored and analysed by the collaboration, so decisions are made in successive steps about which events to keep and which to discard. Events are rejected in two steps, firstly with a hardware and software trigger and secondly by data skims.

2.5.1 Experimental running periods

Belle ran for most of the year, with a shutdown period in Summer when electricity costs become too expensive. This period was used to perform maintenance and upgrades. Experimental running periods, in which the detector and collider conditions are kept constant, are referred to within the collaboration as experiments. Belle experiments use odd numbers for historical reasons. The first experiment that is included in current analyses is experiment 7, with a gap in experiment numbers at experiment 29, when the inner detector configuration was changed from SVD1 to SVD2. After experiment 55, the Belle tracking and reconstruction software was updated and improved and a θ dependent ECL energy threshold was introduced [90][1]. The integrated luminosity, on and off the $\Upsilon(4S)$

[1] Internal Belle collaboration document.

resonance (see Section 2.2), collected by the two Belle inner detector configurations is summarised in Table 2.4.

Table 2.4: Integrated luminosity collected by the Belle detector.

Experiments	Inner Detector	On-resonance (fb^-1)	Off-resonance (fb^-1)	Total (fb^-1)
$7-27$	SVD1	140.9	15.6	156.5
$31-55$	SVD2	463.4	52.4	515.8
$61-65$	SVD2	106.5	12.0	118.5

2.5.2 Trigger

The Belle trigger system is separated into three steps. The first step is the Level 1 hardware trigger, which makes decisions based on the combined output of the various subdetectors. The second step is the Level 3 trigger,[2] which builds the events in an online computer farm and saves the events which pass in a raw format for further analysis. Thirdly, the Level 4 event selection trigger is run offline over the stored raw events. The events that pass are saved in files called Data Summary Tapes (DSTs), which are made available to users. Events that fail the Level 1 and Level 3 triggers are not kept. However events that fail the Level 4 trigger, while not available to users, are still available in a raw format and can be reprocessed when there is a significant improvement to the Level 4 trigger software. Further information on the Belle Level 1 trigger is available in Ref. [91], however information about the Belle Level 3 and Level 4 triggers is only available in Belle internal documents, Ref. [92] and Ref. [93], respectively. An overview of this information is provided in Figure 2.10.

[2]The name "Level 2 trigger" usually refer to a trigger between the hardware trigger and the event builder stage, which is not implemented on Belle.

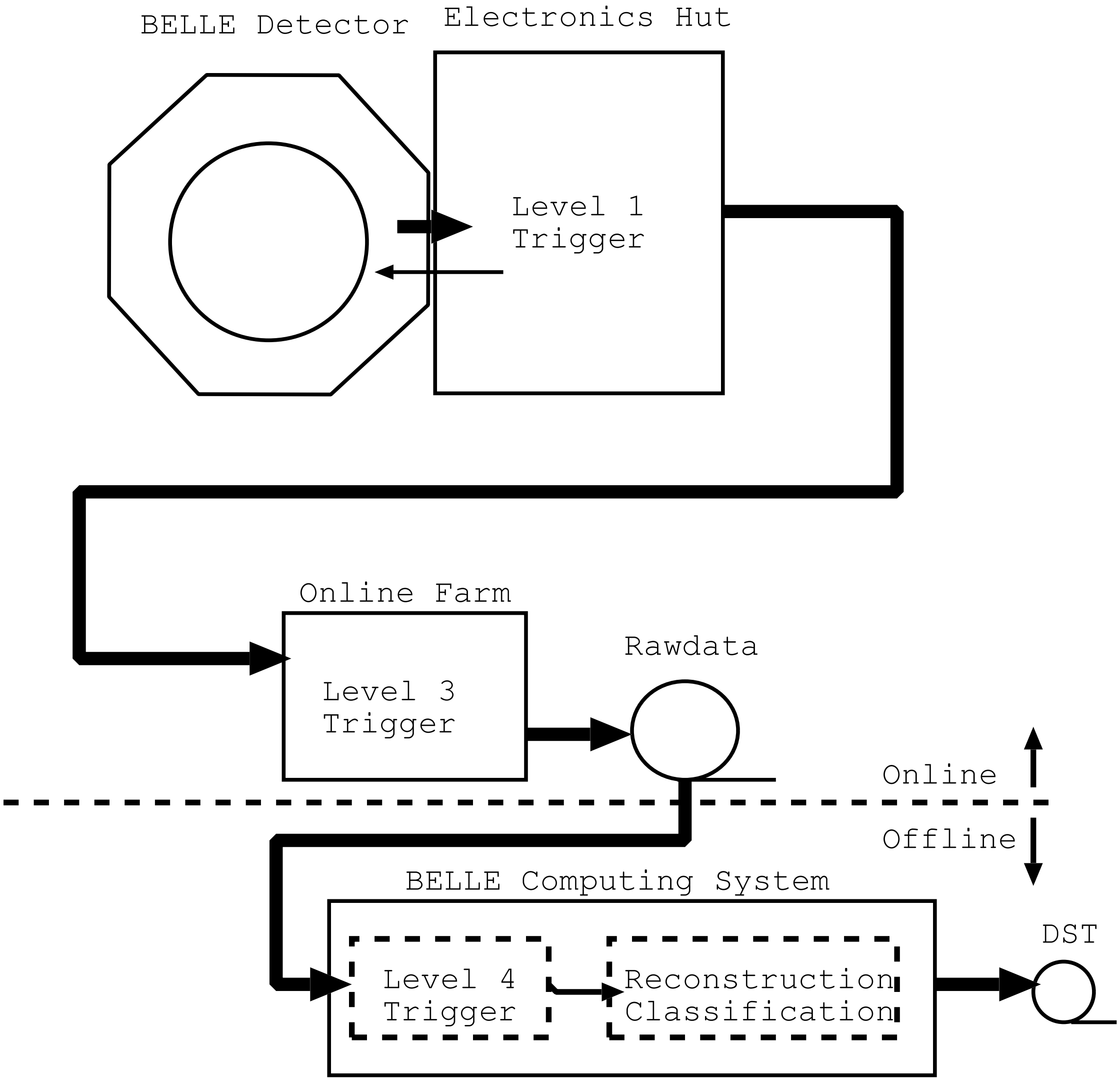

Figure 2.10: Overview of dataflow through the Belle trigger system, reproduced from Ref. [93]. The output from the Belle subdetectors is combined to form a Level 1 hardware trigger. Events that pass the Level 1 trigger are then built in the online computer farm that provides a Level 3 trigger. Events that pass the Level 3 trigger are saved in a raw format for further study. A Level 4 event selection trigger saves the surviving events after reconstruction in Data Summary Tapes (DSTs), which are available to users.

2.5.3 Data skims

Since the Belle dataset is very large and only a small fraction of events are of interest, the dataset is reduced by a process called skimming. Skims are produced by choosing loose cuts that aim to retain almost all signal decays of interest, while eliminating events which are obviously and easily identifiable as not being from signal decays. Events that pass the data skimming process are available for analysis. Some of the main skims used at Belle are summarised in Table 2.5. The data in Chapter 3 is collected from Psi Skim, which is a subset of the HadronA Skim, and the data in Chapters 4 and 5 is from the Low Multiplicity and Tau Skims. The selection criteria for these skims are summarised in Appendix A. There is no dedicated skim for ISR events.

Table 2.5: Data skims used in this analysis. Selection criteria are described in Appendix A.

Skim	Designed to identify	Appendix:
HadronA Skim	$\Upsilon(4S) \to B\overline{B}$ events	
Psi Skim	$B \to J/\psi X$, events, X is a final state	
HadronB(J) Skim	$B\overline{B}$ events with tighter cuts than HadronA	
Low Multiplicity Skim	Two-photon processes	
Tau Skim	$e^+e^- \to \tau^-\tau^-$ events	

2.6 Software

Several software packages developed by different High Energy Physics experiments were used in this thesis. These include the BASF, ROOT and RooFit packages which were used for the reconstruction and analysis of both real and Monte Carlo (MC) simulated data and are described in Sections 2.6.1, 2.6.2 and 2.6.3, respectively. MC events were generated using PHOKHARA, QQ98 and EvtGen, before these generated events were then processed with a description of the detector, GSIM, in GEANT 3. These programs are described in Section 2.6.4.

2.6.1 Belle Analysis Software Framework (BASF)

The BASF has been developed by the Belle collaboration to perform analyses on Belle data, see Ref. [94] for more details. It includes code for reading Belle data and generating Belle MC. It also includes many classes which help analyse the available data. The BASF can be used to extract detailed information about reconstructed particles, such as track helices for high-level analyses and exact hit information from individual subdetectors for low-level computations.

Data from the Belle detector is stored in a computer farm at KEK. This data is processed with BASF. Over the life of the experiment, the BASF is updated with the details of the latest runs and experiments as well as bug fixes and code improvements. The BASF library versions used for analysis are summarised in Table 2.6.

Table 2.6: BASF library versions used in analysis.

Experiments	Compilation date and time
$\pi^+\pi^- J/\psi$ analysis	
07 – 43	2005/03/11 07:38
45 – 49	2006/05/26 03:55
$\pi^0\pi^0 J/\psi$ analysis	
07 – 65	2009/01/27 09:10

2.6.2 ROOT

ROOT is a data analysis framework and real-time C++ interpreter, for more details see Ref. [95]. It was developed at the European Organization for Nuclear Research (CERN) to replace the Physics Analysis Workstation (PAW), an older data analysis package based on FORTRAN that was used for many years by the High Energy Physics community. It includes many classes designed for the different stages of a High Energy Physics analysis, such as 3- and 4-vector classes for analysing reconstructed particles, serialisation functions for saving events and histogramming classes for graphing.

2.6.3 RooFit

RooFit is a package which provides software for modelling and fitting distributions commonly found in Particle Physics analysis. The RooFit software is developed for the *BABAR* collaboration and is designed to operate with the ROOT framework. For more information see Ref. [96].

2.6.4 MC programs

To generate MC, events are first generated with programs which simulate the underlying physics processes. Three software packages were used during the analysis described in this thesis: PHOKHARA, QQ98 and EvtGen. PHOKHARA is a MC event generator designed to simulate ISR events over a range of initial energies up to next-to-leading order accuracy. It was used to generate the kinematics for all ISR MC produced for this thesis (Sections 3.1.1 and 4.1.2) and is described in more detail in Ref. [97]. QQ98 is a MC event generator developed by the CLEO collaboration and adapted for use at Belle. It is used at Belle for generating the kinematics and decays of the initial particles being simulated. QQ98 was mostly used in the early years of the Belle experiment and is now almost entirely superseded by EvtGen for Belle analyses. It was used in this thesis to generate the MC used Chapter 3, for more information see Ref. [98]. EvtGen is a MC event generator developed by the *BABAR* collaboration. It was designed to simulate decays of B mesons and is currently the primary event generator at Belle. It was used to generate the MC events used in Chapter 4, for more details, see Ref. [99]. After the initial MC physics processes were produced, they were processed with a description of the Belle detector in order to simulate the response and output of the detector to these events. All the signal and background MC in this thesis was processed with this software. This description of the Belle detector was called GSIM and it was produced using GEANT 3. GEANT 3 was developed by CERN, and is used to simulate the passage of particles through matter, see Ref. [100].

Chapter 3

Analysis of $\pi^+\pi^- J/\psi$ mode

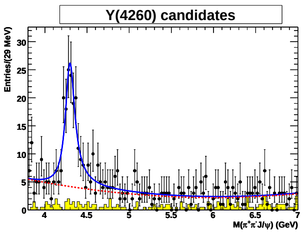

In this chapter the reconstruction of $Y(4260) \to \pi^+\pi^- J/\psi$ in Belle data is described. The $Y(4260)$ signal yield is extracted and the systematics on the yield are studied. Additionally crosschecks and the properties of the $Y(4260)$ peak are presented.

THIS chapter describes a search in Belle data for the $Y(4260)$ which is produced via ISR and decays to $\pi^+\pi^- J/\psi$. This study was originally made public at conferences in the Northern Hemisphere Summer of 2006 (see Ref. [28]), the first of which was Quarkonium Working Group 2006 (Brookhaven) [101].

The first section of this chapter will detail the datasets in which this search was conducted. Then Section 3.2 will describe the reconstruction process and will relate how events were identified. The signal which emerged from the identified events was measured using the fitting procedure described in Section 3.3. Systematic uncertainties were checked and quantified, this process is set out in Section 3.4. The assumption of ISR production is tested in Section 3.5. Additional checks were carried out on the subsamples from the two included J/ψ decay modes, di-electron and di-muon. This is discussed in Section 3.6, in order to make sure the data is well understood. With the data understood, additional kinematic distributions were investigated, see Section 3.7, and calculations of the cross-section were made, see Section 3.8. The relationship between this study and the final Belle publication [29] on this mode is described in Section 3.9. These results are discussed and compared with the results of other experiments in the final section.

3.1 Datasets

The analysis was conducted using several datasets. Firstly MC events were used to develop reconstruction software, determine suitable selection criteria and determine the efficiency of the criteria. Secondly $\psi(2S)$ events in data were used as a control sample. The $\psi(2S)$ and $Y(4260)$ are both capable of being produced via ISR and decay to $\pi^+\pi^- J/\psi$. Additionally, the $\psi(2S)$ is similar in mass to the $Y(4260)$, but it has a much larger signal and it is well known and understood from studies conducted by other experiments. The control sample was used to check differences between data and MC, as well as consistency between this reconstruction and previous results. Finally events in data in the $Y(4260)$ mass region were investigated, which is where the primary measurements were performed.

3.1.1 Monte Carlo (MC) samples

MC simulated data was used primarily to develop cuts and reconstruction programs and techniques in order to test their effect on signal decays and test possible backgrounds. For these purposes several different samples were used. Signal MC, simulating signal decays, was generated specifically for this analysis at the mass of the $\psi(2S)$ control sample, 3686.09 ± 0.04 MeV [102], and several masses around 4260 MeV. Existing Belle MC data and several samples generated specifically for this analysis were used to investigate possible backgrounds.

Most MC in Belle is generated in two stages, the generator step and the detector simulation. As this study was conducted with ISR events, which are non-standard at Belle, the kinematics of the production were generated separately and then included into the generator step. Signal MC for this analysis was generated using the steps described in Table 3.1, while standard Belle MC was produced using the generator and detector simulation step.

Table 3.1: Summary of steps used in simulating signal MC.

Step	Description
Kinematic	The ISR kinematics were simulated.
Generator	The initial physics decays were generated.
Detector simulation	Particles from the generator step were passed through a computer model of the detector to simulate its output.

Signal MC

To study signal decays for the $\psi(2S)$ control sample and events in the $Y(4260)$ mass region, several MC samples with different masses were generated. The samples were generated at the mass of the $\psi(2S)$ and around the mass observed by *BABAR*, $4259 \pm 8^{+2}_{-6}$ GeV. The initial ISR kinematics were simulated using PHOKHARA, which is described in Section 2.6.4. The decays of the signal particles ($Y(4260) \rightarrow \pi^+\pi^- J/\psi$, $J/\psi \rightarrow \ell^+\ell^-$) were generated using one of the two standard Belle MC generators: QQ98 (Section 2.6.4). These particle decays were then boosted and rotated so that they would have kinematics as produced by PHOKHARA.

Events were then processed through the standard description of the Belle detector in GEANT 3 [100], called GSIM, to simulate the detector response. The generated events were all processed with the same code and then passed through simulations of the two separate inner detector configurations used by Belle. The samples were then combined at the analysis level and weighted by the luminosity collected while each inner detector configuration was in operation. Beam backgrounds were overlayed with the signal events at the GSIM stage, to provide readouts of the detector which match real running conditions, for example: additional charged tracks and photons were included which came from beam-gas events, instead of from the primary interaction. The files which contain readouts from the beam backgrounds were taken from Belle experiment 27 and experiment 41. Belle experiment 27 used the first inner detector configuration, SVD1, and Belle experiment 41 used the second inner detector configuration, SVD2:[1] The relevant

[1] Belle experiments are described in Section 2.5.1 and SVD1 and SVD2 are described in Section 2.3.1.

information is summarised in Table 3.2. The particle identification (PID) efficiency in data and MC has been found to be different in collaboration systematic studies, the MC in this analysis was adjusted to match the efficiency found in data from these Belle collaboration PID efficiency studies [103].

Table 3.2: Summary of conditions used to simulate signal MC samples.

	Sample 1	Sample 2
Belle experiment number	27	41
Inner detector	SVD1	SVD2
Scaling by luminosity (fb^{-1})	155.5	397.8

The simulated output from GSIM was used to develop analysis code, which was subsequently used to analyse real data. For this step of the analysis, both the BASF and ROOT were used: these are described in Section 2.6. Table 3.3 sets out the parameters which were used to generate the various signal MC samples and Table 3.4 provides a summary of the software which was used in the generation procedure.

Table 3.3: Parameters used to generate signal MC.

Sample	Mass (MeV)	Shape	Width (MeV)	Events
$\psi(2S)$	3686	Gaussian	$\sigma = 0.1$	100,000
$Y(4260)$	4260	Breit-Wigner	$\Gamma = 80$	50,000
$Y(4310)$	4310	Breit-Wigner	$\Gamma = 80$	80,000
$Y(4360)$	4360	Breit-Wigner	$\Gamma = 80$	100,000

Table 3.4: Software used to generate signal MC.

Step	Program	Ref.
Kinematics	PHOKHARA	[97]
Decays	QQ98	[98]
Detector simulation	GSIM in GEANT 3	[100]
Analysis	BASF and ROOT	[94] and [95]

Background MC

To study possible backgrounds from B-decays as well as continuum processes, MC samples produced by the Belle collaboration, with the aim of studying B-decays, were investigated. It was found that these events did not contribute significantly in the $Y(4260)$ mass region. In order to investigate possible ISR-like backgrounds, a sample of 100,000 $e^+e^- \to \gamma_{ISR}\psi(2S)$ events, where the $\psi(2S)$ was allowed to decay generically, was produced. These events were also found to not contribute in the signal region.

3.1.2 $\psi(2S)$ control sample data

A control sample was used to test differences between data and MC and the consistency of this analysis with other experiments. The $\psi(2S)$ has several desirable control sample properties: It can be produced via ISR; It has a large rate of production; Its decay to $\pi^+\pi^- J/\psi$ has a large branching fraction: $(33.1 \pm 0.5) \times 10^{-2}$ [104]; and the $\psi(2S)$ has a mass of 3686.09 ± 0.04 MeV [104], which is near the mass of the $Y(4260)$. Additionally, its properties have been well studied in other experiments. In order to test the cuts and procedures used in this analysis, the selections and reconstruction procedure used in this analysis were first applied to the control sample.

3.1.3 Real data in the $Y(4260)$ mass region

This analysis was conducted using a sample of the stored Belle dataset. referred to as Psi Skim (Section 2.5.3). Psi Skim was designed to identify events with J/ψ

decaying leptonically, $J/\psi \to \ell^-\ell^+$, in $\Upsilon(4S) \to B\overline{B}$ events. This study uses the data available as of the Northern Hemisphere Summer of 2006, when this study was first made public at conferences. This consists of the data from Belle experiments; numbered 7 through 49 (Section 2.5.1). This data was collected by the Belle collaboration during the KEKB running periods over the years from 1999 till 2006. For each Belle experiment the majority of the data was recorded with the collider tuned to the $\Upsilon(4S)$ resonance for the main physics sample, referred to as on-resonance data, and samples taken 60 MeV below resonance, referred to as off-resonance data, with the purpose of measuring continuum backgrounds. Both on- and off-resonance data contain ISR events with signal decays, and so both datasets are included with appropriate correction for the initial beam energies in relevant kinematic variables. This data corresponds to an integrated luminosity of $497.1\,\mathrm{fb}^{-1}$ for on-resonance data and $56.1\,\mathrm{fb}^{-1}$ for off-resonance data, see Section 2.5.1.

3.2 Reconstruction

Signal decays have four charged tracks in the final state: two leptons and two pions. Events were selected if they had exactly four charged tracks that passed track quality cuts with zero total electric charge. The reconstruction of the ISR photon was not required. Two charged tracks were positively identified as leptons and combined to make a J/ψ candidate. The J/ψ candidate was then added to the remaining two tracks. To see if the resultant $\pi^+\pi^- J/\psi$ candidate was consistent with being produced via ISR, the invariant mass squared recoiling against the candidate was constructed using momentum balance: this should be zero for ISR events, corresponding to the mass of the ISR photon.

3.2.1 Track selection

The full angular acceptance of the detector was used and all reconstructed tracks were passed through track quality cuts, which are described below. Any tracks that failed to pass the quality cuts were ignored for both analysis and track counting purposes.

Tracks that were made by the particles in the decay chain of the $Y(4260)$ or $\psi(2S)$ in MC, the pions and both leptons, are referred to as signal tracks and all other tracks in the event, from beam backgrounds etc., are referred to as non-signal tracks. These tracks were identified from MC truth information. The transverse momentum, P_t, of all tracks was required to pass $P_t > 0.05$ GeV to be included. This removed the majority of non-signal tracks in $\psi(2S)$ signal MC. The P_t distribution for signal tracks, can be seen in the upper plot in Figure 3.1, and the distribution for non-signal tracks can be seen in the lower plot in Figure 3.1. Additionally the track impact parameters dr, dz (the transverse and longitudinal distance between the track and the interaction point, respectively) and χ^2/ndf (the track quality arising from the track fit) were investigated. These track parameters were not found to have enough discrimination between the signal and non-signal tracks in the MC and no selection was implemented.

Figure 3.2 shows the number of tracks per event, after the cut was applied to $\psi(2S)$ MC. Before the cut, 34023 four-track events were found in 100,000 MC events. After the cut, 34153 four-track events were found. There were a considerable number of events with more than four tracks, as can be seen in the figure. Events with exactly four tracks were selected for further analysis, as indicated by the vertical lines in the figure.

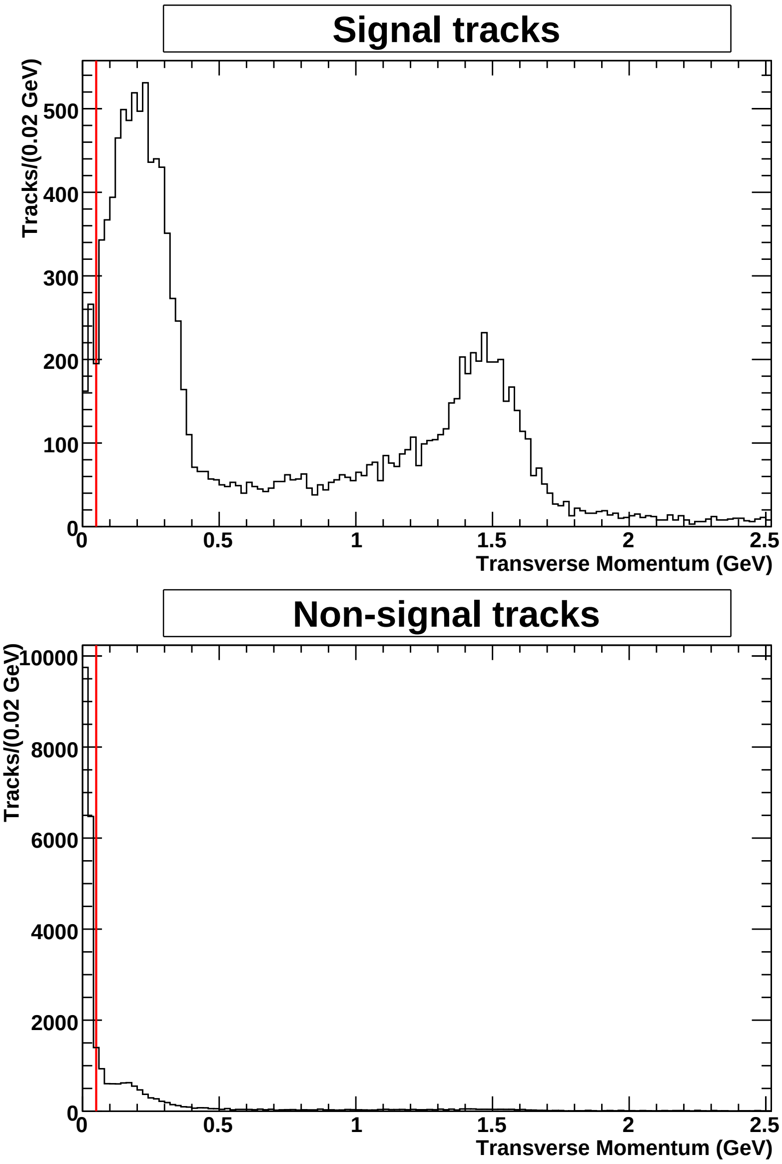

Figure 3.1: Tracks in $\psi(2S)$ signal MC. Top: transverse momentum of signal tracks. Bottom: transverse momentum of non-signal tracks, from beam backgrounds etc. Tracks with $P_t > 0.05$ GeV, i.e. the tracks to the right of the vertical line, were accepted for further study.

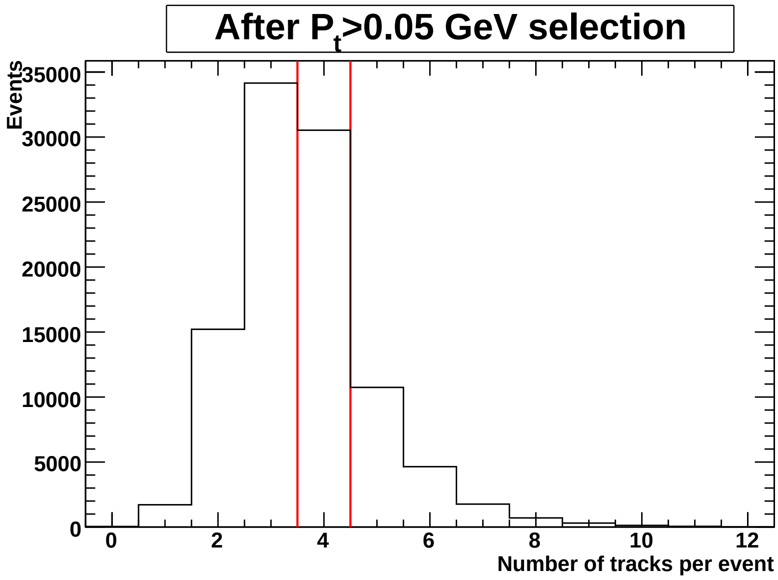

Figure 3.2: Number of charged tracks per event which passed the $P_t > 0.05$ GeV selection in $\psi(2S)$ signal MC events. Events with exactly four tracks were selected for further analysis. Four track events are highlighted by the vertical lines.

3.2.2 Particle Identification (PID)

The next step in the selection process was the identification of the four tracks in the selected events. To qualify for further analysis, all four tracks were required to be positively identified as a pair of leptons: e^+e^- or $\mu^+\mu^-$, and a pair of pions $\pi^+\pi^-$. Electron tracks were identified first, then muon tracks. Tracks that failed the lepton selection were accepted as pions if they passed a kaon veto. The PID methods used at Belle are described in Section 2.4.

Technically, electron tracks were identified using a call to the `probability` function of the EID [87] package in BASF. The function was called with input parameters 3, -1 and 5, which control the methods used to handle information from the ACC, TOF and CDC respectively. 3 and 5 flag that the most recent methods for handling the ACC and CDC information respectively should be used. -1 indicates that TOF information was not used to identify electrons, as it is not useful for electrons in the momentum range being studied. Tracks were accepted as electrons if the probability function returned a value greater than 0.1. The electron identification has an efficiency of 92% for electrons, from signal MC. For electron candidates, to recover radiated photons from bremsstrahlung, the four-momentum of the closest photon within 0.05 radians of the e^+ or e^- direction was added to the four-momentum of the track in subsequent analysis.

Muons were identified using the MuID package in BASF by requiring that the track was not pre-rejected by the software, and that the probability returned by the `Muon_likelihood` function was greater than 0.8. Muons were identified with an efficiency of 88%, from signal MC.

Pions were identified as charged tracks that failed both the electron selection and the muon selection and additionally passed a kaon veto. This was implemented using the `probability` function from the atc_pid package in BASF, with setup parameters 3, 1, 5, 3, 2, described in Table 3.5. The tracks were accepted as pions if the probability function returned a value greater than 0.6. The efficiency for pions to pass the kaon veto has an efficiency of 95%, while kaons have a selection efficiency 13%.

Table 3.5: Parameters input into the BASF atc_pid software package used to discriminate between kaons and pions.

Parameter	Value	Meaning
1	3	Use method 3 for ACC information
		(this is the most recent method)
2	1	Use TOF information
3	5	Use method 5 for CDC information
		(this is the most recent method)
4	3	Particle to identify: Input code for kaon
5	2	Particle to discriminate against: Input code for pion

The PID packages and methods used are summarised in Table 3.6. Electrons were only required to have an EID value greater than 0.1, this, combined with the requirement of two oppositely charged tracks having a combined mass near the mass of the J/ψ was sufficient to identify $J/\psi \to e^+e^-$ events.

Table 3.6: Technical details of the implementation of PID cuts in the BASF used in the $\pi^+\pi^- J/\psi$ analysis.

Particle	Package	Method	Input parameters	Passing criteria
$e^\pm$	EID	`probability`	$3, -1, 5$	result > 0.1
$\mu^\pm$	MuID	`Muon_likelihood`	–	result > 0.8
$\pi^\pm$	atc_pid	`probability`	$3, 1, 5, 3, 2$	result > 0.6

3.2.3 J/ψ reconstruction

J/ψ candidates were reconstructed from pairs of charged tracks which were positively identified as either electrons or muons. J/ψ candidates that fell into either the mass region around the nominal J/ψ mass, $m_{J/\psi} = 3096.916 \pm 0.011$ MeV [104], or two sideband regions were accepted for further study. The J/ψ signal and sideband invariant mass regions are defined in Table 3.7. The candidates in the J/ψ signal region were then constrained to a common vertex and the mass at the nominal J/ψ mass to improve the momentum resolution. The candidates in the J/ψ sideband regions were constrained to a common vertex and the mass at the centre of each sideband region, to mimic the behaviour in the J/ψ signal region. Candidates that were unable to be constrained to a common vertex and which were therefore unlikely to have resulted from a single particle decaying, were removed. Candidates in the J/ψ sideband regions approximate the contribution to the background from random combinations. The perpendicular distance between the J/ψ vertex and the initial collider e^+e^- interaction point, calculated when performing the constraint, was required to be less than $100\,\mu\mathrm{m}$.

Table 3.7: J/ψ signal and sideband mass regions.

Sample	Mass region
J/ψ Signal	$\lvert M(\ell^+\ell^-) - m_{J/\psi}\rvert \in [0, 30]\,\mathrm{MeV}$
J/ψ Sideband	$\lvert M(\ell^+\ell^-) - m_{J/\psi}\rvert \in [90, 150]\,\mathrm{MeV}$

The electron and muon samples were fitted separately and the results are shown in Figure 3.3. The peaks from J/ψ decays in the sample are clearly seen above a combinatorial background. The curves shown are fits using the Crystal Ball function [105], given by:

$$f(x;\bar{x},\sigma,\alpha,n) = N \cdot \begin{cases} \exp(-\frac{(x-\bar{x})^2}{2\sigma^2}), & \text{for } \frac{x-\bar{x}}{\sigma} > -\alpha \\ A\cdot(B-\frac{x-\bar{x}}{\sigma})^{-n}, & \text{for } \frac{x-\bar{x}}{\sigma} \leqslant -\alpha \end{cases} \quad (3.1)$$

where $A = \left(\frac{n}{|\alpha|}\right)^n \cdot \exp\left(-\frac{|\alpha|^2}{2}\right)$, $B = \frac{n}{|\alpha|} - |\alpha|$, N is a normalisation factor, $\bar{x}$ is the mean, σ is the width and α and n are the parameters which control the lower tail. The results of the fits are shown in Table 3.8. The effect of energy loss from bremsstrahlung was not completely recovered, as can be seen in the plot of the e^+e^- invariant mass. The central and outer vertical lines in the figures indicate the signal and sideband regions respectively.

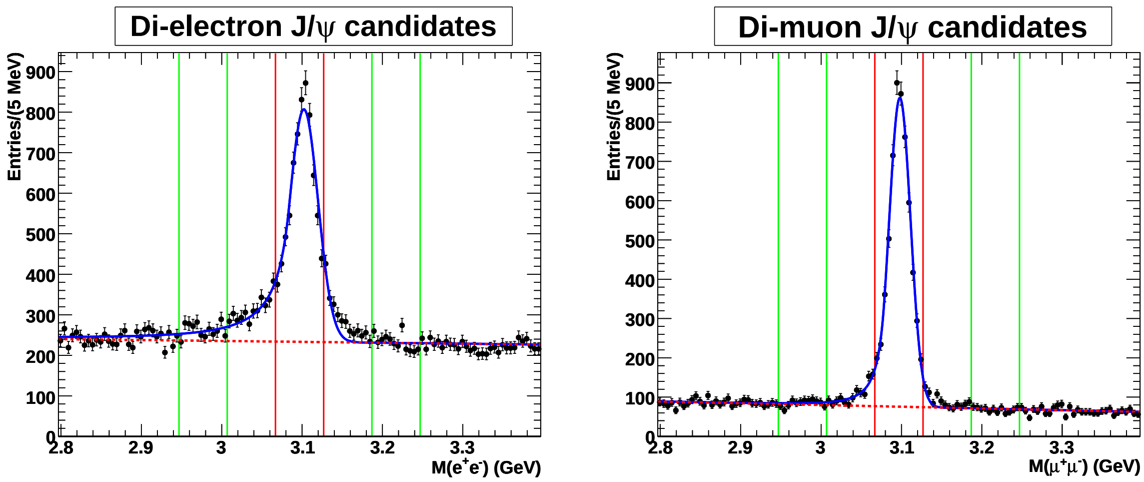

Figure 3.3: Left: invariant mass spectrum of $J/\psi \rightarrow e^+e^-$ candidates. Right: invariant mass spectrum of $J/\psi \rightarrow \mu^+\mu^-$ candidates. Points with error bars are the J/ψ candidates in data and the solid line represents the fit described in the text. The vertical lines indicate the signal (central) and sideband (outer) regions.

Table 3.8: J/ψ fit results with a Crystal ball signal function and linear background.

Function	Parameter	e^+e^- fit	$\mu^+\mu^-$ fit
Signal	Mean (GeV)	3.1022 ± 0.0004	3.0981 ± 0.0002
	σ (GeV)	0.0178 ± 0.0006	0.0133 ± 0.0002
	α	1.06 ± 0.06	1.48 ± 0.06
	n	1.7 ± 0.4	2.5 ± 0.6
	Events	6500 ± 264	5640 ± 116
Background	Slope	-0.029 ± 0.016	-0.17 ± 0.02
	Events	27999 ± 301	9077 ± 129

3.2.4 $\pi^+\pi^-J/\psi$ reconstruction

$Y(4260)$ candidates were reconstructed by combining the J/ψ candidate in each event with the remaining two tracks identified as $\pi^+\pi^-$ pairs. No requirement was made on the reconstruction of the ISR photon. The $\psi(2S)$ control sample was reconstructed in the same manner as the $Y(4260)$ candidates.

To check that candidates were consistent with being produced via ISR, the recoil mass squared of the $Y(4260)$ candidates was formed using the four-momentum of the initial e^+e^- known from beam parameters and that of the candidate using:

$$M^2_{\text{recoil}} = \left(\sqrt{s} - E^*_Y\right)^2 - {p^*_Y}^2, \tag{3.2}$$

where M^2_{recoil} is the recoil mass squared of the candidate, $\sqrt{s}$ is the CM energy and E^*_Y and p^*_Y are the CM energy and momentum of the candidate respectively. This was required to satisfy $|M^2_{\text{recoil}}| < 1$ GeV^2, consistent with the ISR process in which the only other object in the event is the recoiling photon, with $|M^2_{\text{recoil}}| \approx 0$ up to experimental accuracy.

The events from the J/ψ sideband regions were scaled and subtracted from the J/ψ signal region in order to remove the combinatorial background from the distribution. The sideband-subtracted distributions in data were then compared with the distributions from signal MC. These recoil mass squared distributions are shown for the $\psi(2S)$ control sample in Figure 3.4 and for $Y(4260)$ candidates in Figure 3.5. The solid lines shown are from the signal MC described in Section 3.1.1. The $\psi(2S)$ MC events are scaled to the integral of the region shown in the plot, while the $Y(4260)$ MC events are scaled using the events that pass the $|M^2_{\rm recoil}| < 1$ GeV^2 selection. This is due to the excess at high recoil mass squared in the $Y(4260)$ plot, around 6 GeV^2 to 7 GeV^2, which is not expected from signal decays. The J/ψ signal and sideband regions are defined in Table 3.7. The data and MC distributions are in reasonable agreement and a large peak is seen near zero in accordance with the assumption of ISR.

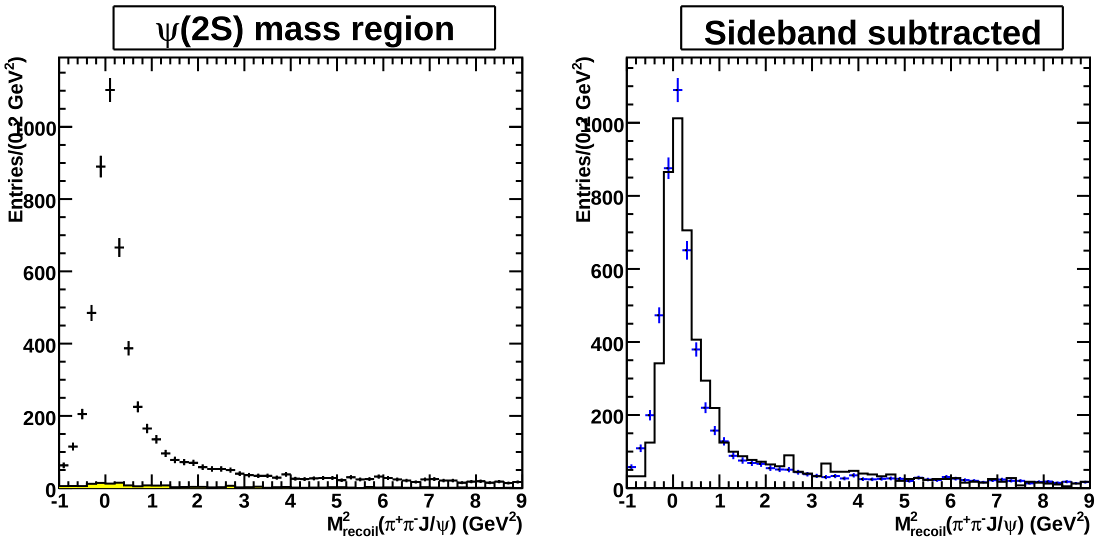

Figure 3.4: Recoil mass squared distribution of $\psi(2S)$ candidates. Left: distribution for J/ψ signal events (points with error bars) and J/ψ sideband events (shaded histogram). Right: the sideband-subtracted distribution (points with error bars) and the prediction from MC (solid line), scaled to the integral of the plot.

In order to suppress the contribution of combinatorial background, including misidentified $\gamma \to e^+e^-$ conversions (i.e. where the $\pi^+\pi^-$ were really e^+e^-), $\pi^+\pi^-$ candidates with mass $M(\pi^+\pi^-) > 0.4$ GeV were selected. The events removed by this cut can be seen in Figure 3.6.[2] The di-pion distribution is discussed in further detail in Section 3.7.1.

[2]The plot shown at Quarkonium Working Group 2006 had the $M(\pi^+\pi^- J/\psi)$ distribution with this binning, however the label on the x-axis was shown as 20 MeV per bin due to a coding mistake. This has been corrected for this thesis.

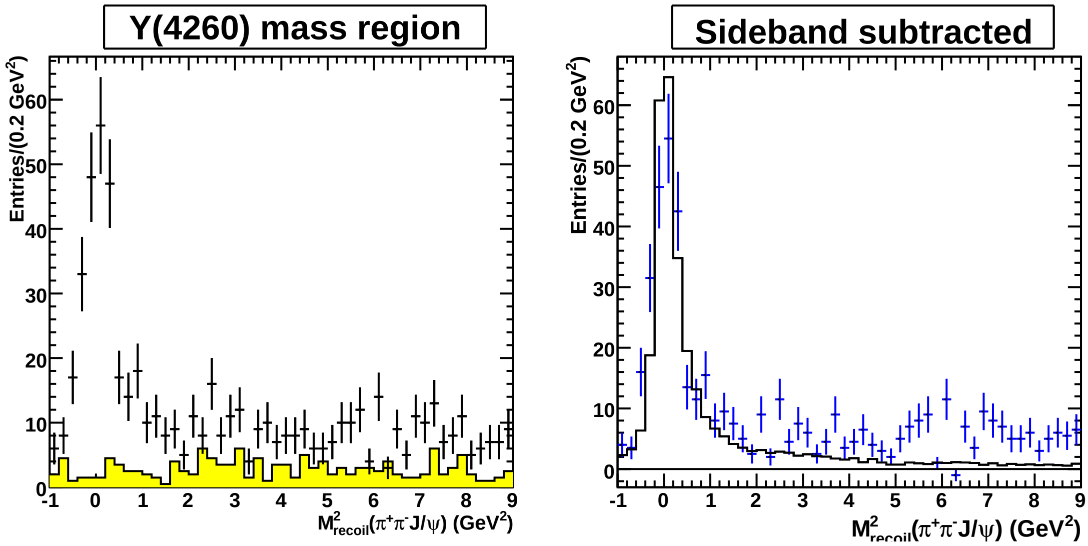

Figure 3.5: Recoil mass squared distribution of $Y(4260)$ candidates. Left: distribution for J/ψ signal events (points with error bars) and J/ψ side-band events (shaded histogram). Right: the sideband-subtracted distribution (points with error bars) and the prediction from MC (solid line), scaled to the integral of the selected events in the interval -1 GeV$^2 < M^2_{\rm recoil} < 1$ GeV^2.

The invariant mass plots for reconstructed events retained for further study can be seen in Figure 3.7 for the $\psi(2S)$ control sample and Figure 3.8 for the candidates in the $Y(4260)$ mass region.

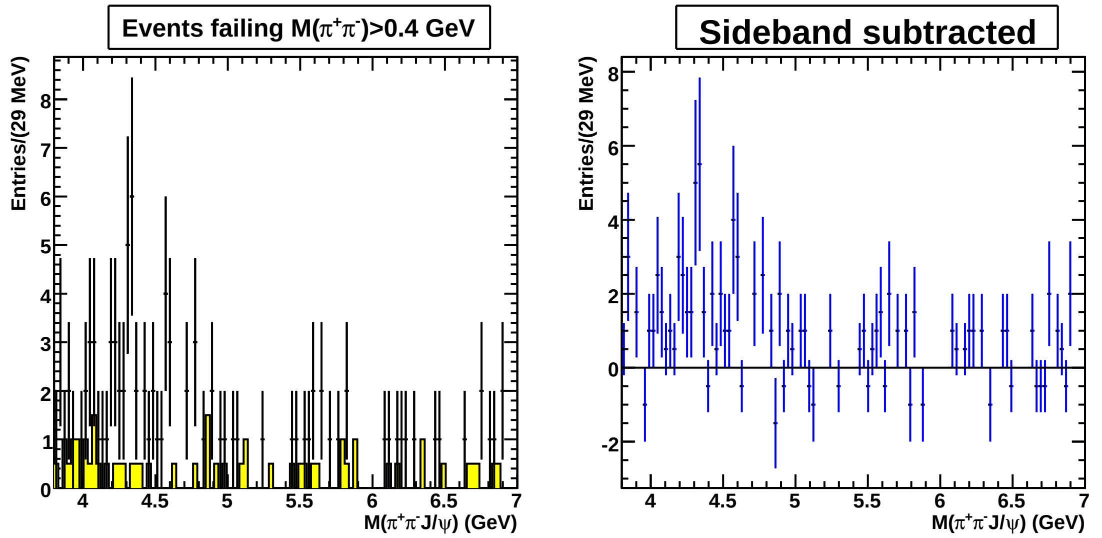

Figure 3.6: Invariant mass of $Y(4260)$ candidates failing $M(\pi^+\pi^-) > 0.4$ GeV. Left: distribution for J/ψ signal events (points with error bars) and J/ψ sideband events (shaded histogram). Right: the sideband-subtracted distribution (points with error bars).

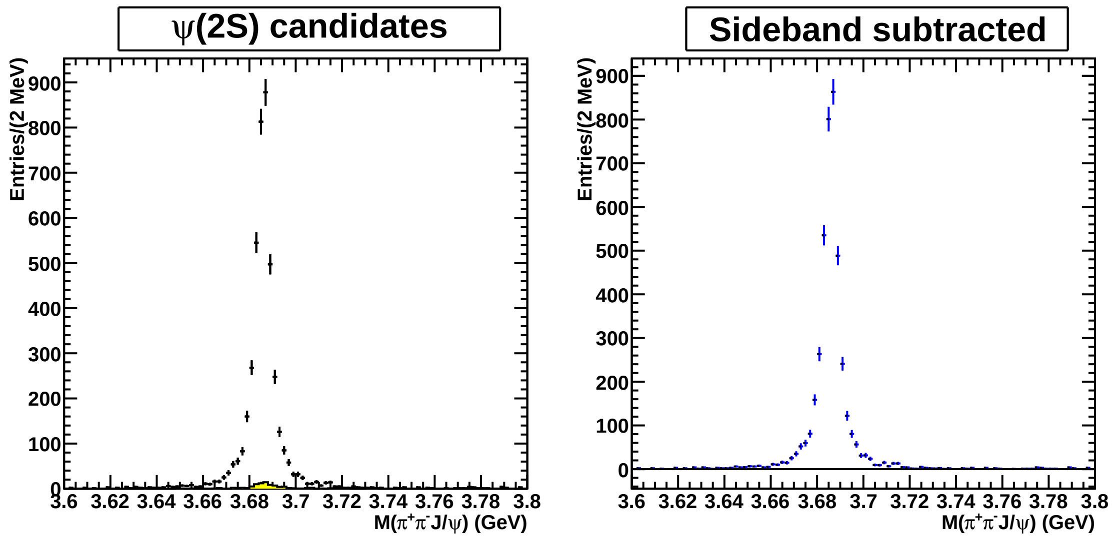

Figure 3.7: $\pi^+\pi^- J/\psi$ invariant mass distribution of candidates in the $\psi(2S)$ mass region. Left: distribution for J/ψ signal events (points with error bars) and J/ψ sideband events (shaded histogram). Right: the sideband-subtracted distribution (points with error bars).

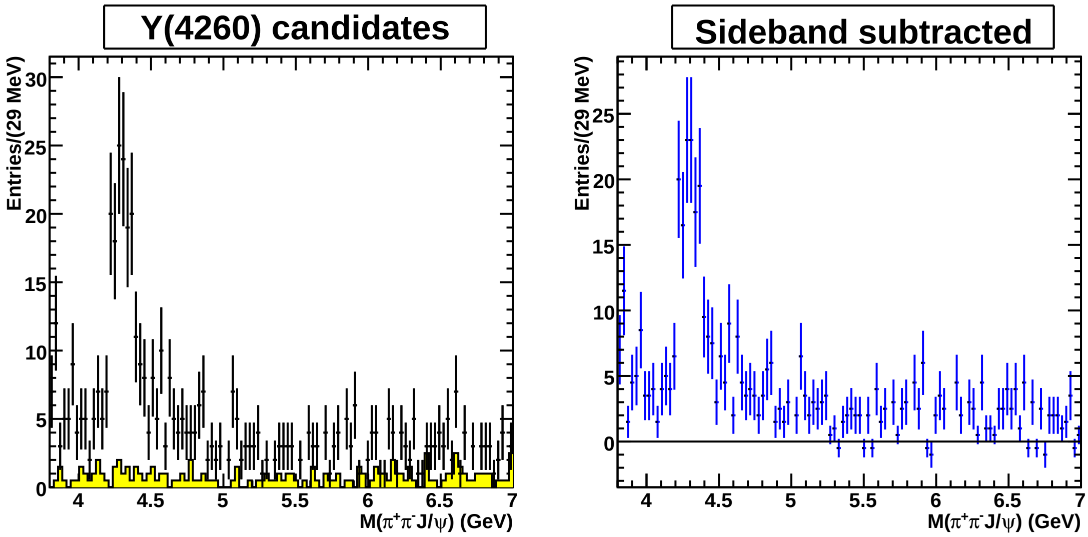

Figure 3.8: $\pi^+\pi^- J/\psi$ invariant mass distribution of candidates in the $Y(4260)$ mass region. Left: distribution for J/ψ signal events (points with error bars) and J/ψ sideband events (shaded histogram). Right: the sideband-subtracted distribution (points with error bars).

3.2.5 Fitting control sample

To test the reconstruction method developed, the $\psi(2S)$ was fitted and the results which were obtained were compared with the results from previous studies. In order to fit a signal shape to the $\psi(2S)$ control sample, a Gaussian, a broader bifurcated Gaussian and an additional broader Gaussian were used. All three Gaussian terms had a common mean $M_{\psi(2S)}$ which was allowed to float in the fit. A straight line was used to represent the background. The slope of the background and the widths and relative normalisation of each of the signal and background components were allowed to float in the fit. The results of the fit are shown in Figure 3.9 and Table 3.9. The fit returned $M_{\psi(2S)} = 3685.3 \pm 0.1\,\mathrm{MeV}$ (statistical errors only), cf. the Particle Data Group average for the $\psi(2S)$ mass: 3686.09 ± 0.34 MeV [104]. The $\psi(2S)$ was reconstructed with mass consistent with previous measurements. The natural width of the $\psi(2S)$ is too small to measure in this study: the width of the $\psi(2S)$ peak in the figure is dominated by experimental resolution.

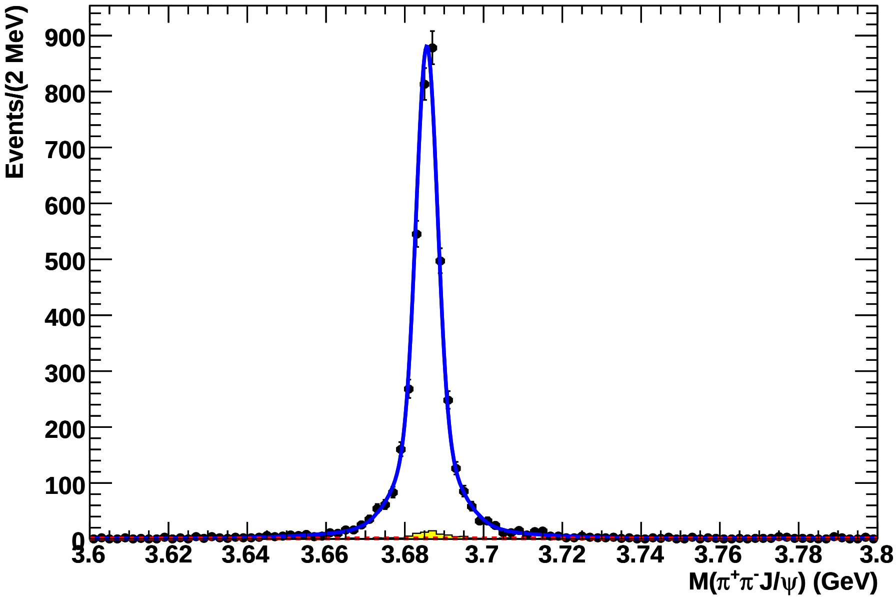

Figure 3.9: Invariant mass distribution for $\psi(2S)$ candidates in J/ψ signal events (points with error bars) and the events from J/ψ sidebands (shaded histogram). The fit to data (solid line) is described in the text.

Table 3.9: Results of fit to invariant mass distribution of $\psi(2S)$ candidates.

Signal parameters	(MeV)
Mean	3685.3 ± 0.1
Width Gaussian 1	2.6 ± 0.1
Left hand side width, Gaussian 2	7.1 ± 0.6
Right hand side width, Gaussian 2	6.6 ± 0.6
Width Gaussian 3	20 ± 2

3.3 Fitting procedure

The invariant mass distribution of the reconstructed candidates was then fitted and the properties of the distribution of the candidates was calculated. Since the $\psi(2S)$ control sample was found to be consistent with previous results; the properties of the $Y(4260)$ can measured with confidence.

3.3.1 $Y(4260)$ fits

The $M(\pi^+\pi^- J/\psi)$ distribution was fitted multiple times in order to investigate different features of the $Y(4260)$ and surrounding mass region. The primary fits were used in order to measure the mass and width of the state. Additionally, fits were performed to the $M(\pi^+\pi^- J/\psi)$ distribution produced in bins of di-pion mass and production angle ($\cos(\theta)$, relative to the z-axis of the e^+e^- collision). These additional fits will be described in subsequent sections.

A binned maximum likelihood fit was used as the primary fit for the $Y(4260)$ mass region. This was performed with the distribution of invariant mass $m = M(\pi^+\pi^- J/\psi)$. The signal function used was the product of a Breit-Wigner function, a phase space term, and a mass-dependent efficiency correction. The function used in the fit was:

$$\frac{dN}{dm} = a \cdot \frac{1}{(m - M_Y)^2 + \frac{1}{4}\Gamma^2} \cdot K(m) \cdot \epsilon(m), \tag{3.3}$$

where a is a normalisation term, M_Y and Γ are the Breit-Wigner mass and width parameters, respectively. The phase space term, $K(m)$ is given by:

$$K(m) = \sqrt{((m^2 + m_{J/\psi}^2 - M_{\pi^+\pi^-}^2)/(2m))^2 - m_{J/\psi}^2}. \tag{3.4}$$

Here, the mass parameter $M_{\pi^+\pi^-}$ was fixed to a nominal value of $0.5\,\mathrm{GeV}$.[3] The correction for the efficiency as a function of mass was based on an interpolation of results from $M(\pi^+\pi^- J/\psi)$ MC samples generated with different central mass values, which are described in Section 3.1.1. The efficiency measured with each sample is shown in Table 3.10. The efficiency at these points was interpolated with a straight line:

$$\epsilon(m) = a_\epsilon \cdot (m - M_0) + b_\epsilon, \tag{3.5}$$

[3] This value is within the range of values of $M(\pi^+\pi^-)$ produced in the events being measured and the results of the fit are not sensitive to the value of this parameter.

where $M_0 = 4.3\,\mathrm{GeV}$. The slope and intercept were determined to be $a_\epsilon = 7.4 \pm 1.3\,(\mathrm{GeV})^{-1}$ and $b_\epsilon = 9.31 \pm 0.07$, respectively. The signal function was added to a second-order polynomial representing the background and the effect of interference with other resonances was neglected. The parameters that were allowed to float in the fit were the number of signal events (N), the mean and width of the Breit-Wigner function (M_Y, Γ), and the background parameters. The fit to the data is shown in Figure 3.10, together with the featureless J/ψ mass sidebands in the shaded histograms. The results of the fit are shown in Table 3.11.

Table 3.10: $\pi^+\pi^- J/\psi$ efficiency at selected masses.

Mass (MeV)	Passing All Cuts (%)
3686	3.76 ± 0.06
4260	9.06 ± 0.13
4310	9.32 ± 0.11
4360	9.80 ± 0.10

Table 3.11: Results of the fit to the $\pi^+\pi^- J/\psi$ invariant mass spectrum. The statistical uncertainties are listed first, followed by the systematic uncertainties which are described in Section 3.4.

Signal parameter	Fit result
N (events)	$165\ ^{+24}_{-22}\ ^{+7}_{-23}$
M_Y (MeV)	$4295 \pm 10^{+11}_{-5}$
Γ (MeV)	$133\ ^{+26}_{-22}\ ^{+13}_{-6}$

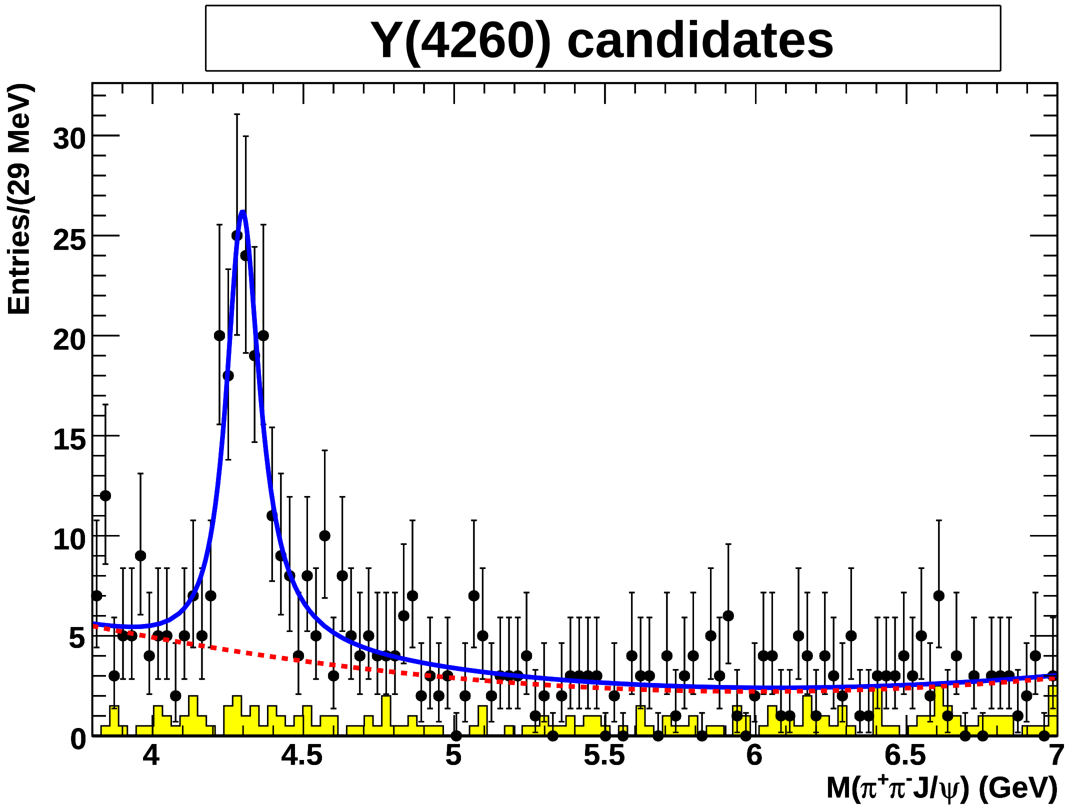

Figure 3.10: Invariant mass distribution for $Y(4260)$ candidates in data (points with error bars) and J/ψ mass sidebands (shaded histogram), with the fit to data (solid line) and its background component (dotted line) described in the text.

3.3.2 Calculation of significance

To estimate the significance of the $Y(4260)$ signal, fits with and without the signal term were compared. This was done by comparing the likelihoods returned by the main fit, and the main fit when the number of $Y(4260)$ events was fixed at zero events. The minimised values of the likelihood fit program are shown in Table 3.12. The significance was found to be 11, which is consistent with the clearly visible signal peak.

Table 3.12: Likelihoods returned by the signal and null fits to the $M(\pi^+\pi^- J/\psi)$ distribution, used in the calculation of the significance of the $Y(4260)$ peak.

Fit	$-2\ln(L)$
With signal term	-2×2149.54
Without signal term	-2×2088.85

3.4 Systematics

The systematic uncertainties were estimated on the main numerical results from the fit: the mass, the width and the cross-section. This was done by varying the fitting procedure, observing the variation in the result, and adding these in quadrature with the other sources of possible uncertainty that were checked.

To check the systematic uncertainty in the fit procedure, fits with variants of the fit function were performed. The variations to the fit were: Signal functions without phase space and efficiency corrections, a linear background shape, 10 MeV binning, and a $M(\pi^+\pi^- J/\psi) \in [3.8, 5.0]$ GeV fit range. The largest deviations in the values of the measured parameters were taken as the positive and negative systematic errors due to fitting. The resulting systematic uncertainties are shown on the top row of Table 3.13.

The possibility of a systematic error introduced by biases in the $Y(4260)$ mass reconstruction was calculated based on fits to the MC. A 2 MeV systematic error from the largest of the differences between the generated and fitted $Y(4260)$ masses in MC was measured. To estimate the total resolution on the mass, the $\psi(2S)$ was used for calibration. The difference between the measured mass of the $\psi(2S)$ and the value found in Ref. [104] was 0.8 MeV. This value was scaled to the $Y(4260)$ mass region, M_Y, using:

$$\frac{M_Y - m_{J/\psi} - 2 * m_\pi}{m_{\psi(2S)} - m_{J/\psi} - 2 * m_\pi},$$

which returns a value for the uncertainty on the mass resolution in the region of the $Y(4260)$ of 2.4 MeV.

The effective luminosity as a function of the energy released by the ISR photon was not accounted for in the fit. A systematic uncertainty was added to the cross-section and Γ_{ee} results from the relative change in the second-order QED radiator $W(s, x)$, calculated using the Equation 1.2 in Section 1.4, as the $\pi^+\pi^- J/\psi$ mass was changed from the fitted mean of the $Y(4260)$ Breit-Wigner by $\pm 1\Gamma$. A summary of systematic errors can be found in Table 3.13.

Table 3.13: Sources of systematic error on $Y(4260)$ measurements.

Source	Mass (MeV)	Width (MeV)	$\sigma \cdot \mathcal{B}$ (fb)	$\Gamma_{ee} \cdot \mathcal{B}$ (eV)
Fitting procedure	$^{+10}_{-2}$	$^{+13}_{-6}$	$^{+1}_{-5}$	$^{+0.2}_{-0.9}$
Measurement of mass in $Y(4260)$ MC	± 2	–	–	–
Mass scale from measurement of $\psi(2S)$	± 2	–	–	–
QED radiator at masses of $\pm 1\Gamma$	–	–	–	± 0.2
Total	$^{+11}_{-4}$	$^{+13}_{-6}$	$^{+1}_{-5}$	$^{+0.3}_{-0.9}$

3.5 Tests of ISR assumption

So far, the reconstruction of the ISR photon had not been required and production via ISR was assumed. To test this assumption, two things were checked: Firstly, ISR events are produced with a characteristic angular distribution, which was measured in Section 3.5.1. Secondly, the sample of events in which the ISR photon was reconstructed by the detector were investigated, in Section 3.5.2.

3.5.1 $\cos(\theta)$ distribution

The angle between the direction of the $\pi^+\pi^- J/\psi$ candidate relative to the direction of the e^- beam in the CM frame is referred to as the production or polar angle, θ. The distribution of θ for ISR events is well known, so we measure the $\cos(\theta)$ distribution and compare this with MC generated according to the theoretical expectation. The ISR process, including the $\cos(\theta)$ distribution, is discussed in Section 1.4.

To measure the $\cos(\theta)$ distribution, $M(\pi^+\pi^- J/\psi)$ fits were performed in bins of $\cos(\theta)$. Smaller bins were used close to $\cos(\theta) = \pm 1$, where the edge of the detector causes the efficiency to change rapidly. The results obtained from these smaller bins were then combined for the final plot, so that each bin had the same width. Signal and background parameters for the fits were fixed to those obtained from the fit to the full sample, and only the normalisation parameters were allowed to vary. These fits are shown in Figures 3.11 and 3.12 and the results of the fits and the efficiency in each bin are shown in Table 3.14. The yield, N_i, in each bin was then corrected using the efficiency, ϵ_i, calculated in the same bin. The efficiency as a function of $\cos(\theta)$ is shown in Figure 3.13. In the figure, it can be noted that the detection efficiency for $\pi^+\pi^- J/\psi$ candidates does not drop to zero at the edge of the detector. While the ISR photon from a candidate produced along the beam-line will escape the detector, the candidate itself will decay, imparting momentum transverse to the beam-line, allowing its daughter particles to be reconstructed. The resultant efficiency-corrected $\cos(\theta)$ distribution for $Y(4260)$ candidates, with the prediction from MC, are shown in Figure 3.14. These events are consistent with the assumption of ISR production.

The same procedure was followed to produce a $\cos(\theta)$ plot for the $\psi(2S)$ reference channel. The resulting plot for the $\psi(2S)$ is shown in Figure 3.15, and the results are consistent with the assumption of ISR production.

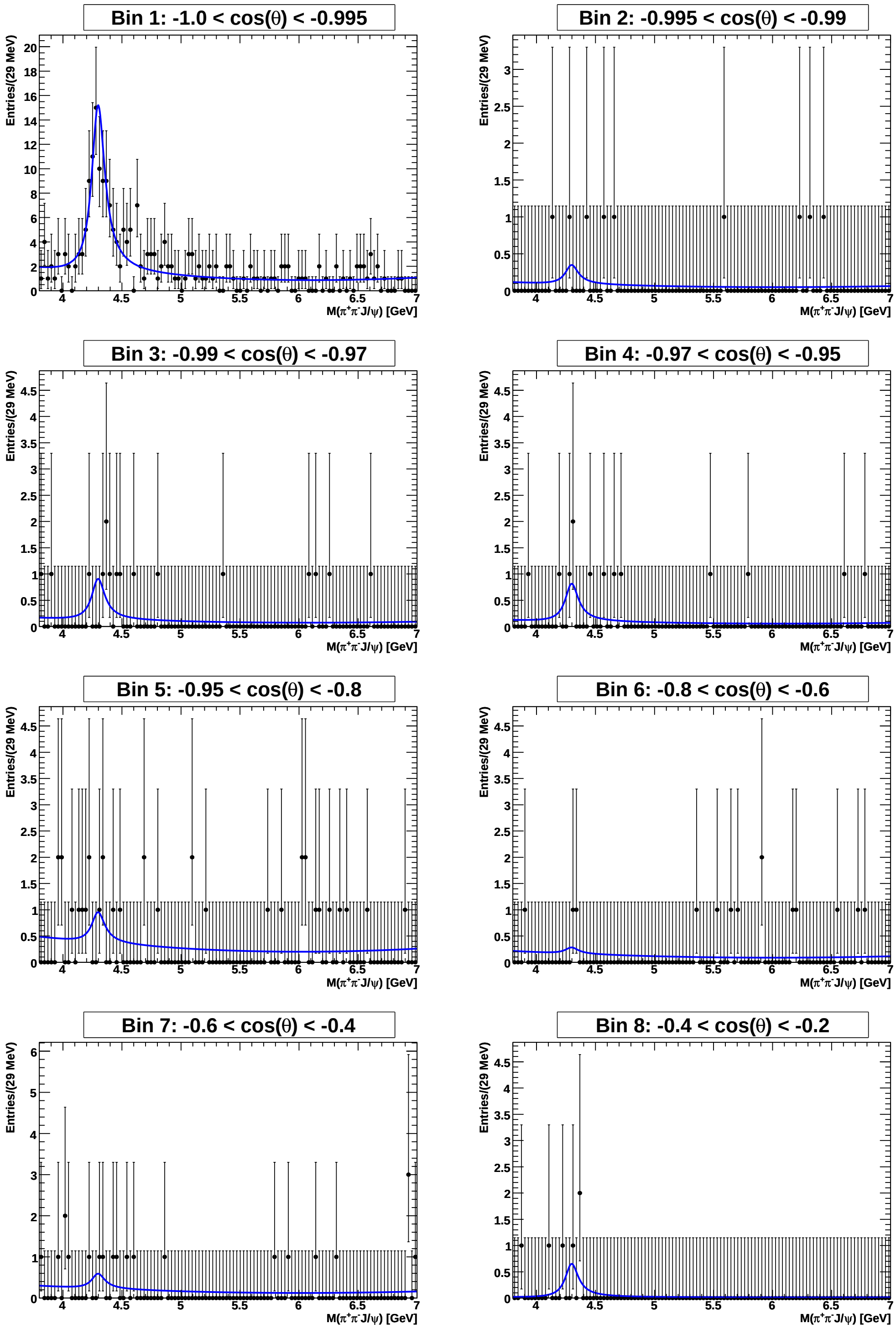

Figure 3.11: Fits (solid line) to $Y(4260)$ candidates (points with error bars), in Bins 1 to 8 of $\cos(\theta)$, described in text.

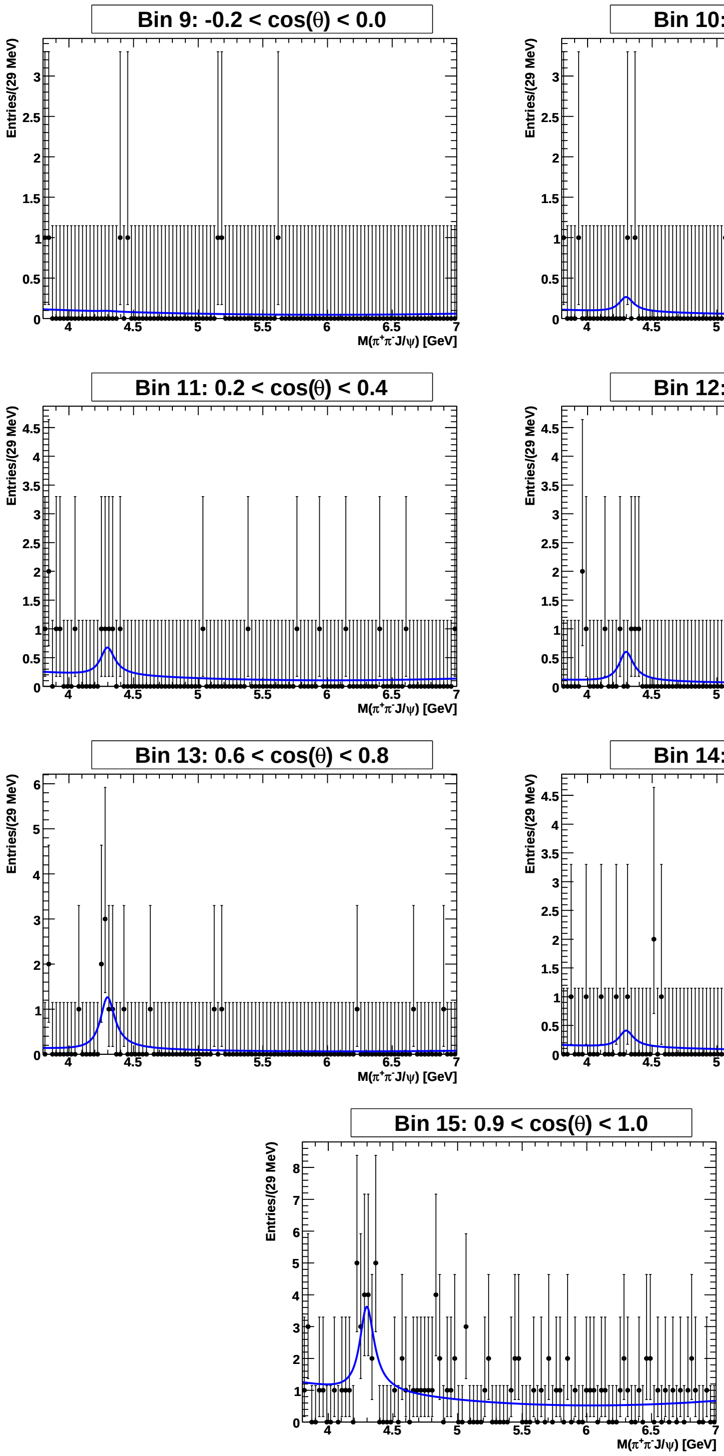

Figure 3.12: Fits (solid line) to $Y(4260)$ candidates (points with error bars), in Bins 9 to 15 of $\cos(\theta)$, described in text.

Table 3.14: Fit results and efficiencies in bins of $\cos(\theta)$. The uncertainty on the efficiency comes from the MC statistics and the systematic uncertainty from the MC PID correction. The uncertainty from the MC statistics dominates.

Bin	Range	N_i	ϵ_i (%)	N_i/ϵ_i
1	-1.000 to -0.995	105 ± 14	11.1 ± 0.1	943 ± 129
2	-0.995 to -0.990	1.99 ± 2.91	10.8 ± 0.5	18.4 ± 26.9
3	-0.99 to -0.97	5.95 ± 3.86	10.6 ± 0.4	56.2 ± 36.5
4	-0.97 to -0.95	5.50 ± 3.63	9.95 ± 0.53	55.2 ± 36.6
5	-0.95 to -0.8	4.45 ± 4.42	7.62 ± 0.28	58.4 ± 58.1
6	-0.8 to -0.6	0.905 ± 2.15	11.9 ± 0.5	7.59 ± 18.1
7	-0.6 to -0.4	2.77 ± 3.46	12.0 ± 0.7	23.1 ± 28.8
8	-0.4 to -0.2	4.85 ± 2.83	12.8 ± 0.8	37.8 ± 22.1
9	-0.2 to 0.0	0.07 ± 2.24	12.2 ± 0.8	0.5 ± 18.4
10	0.0 to 0.2	1.40 ± 2.05	10.5 ± 0.8	13.3 ± 19.5
11	0.2 to 0.4	3.69 ± 3.08	11.9 ± 0.8	31.1 ± 26.0
12	0.4 to 0.6	3.90 ± 3.05	9.87 ± 0.60	39.5 ± 31.0
13	0.6 to 0.8	8.85 ± 3.98	8.22 ± 0.42	108 ± 48.8
14	0.8 to 0.9	2.20 ± 3.10	5.72 ± 0.35	38.5 ± 54.3
15	0.9 to 1.0	20.4 ± 7.3	1.96 ± 0.04	1040 ± 370

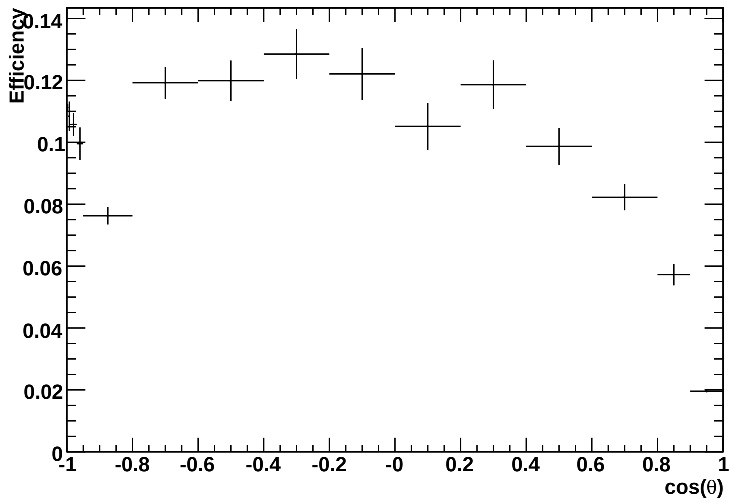

Figure 3.13: Efficiencies in bins of $\cos(\theta)$ for $Y(4260)$ events.

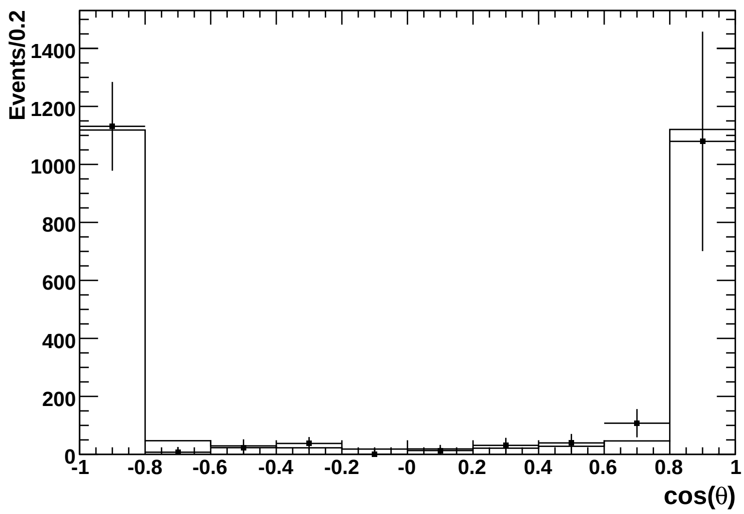

Figure 3.14: Efficiency-corrected $\cos(\theta)$ distribution for $Y(4260)$ candidates in data (points with error bars), shown with the scaled prediction from MC (histogram).

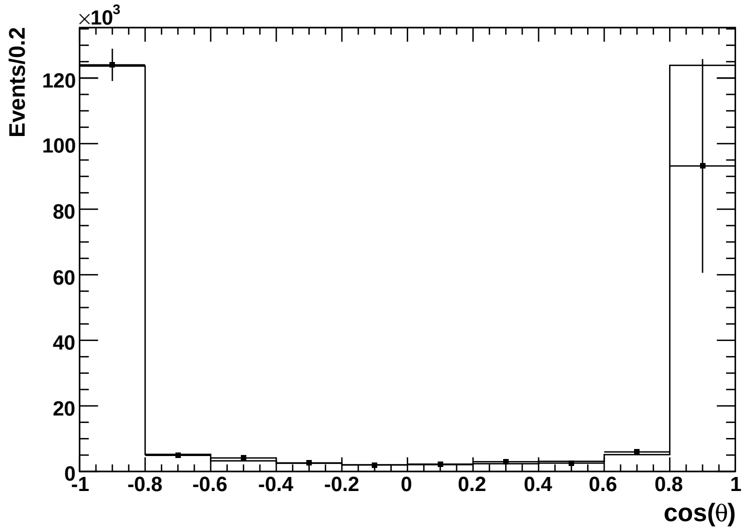

Figure 3.15: Efficiency-corrected $\cos(\theta)$ distribution for $\psi(2S)$ candidates in data (points with error bars), shown with the scaled prediction from MC (histogram).

3.5.2 Fully reconstructed events

The ISR photon is produced opposite the $\pi^+\pi^- J/\psi$ candidate in the CM frame and the production is greatest at small angles to the electron or positron beam, as can be seen in the previous section. This means that the majority of the produced ISR photons are outside the angular acceptance of the detector. However, the $\pi^+\pi^- J/\psi$ candidates that are produced with the ISR photon inside the angular acceptance of the detector, are themselves directed at the detector and have a higher efficiency.

Photons were reconstructed as ECL energy clusters that were unable to be associated with a charged track. The highest energy photon in each event was identified, γ_{max}, and if it satisfied: $E(\gamma_{max}) + E((\pi^+\pi^- J/\psi)) > 10$ GeV then the ISR photon was considered to be reconstructed. The $Y(4260)$ candidates that passed this criterion are shown in Figure 3.16. In this figure a clear enhancement is visible at $M(\pi^+\pi^- J/\psi) \approx 4300$ MeV.

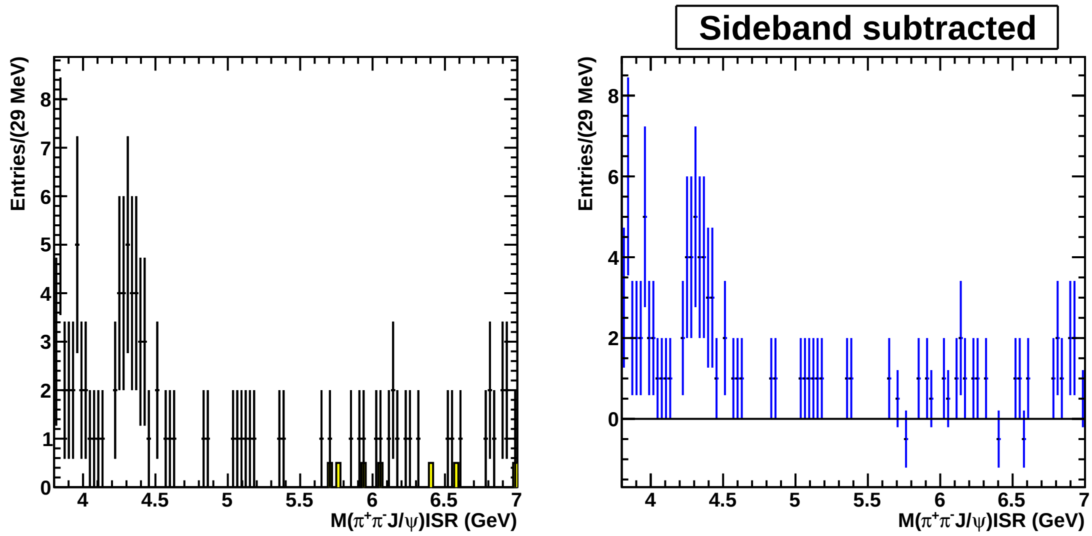

Figure 3.16: $\pi^+\pi^- J/\psi$ invariant mass spectrum for $Y(4260)$ candidates in events with the ISR photon reconstructed. Left: J/ψ signal events (points with error bars) and J/ψ sideband events (shaded histogram with very few events). Right: the sideband-subtracted distribution (points with error bars).

3.6 Di-electron and di-muon subsamples

The $Y(4260) \to \pi^+\pi^- J/\psi$ candidate sample is formed from the two included leptonic decays of the J/ψ. The $J/\psi \to e^+e^-$ and $J/\psi \to \mu^+\mu^-$ branching fractions are similar, so the produced $\pi^-\pi^+e^-e^+$ and $\pi^+\pi^-\mu^+\mu^-$ rates should be similar. The final number of di-electron and di-muon events will then depend on the selections and backgrounds in each case. Additional fits to the $\pi^+\pi^- J/\psi$ invariant mass distribution were conducted on the di-electron and di-muon samples independently. The di-electron and di-muon fractions in data were compared, along with the $Y(4260)$ masses reconstructed in each case and were found to be consistent with the combined result.

The fits to each subsample used the same fit function as the primary result. The sample and fit can be seen in Figure 3.17 for the di-electron sample and Figure 3.18 for the di-muon sample. Table 3.15 shows the results obtained from the two fits. The difference in the central value of the masses was found to be 1.3σ, which is not significant. The fraction of events that were reconstructed in the di-muon sample was checked against the same value from MC and the results are shown in Table 3.16. The fraction in both the $\psi(2S)$ control and $Y(4260)$ samples were found to be consistent between data and MC, with large errors in the $Y(4260)$ sample in data.

Table 3.15: Results of fits to the invariant mass distribution of the di-electron and di-muon subsamples fitted separately.

Function	Parameter	$e^+e^-\pi^+\pi^-$ fit	$\mu^+\mu^-\pi^+\pi^-$ fit
Signal	Mean (MeV)	4295 ± 13	4317 ± 11
	Width (MeV)	127 ± 47	111 ± 43
	Events	82 ± 24	71 ± 19
Background	Slope	-0.08 ± 0.18	-0.7 ± 0.1
	Quadratic term	-0.1 ± 0.2	0.01 ± 0.25
	Events	144 ± 25	91 ± 19

Table 3.16: Comparison of the fraction of events reconstructed in the di-muon channel in data and MC.

	$\psi(2S)$	$Y(4260)$
Data	0.61 ± 0.01	0.46 ± 0.16
MC	0.64 ± 0.03	0.63 ± 0.01

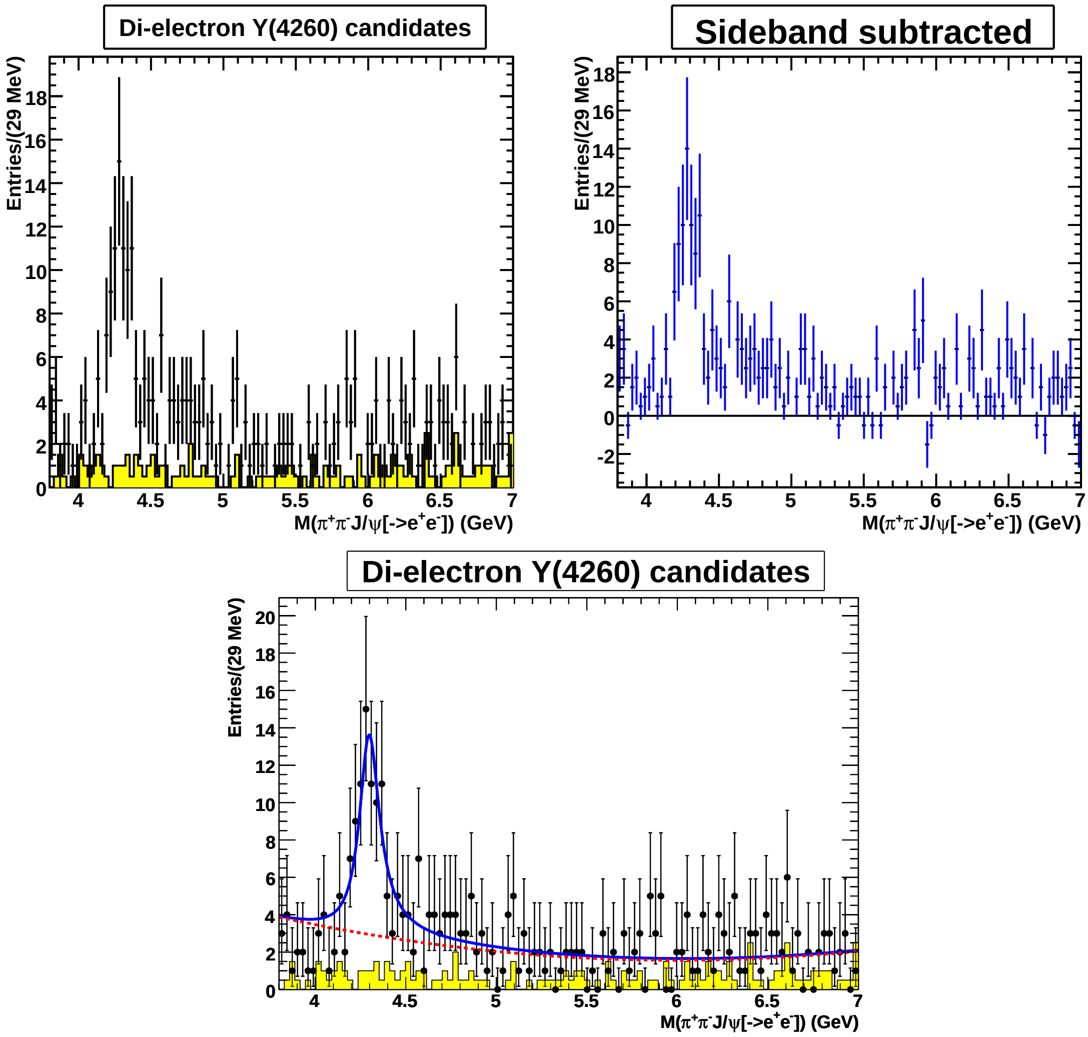

Figure 3.17: Top left: $\pi^+\pi^- J/\psi$ invariant mass spectrum for di-electron $Y(4260)$ candidates; J/ψ signal events (points with error bars) and J/ψ sideband events (shaded histogram). Top right: the sideband-subtracted distribution (points with error bars). Bottom: fit to the data in the top left plot (solid line) with the background contribution in the fit (dotted line).

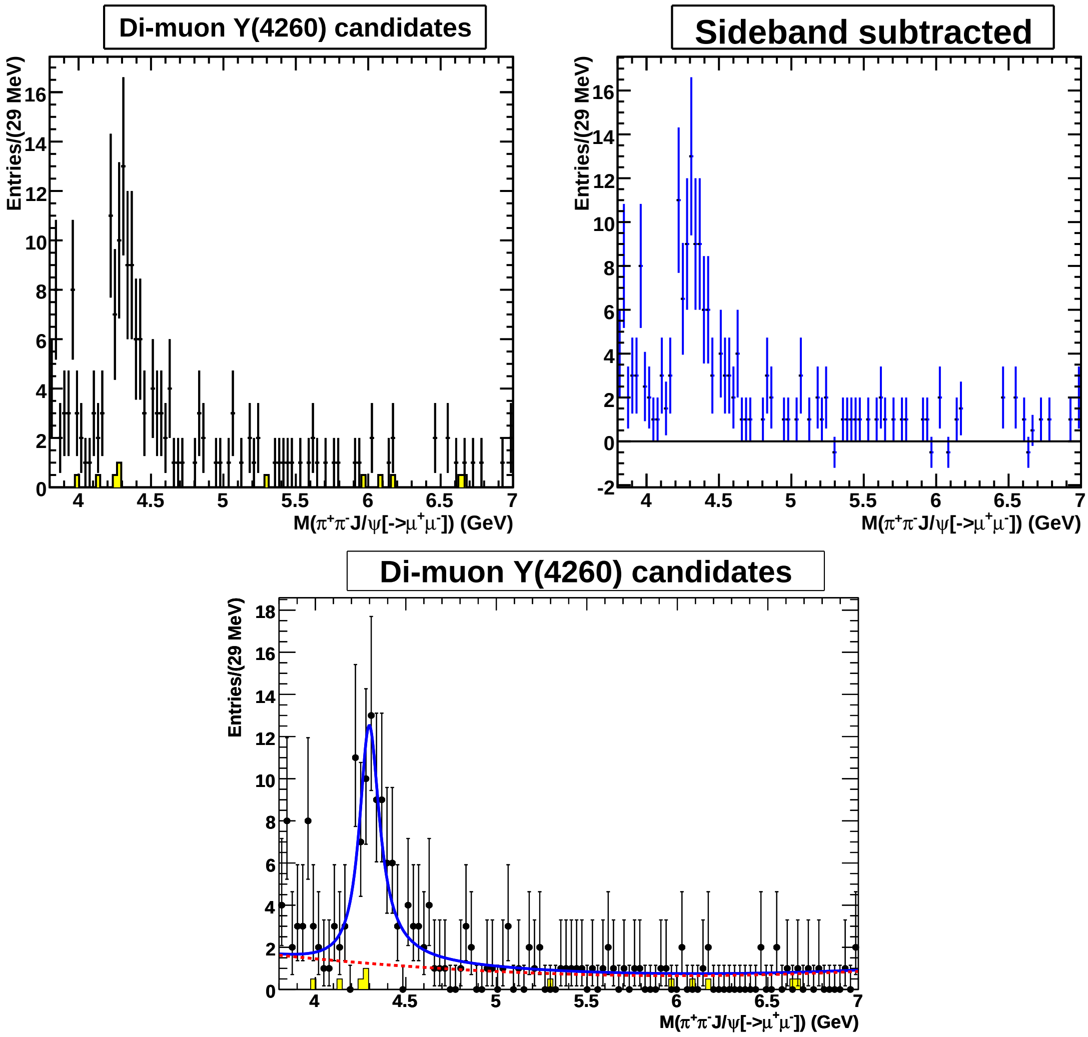

Figure 3.18: Top left: $\pi^+\pi^- J/\psi$ invariant mass spectrum for di-muon $Y(4260)$ candidates; J/ψ signal events (points with error bars) and J/ψ sideband events (shaded histogram). Top right: the sideband-subtracted distribution (points with error bars). Bottom: fit to the data in the top left plot (solid line) with the background contribution in the fit (dotted line).

3.7 Kinematic distributions

Several kinematic quantities are not constrained by the primary J^{PC} quantum numbers; the invariant mass of the pion pair, the invariant mass a single pion and the J/ψ particle and the various decay angles.

3.7.1 Di-pion mass

The invariant mass of the two pion combination, the di-pion mass, is of theoretical and experimental interest. Its distribution is not determined from the primary quantum numbers, J^{PC}, which are known from the ISR production mechanism to be 1^{--}. So its shape has to be measured. The shape of this distribution may assist in isolating a description of the state from the competing theoretical models of the $Y(4260)$.

In order to measure the di-pion mass distribution, fits to the $M(\pi^+\pi^- J/\psi)$ distribution in bins of $M(\pi^+\pi^-)$ were produced and the resulting yields plotted. The effect of the $\pi^+\pi^- J/\psi$ mass threshold which was introduced by the $M(\pi^+\pi^-)$ binning was taken into account by multiplying the signal and background terms by an appropriate threshold function in each bin:

$$\sqrt{m - M_{\min}},$$

where $m = M(\pi^+\pi^- J/\psi)$ and M_{min} is the minimum $M(\pi^+\pi^- J/\psi)$ mass able to be produced by events in each $M(\pi^+\pi^-)$ bin. For each of the binned fits, the signal and background parameters were fixed to the values measured in a fit to the full sample, without the $M(\pi^+\pi^-) > 40$ MeV cut. Only the signal and background yields were allowed to vary. The threshold value was calculated and fixed in each fit. The individual fits in $M(\pi^+\pi^-)$ bins are shown in Figures 3.19 and 3.20. The results were tabulated and are shown in Table 3.17. The yield (N_i) in each bin was corrected using the efficiency (ϵ_i), calculated in the same bin using $Y(4260)$ MC. To determine the efficiency at M_Y, the fit results from the three MC samples were interpolated. The errors on the efficiency were taken from the MC sample closest in mass to the fitted result in data, which is the sample generated with a mass of 4310 MeV. These efficiencies in bins of $M(\pi^+\pi^-)$ are shown in Figure 3.21. The final result for the di-pion mass with yields from each fit, with efficiency-corrected bin by bin, is shown in Figure 3.22 along with a prediction from the $M = 4310$ MeV MC sample. In this MC sample, the mass of the pion pair was generated according to phase space. As can be seen in the figure, the measured di-pion distribution is inconsistent with a decay via phase space.

Table 3.17: Fit results and efficiencies in bins of $M(\pi^+\pi^-)$. The uncertainty on the efficiency comes from the MC statistics and the systematic error from the MC PID correction. The error from the MC statistics dominates.

Bin	Range (GeV)	N_i	ϵ_i (%)	N_i/ϵ_i
1	0.28 to 0.38	21.6 ± 7.3	4.81 ± 1.87	448 ± 151
2	0.38 to 0.49	13.7 ± 5.7	4.82 ± 0.64	284 ± 119
3	0.49 to 0.60	9.1 ± 5.0	4.94 ± 0.39	185 ± 101
4	0.60 to 0.70	10.2 ± 5.1	5.18 ± 0.30	197 ± 99
5	0.70 to 0.81	0.0 ± 3.6	5.55 ± 0.27	0.0 ± 65
6	0.81 to 0.91	38.7 ± 7.9	6.03 ± 0.27	641 ± 131
7	0.91 to 1.02	42.6 ± 8.4	6.63 ± 0.29	642 ± 127
8	1.02 to 1.12	32.3 ± 6.9	7.35 ± 0.32	439 ± 94
9	1.12 to 1.23	22.8 ± 5.8	8.20 ± 0.37	279 ± 70
10	1.23 to 1.33	16.0 ± 4.3	9.16 ± 0.55	175 ± 47

The di-pion mass distribution was also generated for the control sample in data and MC. Figure. 3.23 shows this result, which was corrected using a second order polynomial fit to the binned efficiency from MC produced at the nominal $\psi(2S)$ mass. The errors here are dominated by the MC error in the binned efficiencies. The di-pion distribution in the control sample agrees with the prediction from MC, which was generated using the known di-pion mass distribution for $\psi(2S)$ decays.

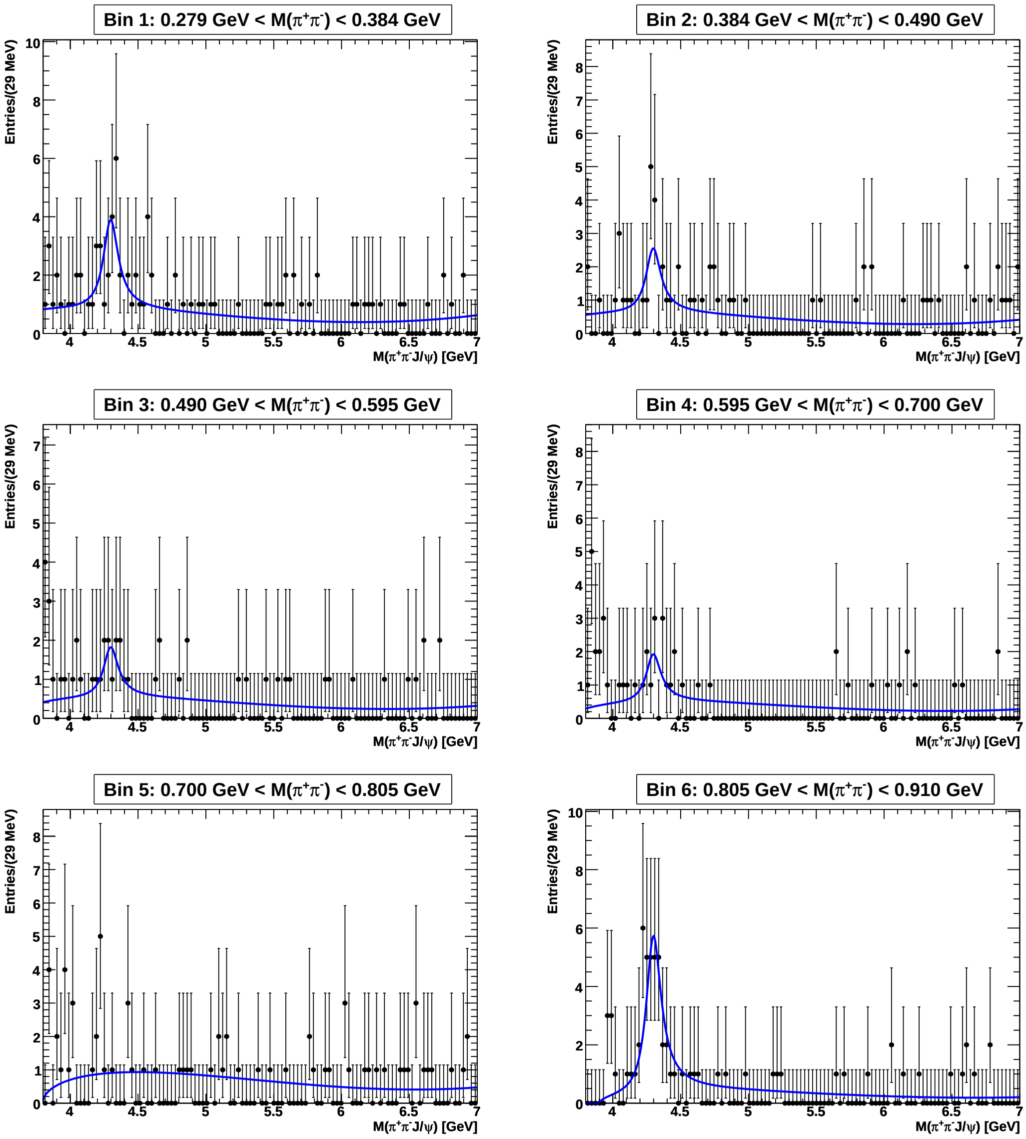

Figure 3.19: Fits (solid line) to $Y(4260)$ candidates (points with error bars), in Bins 1 to 6 of $M(\pi^+\pi^-)$, described in text.

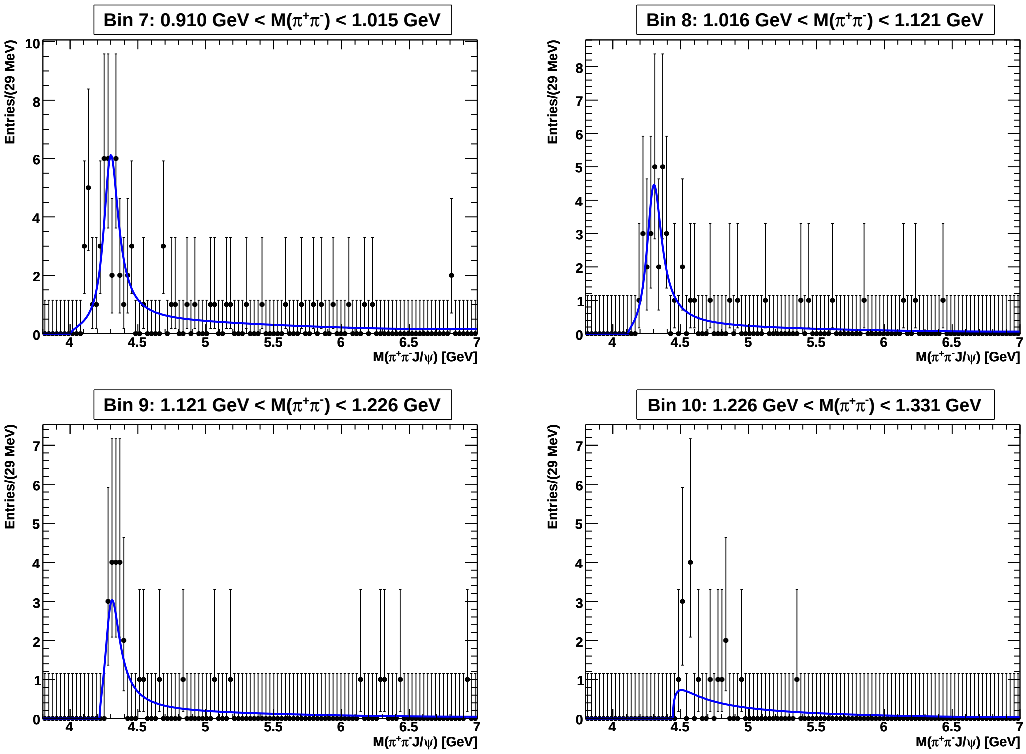

Figure 3.20: Fits (solid line) to $Y(4260)$ candidates (points with error bars), in Bins 7 to 10 of $M(\pi^+\pi^-)$, described in text.

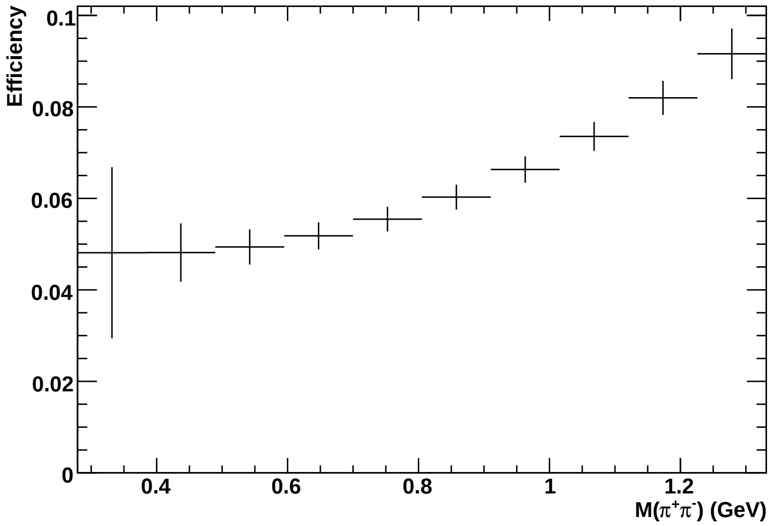

Figure 3.21: Efficiency for $Y(4260)$ in bins of $M(\pi^+\pi^-)$ with errors taken from the MC sample produced with a central mass of 4310 MeV.

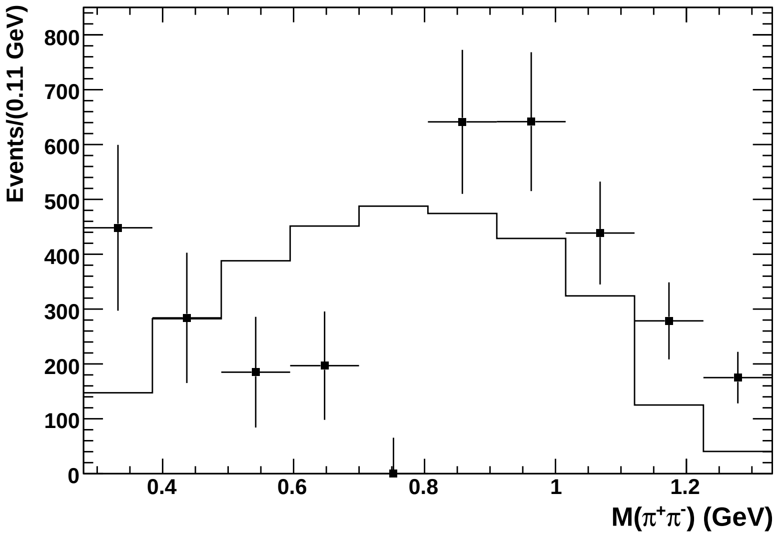

Figure 3.22: Invariant mass of $\pi^+\pi^-$ combinations in $Y(4260)$ candidates from fitted yields, after an efficiency correction in data (points with error bars), shown with the scaled prediction from MC with di-pion distribution generated according to phase space (solid line).

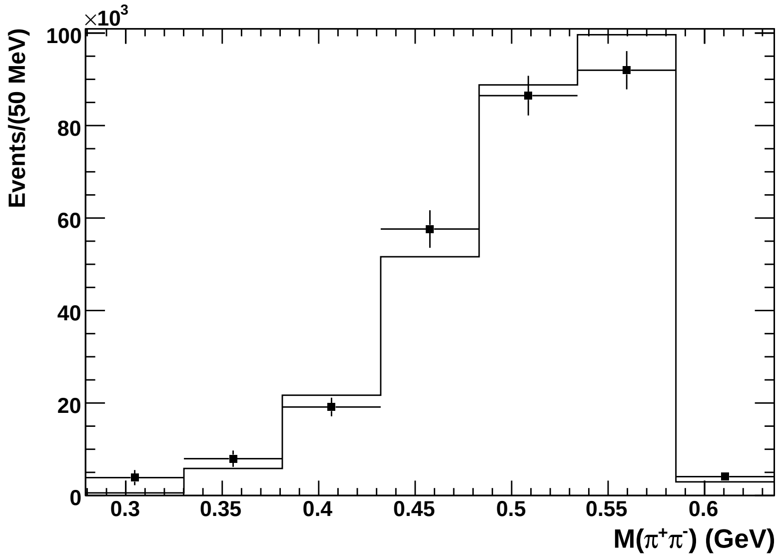

Figure 3.23: Invariant mass of $\pi^+\pi^-$ combinations in $\psi(2S)$ candidates, after efficiency correction in data (points with error bars), shown with the scaled prediction from $\psi(2S)$ MC (solid line).

3.7.2 $M(\pi^+ J/\psi)$

In 2008, Belle discovered a resonance-like structure in the $\pi^\pm\psi(2S)$ mass distribution in $B \to K\pi^\pm\psi(2S)$ decays [106]. If confirmed, this state would be manifestly exotic in nature, containing $c\bar{c}$ content as well as a net charge. The $Y(4260)$ is considered a strong candidate for being an exotic meson; the $\pi^+ J/\psi$ distribution in $Y(4260)$ decays was investigated to see if this distribution showed any structure. This invariant mass distribution was formed for four mass regions, as shown in Figure 3.24. No additional features were observed when the events from the $Y(4260)$ peak were compared to the regions on either side of the peak.

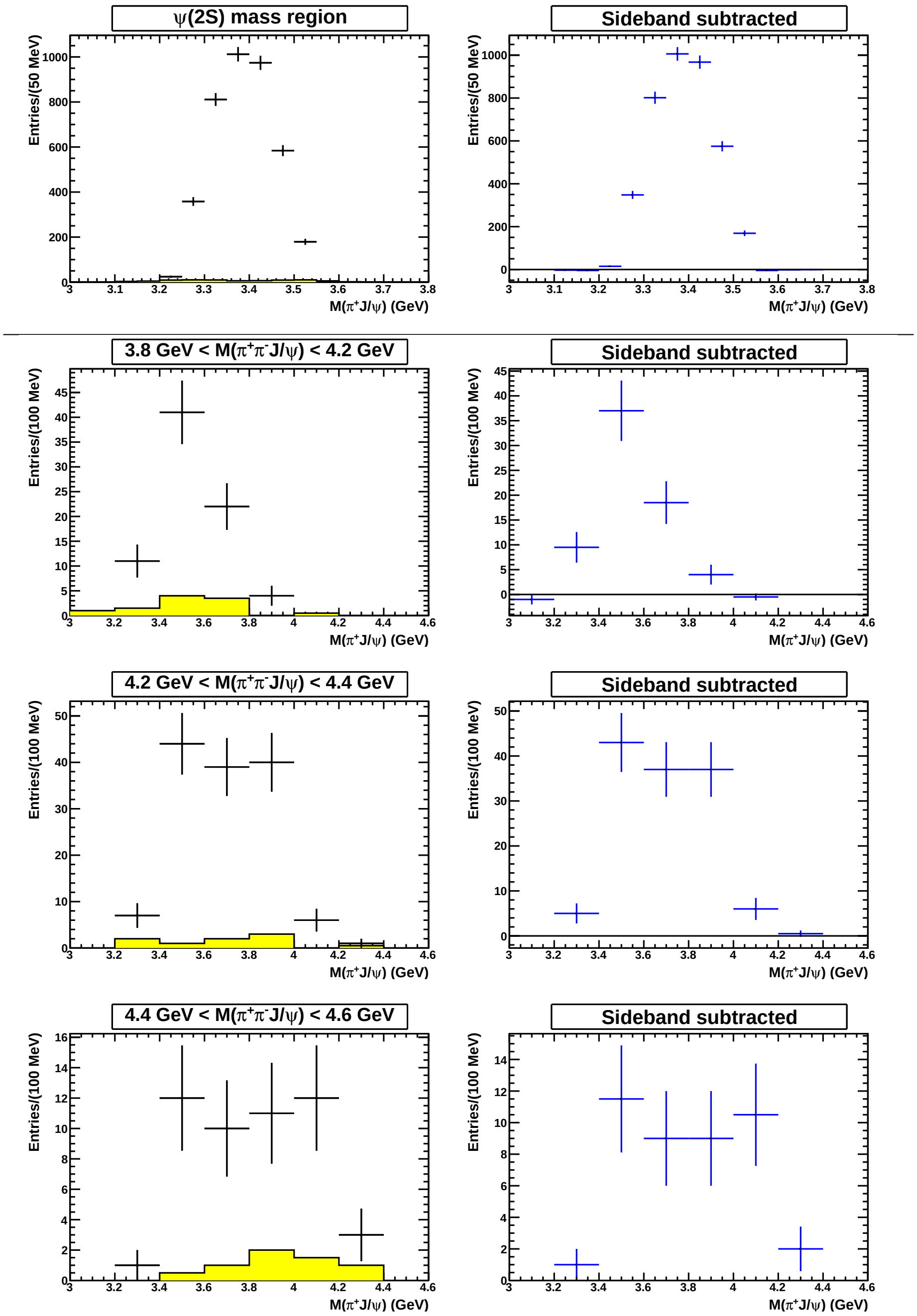

Figure 3.24: $M(\pi^+ J/\psi)$ distributions. Left hand column: J/ψ signal events (points with error bars) and J/ψ sideband events (shaded histogram). Right hand column: the sideband-subtracted distribution (points with error bars). Row 1: Events in the $\psi(2S)$ mass region. Row 2: Events in $M(\pi^+\pi^-\ell^+\ell^-) \in [3.8, 4.2]$ GeV. Row 3: Events in $M(\pi^+\pi^-\ell^+\ell^-) \in [4.2, 4.4]$ GeV. Row 4: Events in $M(\pi^+\pi^-\ell^+\ell^-) \in [4.4, 4.6]$ GeV. Note: Rows 2, 3 and 4 all have the same range and binning, but the $M(\pi^+ J/\psi)$ threshold increases as the $M(\pi^+\pi^-\ell^+\ell^-)$ mass increases.

3.7.3 Decay angles

The decay angles of the various daughter particles are not constrained by theory and are of interest in distinguishing between different models of the structure of the $Y(4260)$. The $J/\psi \to \ell^+\ell^-$ and $\pi^+\pi^-$ helicity angle distributions were investigated.

To get the angles related to the ℓ^+ in the J/ψ frame, the system was boosted to the J/ψ frame and the axes were rotated to align with the local z-axis, which was taken as the direction of the J/ψ in the $Y(4260)$ rest frame. Figure 3.25 shows a diagram of the angles in the decay of the $\psi(2S)$ and $Y(4260)$: these are denoted by X in the diagram. The angles in the figure that are highlighted in red, $\theta_{J/\psi}$, $\phi_{J/\psi}$ and $\theta_{\pi\pi}$, are shown this section. The $\cos(\theta_{J/\psi})$ and $\phi_{J/\psi}$ distributions are shown in Figures 3.26 and 3.27 respectively. Figure 3.28 shows the π^+ helicity in the $\pi^+\pi^-$ rest frame, which is the angle between the π^+ direction and the $\pi^+\pi^-$ thrust direction. In the figures, these distributions are shown for events from four $M(\pi^+\pi^- J/\psi)$ mass regions: on-peak, $M \in [4.2, 4.4]$ GeV; and above and below the peak, for $M \in [4.4, 4.6]$ GeV and $M \in [3.8, 4.2]$ GeV, respectively; and the $\psi(2S)$ mass region. In each case, there is a possible hint of structure in the on-peak distributions, while the off-peak distributions show a large scatter.

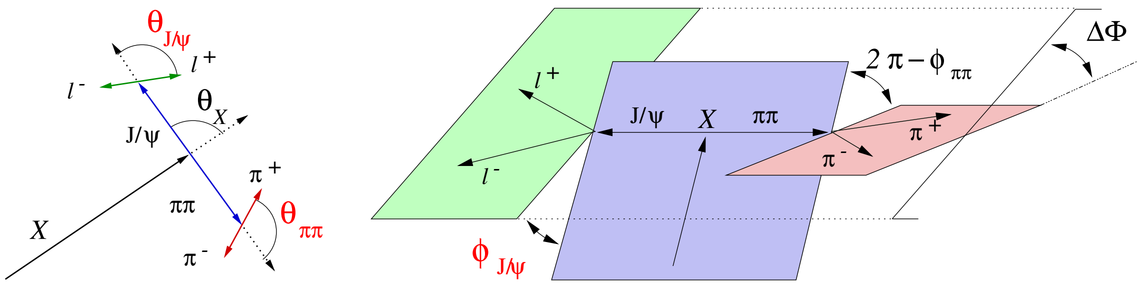

Figure 3.25: Diagram of the angles between the daughter particles in decays of $\psi(2S)$ and $Y(4260)$ particles, denoted by X in the diagram. Left: diagram showing the angles in plane. Right: diagram showing the angles between the planes in the decay chain. The distribution of the angles with labels in red, $\theta_{J/\psi}$, $\phi_{J/\psi}$ and $\theta_{\pi\pi}$, were measured for candidates. Reproduced from Ref. [107].

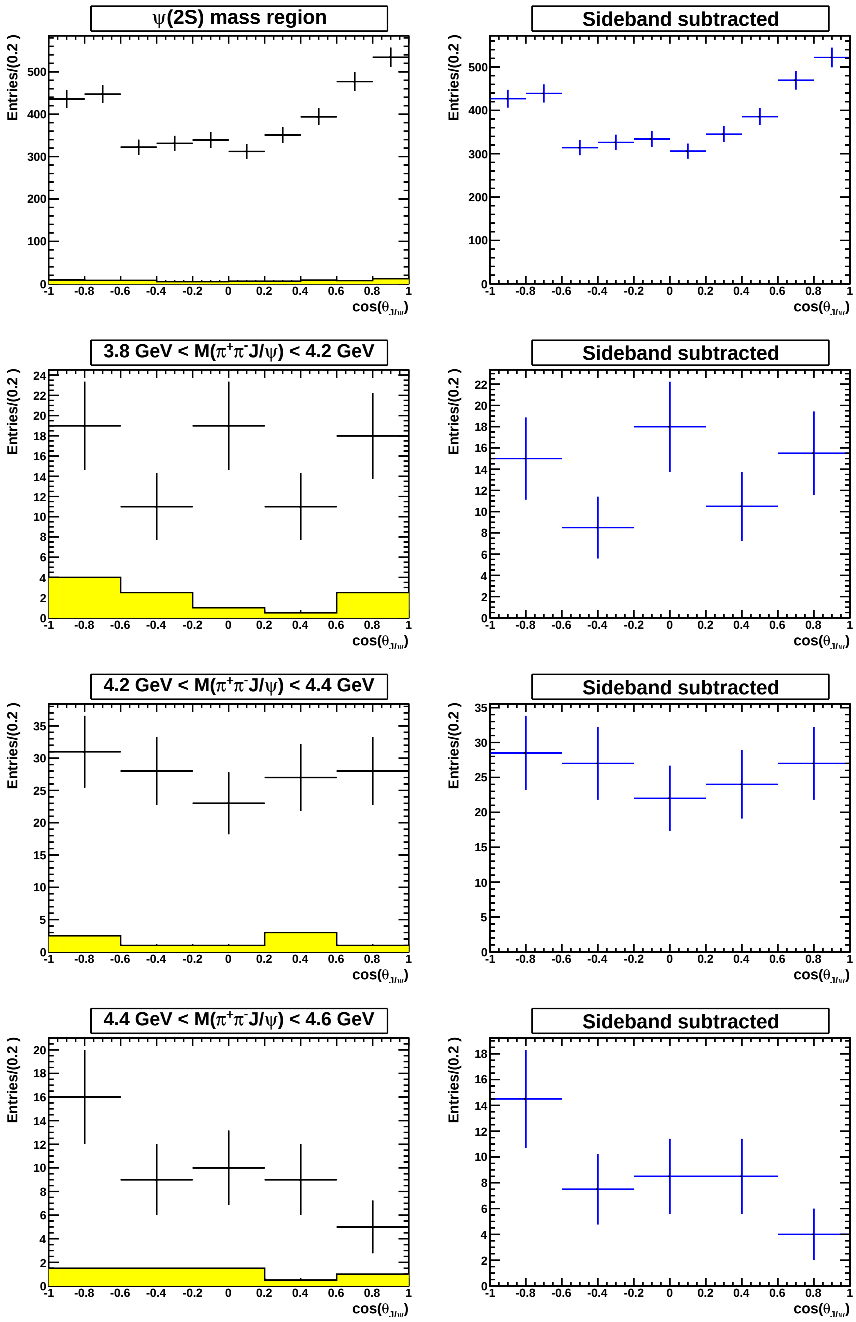

Figure 3.26: $\cos(\theta_{J/\psi})$ distributions. Left hand column: J/ψ signal events (points with error bars) and J/ψ sideband events (shaded histogram). Right hand column: the sideband-subtracted distribution (points with error bars). Row 1: Events in the $\psi(2S)$ mass region. Row 2: Events in $M(\pi^+\pi^-\ell^+\ell^-) \in [3.8, 4.2]$ GeV. Row 3: Events in $M(\pi^+\pi^-\ell^+\ell^-) \in [4.2, 4.4]$ GeV. Row 4: Events in $M(\pi^+\pi^-\ell^+\ell^-) \in [4.4, 4.6]$ GeV.

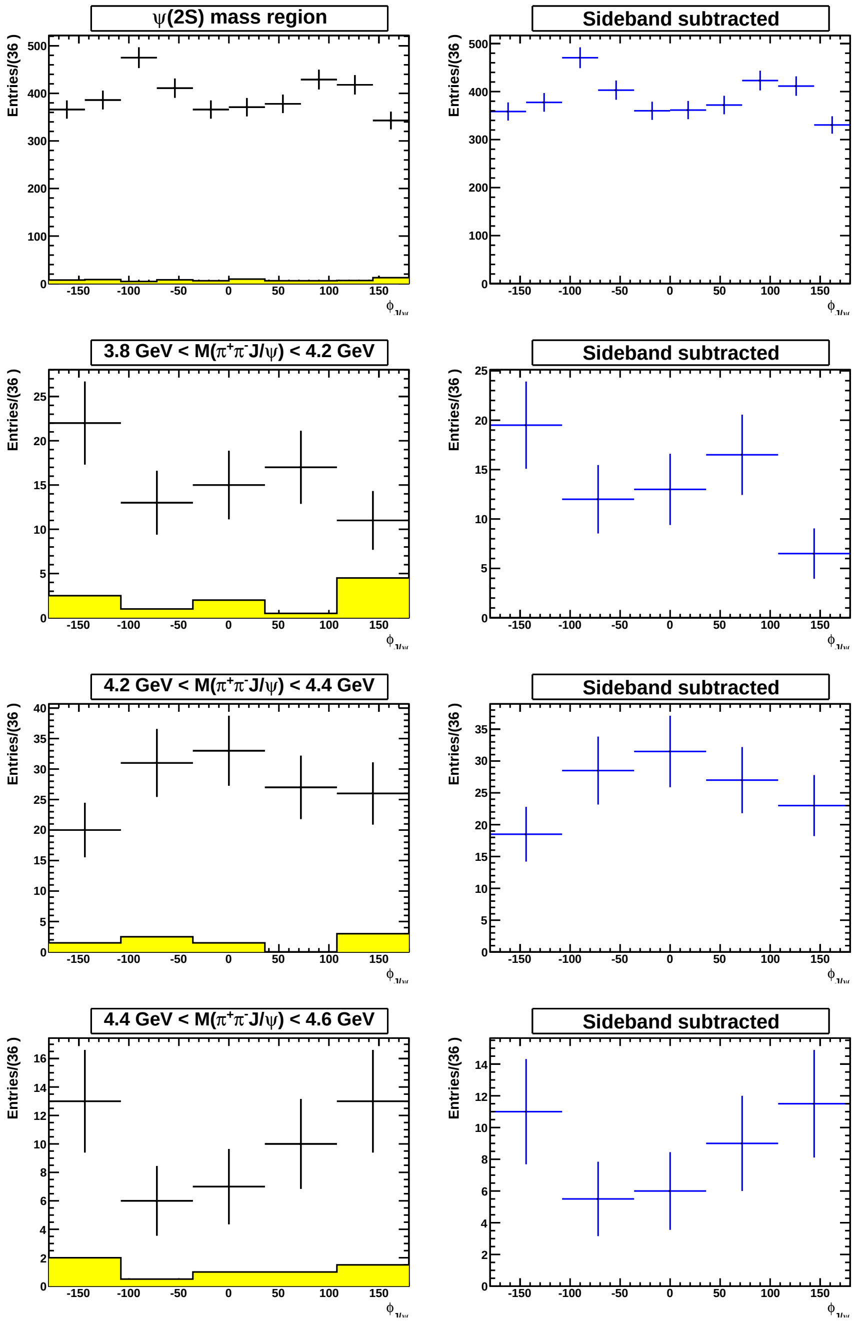

Figure 3.27: $\phi_{J/\psi}$ distributions. Left hand column: J/ψ signal events (points with error bars) and J/ψ sideband events (shaded histogram). Right hand column: the sideband-subtracted distribution (points with error bars). Row 1: Events in the $\psi(2S)$ mass region. Row 2: Events in $M(\pi^+\pi^-\ell^+\ell^-) \in [3.8, 4.2]$ GeV. Row 3: Events in $M(\pi^+\pi^-\ell^+\ell^-) \in [4.2, 4.4]$ GeV. Row 4: Events in $M(\pi^+\pi^-\ell^+\ell^-) \in [4.4, 4.6]$ GeV.

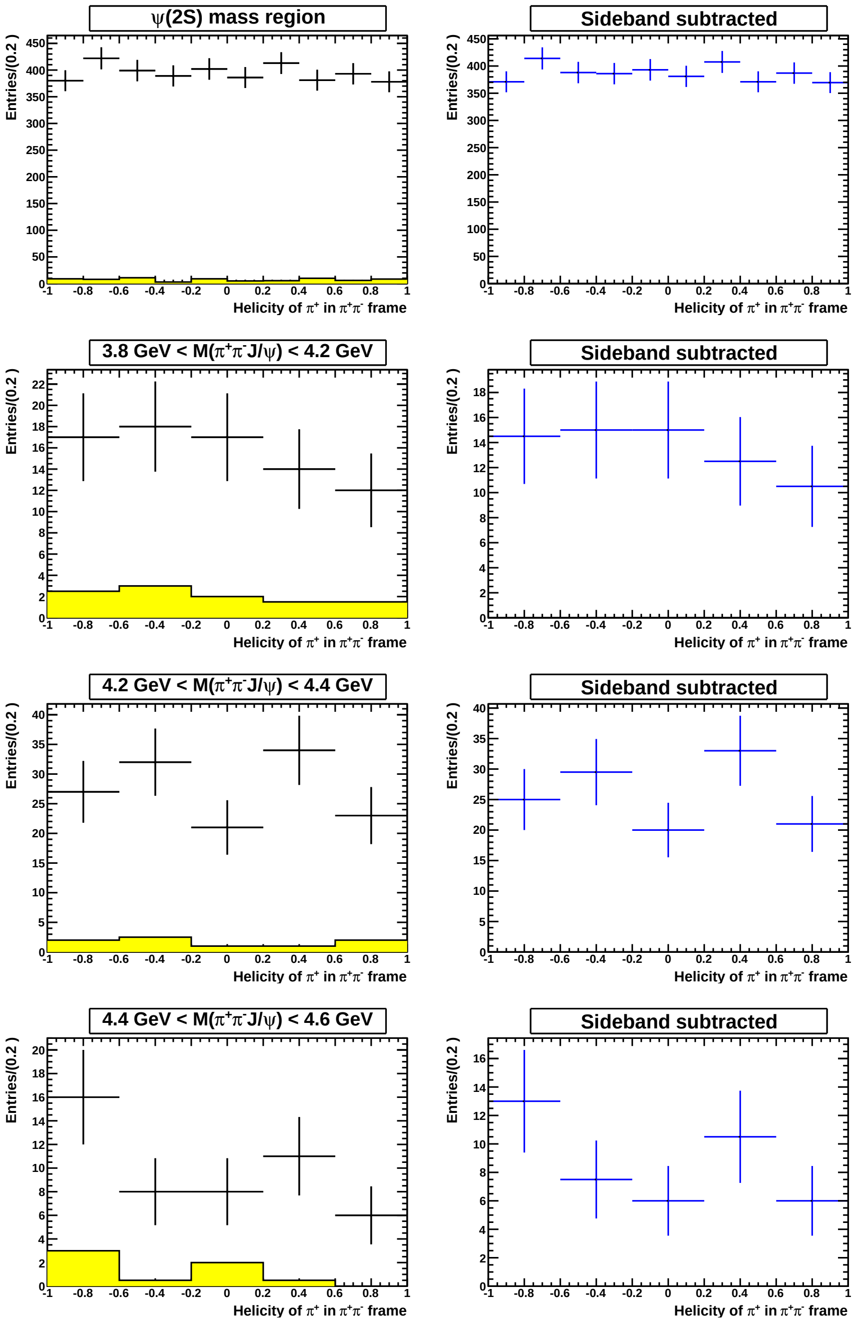

Figure 3.28: $\cos(\theta_{\pi\pi})$ distributions. Left hand column: J/ψ signal events (points with error bars) and J/ψ sideband events (shaded histogram). Right hand column: the sideband-subtracted distribution (points with error bars). Row 1: Events in the $\psi(2S)$ mass region. Row 2: Events in $M(\pi^+\pi^-\ell^+\ell^-) \in [3.8,\, 4.2]$ GeV. Row 3: Events in $M(\pi^+\pi^-\ell^+\ell^-) \in [4.2,\, 4.4]$ GeV. Row 4: Events in $M(\pi^+\pi^-\ell^+\ell^-) \in [4.4,\, 4.6]$ GeV.

3.8 Cross-section

Various cross-sections were investigated with this sample of data. Firstly, the cross-section of the $\psi(2S)$ control sample was compared with previous measurements. This was followed by calculations of the $Y(4260)$ cross-section, however, with the dataset used in this study, it was not possible to separate the production of the $Y(4260)$ from its decay to $\pi^+\pi^- J/\psi$. Therefore, the cross-section multiplied by this branching fraction was measured.

3.8.1 $\psi(2S)$ crosscheck

To check the cross-sections, a prediction of the yield of $\psi(2S)$ events in data was produced using the $\psi(2S)$ two-electron width, $\Gamma_{ee}(\psi(2S))$, and relevant branching fraction measurements listed in Ref. [104], which was produced by the PDG. The $\psi(2S)$ yield was predicted to be 3911 ± 390, with an uncertainty which was dominated by the error from MC statistics. This was compared to the observed $\psi(2S)$ yield of 4190 ± 386, where the error was statistical only. These two values are consistent.

3.8.2 $Y(4260)$ crosscheck

The $Y(4260)$ cross-section multiplied by the branching fraction for $Y(4260) \rightarrow \pi^+\pi^- J/\psi$ was measured using the fits in bins of di-pion mass described in Section 3.7.1. The use of $M(\pi^+\pi^-)$ bins reduced the model dependence of the result at the cost of increasing the statistical error. In each $M(\pi^+\pi^-)$ bin, efficiencies were calculated for the three $Y(4260)$ MC samples at different masses, and an interpolation was performed to produce the final efficiency, ϵ_i, for that bin. Taking the fitted $Y(4260)$ yield (N_i) and the efficiency (ϵ_i) in bins of di-pion mass from Section 3.7.1, the cross-section was determined using:

$$\begin{aligned}\sum \frac{N_i}{\epsilon_i} = \int \mathrm{d}t\mathcal{L} \cdot \sigma(e^+e^- \rightarrow \gamma_{ISR} Y(4260);\ \sqrt{s} = 10.58)\cdot \\ \mathcal{B}(Y(4260) \rightarrow \pi^+\pi^- J/\psi) \cdot \mathcal{B}(J/\psi \rightarrow \ell^+\ell^-),\end{aligned} \tag{3.6}$$

where $\int \mathrm{d}t\mathcal{L}$ was the integrated luminosity used in this study, 553.2 fb^{-1}, and using the world average value for $\mathcal{B}(J/\psi \rightarrow \ell^+\ell^-)$ [104]. For plots and values of the binned fits, see Section 3.7.1. Formula 3.6 gives the result:

$$\sigma(e^+e^- \rightarrow \gamma_{ISR} Y;\ \sqrt{s} = 10.58) \cdot \mathcal{B}(Y(4260) \rightarrow \pi^+\pi^- J/\psi) = 48 \pm 6^{+1}_{-5}\,\mathrm{fb}.$$

3.8.3 $\Gamma_{ee} \cdot \mathcal{B}$

The $Y(4260)$ cross-section was used to measure the two-electron width, Γ_{ee}, multiplied by the branching fraction. This was done using Equation (7) from Ref. [24]:

$$\sigma_V(s) = \frac{12\pi^2 B_{ee}\Gamma_V}{m_V \cdot s} \cdot W(s, x_V),$$

where $\sigma_V(s)$ is an approximation to the total cross-section for the process, B_{ee} is the branching fraction for the state to decay to two electrons, m_V and Γ_V are the mass and width of the state, and $W(s, x_V)$ is the probability of photon emission. The final result was found to be:

$$\Gamma_{ee} \cdot \mathcal{B}(Y(4260) \to \pi^+\pi^- J/\psi) = 8.7 \pm 1.1^{+0.3}_{-0.9}\,\mathrm{eV}.$$

3.8.4 Cross-section of highest bin

To measure the peak cross-section for $\pi^+\pi^- J/\psi$ produced via ISR without relying on any models or assumptions about the $Y(4260)$, the cross-section in the highest bin of Figure 3.10 was produced.

This was done using the signal function of a fit to the full sample without applying an $M(\pi^+\pi^-)$ cut in the highest bin. The value was calculated using the following equation:

$$\sigma_{\text{highest bin}} = \frac{N/\epsilon}{\int \mathrm{d}t\mathcal{L} \cdot \mathcal{B}(J/\psi \to \ell^+\ell^-) \cdot W(s, x_H) \cdot (m_2^2 - m_1^2)/s}, \tag{3.7}$$

where $x_H = 1 - m_H^2/s$ and m_H was the central mass of the highest bin, m_1 and m_2 were the lower and upper bin boundaries, respectively, and $W(s, x_H)$ was the second order QED radiator [24]. The cross-section at the peak value of 4.295 GeV for $e^+e^- \to (\gamma_{ISR})Y(4260) \to (\gamma_{ISR})\pi^+\pi^- J/\psi$ was found to be 43 pb.

3.9 Final Belle result

This section describes the final measurement of the $\pi^+\pi^- J/\psi$ cross-section in Belle data, in the region around 4260 MeV. It was produced by a different research group and was published in the journal paper, Ref. [29], where more detail can be found. The analysis described in this section used the same dataset, but had an improved efficiency for detecting ISR events in this decay mode and used a different assumption for background under the $Y(4260)$ peak. A cross-section was produced across the entire mass range and evidence for an additional broad enhancement at 4008 MeV was also seen.

The published analysis made use of Tau Skim, which has a higher efficiency for ISR-like events than this study which used Psi Skim; Psi Skim and Tau Skim selection criteria are reproduced in Section 2.5.3. Psi Skim loses efficiency for ISR events from energy threshold cuts in the ECL which are not present in Tau Skim.

Both analyses select four-track events, without requiring the reconstruction of the ISR photon. The PID method for pions is then similar, with a difference in the lepton PID requirements; the published analysis used a one-hard one-easy lepton PID. One track was required to pass a hard cut in its relevant lepton PID, while the track it was combined with used a much looser cut. This, in conjunction with requirements on the J/ψ candidates mass, is effective at reducing background and retaining high efficiency. The events that pass this selection are shown in Figure 3.29, which can be compared with Figure 3.8, shown earlier.[4] The mass distribution shown here and the distribution shown in Section 3.2 are of different quantities. In the earlier section, the tracks forming the J/ψ have been constrained to a common vertex and to the nominal mass of the J/ψ from Ref. [104], to improve the final mass resolution, while here, the quantity shown is $M(\pi^+\pi^-\ell^+\ell^-) - M(\ell^+\ell^-) + m_{J/\psi}$. This mass difference improves the mass resolution compared to $M(\pi^+\pi^-\ell^+\ell^-)$, while the mass-vertex constraint improves the mass resolution and results in a better momentum resolution, which influences the recoil mass squared and other kinematic quantities.

[4]The plots shown in this section are reproduced as they appear in the journal publication with the factor c stated explicitly in mass and related units, but with a slightly adjusted colour scheme.

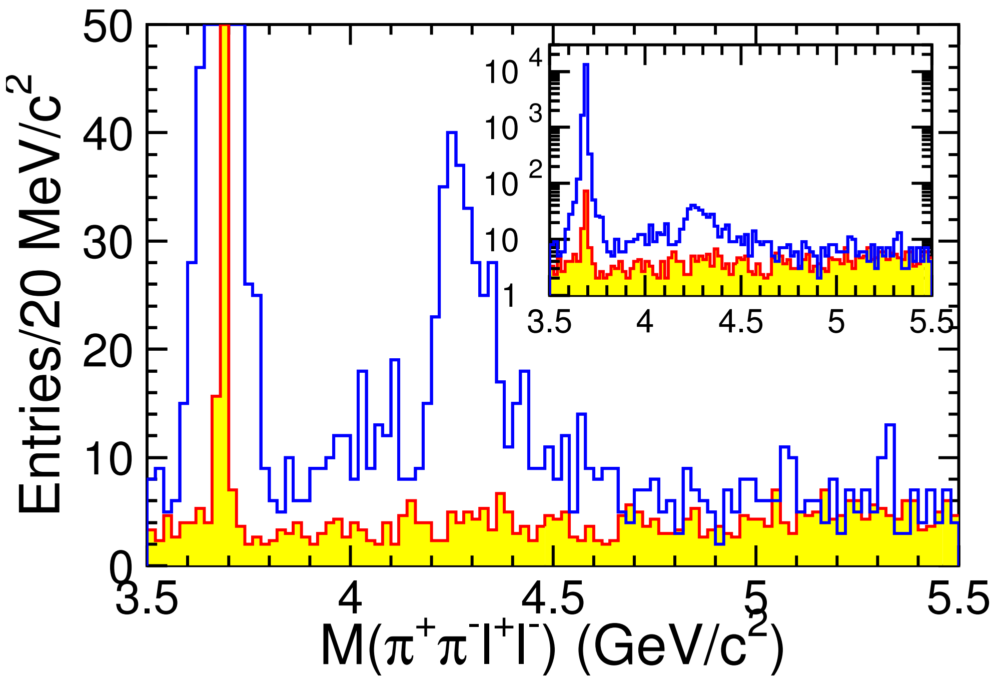

Figure 3.29: Invariant mass spectrum of $\pi^+\pi^-\ell^+\ell^-$ events, from the J/ψ signal region (histogram) and J/ψ sideband regions (shaded histogram) with log scale inset. Reproduced from Ref. [29].

The J/ψ sideband-subtracted recoil mass squared (M^2_{rec}) and $\cos(\theta)$ distributions that these events produce can be seen in Figure 3.30. The recoil mass squared distribution peaks strongly near zero and the $\cos(\theta)$ distribution peaks near ±1, consistent with the assumption of ISR production. Similar quantities were also checked in the earlier analysis, the sideband-subtracted recoil mass squared distribution can be seen on the right of Figure 3.5, with the difference that the J/ψ candidates in the events in Figure 3.5 were constrained to a common vertex and to the nominal J/ψ mass. Instead of a sideband-subtracted $\cos(\theta)$ distribution, the earlier analysis produced a $\cos(\theta)$ distribution from the efficiency corrected $Y(4260)$ yields from fits to $M(\pi^+\pi^- J/\psi)$ in bins of $\cos(\theta)$, shown in Figure 3.14. In both analyses the measured events were found to be consistent with production via ISR.

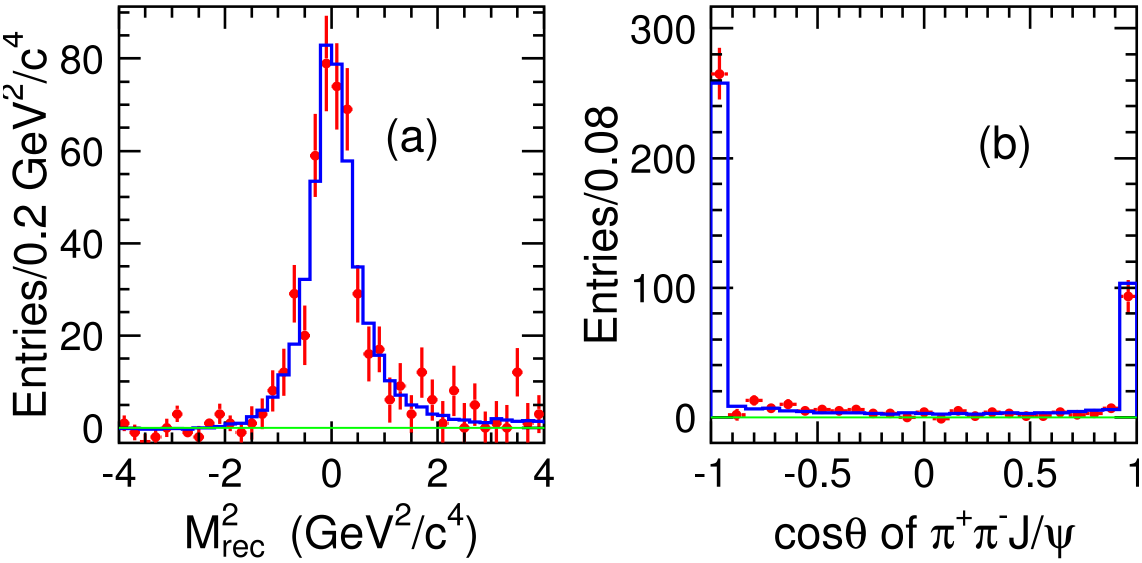

Figure 3.30: Left: recoil mass squared distribution from events with $M(\pi^+\pi^-\ell^+\ell^-) \in [3.8, 4.6]$ GeV. Right: $\cos(\theta)$ distribution from events with $M(\pi^+\pi^-\ell^+\ell^-) \in [3.8, 4.6]$ GeV. Points with error bars are J/ψ sideband-subtracted events in data, and solid histograms are the predictions from MC. Reproduced from Ref. [29].

The event counts in each bin, from this section, were then combined with the efficiency and effective luminosity as a function of mass to produce a cross-section as a function of mass using:

$$\sigma_i = \frac{n_i^{obs} - n_i^{bkg}}{\varepsilon_i \, \mathcal{L}_i \, \mathcal{B}(J/\psi \to \ell^+\ell^-)}$$

where n_i^{obs}, n_i^{bkg}, ε_i and $\mathcal{L}_i$ are number of events observed in data, number of background events measured in J/ψ sidebands, efficiency, and effective luminosity in the i-th $M(\pi^+\pi^-J/\psi)$ mass bin, respectively; $B(J/\psi \to \ell^+\ell^-) = 11.87\%$, from Ref. [104]. The results of this cross-section as a function of mass are shown in Figure 3.31.

The J/ψ sideband-subtracted di-pion mass distribution ($M(\pi^+\pi^-)$) was also measured for three $M(\pi^+\pi^-J/\psi)$ regions, shown in Figure 3.32 with the prediction from MC produced according to phase space. The di-pion mass distribution shown here shows similar features to the di-pion mass distribution shown in Figure 3.22, which was produced using the efficiency corrected $Y(4260)$ yield from fits to the $M(\pi^+\pi^-J/\psi)$ distribution in bins of $M(\pi^+\pi^-)$.

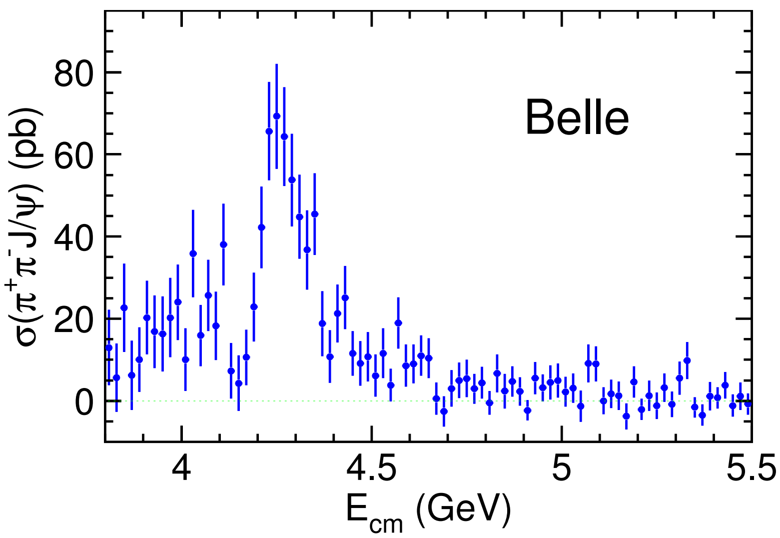

Figure 3.31: Cross-section for $e^+e^- \to \pi^+\pi^- J/\psi$ from Ref. [29].

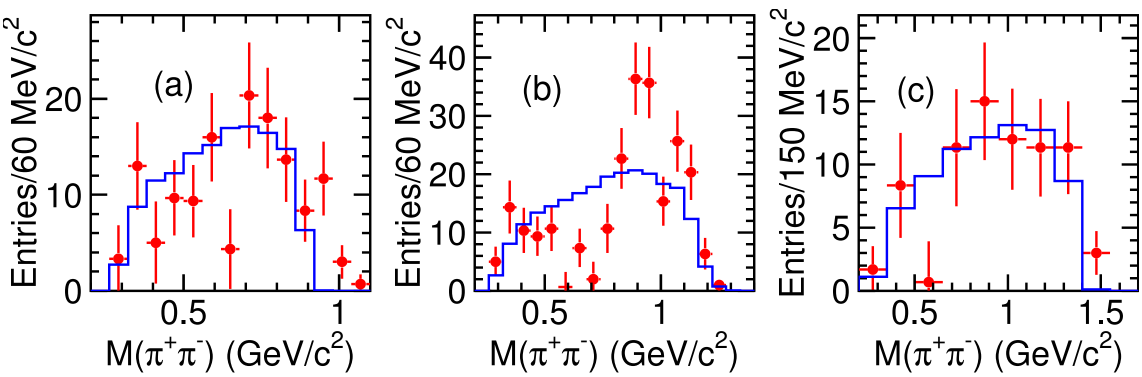

Figure 3.32: Di-pion mass distributions for candidates with $M(\pi^+\pi^-\ell^+\ell^-) \in [3.8, 4.2]$ GeV, (a), $M(\pi^+\pi^-\ell^+\ell^-) \in [4.2, 4.4]$ GeV, (b), and $M(\pi^+\pi^-\ell^+\ell^-) \in [4.4, 4.6]$ GeV, (c), for candidate events in data (points with errors), shown with the prediction from MC generated according to phase space (solid histogram), from Ref. [29].

The $M(\pi^+\pi^-\ell^+\ell^-)$ distribution was then fitted. The primary fit used for publication involved two interfering resonances, one for the $Y(4260)$, referred to as $R2$, and one for a broad enhancement seen at lower mass, referred to as $R1$. This interference leads to the production of two degenerate solutions. A linear fit was performed to the J/ψ sidebands, which was then fixed and taken as the background to the signal, where the fit described in Section 3.3 used a quadratic background with parameters allowed to float in the fit. The events in the region 3.8 GeV to 4.2 GeV are well above the J/ψ sideband and a fit with a $Y(4260)$ resonance and an additional resonance was found to perform much better than a fit with $Y(4260)$ resonance alone. The fit results are shown in Table 3.18 and Figure 3.33.

Table 3.18: Results of the primary fit to the $\pi^+\pi^-J/\psi$ invariant mass spectrum produced via ISR measured by Belle in 2007. This table is a repeat of Table 1.5 from Section 1.5. Resonance $R2$ corresponds to the $Y(4260)$. Solutions I and II are the results of the fit with constructive and destructive interference, with the interference parameter, ϕ, shown in the bottom row. Here the first errors are statistical and the second errors are systematic.

Parameters			Solution I	Solution II
M	(MeV)	$R1$	$4008 \pm 40^{+114}_{-28}$	
Γ	(MeV)	$R1$	$226 \pm 44 \pm 87$	
$\Gamma_{ee} \cdot \mathcal{B}$	(eV)	$R1$	$5.0 \pm 1.4^{+6.1}_{-0.9}$	$12.4 \pm 2.4^{+14.8}_{-1.1}$
M	(MeV)	$R2$	$4247 \pm 12^{+17}_{-32}$	
Γ	(MeV)	$R2$	$108 \pm 19 \pm 10$	
$\Gamma_{ee} \cdot \mathcal{B}$	(eV)	$R2$	$6.0 \pm 1.2^{+4.7}_{-0.5}$	$20.6 \pm 2.3^{+9.1}_{-1.7}$
ϕ	(degrees)		$12 \pm 29^{+7}_{-98}$	$-111 \pm 7^{+28}_{-31}$

As a cross-check, the data in Figure 3.29 was fitted with a single Breit-Wigner over a polynomial background, similar to the fit described in Section 3.3, but without an efficiency correction term. The results of these two fits, one shown at conferences in 2006 and the other published in 2007, are shown in Table 3.19, along with the results from similar fits in other experiments. While the width and $\Gamma_{ee} \cdot \mathcal{B}$

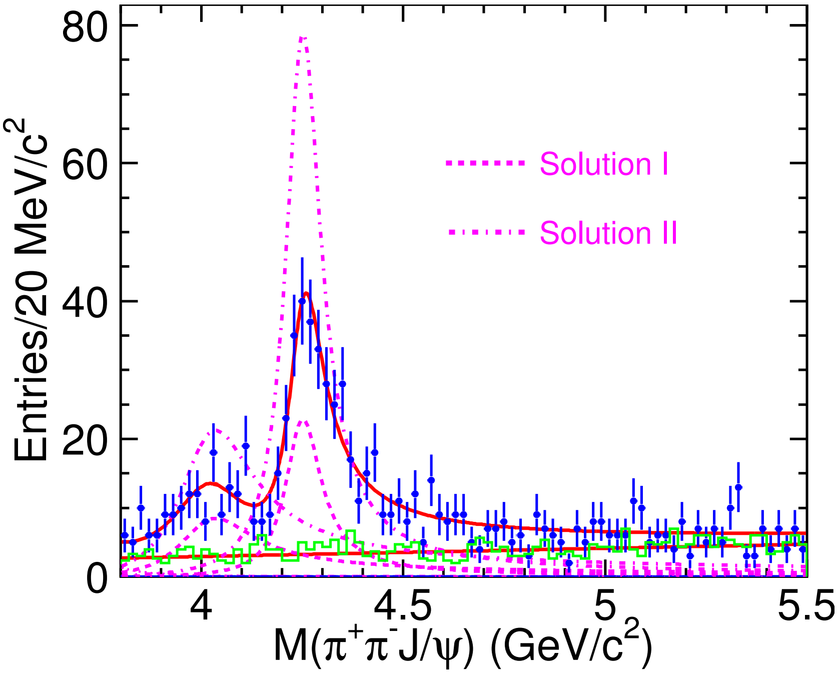

Figure 3.33: Fit to the $\pi^+\pi^-\ell^+\ell^-$ invariant mass distribution with two coherent resonances. Points with error bars are events from the J/ψ signal region and the solid histogram represents events from the scaled J/ψ sideband regions. The dashed line shows Solution I and the dotted and dashed line shows Solution II of the fit described in text. Reproduced from Ref. [29].

measurements agree with each other, as would be expected from similar measurements conducted with overlapping datasets, the central mass is different and is higher in the conference result. This is due to the difference in the resonance parameters between the two fits. In the fits in Section 3.3, there is an additional term for the change in efficiency across the fit range, this has the effect of increasing the central mass term returned by the fit. The data in each subsample of the total Belle dataset were compared and are consistent. The largest differences between the two analyses are the reconstruction efficiency from different skim cuts and the different assumptions about the nature of the data, such as the assumptions regarding the background and the various fitting procedures.

Table 3.19: The results of fitting a non-relativistic Breit-Wigner to the $\pi^+\pi^- J/\psi$ invariant mass spectrum produced via ISR in various experiments. This table is a repeat of Table 1.4 from Section 1.5. The results in Belle (2006) were superseded by the results in Belle (2007). In Belle (2007), the fit involving a single non-relativistic Breit-Wigner was not the primary fit used in the analysis; for the results of the main fit, see Table 3.18. The results of *BABAR* (2005) were updated in *BABAR* (2008). Here the first errors are statistical and the second, where available, are systematic.

	Yield	Mass (MeV)	Width (MeV)	$\Gamma_{ee} \cdot \mathcal{B}$ (eV)
BABAR (2005) [25]	125 ± 23	$4259 \pm 8 \,^{+2}_{-6}$	$88 \pm 23 \,^{+6}_{-4}$	$5.5 \pm 1.0 \,^{+0.8}_{-0.7}$
CLEO (2006) [27]	$13.6 \,^{+4.7}_{-3.9}$	$4284 \,^{+17}_{-16} \pm 4$	$73 \,^{+39}_{-25} \pm 5$	$8.9 \,^{+3.9}_{-3.1} \pm 1.8$
Belle (2006) [28]	165 ± 24	$4295 \pm 10 \,^{+10}_{-3}$	$133 \pm 26 \,^{+13}_{-6}$	$8.7 \pm 1.1 \,^{+0.3}_{-0.9}$
Belle (2007) [29]	–	4263 ± 6	126 ± 18	9.7 ± 1.1
BABAR (2008) [30]	344 ± 39	$4252 \pm 6 \,^{+2}_{-3}$	$105 \pm 18 \,^{+4}_{-6}$	$7.5 \pm 0.9 \pm 0.8$

3.10 Conclusion

The $Y(4260) \to \pi^+\pi^- J/\psi$ signal was confirmed with a significance of 11σ. The dipion mass distribution favours high values of $M(\pi^+\pi^-)$, which is consistent with *BABAR*'s result; there was also some evidence for a rise in cross-section near the $M(\pi^+\pi^-)$ threshold, although statistical errors were large. The $\cos(\theta)$ distribution peaks strongly at values near ± 1, consistent with the interpretation that the events were due to ISR. Additionally when requiring the reconstruction of the ISR photon, an enhancement near the central mass value is seen.

From the signal in Belle data a mass of $4295 \pm 10^{+11}_{-5}$ MeV is found. There have been predictions that a hybrid would favour decays to an S-wave plus a P-wave state [108]. The relevant mass threshold is $M(D^0 D_1^0) = 4287\,\mathrm{MeV}$ and a mass above this value was found, although the difference is not statistically significant. CLEO measured $4284^{+17}_{-16} \pm 4\,\mathrm{MeV}$ [27] near the threshold and consistent with this value; *BABAR*'s published mass was $4259 \pm 8^{+2}_{-6}\,\mathrm{MeV}$, which was below threshold and is 2.6σ below this value. The measurement of the width, $\Gamma = 133 \pm 26^{+13}_{-6}$ MeV, was marginally consistent with those of CLEO: $73^{+39}_{-25} \pm 5$ MeV and *BABAR*: $88 \pm 23^{+6}_{-4}$ MeV; errors were large. The result for $\Gamma_{ee} \cdot \mathcal{B}(Y \to \pi^+\pi^- J/\psi)$ was about 1.6σ higher than *BABAR*'s reported value: $5.5 \pm 1.0^{+0.8}_{-0.7}$ eV and similar to CLEO's measurement of $8.9^{+3.9}_{-3.1} \pm 1.8$ eV, within large errors.

3.10.1 Summary

The properties of the $Y(4260)$ have been investigated using the initial-state radiation process $e^+e^- \to \gamma_{ISR} Y(4260)$. A significant signal described by a Breit-Wigner with mass $4295 \pm 10^{+11}_{-5}$ MeV, width $133 \pm 26^{+13}_{-6}$ MeV was found with $\Gamma_{ee} \cdot \mathcal{B}(Y(4260) \to \pi^+\pi^- J/\psi) = 8.7 \pm 1.1^{+0.3}_{-0.9}$ eV.

Chapter 4

Reconstruction of $\pi^0\pi^0 J/\psi$ mode

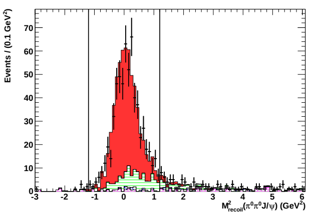

In this chapter, reconstruction techniques are developed for a search for $Y(4260) \to \pi^0\pi^0 J/\psi$. This involved developing a best candidate selection method; optimising the values of the selection cuts; comparing the data and MC in the control sample; and measuring the systematic uncertainties, while blind to the data in the $Y(4260)$ mass region.

THIS chapter describes the development of reconstruction techniques for a search for the $Y(4260)$ decaying to $\pi^0\pi^0 J/\psi$, using ISR events in Belle data. The search was conducted as a blind analysis: the reconstruction and event selection detailed in this chapter was finalised without any information from events in data in the range 4.0 GeV $< M(\pi^0\pi^0 J/\psi) < 4.7$ GeV. After the selection was finalised the events in the blind region were analysed, as will be discussed in Chapter 5.

This decay mode was expected to be considerably more difficult to detect than the $\pi^+\pi^- J/\psi$ mode: from isospin considerations $\pi^0\pi^0 J/\psi$ was expected to have half the production rate of the $\pi^+\pi^- J/\psi$ mode and π^0 reconstruction has a lower efficiency and a larger fake contribution than $\pi^\pm$ reconstruction. The details of the data sample that was used in this analysis are discussed in Section 4.1. Section 4.2 relates how events were reconstructed and the initial selection cuts that were used to identify events. There were many photons in each event from the signal decay and background processes, which led to multiple π^0 and $\pi^0\pi^0 J/\psi$ candidates being reconstructed. To identify a single $\pi^0\pi^0 J/\psi$ candidate in each event for further study, a best candidate selection was implemented, which is discussed in Section 4.3. The particle identification (PID) of the J/ψ daughters was studied using best candidates from the $\psi(2S)$ control sample in data and MC, which is detailed in Section 4.4. The different subsamples of the $\psi(2S)$ control sample in data are described in Section 4.5, before studies of the di-electron and di-muon subsamples are detailed in Sections 4.6 and 4.7, respectively. From these studies, it was determined that the fully reconstructed subsample, with the ISR photon reconstructed, was the only subsample where a result could be expected in the $Y(4260)$ mass region. Unfortunately, only the di-muon events in the fully reconstructed sample pass skim selection. The selection cuts were then optimised using this subsample, which is discussed in Section 4.8. The agreement between data and MC in the $\psi(2S)$ control sample was checked and the systematic uncertainties estimated. These checks are presented in Sections 4.9 and 4.10, respectively, before this chapter is concluded. All of these steps were finalised before the data in the blind region was analysed, which will be discussed in the next chapter.

4.1 Datasets

Reconstruction techniques were first developed with MC and then the differences between the data and the MC were studied using the $\psi(2S)$ as a control sample. Unlike the analysis in Chapter 3, the analysis described in this chapter was conducted as a blind analysis. This analysis was conducted using the data from Belle experiments 7-65 which were produced at the $\Upsilon(4S)$ resonance and nearby continuum and had a total integrated luminosity of 790.9 fb^{-1} (see Section 2.5.1). Here, the reasons for conducting a blind analysis are presented, the method used to produce the MC samples is described, and finally, the data skims chosen for this analysis are discussed.

4.1.1 Blind analysis

A blind analysis is conducted without any knowledge of the main region of interest, until the analysis technique is finalised; for example, concealing the invariant mass plot to be measured. This is done in order to reduce unintended biases introduced by the experimenter, such as, choosing cuts based on the effect they have on the events in the signal region. Blind analysis in particle physics is discussed in Ref. [109]. This represents an improvement over the analysis of the $\pi^+\pi^- J/\psi$ decay mode, where the signal had already been established by a previous analysis;

while in the $\pi^0\pi^0 J/\psi$ channel, the signal yield was expected to be small, which made reducing the experimenter bias especially important.

In this case, the events in data from the mass region above 4.0 GeV were blinded and progressively revealed. Initially, only events from the $\psi(2S)$ control region, $M(\pi^0\pi^0 J/\psi) < 4.0$ GeV, were studied. Later, the events with mass above the $Y(4260)$ mass region, $M(\pi^0\pi^0 J/\psi) > 4.7$ GeV, and the events from the J/ψ sidebands were unblinded to study the background. This meant that the analysis was finalised before events in the range 4.0 GeV $< M(\pi^0\pi^0 J/\psi) < 4.7$ GeV were investigated.

4.1.2 MC samples

Several MC samples were used to develop the reconstruction and investigate backgrounds. Signal MC samples were generated using the procedure detailed in Section 3.1.1, with three improvements:

- A newer program, EvtGen [99], was used to generate the decays of the signal particles. (QQ98 [98] was used in the $\pi^+\pi^- J/\psi$ analysis.)
- The events were processed using the experimental conditions from each experiment, instead of using the conditions from two representative experiments. Here, the number of events generated corresponded to the integrated luminosity collected by that experiment.[1]
- The response of the Level 1 trigger was simulated. In the previous analysis, only the response of the Level 4 trigger was simulated, as the four charged tracks of the $\pi^+\pi^- J/\psi$ decay mode were not expected fail this trigger.

The Belle trigger simulation software was run using two sets of conditions during this analysis, which are described in Appendix B. The results from the two simulations were compared and the difference between them found to be small.

The main MC samples that were used in this analysis are summarised in Table 4.1. The samples in the top three rows of the table were used to analyse signal

[1] This was with the exception of Belle experiment 7, for which the trigger simulation code was not available in the software used to analyse this experiment. The integrated luminosity of experiment 7 was small when compared with the total sample and this data was included in the analysis assuming that the efficiency of experiment 7 was the same as that measured for the other SVD1 experiments (9-27).

events in the $Y(4260)$ and $\psi(2S)$ mass region, with the $\psi(2S) \rightarrow generic$ sample used to estimate the contamination from the other $\psi(2S)$ decay modes. The samples from the bottom three rows of the table were used to investigate potential backgrounds:

- J/ψ events produced directly via ISR, which was considered as a background in the di-muon sample.
- A radiative Bhabha sample, which simulates events with two electrons undergoing Bhabha scattering, with one of the electrons radiating a hard photon: this was considered as a background to the di-electron sample.
- An $e^+e^- \rightarrow \tau^+\tau^-$ sample, with each τ lepton allowed to decay generically, was studied as it contained di-lepton events that were considered as a possible non-J/ψ background.

In the table, the samples described in the top four rows were generated specifically for this analysis and the samples in the bottom two rows were generated previously by the Tau Studies group, for the study of $\tau^\pm$ decays. A Gaussian is used to generate the $\psi(2S)$ signal MC, as the width of the $\psi(2S)$ is significantly smaller than the experimental resolution of this analysis. The number of events in the signal MC samples corresponded to approximately three times the number of events in data for the $\psi(2S) \rightarrow \pi^0\pi^0 J/\psi$ sample and 1.4 times for the $\psi(2S) \rightarrow generic$ sample. Signal MC samples were also produced at several mass points, in order to measure the efficiency as a function of mass, as discussed in Section 5.2.1.

Table 4.1: Summary of MC samples used in $\pi^0\pi^0 J/\psi$ analysis. The samples in the top four rows were produced using the method described in test, while the samples in the bottom two rows were existing samples generated by the Tau Studies group at Belle.

Sample	Notes	Events ($\times 10^6$)
$Y(4260) \to \pi^0\pi^0 J/\psi$	Breit-Wigner ($M = 4260$ MeV, $\Gamma = 100$ MeV)	0.93
$\psi(2S) \to \pi^0\pi^0 J/\psi$	Gaussian ($M = 3686$ MeV, $\sigma = 0.15$ MeV)	0.90
$\psi(2S) \to generic$	Gaussian ($M = 3686$ MeV, $\sigma = 0.15$ MeV)	16.00
$e^+e^- \to \gamma_{ISR} J/\psi$	$J/\psi \to \ell^+\ell^-$	0.43
$e^+e^- \to e^+e^-\gamma$	Radiative Bhabha scattering	7529.30
$e^+e^- \to \tau^+\tau^-$	$\tau^\pm$ decaying generically	3089.35

4.1.3 Skims

Using signal MC, the Belle data skims with the highest efficiency for signal decays were identified as the Tau and Low Multiplicity (LM) Skims (described in Section 2.5.3). This analysis was conducted using the union of these two skims, with the exclusion of the Tau Skim events that also passed the HadronB Skim. The efficiency of these skims along with the efficiency for this decay mode in two other skims is presented in Table 4.2. In the table, three cases are considered: all the events that pass skim selection; the subsample with all of the $Y(4260)$ daughters detected (two charged tracks and four photons); and the fully reconstructed case, where the $Y(4260)$ daughters and the ISR photon are reconstructed. Considering the events with all the $Y(4260)$ daughters detected, the skim behaviour of the di-electron and di-muon samples varies greatly between the samples with and without the ISR photon detected. Specifically, there is no skim with a significant efficiency for fully reconstructed di-electron events.

Table 4.2: Efficiencies of selected data skims for $\pi^0\pi^0 J/\psi$ events. Efficiencies were measured using signal MC and are provided to an accuracy of 0.1% in this table. Three cases are considered: Left two columns: all the events that pass skim selection. Upper rows of right two columns: the subsample with all of the $Y(4260)$ daughters detected (two charged tracks and four photons). Lower rows of right two columns: the fully reconstructed case, where the $Y(4260)$ daughters and the ISR photon are reconstructed.

	Any events		**All daughters in detector**	
Data skim (%)	di-electron	di-muon	di-electron	di-muon
Total	100.0	100.0	$4.3 \pm < 0.1$	$4.8 \pm < 0.1$
Passing trigger	74.3 ± 0.2	42.3 ± 0.1	$3.9 \pm < 0.1$	$3.4 \pm < 0.1$
Psi Skim	$1.9 \pm < 0.1$	$1.2 \pm < 0.1$	< 0.1	$0.1 \pm < 0.1$
HadronB (HadB)	$1.1 \pm < 0.1$	$1.0 \pm < 0.1$	< 0.1	$0.1 \pm < 0.1$
Tau	$9.7 \pm < 0.1$	16.5 ± 0.1	$0.6 \pm < 0.1$	$2.0 \pm < 0.1$
Tau and not HadB	$8.9 \pm < 0.1$	15.6 ± 0.1	$0.6 \pm < 0.1$	$2.0 \pm < 0.1$
LM	21.1 ± 0.1	11.0 ± 0.1	$1.6 \pm < 0.1$	$1.2 \pm < 0.1$
LM and (Tau and not HadB)	27.0 ± 0.1	23.4 ± 0.1	$1.9 \pm < 0.1$	$2.8 \pm < 0.1$

	Fully reconstructed	
Data skim (%)	di-electron	di-muon
Total	$2.0 \pm < 0.1$	$2.2 \pm < 0.1$
Passing trigger	$2.0 \pm < 0.1$	$2.1 \pm < 0.1$
Psi Skim	< 0.1	< 0.1
HadronB (HadB)	< 0.1	< 0.1
Tau	< 0.1	$1.6 \pm < 0.1$
Tau and not HadB	< 0.1	$1.6 \pm < 0.1$
LM	< 0.1	$0.1 \pm < 0.1$
LM and (Tau and not HadB)	< 0.1	$1.6 \pm < 0.1$

4.2 Reconstruction

$\pi^0\pi^0 J/\psi$ candidates were reconstructed from events with two charged tracks and at least four photons. Events were selected if they had exactly two oppositely charged tracks that passed track quality cuts, which are detailed in Section 4.2.1. These charged tracks were required to be positively identified as either e^+e^- or $\mu^+\mu^-$ and they were then combined to make a J/ψ candidate for each event: this is discussed in Section 4.2.2. Photons that passed a minimum energy cut and were not measured to be outside the timing window for each event were selected to make π^0 candidates, as described in Section 4.2.3. The π^0 candidates formed from selected photons are discussed in Section 4.2.4. Pairs of π^0 candidates were combined with the J/ψ candidate in each event to form $\pi^0\pi^0 J/\psi$ candidates. There were multiple $\pi^0\pi^0 J/\psi$ candidates in each event, so it was necessary to implement a best candidate selection to identify a single candidate for further study: this is discussed in Section 4.3.

4.2.1 Track selection

As with the $\pi^+\pi^- J/\psi$ channel, only the tracks that passed track quality cuts were used to select events and form candidates. The solid lines in the plots in Figure 4.1 indicate the track multiplicity of events in MC before track quality selection. There are additional tracks in these events which are from beam background processes: these are overlayed with the signal events, to reproduce the detector response during real running, as discussed in Section 3.1.1. Three track quality cuts were used: a minimum transverse momentum cut, P_t, and cuts on the transverse and longitudinal distance between the track and the interaction point, dr and dz, respectively. Here, the dr parameter is given a sign indicating the sign of the electric charge of the track. The distributions of these three variables for signal and non-signal tracks in $\psi(2S) \to \pi^0\pi^0 J/\psi$ and $Y(4260) \to \pi^0\pi^0 J/\psi$ MC can be seen in Figure 4.2. In the figure, vertical lines indicate the chosen selection cuts, which are detailed in Table 4.3. The dashed lines in the plots of Figure 4.1 indicate the track multiplicity of event in MC after track quality cuts. It was required that there were no extra tracks in each event and as can be seen in the figure, before track quality selection there were a large number of events in both samples which would have failed this criterion.

A bremsstrahlung correction was applied to electron tracks: the four-momentum of all photons within an 80 mrad cone were added to the four-momentum of the tracks and the photon was removed from the event.

Table 4.3: Track quality cuts used in $\pi^0\pi^0 J/\psi$ analysis.

Variable	Selection
Transverse momentum	$P_t > 0.3$ GeV
Radial distance to interaction point	$\lvert dr\rvert < 0.2$ cm
Longitudinal distance to interaction point	$\lvert dz\rvert < 1.5$ cm

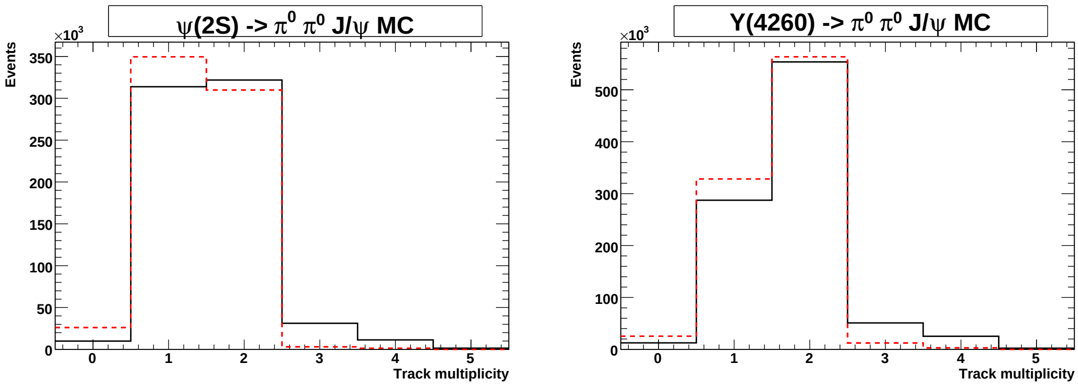

Figure 4.1: The effect of track quality cuts used in $\pi^0\pi^0 J/\psi$ analysis on track multiplicity in signal MC. The total track multiplicity of events before (after) track quality selection is shown with solid (red dashed) lines. Left: $\psi(2S) \to \pi^0\pi^0 J/\psi$ signal MC. Right: $Y(4260) \to \pi^0\pi^0 J/\psi$ signal MC.

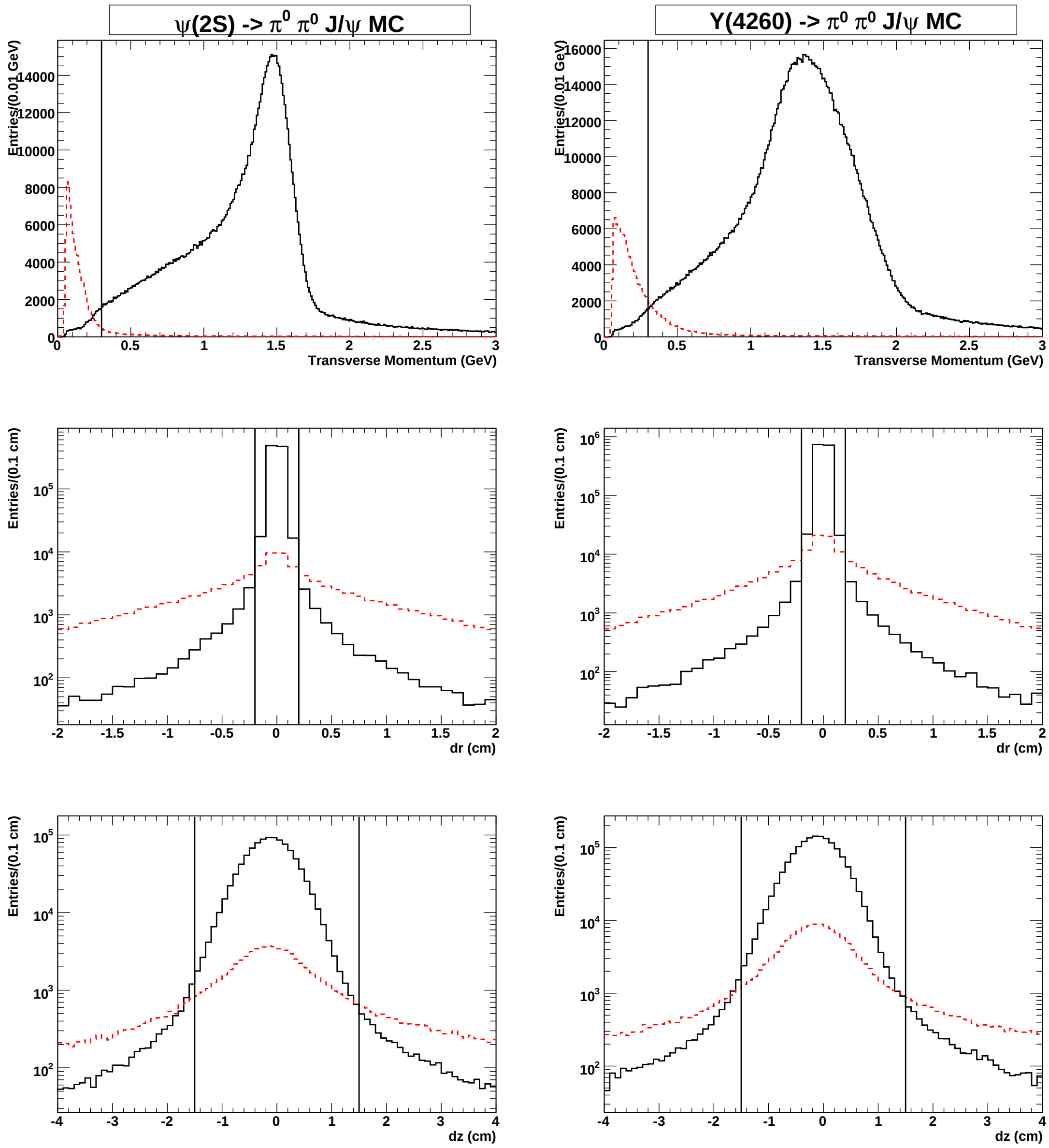

Figure 4.2: Track quality selection used in $\pi^0\pi^0 J/\psi$ analysis. Top row: track transverse momentum, P_t. Middle row: closest radial approach to the interaction point, dr. The sign of dr indicates the sign of the electric charge of the track. Bottom row: closest longitudinal approach to the interaction point, dz. Left column: $\psi(2S) \to \pi^0\pi^0 J/\psi$ signal MC. Right column: $Y(4260) \to \pi^0\pi^0 J/\psi$ signal MC. Solid lines represent the distribution for signal tracks in signal MC and red dashed lines represent the distribution of non-signal tracks. Vertical lines indicate the cuts described in the text.

4.2.2 J/ψ reconstruction

J/ψ candidates were reconstructed from pairs of oppositely charged tracks that passed track quality cuts. (A bremsstrahlung correction was applied to electron tracks, as discussed in the previous section.) J/ψ particles decay to e^+e^- and $\mu^+\mu^-$ with branching fractions $(5.94 \pm 0.06)\%$ and $(5.93 \pm 0.06)\%$, respectively [102]. Initially, track pairs were loosely identified as either two electrons or two muons (the PID is studied in more detail in Section 4.4). Candidates that were unable to be constrained to a common vertex and which were therefore unlikely to be from a single parent, were removed.[2] Events where at least one $\pi^0\pi^0 J/\psi$ candidate passed a very loose M^2_{recoil} cut: -5 GeV^2 $< M^2_{\text{recoil}} < 10$ GeV^2, were selected for further analysis (where M^2_{recoil} is defined in Equation 3.2 in Section 3.2.4). The di-electron and di-muon invariant mass distributions for these events are shown in Figure 4.3. These events were divided into J/ψ signal and sideband regions, which are indicated by the vertical lines in the figure and detailed in Table 4.4. J/ψ candidates were then constrained to a common vertex and to the mass at the centre of each region to improve the momentum resolution. For the J/ψ signal region this was the nominal mass of the J/ψ, $m_{J/\psi} = 3096.916 \pm 0.0011$ MeV [1], while for the sideband regions it was $m_{J/\psi} \pm 120$ MeV.

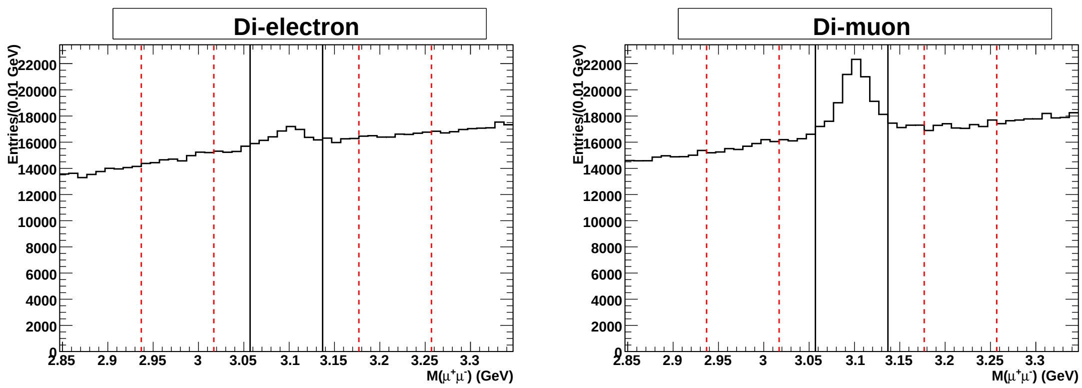

Figure 4.3: Invariant mass spectra in data for loosely identified J/ψ candidates. Left: $J/\psi \to e^+e^-$ candidates. Right: $J/\psi \to \mu^+\mu^-$ candidates. The solid and red dashed vertical lines indicate initial selection of the signal and sideband regions respectively. The widths of the signal and sideband regions were optimised later.

[2] The vertex constraint was applied with the Belle software package `kfitter` [110].

Table 4.4: Initial selection of the J/ψ signal and sideband mass regions used in the $\pi^0\pi^0 J/\psi$ analysis (selection optimised later, see Section 4.8).

Sample	Mass region
J/ψ signal	$\lvert M(\ell^+\ell^-) - m_{J/\psi}\rvert \in [0, 40]\,\mathrm{MeV}$
J/ψ sideband	$\lvert M(\ell^+\ell^-) - m_{J/\psi}\rvert \in [80, 160]\,\mathrm{MeV}$

4.2.3 Photon selection

Photons were reconstructed from clusters in the ECL which could not be matched to a track in the CDC. All photons were required to pass a minimum energy cut and a selection based on the timing information recorded by the ECL cluster. All photons that passed selection were used to make π^0 candidates, with the exception of those identified as bremsstrahlung photons (as discussed in Section 4.2.1).

The energy distribution of photons from π^0 particles in $\gamma_{ISR}\pi^0\pi^0 J/\psi$ events extended to very low values. Figure 4.4 shows the energy distribution of all π^0 photons in signal MC, along with the distribution of the lowest energy π^0 photon in each event and the distribution from non-signal photons. Non-signal photons were those generated by beam backgrounds which were included in the MC to simulate real running, as discussed in Section 3.1.1. Non-signal photon can possibly be used to reconstruct fake π^0 candidates; or in the case of one signal photon and one non-signal photon, a broken candidate. As can be seen in Figure 4.4, the distribution of the lowest energy π^0 photon in each event extended to energies where there were significant numbers of non-signal photons. There was a minimum cut in the Belle reconstruction code at 22 MeV, below which ECL clusters were not recorded. A minimum energy cut for photons of 50 MeV was common at Belle, however, this cut would have been too restrictive for these events. An initial cut of $E > 30$ MeV was selected for study of the best candidate selection (this was optimised later, see Section 4.8).

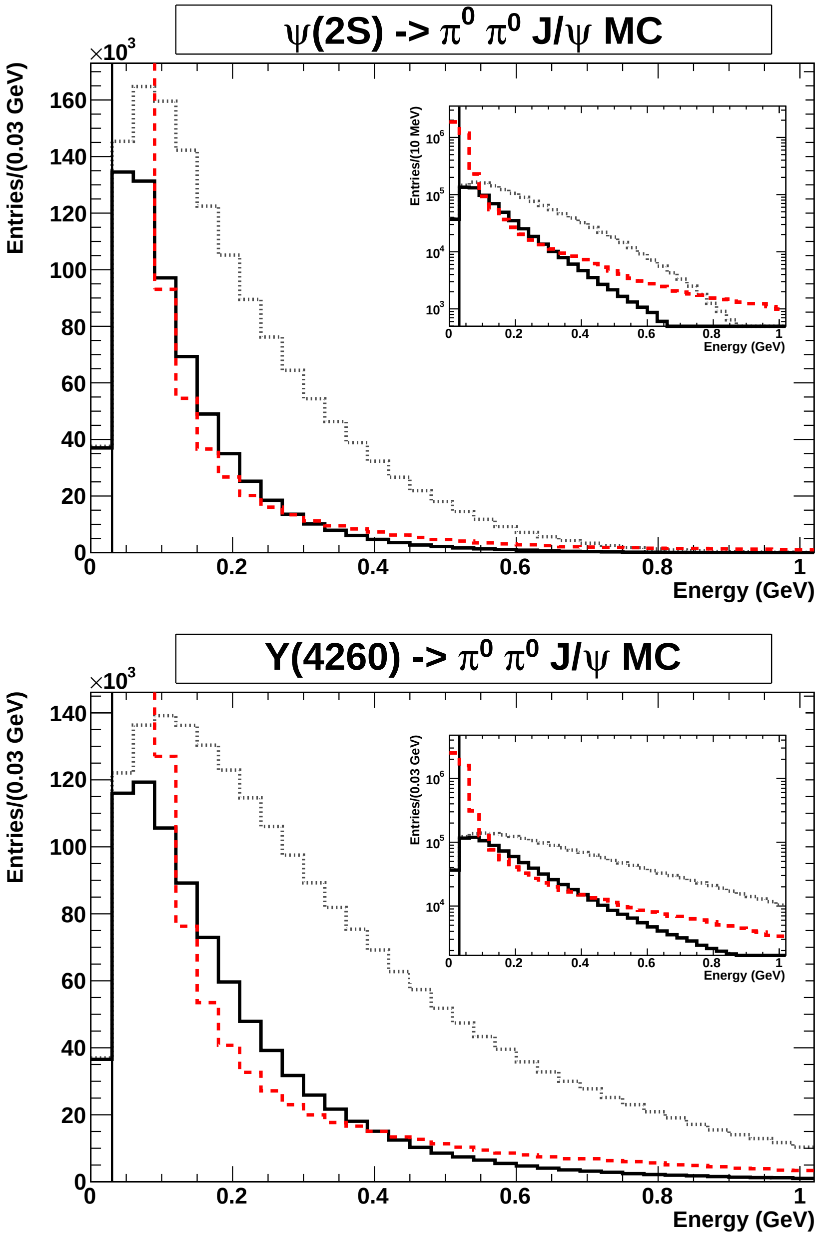

Figure 4.4: Energy distribution of photons in $\pi^0\pi^0 J/\psi$ MC. The grey dotted line indicates the distribution of all π^0 photons. The solid line represents the distribution of the lowest energy π^0 photon in each event. The distribution from non-signal photons in the MC is indicated by the red dashed line. A selection of 30 MeV was applied, indicated by the vertical line. Top: $\psi(2S) \to \pi^0\pi^0 J/\psi$ MC. Bottom: $Y(4260) \to \pi^0\pi^0 J/\psi$ MC. The height of the spectrum of non-signal photons is cut off in the outer plots which use linear scale and is complete in the inset plots which use log scale.

Timing information from ECL clusters became available from Belle experiment 39 onwards and was provided in the form of Time to Digital Converter (TDC) counts. Each ECL cell that formed part of an ECL cluster and passed an energy threshold cut, could record up to two TDC counts: one each corresponding to the rising and falling edges of the signal measured by that cell. The TDC counts corresponding to the two earliest times recorded by cells in each cluster were then stored for that cluster. The distribution of TDC counts from π^0 candidates in data, in events that contained at least one $\pi^0\pi^0 J/\psi$ candidate, can be seen in Figure 4.5. A TDC count of 10,000 corresponded to the cluster being "on-time" with the bunch crossing of the collider. Photons were excluded from this analysis if timing information was available for that photon and it failed the selection: $9000 <$ TDC count < 11000, for both TDC count 1 and TDC count 2.

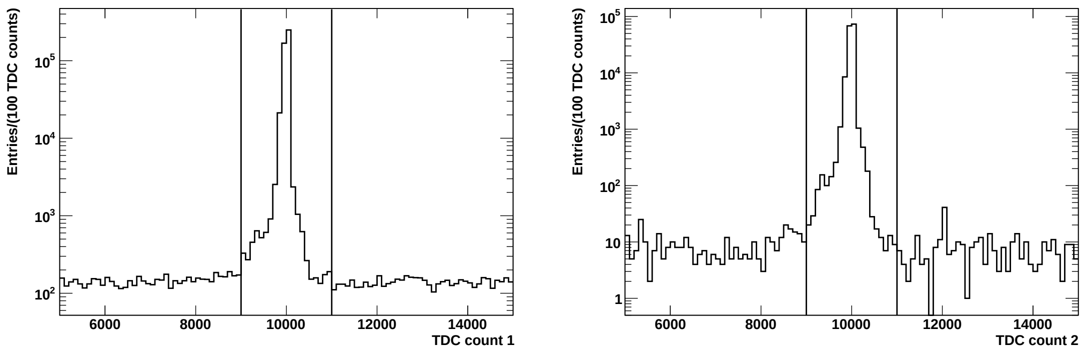

Figure 4.5: TDC count of photons in $\pi^0\pi^0 J/\psi$ events. Left: TDC count 1. Right: TDC count 2. Vertical lines indicate the selection described in the text.

4.2.4 π^0 reconstruction

π^0 candidates were reconstructed from pairs of selected photons.[3] The measured branching fraction for π^0 decaying to two photons is $(98.823 \pm 0.034)\%$ [102]. π^0 candidates which passed an invariant mass selection of $0.08\,\mathrm{GeV} < M(\gamma\gamma) < 0.18\,\mathrm{GeV}$ were selected for further study. There were multiple π^0 candidates per

[3] Technically, this was performed using the `mdst_pi0` and `mdst_gamma` code in the BASF (see Section 2.6.1).

event, produced from combinations of both signal and non-signal photons. In addition to $M(\gamma\gamma)$, another important quantity for distinguishing genuine π^0 candidates from random combinations of photons is the decay angle, $|\cos(\theta_\gamma)|$, where θ_γ is the angle between the π^0 candidate thrust vector and the direction of one of the photons in the π^0 rest frame. As the π^0 is a spin zero particle there can be no preferred direction for π^0 particles to decay: this means that for real π^0 particles the $\cos(\theta_\gamma)$ distribution is flat. This was calculated using:

$$\cos(\theta_\gamma) = \frac{E(\pi^0)}{p(\pi^0)} \cdot \frac{E(\gamma_1) - E(\gamma_2)}{E(\gamma_1) + E(\gamma_2)}, \tag{4.1}$$

where E and p are the energy and momentum of the specified particles and γ_1 and γ_2 are the π^0 daughters. As can be seen in the equation, $\cos(\theta_\gamma)$ is related to the energy asymmetry of the photon energies when measured in any frame other than the π^0 rest frame. As non-signal photons were strongly peaked at low energies, the $|\cos(\theta_\gamma)|$ distribution for non-signal and broken π^0 candidates peaked near one. A broken π^0 candidate is a combination of a signal photon (from a π^0) and non-signal photon pair. The invariant mass and $|\cos(\theta_\gamma)|$ distributions for π^0 candidates in data are shown in Figure 4.6. Because of the large number of non-signal photons in these events, a large number of π^0 candidates were produced and both distributions in the figure show a large broken and non-signal contribution.

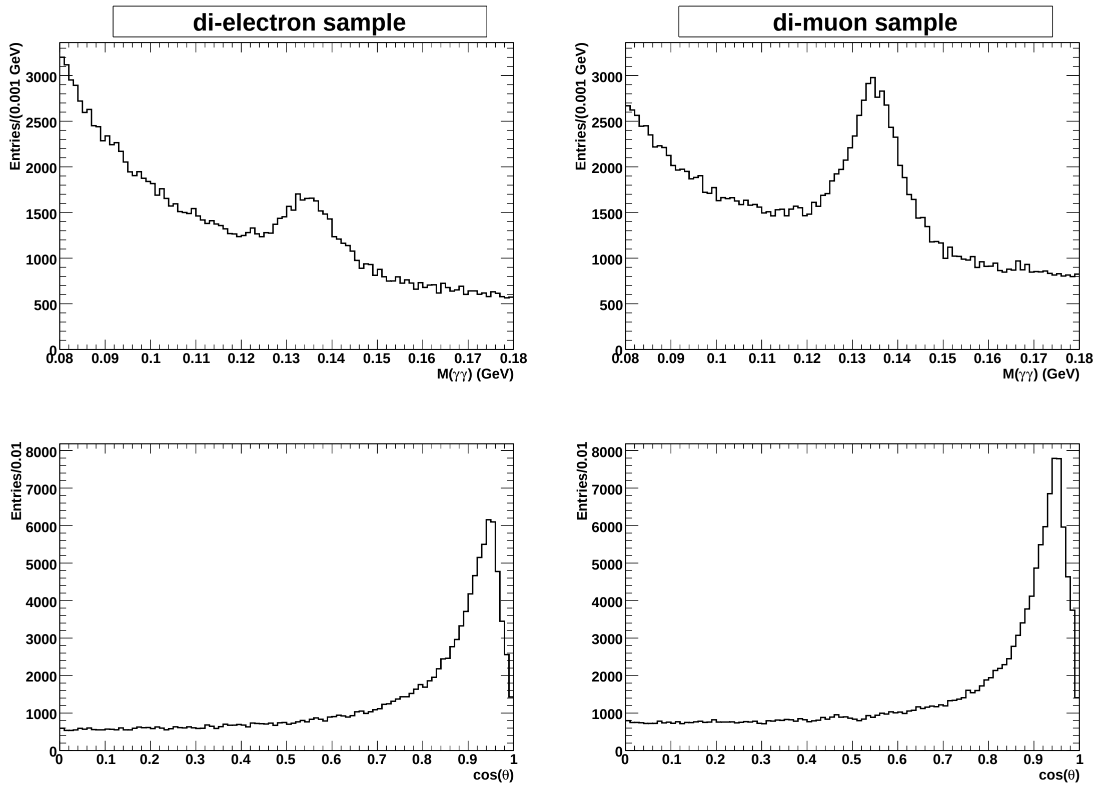

Figure 4.6: Top row: invariant mass of π^0 candidates in data. Bottom row: $|\cos(\theta_\gamma)|$ distribution of π^0 candidates in data. Candidates from di-electron and di-muon events are shown on the left and right respectively.

4.3 $\pi^0\pi^0 J/\psi$ best candidate selection

The J/ψ candidate in each event was combined with pairs of π^0 candidates to form $\pi^0\pi^0 J/\psi$ candidates, with care taken to avoid photons being shared between the π^0 daughters of a single $\pi^0\pi^0 J/\psi$ candidate. The $M^2_{\text{recoil}}(\pi^0\pi^0 J/\psi)$ of candidates was required to be zero up to experimental accuracy, consistent with the mass of the recoiling ISR photon. The large number of photons available in the each event led to a large number of π^0 candidates and therefore $\pi^0\pi^0 J/\psi$ combinations. Two best candidate selection methods were investigated in order to choose a single $\pi^0\pi^0 J/\psi$ candidate in each event for further study. After the best candidate selection method was chosen, a cut on the momentum of the candidate perpendicular to the direction of the ISR photon was investigated, which is discussed in Section 4.3.1.

Two methods of selecting $\pi^0\pi^0 J/\psi$ best candidates were investigated:

- $M(\gamma\gamma)$-based: The candidate with the minimum value of $|M(\pi^0_1) - m_{\pi^0}| + |M(\pi^0_2) - m_{\pi^0}|$ was accepted for further study, where m_{π^0} is the nominal mass of the π^0 [102] and π^0_i is the i-th π^0 candidate in the $\pi^0\pi^0 J/\psi$ candidate.

- $\cos(\theta_\gamma)$-based: The candidate with the minimum value of $|\cos(\theta_\gamma(\pi^0_1))| + |\cos(\theta_\gamma(\pi^0_2))|$ was accepted for further study, where $\cos(\theta_\gamma)$ is the decay angle defined in Equation 4.1 in Section 4.2.4.

Two cases were considered for the $\cos(\theta_\gamma)$-based selection: those candidates with a loose initial selection on π^0 mass, $0.08\,\mathrm{GeV} < M(\gamma\gamma) < 0.18\,\mathrm{GeV}$, and those candidates which passed a tighter mass precut, $|M(\gamma\gamma) - m_{\pi^0}| < 0.02\,\mathrm{GeV}$ (this was optimised later, as discussed in Section 4.8).

The $M(\gamma\gamma)$ and $|\cos(\theta_\gamma)|$ distributions for the best candidates selected by each method can be seen in Figure 4.7, for di-muon events in $\psi(2S) \to \pi^0\pi^0 J/\psi$ MC. These distributions were divided into fractions based on how many of the π^0 photons in each $\pi^0\pi^0 J/\psi$ candidate corresponded to signal and non-signal photons (two π^0 candidates per event in each plot). As can be seen in the $M(\gamma\gamma)$ plots, the signal candidates peaked at the mass of the π^0. In the intermediate case, where one of the four π^0 photons has been lost, the distribution had a peaking component (from the signal π^0) and a non-peaking component (from the broken π^0). There is no peaking component in the case with two π^0 photons lost, in the plots using the $\cos(\theta_\gamma)$-based best candidate selection; however, the $M(\gamma\gamma)$-based selection is sculpting the $M(\gamma\gamma)$ distribution of these events and forming a peak. The $|\cos(\theta_\gamma)|$ distribution was mostly flat for signal candidates, except for the drop-off near one, where the minimum photon energy cut came into play. In this distribution, the broken candidates had a peak near 0.9, due to the π^0 candidates that could be formed by a moderate energy photon with many of the large number of low-energy non-signal photons.

The $M^2_{\mathrm{recoil}}(\pi^0\pi^0 J/\psi)$ and $M(\pi^0\pi^0 J/\psi)$ distributions of the selected candidates can be seen in Figure 4.8.[4] Again, this plot shows di-muon events in $\psi(2S) \to \pi^0\pi^0 J/\psi$ MC divided according to the number of signal π^0 photons in the candidate. As expected, the distribution of signal candidates peaked at the mass of the

[4] The distributions of $M(\gamma\gamma)$, $|\cos(\theta_\gamma)|$, $M^2_{\mathrm{recoil}}(\pi^0\pi^0 J/\psi)$ and $M(\pi^0\pi^0 J/\psi)$ for di-electron $\psi(2S)$ MC events and both di-electron and di-muon events from the $Y(4260) \to \pi^0\pi^0 J/\psi$ MC are shown in Appendix C.

$\psi(2S)$ in $M(\pi^0\pi^0 J\psi)$ and at zero in the $M^2_{\text{recoil}}(\pi^0\pi^0 J\psi)$ distribution. In the case of broken candidates, the distributions were broader and they peaked at slightly shifted values.

The number of events where the selected best candidate subsequently passed the selection: $|M^2_{\text{recoil}}(\pi^0\pi^0 J/\psi)| < 2\,\text{GeV}^2$, can be seen in Table 4.5, where the entries have been divided according to whether the best candidate was a signal or a broken candidate. The $\cos(\theta_\gamma)$-based selection with the tighter mass cut returned the greatest number of correctly identified signal candidates, while the the mass-based best candidate selection returned a greater total number of events. The $\cos(\theta_\gamma)$-based selection with the tighter π^0 mass cut returned approximately half the number of broken candidates compared with the mass-based or $\cos(\theta_\gamma)$ with loose π^0 mass cut selections. For these reasons, the $\cos(\theta_\gamma)$-based selection with the tighter cut on π^0 mass was chosen.

Table 4.5: Number of events passing the cut: $|M^2_{\text{recoil}}(\pi^0\pi^0 J/\psi)| < 2\,\text{GeV}^2$ arranged by best candidate selection method used in the $\pi^0\pi^0 J/\psi$ analysis. Events were divided into columns based on whether the selected best candidate was a correctly identified or broken candidate.

Best candidate	Di-electron		Di-muon	
selection method	Signal	Broken	Signal	Broken
	$\psi(2S) \to \pi^0\pi^0 J/\psi$ signal MC			
$\cos(\theta_\gamma)$ loose mass cut	954	2382	3308	6135
$\cos(\theta_\gamma)$ tight mass cut	1204	1374	4299	3701
$M(\gamma\gamma)$	1218	2490	4220	6435
	$Y(4260) \to \pi^0\pi^0 J/\psi$ signal MC			
$\cos(\theta_\gamma)$ loose mass cut	3389	4378	11269	12797
$\cos(\theta_\gamma)$ tight mass cut	4004	2609	13319	8020
$M(\gamma\gamma)$	3917	4382	12700	12884

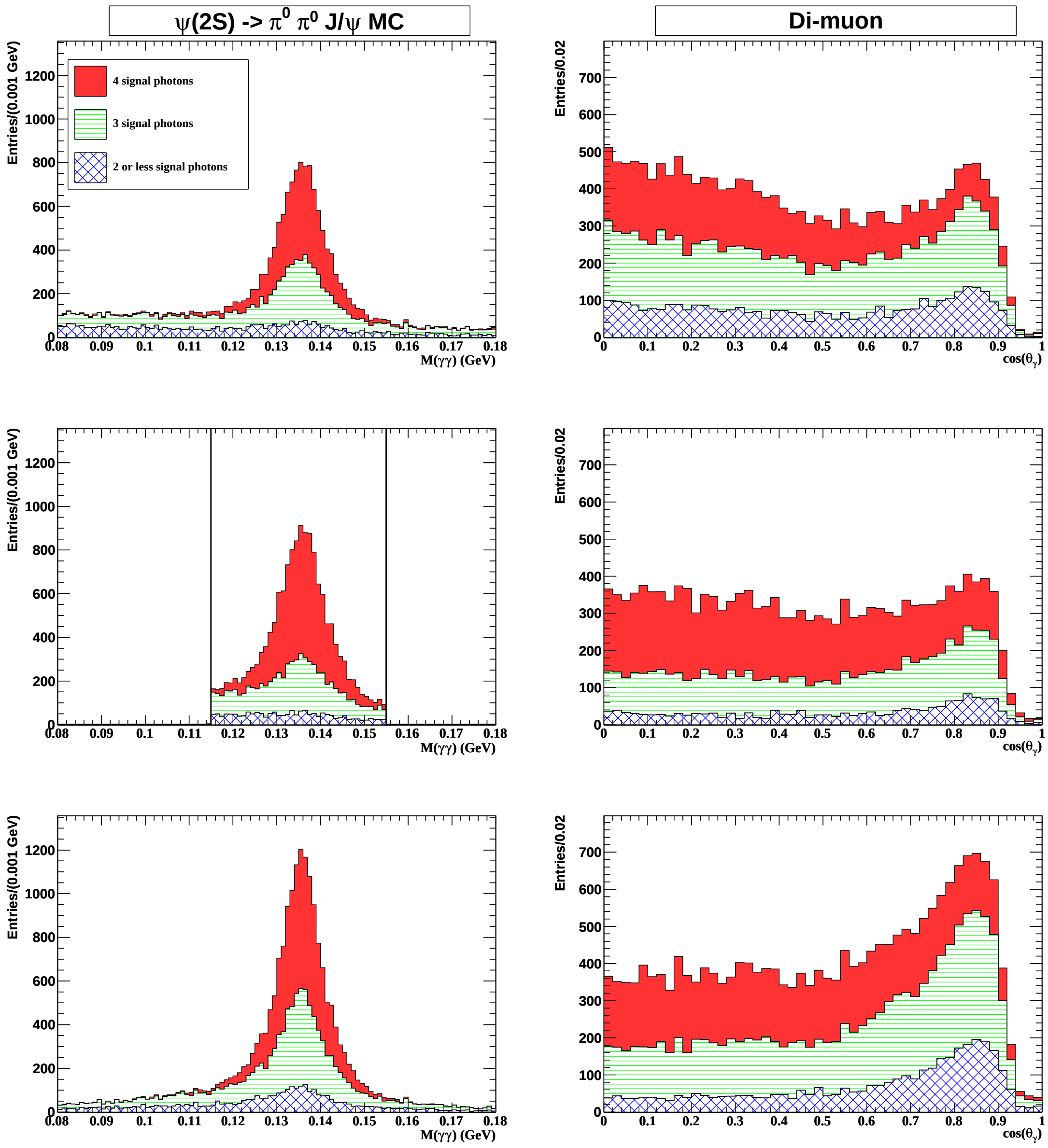

Figure 4.7: Best candidate selection variables for di-muon $\psi(2S)$ signal MC events: Left column: $\gamma\gamma$ mass. Right column: $|\cos(\theta_\gamma)|$. Top row: best candidates from the $\cos(\theta_\gamma)$-based selection, passing $0.08\,\mathrm{GeV} < M(\gamma\gamma) < 0.18\,\mathrm{GeV}$. Middle row: best candidates from the $\cos(\theta_\gamma)$-based selection, passing $|M(\gamma\gamma) - m_{\pi^0}| < 0.02\,\mathrm{GeV}$ (indicated by the vertical lines). Bottom row: best candidates from the $M(\gamma\gamma)$-based selection. Events are divided according to the number of correctly identified signal π^0 photons in the selected $\pi^0\pi^0 J/\psi$ candidate: all four photons correct (solid red histogram), three correct (green horizontally lined histogram) and two or less correct (blue diagonally hatched histogram).

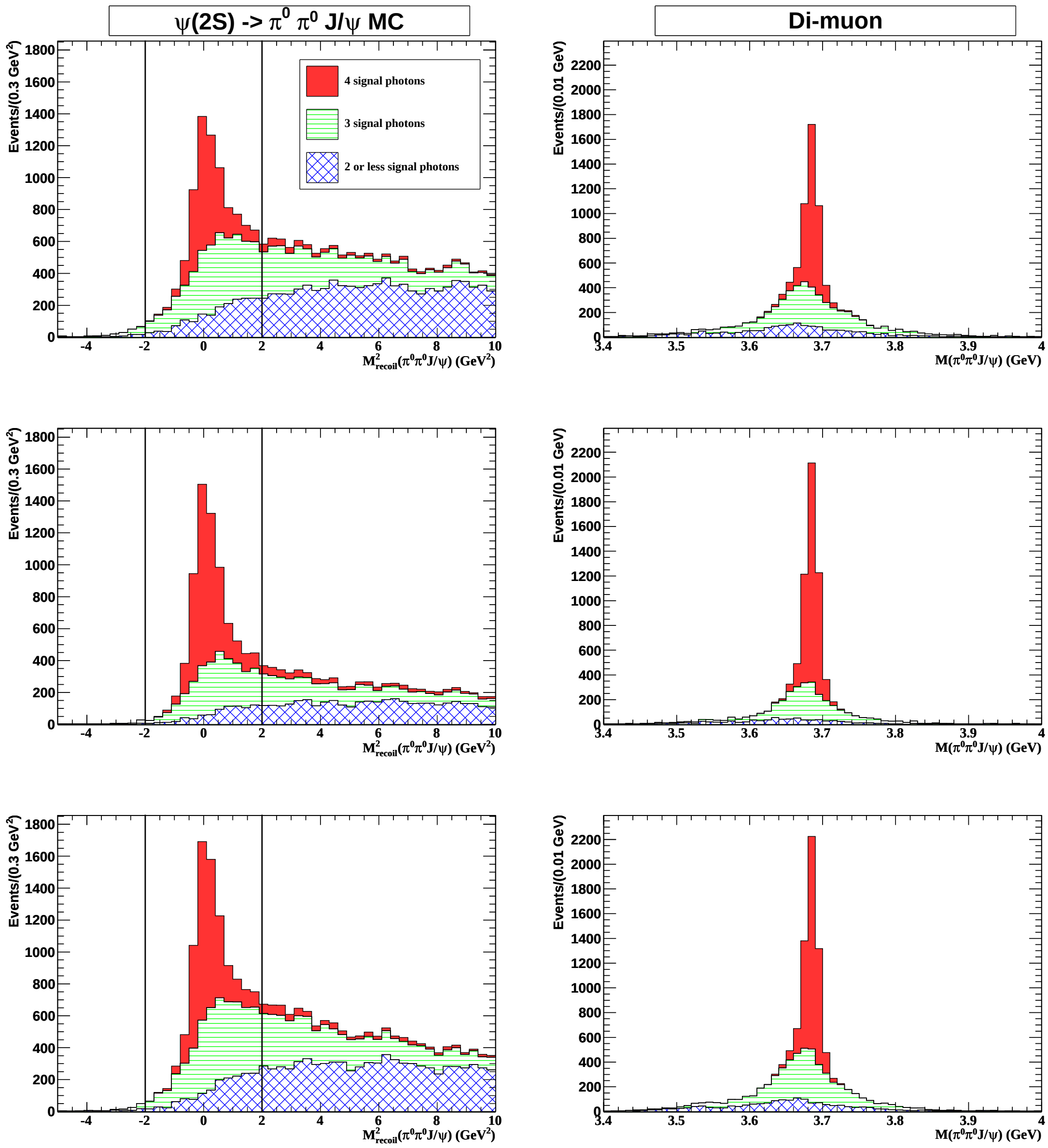

Figure 4.8: Selected best candidates in di-muon $\psi(2S)$ signal MC events. Left column: $M^2_{\mathrm{recoil}}(\pi^0\pi^0 J/\psi)$. Right column: $M(\pi^0\pi^0 J/\psi)$ of candidates passing cut: $|M^2_{\mathrm{recoil}}(\pi^0\pi^0 J/\psi)| < \mathrm{GeV}^2$ (indicated by vertical lines in left column). Top row: best candidates from the $\cos(\theta_\gamma)$-based selection, passing $0.08\,\mathrm{GeV} < M(\gamma\gamma) < 0.18\,\mathrm{GeV}$. Middle row: best candidates from the $\cos(\theta_\gamma)$-based selection, passing $|M(\gamma\gamma) - m_{\pi^0}| < 0.02\,\mathrm{GeV}$. Bottom row: best candidates from the $M(\gamma\gamma)$-based selection. Events are divided according to the number of correctly identified signal π^0 photons in the selected $\pi^0\pi^0 J/\psi$ candidate: all four photons correct (solid red histogram), three correct (green horizontally lined histogram) and two or less correct (blue diagonally hatched histogram).

4.3.1 Momentum perpendicular to the ISR photon direction

Up to this point, the reconstruction of the ISR photon was not been required. Events in which the ISR photon was reconstructed had more information which could be used to choose best candidates, specifically: in the CM frame, the ISR photon and the $\pi^0\pi^0 J/\psi$ combination are produced back to back. The momentum of the $\pi^0\pi^0 J/\psi$ candidate perpendicular to the direction of the ISR photon, $P_{\perp}^{ISR}$, measures the deviation of the candidate with respect to its expected direction. This was investigated and a cut was placed against broken candidates.

The energy distribution of the highest energy photon in each event is plotted in Figure 4.9 and photons with an energy of 3.0 GeV or greater were accepted as ISR photons. In the di-electron sample, no events with ISR photons reconstructed pass trigger and skim cuts (left hand side plots of the figure). The majority of di-electron candidates came from the LM Skim, which had a maximum energy cut in the ECL of $E_{sum} < 6$ GeV, where E_{sum} is the sum of the energy in the ECL, primarily from photon and electrons.[5] This means that di-electron events with the ISR photon reconstructed did not pass skim selection, however, in the di-muon sample, which is primarily selected from the Tau Skim, a clear peak can be seen for the ISR photons near $4.5\,\mathrm{GeV}$ (right hand side plots of the figure). The skim efficiencies for these samples are shown in Table 4.2 in Section 4.1.3.

The $P_{\perp}^{ISR}$ distribution of $\pi^0\pi^0 J/\psi$ candidates in events where an ISR photon was detected is shown in Figure 4.10. In the figure, it can be seen that signal candidates peaked closer to zero than broken candidates. In events with an ISR photon, a selection: $P_{\perp}^{ISR} < 0.1\,\mathrm{GeV}$, was applied prior to best candidate selection (this selection was optimised later, as discussed in Section 4.8). Without the $P_{\perp}^{ISR}$ precut, a candidate with large $P_{\perp}^{ISR}$, which would subsequently fail the cut on M^2_{recoil}, can be selected as the best candidate. With this precut, the number of correctly identified signal candidates which subsequently passed the recoil mass squared cut was increased, while the number of broken candidates was reduced, as can be seen in Table 4.6. With this selection, the total number of events that subsequently passed the recoil mass squared cut was slightly increased. The π^0 mass, $|\cos(\theta_\gamma)|$, $\pi^0\pi^0 J/\psi$ mass and M^2_{recoil} distributions for best candidates selected with and without the $P_{\perp}^{ISR}$ precut are shown in Appendix D.

[5] Data skims are described in Section 2.5.3.

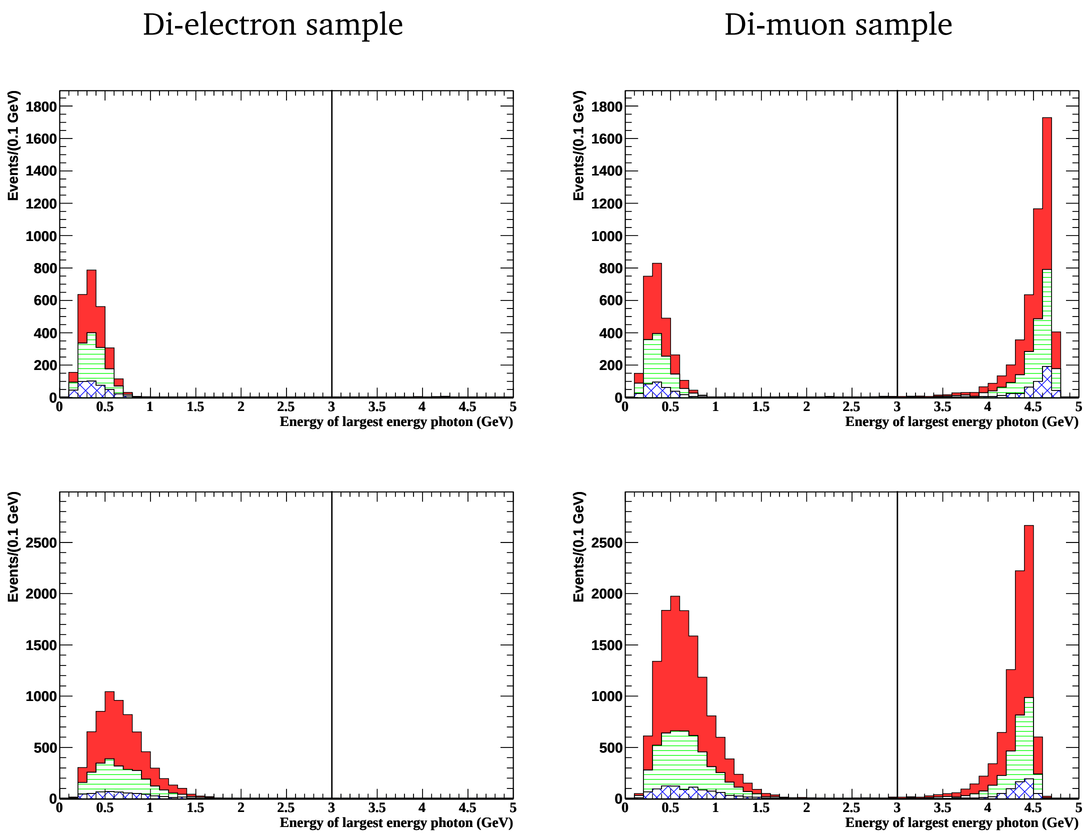

Figure 4.9: Energy of the highest energy photon in signal MC events. Top row: $\psi(2S) \to \pi^0\pi^0 J/\psi$ signal MC. Bottom row: $Y(4260) \to \pi^0\pi^0 J/\psi$ signal MC. Left column: di-electron events. Right column: di-muon events. Photons to the right of the vertical line were accepted as ISR photons (no events with ISR photons detected pass skim cuts in the di-electron sample). Events are divided according to the number of correctly identified signal photons in the selected $\pi^0\pi^0 J/\psi$ candidate: all four photons correct (solid red histogram), three correct (green horizontally lined histogram) and two or less correct (blue diagonally hatched histogram).

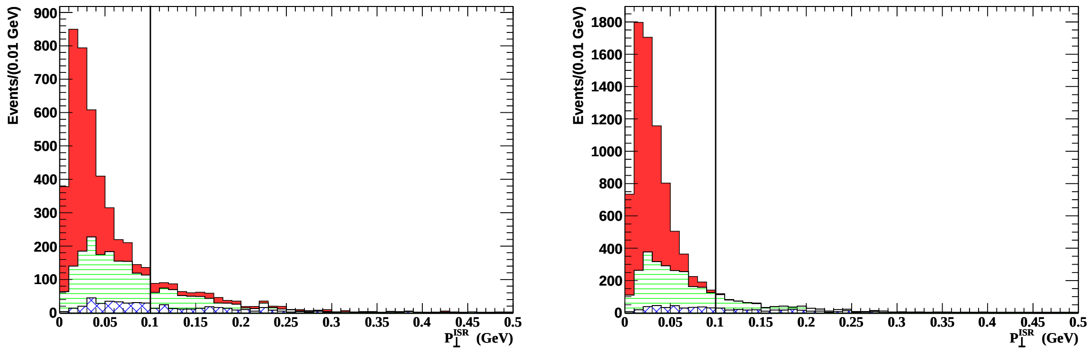

Figure 4.10: $P_\perp^{ISR}$ of the best candidates di-muon MC events. Left: $\psi(2S) \to \pi^0\pi^0 J/\psi$ signal MC. Right: $Y(4260) \to \pi^0\pi^0 J/\psi$ signal MC. The vertical line indicates the selection described in the text. Events are divided according to the number of correctly identified signal photons in the selected $\pi^0\pi^0 J/\psi$ candidate: all four photons correct (solid red histogram), three correct (green horizontally lined histogram) and two or less correct (blue diagonally hatched histogram).

Table 4.6: Number of best candidates passing the $|M^2_{\mathrm{recoil}}(\pi^0\pi^0 J/\psi)| < 2\,\mathrm{GeV}^2$ selection, with and without a selection of: $P_\perp^{ISR} < 0.1\,\mathrm{GeV}$. Events are divided into correctly identified signal candidates and broken candidates in $\psi(2S)$ and $Y(4260)$ signal MC for the di-muon channel.

Best Candidate	Di-muon	
Selection	Signal	Broken
	$\psi(2S) \to \pi^0\pi^0 J/\psi$ signal MC	
$\cos(\theta_\gamma)$	2847	2186
$\cos(\theta_\gamma)$, $P_\perp^{ISR}$ precut	2956	1795
	$Y(4260) \to \pi^0\pi^0 J/\psi$ signal MC	
$\cos(\theta_\gamma)$	5333	3114
$\cos(\theta_\gamma)$, $P_\perp^{ISR}$ precut	5828	2599

4.4 Particle Identification (PID)

Charged track pairs that formed J/ψ candidates were required to be positively identified as either e^+e^- or $\mu^+\mu^-$. The mass of the charged track was used when the tracks were fitted to hits in the detector and when the track pair was fitted to form a J/ψ candidate. Additionally, the PID requirements reduced the non-J/ψ background. The PID was studied using the $\psi(2S)$ control sample in data and MC: this is discussed in Sections 4.4.1 and 4.4.2 for the di-electron and di-muon subsamples, respectively.[6]

4.4.1 Electron identification

Both J/ψ daughter tracks were required to be positively identified as electrons before a di-electron candidate was accepted. The electron identification was performed using the EID method of the Belle PID software, described in Section 2.4.

The value of EID output from the software takes a value between one (meaning that the detector response for the track was very electron-like) and zero (meaning that the detector response for the track was not electron-like). The EID of J/ψ candidate tracks are shown in Figure 4.11. The EID of the tracks from the J/ψ signal region and the scaled J/ψ sidebands are shown in the top row of the figure, where the J/ψ sidebands were scaled by 1/2, the ratio of the width of the J/ψ signal and sideband regions. The sideband-subtracted data was then compared with the expectation from MC and is shown in the bottom row of the figure. To prepare the MC expectation, the $\psi(2S)$ signal MC was scaled according to the luminosity measured in data and the contamination from other $\psi(2S)$ decay modes was accounted for using the $\psi(2S) \rightarrow generic$ MC sample. Of the two tracks, the track with the greater value returned by the EID software is shown on the left hand side of Figure 4.11. This track was required to have an EID value greater than 0.9. After the selection, the EID of the other track was plotted and is shown on the right hand side of the figure. The EID of the second track was required to be greater than 0.8. J/ψ candidates that passed these selection criteria were accepted as di-electron candidates. From $\psi(2S)$ signal MC this electron identification had an efficiency of 80%.

[6] The technical details of the usage of the Belle PID software are discussed in Section 3.2.2.

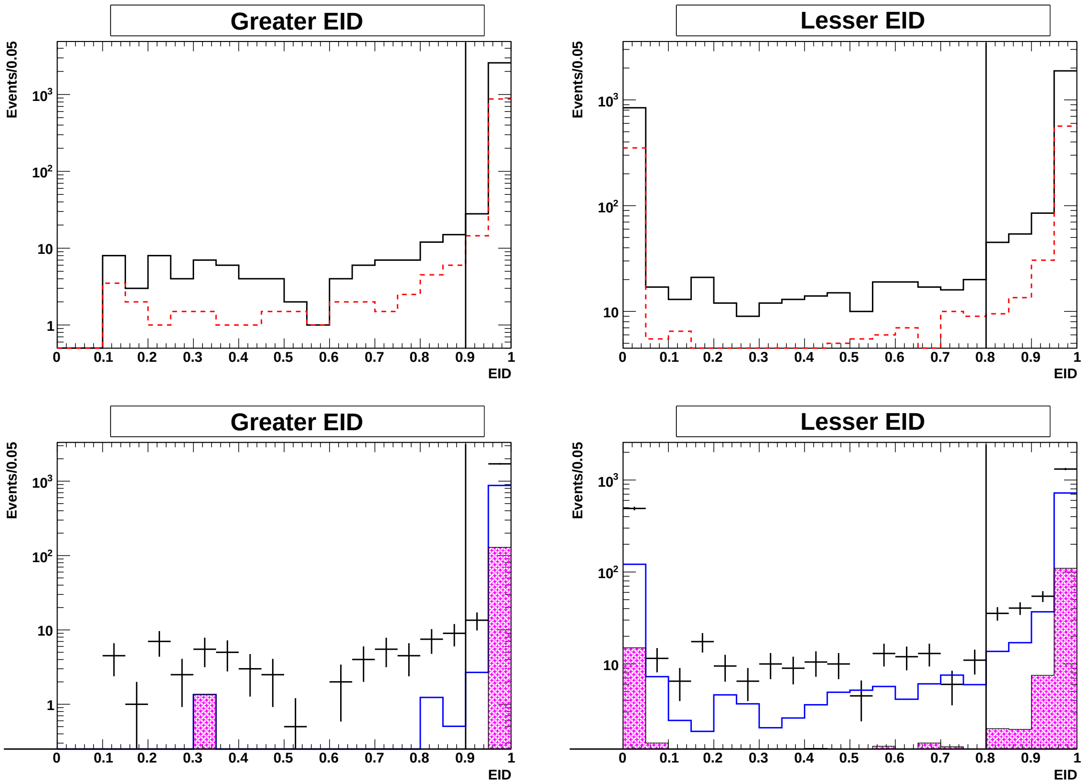

Figure 4.11: EID (or "Electron identification") likelihood of candidate tracks. Top: tracks in data in the J/ψ signal (solid line) and the scaled J/ψ sideband regions (dashed red line). Bottom: the sideband-subtracted data (data points) are compared with the prediction from MC (unshaded histogram) scaled to the luminosity in data, including the contribution from non-signal $\psi(2S)$ decay modes (magenta shaded histogram). Left: the track with greater value of EID, with the selection indicated by the vertical line. Right: the EID likelihood of the other J/ψ candidate track, after the first selection, with the selection on this track indicated by the vertical line. Plots are shown in log scale.

4.4.2 Muon identification

Two criteria were required to identify di-muon J/ψ candidates. Firstly, one of the daughter tracks was required to be positively identified as a muon, and secondly, the two tracks were required to combine to form an object with the mass of the J/ψ particle. These two criteria were sufficient to identify $J/\psi \rightarrow \mu^+\mu^-$ and no muon identification requirements were placed on the second track. In the special case where the second track has no muon identification information available, a cut against background was made on the production angle of the track.

The muon identification software (see Section 2.4) returned the likelihood for a track to be a muon, called the MuID. The MuID output from the PID software for the two J/ψ candidate tracks is shown in Figure 4.12. The distribution of MuID for tracks from the J/ψ signal and scaled sideband regions are shown at the top of the figure and the sideband-subtracted data is shown with the prediction from MC in the bottom row of the figure. The left hand side of the figure shows the MuID of the track with the greater value of MuID. The majority of events had at least one track with a large value of MuID in each J/ψ candidate and J/ψ candidates were required to have at least one track with MuID greater than 0.9. After the selection, the muon likelihood of the second J/ψ track (with the lesser MuID) was plotted, this is shown on the right hand side of Figure 4.12. The data and MC show good agreement over the whole range for the second J/ψ track, with a significant contribution at MuID equal to zero, and no cut was applied to the MuID of this track.

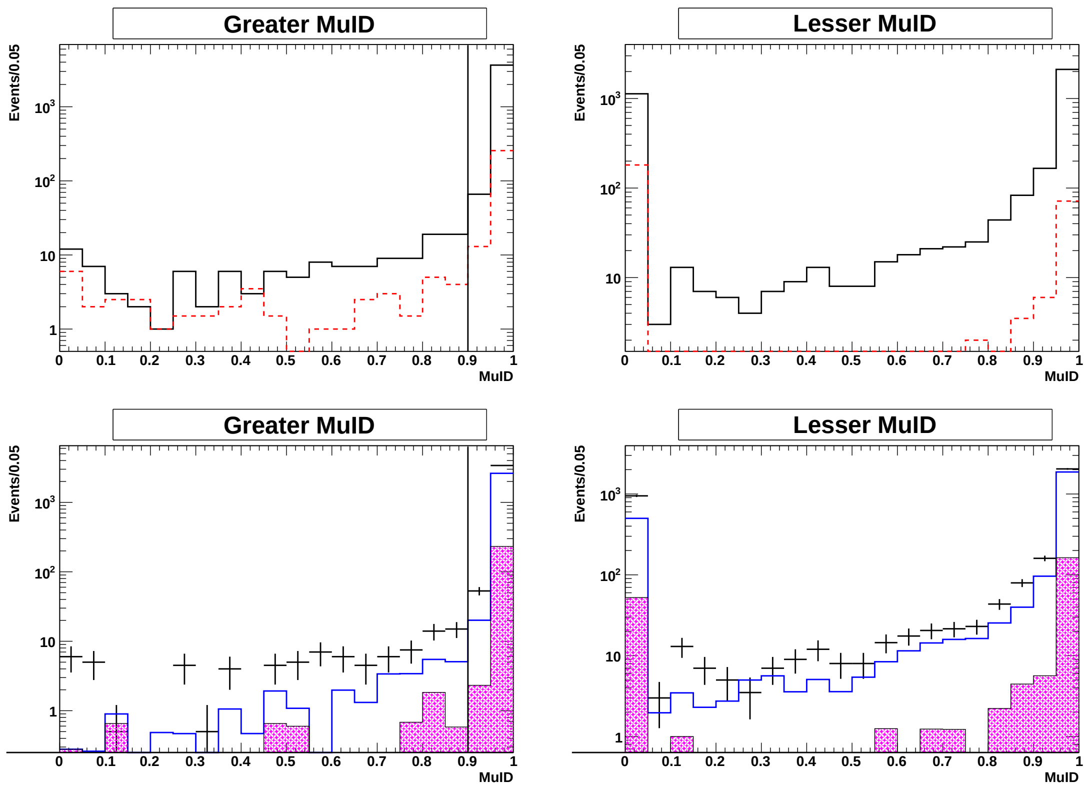

Figure 4.12: MuID (or muon identification likelihood) of candidate tracks. Top row: tracks in data in the J/ψ signal (solid line) and the scaled J/ψ sideband regions (dashed red line). Bottom row: the sideband-subtracted data (data points) are compared with the expectation from $\psi(2S) \rightarrow \pi^0\pi^0 J/\psi$ signal MC (unshaded histogram) and the expected contamination from other $\psi(2S)$ decay modes as predicted by $\psi(2S) \rightarrow$ *generic* MC (magenta shaded histogram). Left column: the track with greater value of MuID, with the selection indicated by the vertical line. Right column: the MuID of the other J/ψ candidate track, after selection. Plots are shown in log scale.

The published Belle $\pi^+\pi^- J/\psi$ analysis [29] found a significant contribution from muon tracks with MuID equal to zero. The KLM sub-detector, which contributes the main information used by the muon identification, had less coverage than the other sub-detectors (see Section 2.3.6). Because of this, there was no MuID information available for some tracks, which was flagged in the software with a zero for MuID. Those tracks were included in the $\pi^+\pi^- J/\psi$ analysis and it was found that the background contribution in these events could be reduced with a cut on the production angle of these tracks, θ. The production angle was investigated for tracks in the $\pi^0\pi^0 J/\psi$ sample with MuID equal to zero and is shown Figure 4.13. Tracks in the J/ψ signal and sideband regions and the sideband-subtracted data with the prediction from MC are shown on the left and right hand sides of the figure, respectively. It was found that there was a significant excess of tracks in the data in the region below -0.85, when compared with MC. Therefore, these events were excluded with an angular cut when the value of MuID was zero.

From $\psi(2S)$ signal MC, the muon identification described in this section had an efficiency of 96%.

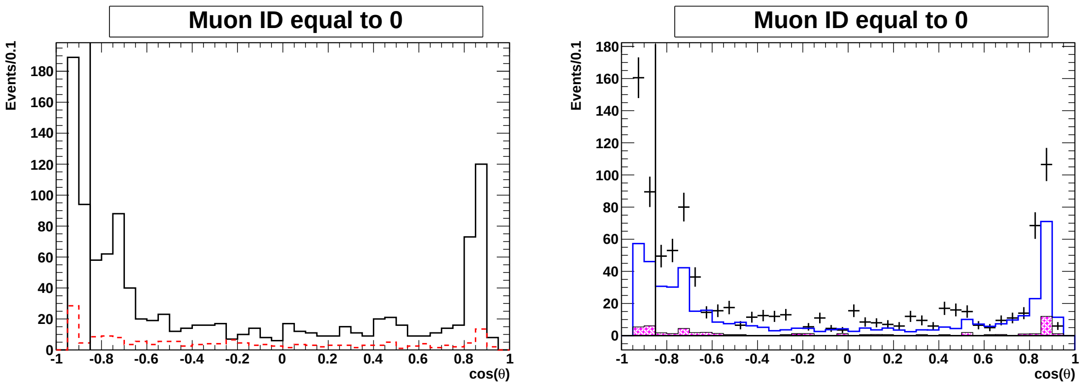

Figure 4.13: Production angle of tracks with muon likelihood (MuID) equal to zero. Left: production angle for tracks in data in the J/ψ signal region (solid line) and the scaled J/ψ sideband regions (dashed red line). Right: the sideband-subtracted data (data points) with the prediction from $\psi(2S) \to \pi^0\pi^0 J/\psi$ signal MC (unshaded histogram) and the contamination from other $\psi(2S)$ decay modes as predicted by $\psi(2S) \to \textit{generic}$ MC (magenta shaded histogram). The vertical line indicates the selection described in the text.

4.5 Overview of the $\psi(2S)$ control sample

The $\pi^0\pi^0 J/\psi$ best candidates in the $\psi(2S)$ mass region in data, were investigated in four subsamples that were considered separately: the di-electron sample, with and without the ISR photon reconstructed, and the di-muon sample, with and without the ISR photon reconstructed. In this section, a brief overview of the subsamples is presented before each of the subsamples is discussed further in the following sections.

The invariant mass spectrum in the $\psi(2S)$ control sample region (chosen to be 3.4 GeV to 4.0 GeV) for each of these subsamples is shown in Figure 4.14. Each of the four subsamples responded differently to the trigger conditions and the different skims used, as was discussed in Section 4.1.3. The top row of the figure shows the samples with the ISR photon reconstructed. In this case, the di-electron sample was completely eliminated by the skim conditions,[7] by contrast, the di-muon sample contained the largest number of on-peak events, with the lowest number of off-peak events. The bottom row of Figure 4.14 shows the two samples where the ISR photon was not reconstructed: this primarily occurred when the ISR photon was outside the angular acceptance of the detector. In these two plots, the di-electron and di-muon samples both have similar sized $\psi(2S)$ peaks but there is a much larger off-peak contribution in the di-electron channel.

Because of the different signal sizes and backgrounds, the three subsamples that contained events were investigated separately. The analysis of the di-electron sample is discussed in Section 4.6. The analysis of the di-muon sample is described in Section 4.7 and the fully reconstructed di-muon subsample, with ISR photon reconstructed, is further discussed in Section 4.7.4. As will be discussed in these sections, the background in the samples without the ISR photon in the detector was found to be high with respect to the size of the predicted $Y(4260)$ signal yield. These samples were not expected to contribute to the result from the sample with the ISR photon reconstructed (di-muon only) and were therefore dropped from the analysis. After this, the selection cuts were optimised as will be discussed in Section 4.8.

[7] See Table 4.2 in Section 4.1.3.

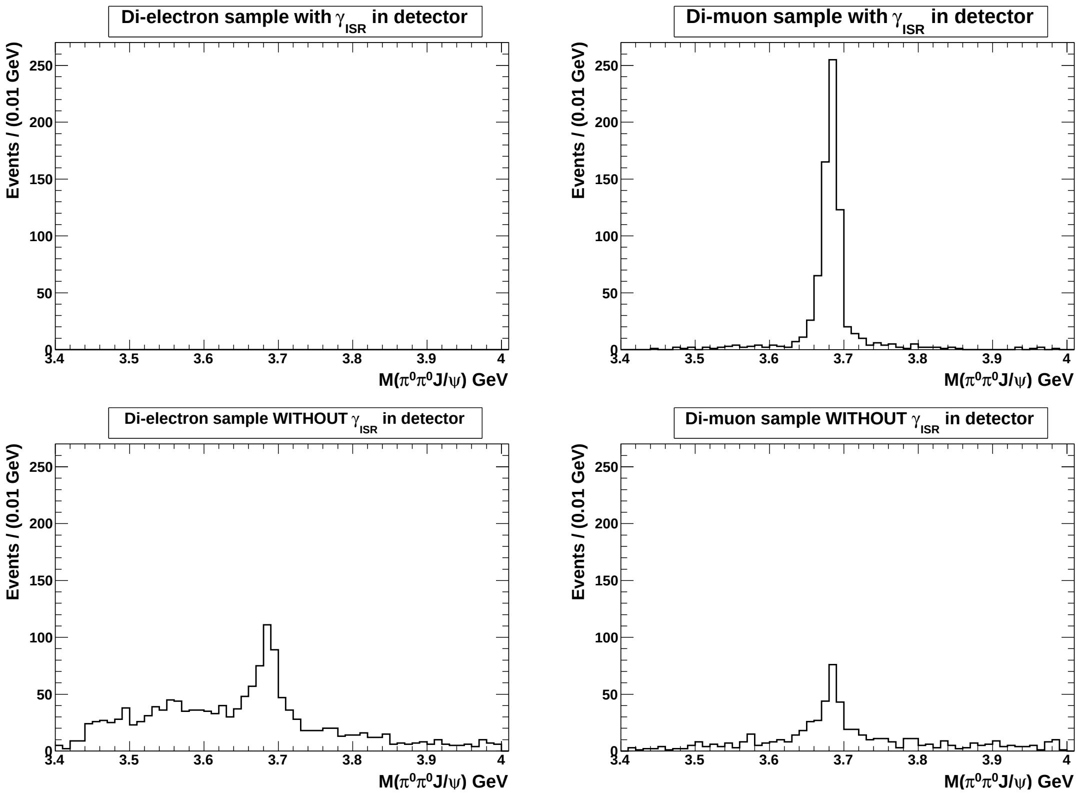

Figure 4.14: $\psi(2S)$ control sample in data. Left column: di-electron events. Right column: di-muon events. Top row: events with the ISR photon reconstructed. (No di-electron events pass skim cuts in this sample.) Bottom row: events where the ISR photon is not reconstructed.

4.6 Control sample in di-electron channel

The di-electron best candidates in the $\psi(2S)$ control sample were analysed. Di-electron events with the ISR photon in the detector do not pass skim selection and were unable to be used in this analysis. In the sample without the ISR photon reconstructed, firstly, the candidates for the daughter particles are discussed in Section 4.6.1 and the $\pi^0\pi^0 J/\psi$ best candidates are discussed in Section 4.6.2. Large backgrounds to the $\psi(2S)$ were observed in this sample and these events were studied with a view to reducing the background in Section 4.6.3. Ultimately they were unable to be reduced to the point were the $Y(4260)$ would be visible in the di-electron sample and this sample was dropped from the analysis, as discussed in Section 4.6.4.

4.6.1 Investigating daughters of di-electron best candidates

The J/ψ and π^0 candidates of the selected di-electron $\pi^0\pi^0 J/\psi$ best candidates in the $\psi(2S)$ control sample were studied. The e^+e^- invariant mass spectrum in best candidates can be seen in Figure 4.15, where the J/ψ signal and sideband regions are indicated by the solid and dashed vertical lines in the figure, respectively. The peak at the J/ψ mass is clear, however, there is a large combinatorial background under the peak. This background is not linear between the two sidebands: the background on the low-mass sideband is rising, while the background on the high-mass side is almost constant. It was checked that the π^0 photons were not contaminating the bremsstrahlung correction applied to the electron tracks. Because the shape of the background is not linear between the sidebands, the scaled sidebands will not correctly represent background under the J/ψ peak, however, the sidebands will approximate some of this background. Sideband-subtracted plots, with the data from sidebands scaled as though they were linear, will be shown in the remainder of the sections on the di-electron sample as a guide.

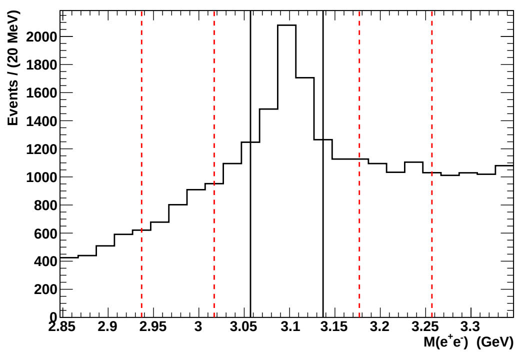

Figure 4.15: Invariant mass spectrum of J/ψ candidates after electron identification for $\psi(2S)$ best candidates. The vertical lines indicates the J/ψ signal (solid) and sideband regions (dashed red).

The $|\cos(\theta_\gamma)|$ and invariant mass distributions from the π^0 candidates (two per event) are shown in the left and right hand plots of Figure 4.16. In the $|\cos(\theta_\gamma)|$ distribution, the peak at around 0.9 indicates a large contribution from broken and fake π^0 candidates. There are a large number of low energy photons in Belle data from beam background and other processes and a comparatively energetic photon can combine with a large number of low energy photons to produce many fake π^0

combinations. The $|\cos(\theta_\gamma)|$ distribution is flat for true π^0 particles, as discussed in the section on π^0 reconstruction in Section 4.2.4. On the right hand side of the figure, the π^0 mass distribution appears to be dominated by background with just a hint of a peak at the nominal π^0 mass of 134.9766 ± 0.0006 MeV [1]. Therefore the $\pi^0\pi^0 J/\psi$ candidates in the $\psi(2S)$ mass region appear to be background dominated.

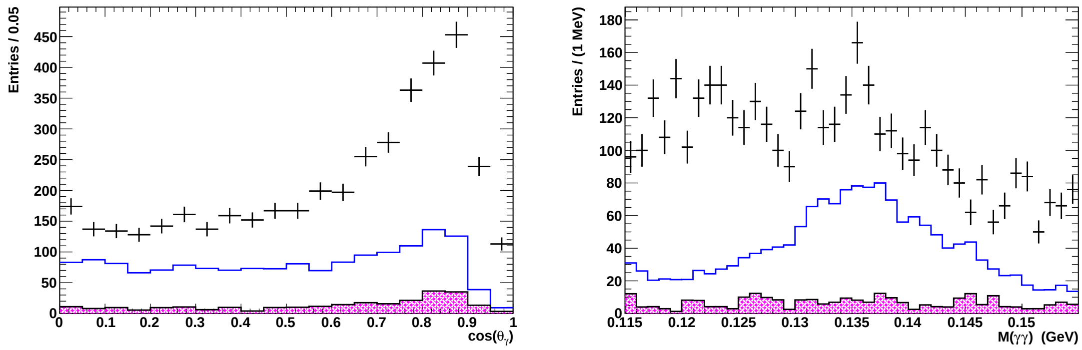

Figure 4.16: π^0 candidates in di-electron $\psi(2S)$ candidates. Left: $|\cos(\theta_\gamma)|$. Right: invariant mass. The J/ψ sideband subtracted data (data points) are compared with the prediction from MC (unshaded histogram) scaled to the luminosity in data, including the contribution from non-signal $\psi(2S)$ decay modes (magenta shaded histogram).

4.6.2 Di-electron $\psi(2S)$ best candidates

The di-electron $\pi^0\pi^0 J/\psi$ combination of selected $\psi(2S)$ best candidates were investigated. The recoil mass squared of these candidates is shown on the left hand side of Figure 4.17 and on the right hand side of the figure, the mass of the candidates that pass $|M^2_{\text{recoil}}| < 2$ GeV^2 can be seen. The M^2_{recoil} distribution peaks near zero, with a large number of off-peak events from broken and background candidates. Despite the difficulties in distinguishing the π^0 mass peak, a clear peak is seen at the $\psi(2S)$ mass in $M(\pi^0\pi^0 J/\psi)$. However, there are a large number of off-peak events and the MC appears to predict a greater number of $\psi(2S)$ events than were reproduced in data. In the next section, the background is investigated with a view to reducing it.

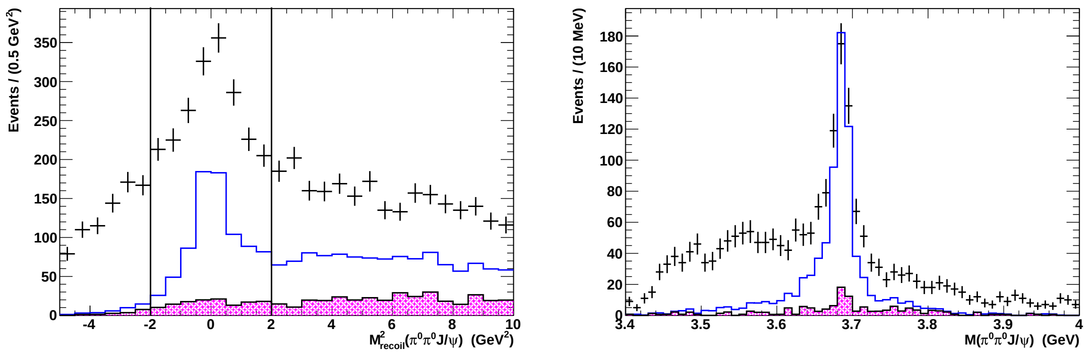

Figure 4.17: Di-electron $\pi^0\pi^0 J/\psi$ best candidates. Left: recoil mass squared distribution. Right: invariant mass distribution. The J/ψ sideband subtracted data (data points) are compared with the prediction from MC (unshaded histogram) scaled to the luminosity in data, including the contribution from non-signal $\psi(2S)$ decay modes (magenta shaded histogram).

4.6.3 Investigating the background in the di-electron sample

In order to investigate the background further, a series of checks were performed on the photons and charged tracks of best candidates and the kinematic distributions of these particles were investigated. This included the specific possibility that radiative Bhabha decays could be contributing to the background, which is discussed in the next section. However, no selections capable of reducing the background without significantly reducing the signal were found.

The possibility that some of the background was from events where the J/ψ candidates had gained or lost significant energy was checked using the π^0 mass distribution from the J/ψ sidebands, which showed no peaks at the π^0 mass. To check that the background was not being caused by the the bremsstrahlung recovery procedure, the angle between the π^0 photons and the electron tracks was checked and a clear separation was found between the electron tracks and the π^0 photons. The momentum spectrum of the electron tracks in $\psi(2S)$ candidates is shown with the prediction from $\psi(2S)$ MC in the top plot of Figure 4.18. In the plot, the data and MC distributions are different and the data shows a two peaked structure across the whole momentum range where signal electrons and positrons are expected. The angle with respect to the z-axis, $\cos(\theta)$, that the electron and positron tracks make in the detector are shown in bottom row of Figure 4.18, in the left and right hand plots, respectively. Both the electron and positron tracks occurred mostly at large negative values of $\cos(\theta)$, however, the positrons showed a peak at -0.9, where the electrons showed no clear peak. A cut on the angle of the positron track in the detector was attempted, however it significantly reduced the efficiency of the signal and did not significantly increase the signal to background ratio. The enhancement of positrons in the backward region of the detector suggested a possible contribution from Bhabha events, which is discussed below.

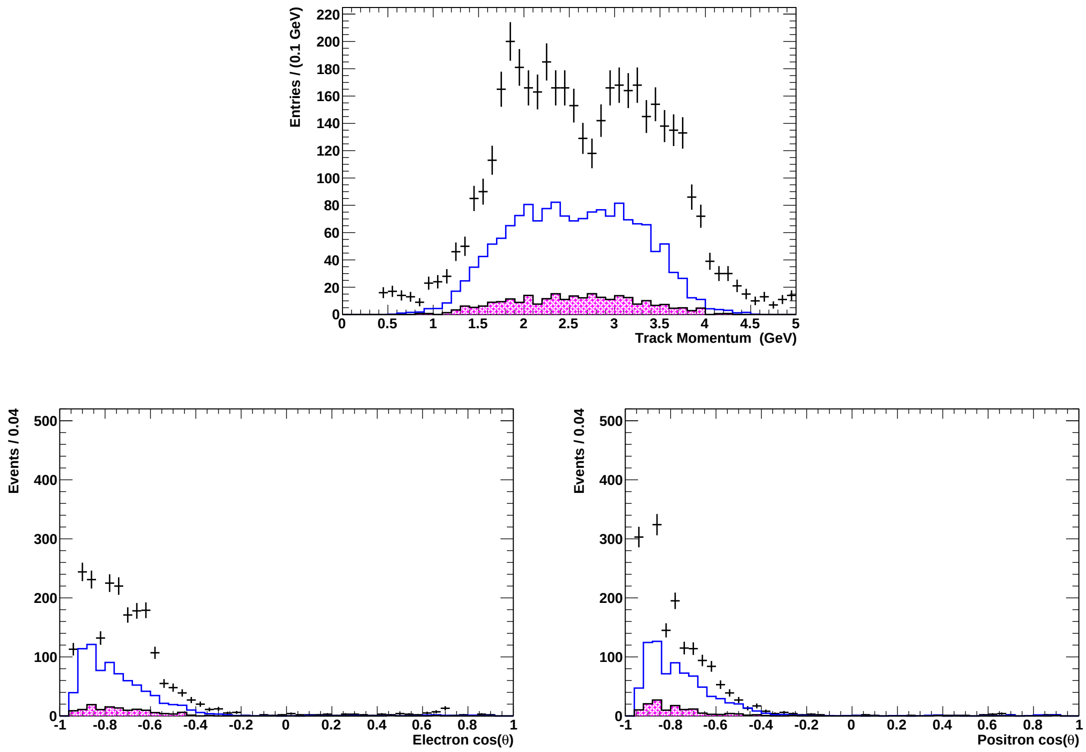

Figure 4.18: Kinematic distributions of e^+e^- tracks in the $\psi(2S)$ control sample. Top: the momentum of tracks in the detector. Bottom row: the angle of electron and positron tracks in the detector, shown in the left and right hand plots, respectively. The J/ψ sideband subtracted data (data points) are compared with the prediction from MC (unshaded histogram) scaled to the luminosity in data, including the contribution from non-signal $\psi(2S)$ decay modes (magenta shaded histogram).

Background from radiative Bhabha events

Bhabha scattering occurs when the initial e^+ and e^- from the beams interact electromagnetically and scatter. Radiative Bhabha events occur when one or both of these particles radiates a photon and the signature of these events is two electron tracks and energy from photons in the detector. In this case, the radiated photons may combine with low energy photons from other background processes to form π^0 candidates. In radiative Bhabha events, the two tracks occur predominately close to the beam-line, near their initial direction of travel. The excess of positron tracks at large negative $\cos(\theta)$ (see Figure 4.18 above) and the fact that $\gamma_{ISR}\pi^0\pi^0[J/\psi \to e^+e^-]$ share a similar event signature suggested radiative Bhabha events as a possible background.

A sample of radiative Bhabha MC that was produced by the Tau Studies group at Belle was investigated and as expected from the beam directions, the electrons peaked towards the forward end of the detector (positive z) and the positrons peaked towards the backward end of the detector(negative z). In non-radiative Bhabha events, the two tracks are back to back in the CM frame, in contrast to J/ψ decays which occur at smaller angles to each other. In radiative Bhabha events, the angle between the tracks decreases as the energy of the radiated photon increases. The angle between the electron and positron tracks in di-electron $\psi(2S)$ events was investigated and is shown in Figure 4.19. As can be seen in the figure, J/ψ daughter tracks in the data and MC peak at an angle of approximately 75°. In the data, there is a small component of the distribution which peaks near 180° (note that the plot is shown on a log scale): this does not appear in the MC and is consistent with a contribution from radiative Bhabha events. An acolinearity cut on the two tracks was attempted, but this selection did not reduce the background enough for the expected $Y(4260)$ yield to be visible above background.

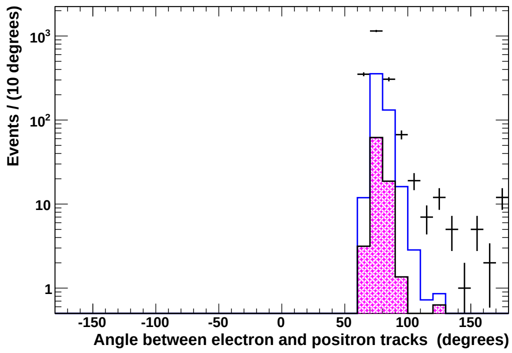

Figure 4.19: Angle between the e^+ and e^- tracks in the detector, shown on a log scale. The J/ψ sideband subtracted data (data points) are compared with the prediction from MC (unshaded histogram) scaled to the luminosity in data, including the contribution from non-signal $\psi(2S)$ decay modes (magenta shaded histogram).

4.6.4 Excluding the di-electron sample

The di-electron sample with the ISR photon reconstructed was completely rejected by skim conditions and unavailable for this study. The di-electron sample without the ISR photon was found to have a large fake J/ψ component and the π^0 distributions were found to be background dominated. Additionally, the combinatorial background in the J/ψ spectrum was not linear between the two sidebands. These two points would make the systematics associated with the di-electron sample difficult to control and the background in this sample is also large compared to the expected signal size of the $Y(4260)$. For these reasons the di-electron sample was not expected to contribute to a potential result in the $Y(4260)$ region and the di-electron sample was not studied further.

4.7 Control sample in di-muon channel

The di-muon best candidates were investigated in data and MC in the $\psi(2S)$ mass range, $M(\pi^0\pi^0 J/\psi) \in [3.4,\ 4.0]$ GeV. J/ψ particles produced directly via ISR were identified as a background and excluded with cuts: this is discussed in Section 4.7.1. The π^0 and J/ψ daughter candidates in the selected best candidates were investigated, which is presented in Section 4.7.2, before the $\pi^0\pi^0 J/\psi$ combination was studied in the two available data skims: the Tau and LM Skims, as is discussed in Section 4.7.3. The requirement of an ISR photon with $E > 3$ GeV in an event, combined with the requirement that the $\pi^0\pi^0 J/\psi$ candidate be aligned in the opposite direction to this photon, reduced the majority of possible backgrounds,[8] as is detailed in Section 4.7.4, which describes the fully reconstructed sample. These extra requirements meant that the fully reconstructed sample was very clean and it also happened to be the largest of the four samples. For these reasons, the fully reconstructed sample was the sample that was selected for further study.

4.7.1 ISR J/ψ background

When investigating the M^2_{recoil} distribution of $\psi(2S)$ candidates in the di-muon channel, a background with large negative recoil mass squared was noticed. These events were identified as J/ψ events produced directly via ISR and were removed with a cut on the recoil mass squared of the J/ψ candidate.

The J/ψ sideband-subtracted recoil mass squared distribution of $\psi(2S)$ candidates is shown in the left hand side of Figure 4.20, with the prediction from MC. The first item investigated in this distribution was the events with $M^2_{\mathrm{recoil}}(\pi^0\pi^0 J/\psi) < -2\,\mathrm{GeV}^2$, as there was nothing in the MC that could produce them. The $M(\mu^+\mu^-)$ spectrum for J/ψ candidates in these events is shown on the right hand side of Figure 4.20 and the peak at the J/ψ mass confirmed that these were events containing a real J/ψ particle. Broken $\pi^0\pi^0 J/\psi$ candidates (where one or more daughter particles is missed) in general produced an $M^2_{\mathrm{recoil}}(\pi^0\pi^0 J/\psi)$ which was large and positive. Leading from this it was hypothesised that these events could be complete ISR candidates, with extra particles from the background added to form a $\pi^0\pi^0 J/\psi$ candidate. So, the hypothesis that these events were J/ψ events produced directly via ISR, combined with background photons that were faking a pair of π^0 candidates was tested. To do this, the recoil mass squared of the J/ψ candidate, $M^2_{\mathrm{recoil}}(J/\psi)$, in these events was investigated and is shown in the left hand plot of Figure 4.21.[9] A clear peak at zero, consistent with the J/ψ particle being produced directly via ISR can be seen in this distribution. To remove these events, a selection of: $|M^2_{\mathrm{recoil}}(J/\psi)| > 2\,\mathrm{GeV}^2$, was required for $\pi^0\pi^0 J/\psi$ candidates.

The $M^2_{\mathrm{recoil}}(\pi^0\pi^0 J/\psi)$ distribution of candidates that failed the selection can be

[8] 3 GeV is greater than the energy of photons possible from B meson decays.
[9] M^2_{recoil} will refer to $M^2_{\mathrm{recoil}}(\pi^0\pi^0 J/\psi)$ unless specifically noted as $M^2_{\mathrm{recoil}}(J/\psi)$.

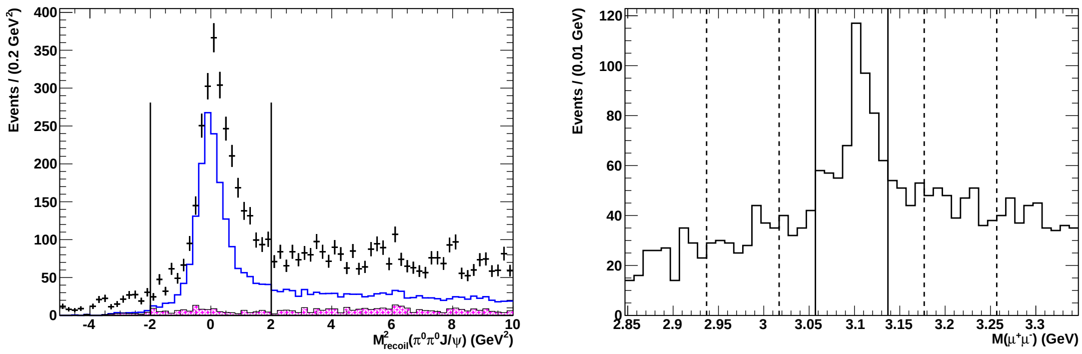

Figure 4.20: Left: J/ψ sideband-subtracted $M^2_{\mathrm{recoil}}(\pi^0\pi^0 J/\psi)$ distribution for di-muon $\psi(2S)$ candidates (data-points) compared with the prediction from $\psi(2S) \to \pi^0\pi^0 J/\psi$ MC (unshaded histogram) and the contamination from other $\psi(2S)$ decay modes as predicted by the $\psi(2S) \to generic$ MC (magenta shaded histogram). Right: the $M(\mu^+\mu^-)$ distribution of J/ψ candidates in events with $M^2_{\mathrm{recoil}}(\pi^0\pi^0 J/\psi) < -2\,\mathrm{GeV}^2$.

seen in the right hand side of Figure 4.21. As can be seen in the figure, events removed by this selection all occur with large negative $M^2_{\mathrm{recoil}}(\pi^0\pi^0 J/\psi)$. A sample of 434,000 ISR J/ψ MC events was produced to confirm the hypothesis and the $M^2_{\mathrm{recoil}}(J/\psi)$ and $M^2_{\mathrm{recoil}}(\pi^0\pi^0 J/\psi)$ of MC candidates that pass $\pi^0\pi^0 J/\psi$ selection (without the $M^2_{\mathrm{recoil}}(J/\psi)$ cut) is shown in Figure 4.22. The ISR J/ψ MC sample had a very low efficiency to be reconstructed as a $\pi^0\pi^0 J/\psi$ candidate. The events that survive are consistent with what is seen in data, within the large statistical errors for this sample. The events from the ISR J/ψ background were removed with the $M^2_{\mathrm{recoil}}(J/\psi)$ cut and the di-muon events that pass this selection used in the remainder of the analysis.

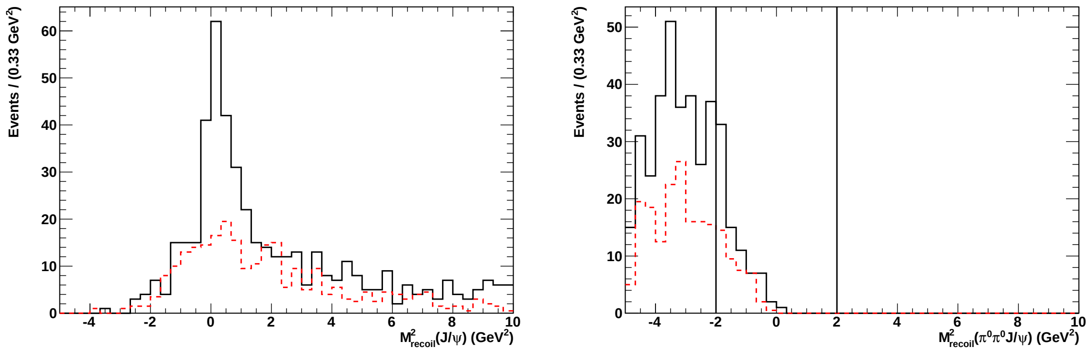

Figure 4.21: Left: $M^2_{\mathrm{recoil}}(J/\psi)$ distribution of di-muon $\psi(2S)$ candidates with $M^2_{\mathrm{recoil}}(\pi^0\pi^0 J/\psi) < -2\,\mathrm{GeV}^2$, for the J/ψ signal (solid lines) and side-band (dashed red lines) regions. Right: $M^2_{\mathrm{recoil}}(\pi^0\pi^0 J/\psi)$ distribution of candidates failing the $|M^2_{\mathrm{recoil}}(J/\psi)| > 2\,\mathrm{GeV}^2$ selection.

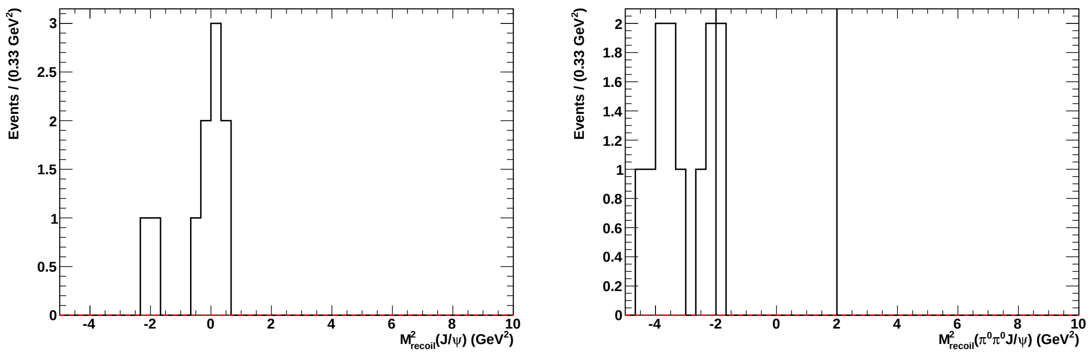

Figure 4.22: Left: $M^2_{\mathrm{recoil}}(J/\psi)$ distribution of di-muon $\psi(2S)$ candidates from ISR J/ψ MC with $M^2_{\mathrm{recoil}}(\pi^0\pi^0 J/\psi) < 2\,\mathrm{GeV}^2$. Right: $M^2_{\mathrm{recoil}}(\pi^0\pi^0 J/\psi)$ distribution of $\pi^0\pi^0 J/\psi$ candidates failing the $|M^2_{\mathrm{recoil}}(J/\psi)| > 2\,\mathrm{GeV}^2$ selection in ISR J/ψ MC.

4.7.2 Investigating the daughters of di-muon best candidates

The J/ψ and π^0 candidates that were daughters of the selected $\pi^0\pi^0 J/\psi$ best candidate in each event, were studied for the data and MC in the $\psi(2S)$ control sample. Di-muon events were selected from two data skims: the LM and Tau Skims (described in Section 2.5.3), which had different properties and backgrounds. Unlike in the di-electron sample, the fully reconstructed case with the ISR photon detected, passed the skim cuts and was available in the Tau Skim data (see Table 4.2 in Section 4.1.3).

The mass distribution of J/ψ candidates can be seen in Figure 4.23, for Tau Skim events on the left and LM Skim events on the right. Events that were common to both skims are shown in the Tau Skim plots in this section. The J/ψ mass peak is clearly visible in both samples and the peak in the Tau Skim data is larger, however, this sample also has a much larger non-J/ψ component. The scaled data from the J/ψ sidebands approximates the background from random track combinations under the J/ψ peak and the majority of the following plots show sideband-subtracted distributions.

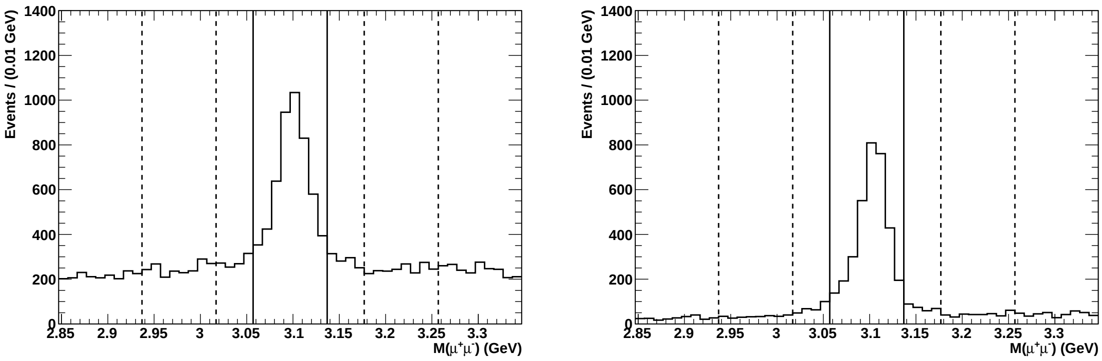

Figure 4.23: Invariant mass spectrum of J/ψ candidates after muon identification for $\psi(2S)$ best candidates. Left: Tau Skim. Right: LM Skim. The vertical lines indicates the J/ψ signal (solid) and sideband regions (dashed).

The mass of π^0 candidates in $\psi(2S)$ best candidates are shown in the top row of Figure 4.24, while the $|\cos(\theta_\gamma)|$ distribution of these candidates is shown in the bottom row. In the figure, events from the Tau Skim are shown in the left hand column, while events from the LM Skim are shown in the right hand column. In the LM Skim sample a large excess of events in data can be seen, compared to the prediction from $\psi(2S)$ MC. This excess is seen across the whole range of the $|\cos(\theta_\gamma)|$ plot, but also peaks near 0.9, consistent with a large contribution from fake π^0 candidates. The $\psi(2S)$ candidates that these J/ψ and π^0 candidates form will be discussed in the next section.

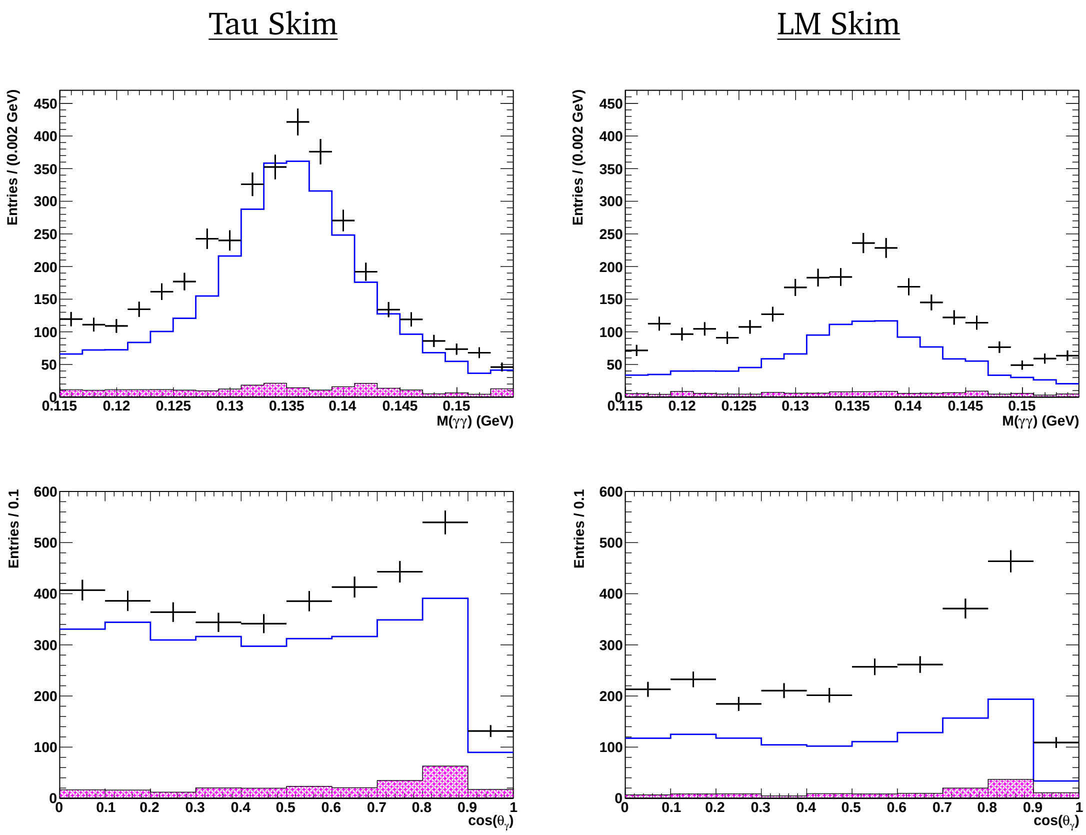

Figure 4.24: π^0 candidates in $\psi(2S)$ best candidates (two per event). Candidates from the Tau and LM Skim are shown on the left and right, respectively. Top row: invariant mass of π^0 candidates. Bottom row: $|\cos(\theta_\gamma)|$ of π^0 candidates. The J/ψ sideband-subtracted data (data points) is compared with the prediction from $\psi(2S)$ MC (unshaded histogram) including the contribution from other $\psi(2S)$ decay modes (magenta shaded histogram).

4.7.3 Di-muon $\psi(2S)$ best candidates

$\pi^0\pi^0 J/\psi$ best candidates were investigated using data and MC from the $\psi(2S)$ control sample. The J/ψ sideband-subtracted M^2_{recoil} and invariant mass distributions for $\psi(2S)$ best candidates is shown in Figure 4.25, for the events in Tau Skim in the left hand column and LM Skim events in the right hand column. Data and MC show reasonable agreement for Tau Skim candidates, except for the excess in data at high M^2_{recoil}, away from the signal region. However, the data and MC in the LM Skim sample do not agree and the $\psi(2S)$ peak in data is larger than the peak expected from MC.

From the π^0 mass and $|\cos(\theta_\gamma)|$ distributions for the candidates in the LM Skim (see previous section), there was a larger component of fake or broken π^0 candidates in these events than the MC was predicting. This analysis used a minimum photon energy requirement of 30 MeV, which was a lower cut than was used by the majority of analyses at Belle, where a minimum photon energy cut of 50 MeV or 100 MeV was common. The normal cut at Belle was used to exclude the large number of low energy photons from background processes and beam gas events, however, this cut would reject almost all of the $\pi^0\pi^0 J/\psi$ events produced via ISR. The events in the LM Skim, peak at the $\psi(2S)$ mass and occurred in real J/ψ events, therefore, they were most likely from $\psi(2S) \to J/\psi X$ events, where X is some other combination of particles. The M^2_{recoil} distribution in the LM Skim peaked at zero, so there was an ISR component. However, the tail of the M^2_{recoil} distribution was larger compared to the peak at zero in the LM Skim events, compared with Tau Skim events, so there may be contamination from other events.

The production angle of the $\psi(2S)$ candidates with respect to the beam line is shown in Figure 4.26. In the left hand plot, the Tau Skim sample shows good agreement across most of the range, however, there is an excess in the first bin, which corresponds to the extreme backward edge of the detector. In the right hand plot showing LM Skim events, only the first bin is occupied. The excess events in the di-muon sample occurred in both skims at the backward edge of the detector. The majority of analyses at Belle investigate B meson decays, which primarily decay into the barrel region of the detector and the tracking and π^0 efficiency at the edge of the detector is not as well understood. This, combined with the low energy photons used in this analysis, means that the MC may not be representing these events correctly. Because the events in this bin are almost aligned with the beam line, the ISR photon was lost in the majority of these events.

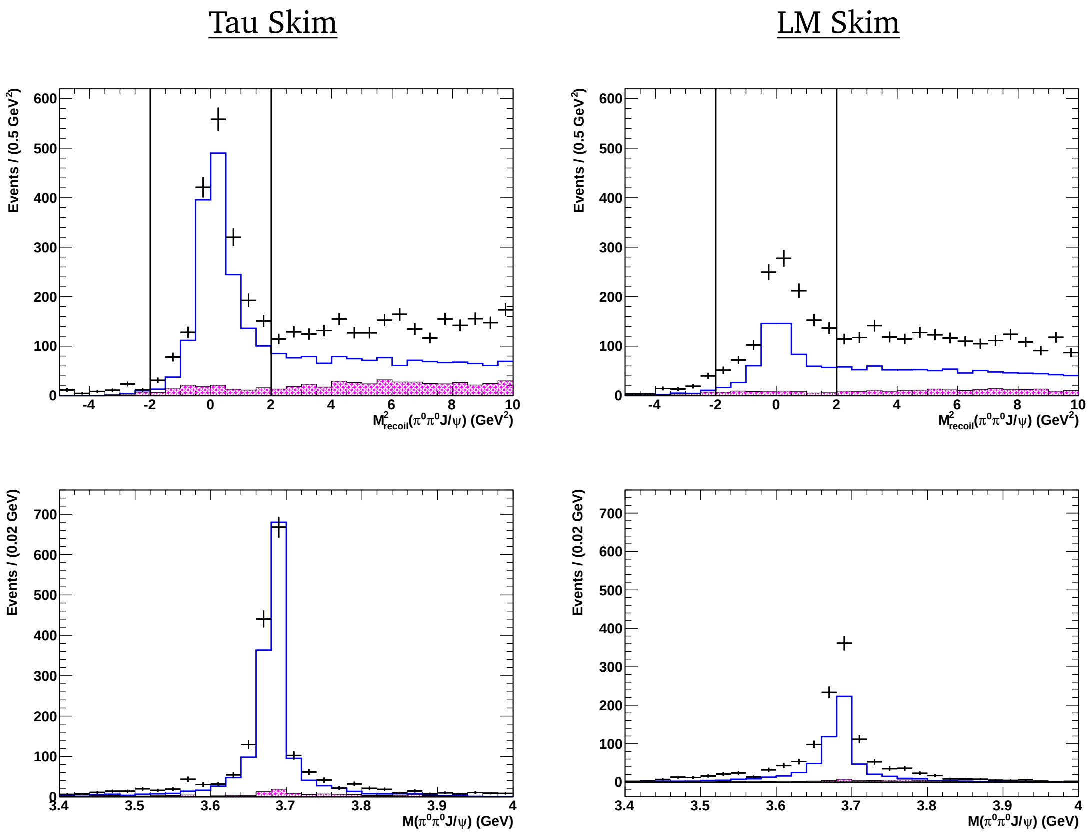

Figure 4.25: $M^2_{\rm recoil}$ and mass distribution of di-muon $\psi(2S)$ best candidates in the Tau and LM Skim are shown, on the left and right respectively. Top row: recoil mass squared. Bottom row: invariant mass. The J/ψ sideband-subtracted data (data points) are compared with the prediction from $\psi(2S)$ MC (unshaded histogram) including the contribution from other $\psi(2S)$ decay modes (magenta shaded histogram).

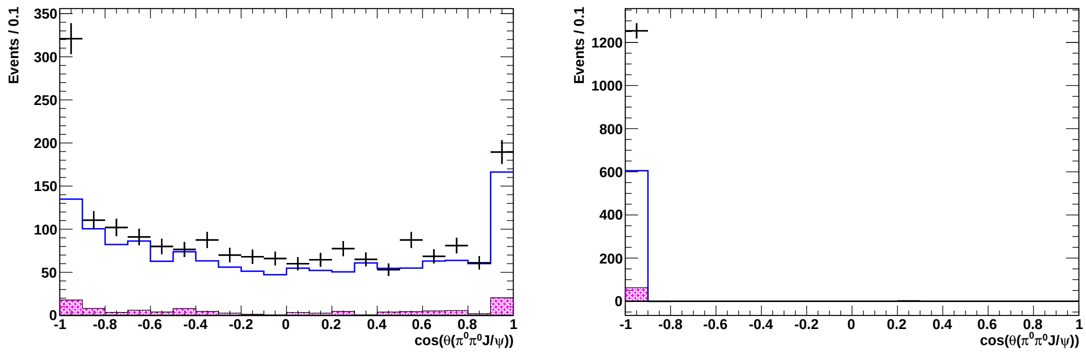

Figure 4.26: Production angle of $\psi(2S)$ best candidates. Left: Tau Skim. Right: LM Skim. The J/ψ sideband-subtracted data (data points) are compared with the prediction from $\psi(2S)$ MC (unshaded histogram) including the contribution from other $\psi(2S)$ decay modes (magenta shaded histogram). (Note the different vertical scales.)

4.7.4 Fully reconstructed events

In the previous sections the di-muon sample was investigated and these events showed a large excess of events in data at the extreme backwards end of the detector. In this section, the fraction of di-muon events that were fully reconstructed (with the ISR photon detected) is investigated and compared with the sample where the ISR photon was not reconstructed by the detector.

Fully reconstructed events only occurred in the di-muon sample in Tau Skim data. The production angle of all Tau Skim $\psi(2S)$ candidates is shown in the left hand plot of Figure 4.27 and the the production angle of the fully reconstructed subsample is shown in the right hand plot of the figure. The fully reconstructed $\psi(2S)$ events in data agree well with the prediction from MC and from signal MC (81 ± 3) % of Tau Skim $\psi(2S)$ events passing all selection criteria have an ISR photon reconstructed. High energy photons were easily identified in the detector and both fake and real J/ψ backgrounds in events with the ISR photon reconstructed were very small. However, in the sample without the ISR photon reconstructed, the expected $Y(4260)$ yield was found to be consistent with the size of the statistical uncertainty from event counts in each of the bins near 4.0 GeV. For this reason and because of the additional difficulties involved in understanding the efficiency and systematic uncertainties in the sample without the ISR photon detected, it was not expected to contribute significantly to the final result based purely in the fully reconstructed sample. To check this, the expected significance of the $Y(4260)$ sample was estimated after the selection criteria were optimised, as is discussed in Section 4.9.1. The fully reconstructed di-muon sample was chosen for the final result and was used in the remainder of this analysis.

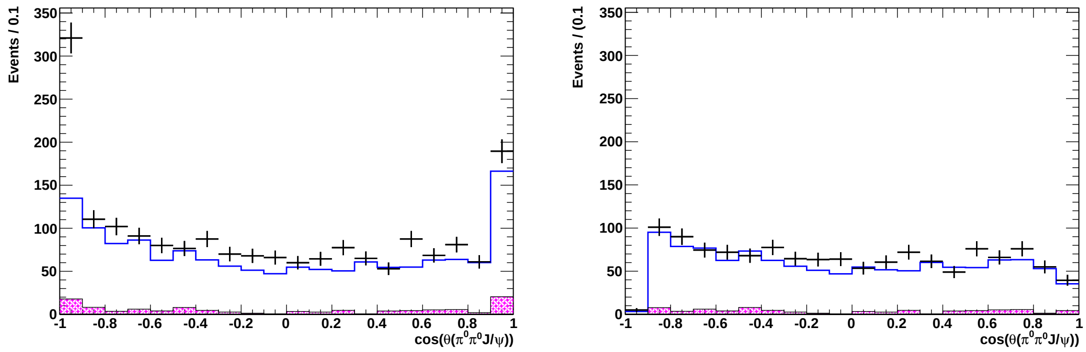

Figure 4.27: $\cos(\theta)$ distribution of J/ψ sideband-subtracted data (data points) from candidates in the $\psi(2S)$ region are compared with the prediction from $\psi(2S)$ MC (magenta shaded histogram). The left hand plot shows all Tau Skim events, while the right hand plot shows the Tau Skim events with ISR photon reconstructed.

4.8 Optimising selection

The selection criteria used up to this point to study the best candidate selection and $\psi(2S)$ control sample were not optimised. In this section, the optimisation of the selection cuts is discussed. Cuts were optimised to maximise the significance of a potential $Y(4260)$ signal and the method of estimating the potential significance is described in Section 4.8.1. Using this method, a scan of cut values was performed with the fully reconstructed di-muon sample, which is described in Section 4.8.2.

4.8.1 Estimating the potential $Y(4260)$ significance

To estimate the significance of a potential $Y(4260)$ signal with a given set of cuts, many toy MC samples were generated using data from the $\psi(2S)$ region and the mass region above the $Y(4260)$ and the $Y(4260)$ signal MC. These toy MC samples were then fitted with the shapes to be used in the fit to data and the significance of the $Y(4260)$ peak in each fit measured.

To produce toy MC, a fit was performed simultaneously to the data in the $\psi(2S)$ region and high mass region, $M(\pi^0\pi^0 J/\psi) \in [3.4, 4.0]$ GeV and $M(\pi^0\pi^0 J/\psi) \in [4.7, 6.0]$ GeV, respectively. The results of this fit were then interpolated to cover the blind region in data: $M(\pi^0\pi^0 J/\psi) \in [4.0, 4.7]$ GeV, so that the interpolated region formed the expected background under a potential $Y(4260)$ peak. In order to fit the $\psi(2S)$ peak in data, the fit shape was first found in MC. As the values of each selection cut changed, the total $\psi(2S)$ yield and the ratio of the correctly identified and the broken candidates changed, modifying the overall shape of the $\psi(2S)$ peak. MC $\psi(2S)$ mass distributions were divided according to the number of correctly identified π^0 photons in each selected $\psi(2S)$ candidate: an example of this division can be seen in Figure 4.8 in Section 4.3. The mass distributions of the correctly identified and the broken candidates were first fitted independently with shapes that were chosen to fit each $\psi(2S)$ component; fit shapes are summarised in Table 4.7. These shapes were then combined to form a function used to fit the $\psi(2S)$ peak in data. In the fit to data, the widths for each component were fixed to their values from the MC, while the ratios of events in each component were allowed to float. An exponential function with a threshold was included in the fit to account for a possible non-resonant contribution. The non-resonant function used was:

$$\frac{dN}{dm} = \sqrt{m - m_{min}} \times e^{c_{exp}(m - m_{min})}$$

where the shape parameter c_{exp} was floated in each fit and $m_{min} = m_{J/\psi} + 2m_{\pi^0}$. A fit is shown in Figure 4.28, indicating the $\psi(2S)$, high mass and interpolated mass regions.

Table 4.7: Shapes used to fit correctly identified and broken $\psi(2S)$ candidates in MC. The contribution from other $\psi(2S)$ decay modes, from the $\psi(2S) \to generic$ MC, is included in the "2 or less" category.

Number of correctly identified π^0 photons	Fitting shape
4	Narrow Gaussian
3	Bifurcated Gaussian plus second Gaussian
2 or less	Two wide Gaussians

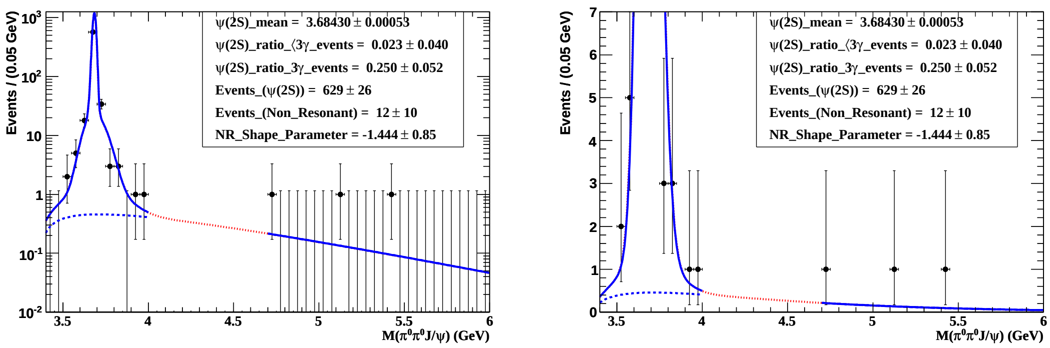

Figure 4.28: Fit to the $\psi(2S)$ and the mass region above 4.7 GeV in data. Left: log scale. Right: cut-off linear scale. The regions were fitted simultaneously, while $M(\pi^0\pi^0 J/\psi) \in [4.0, 4.7]$ GeV was blind and excluded from the fit. The fit was produced in 10 MeV bins and projected onto 50 MeV bins for display (data-points). The fit results (solid line) including the non-resonant term (dashed line) are shown with the projection of the fit function into the blind region (dotted red line).

In order to obtain a prediction for the $Y(4260)$ signal, the $Y(4260)$ MC was scaled to the luminosity in data assuming:

$$\frac{\mathcal{B}(Y(4260) \to \pi^0\pi^0 J/\psi)}{\mathcal{B}(Y(4260) \to \pi^+\pi^- J/\psi)} = \frac{1}{2},$$

which is the expectation from isospin considerations. Toy MC samples were generated for each set of cut values using the shape from the fit to data combined with the prediction from $Y(4260)$ MC.[10] Each of these sample were fitted using the combined shape and the significance of the $Y(4260)$ peak in each sample was calculated as:

$$\sqrt{-2\ln(\mathcal{L}/\mathcal{L}_0)},$$

where $\mathcal{L}$ is the maximum likelihood returned by the signal fit and $\mathcal{L}_0$ is the likelihood returned by a null fit with the $Y(4260)$ signal yield set to zero. The average of the significances found in each of the toy MC samples was then accepted as the expected significance for that set of cut values.

4.8.2 Cut scan using toy MC

A scan of the cut values used in the selection of $\pi^0\pi^0 J/\psi$ events was performed to optimise the expected significance of a possible $Y(4260)$ signal. Each cut was scanned independently with the values of the other selection criteria held constant and the selection cuts were iterated in order, with the updated value of each cut. For each value of the cut being investigated, the potential significance of the $Y(4260)$ signal was measured using the procedure detailed in Section 4.8.1. In this case, 500 toy MC samples were generated for each of the selected cut values and the cut value with the highest average significance, $\langle\sqrt{-2\ln(\mathcal{L}/\mathcal{L}_0)}\rangle$, for the $Y(4260)$ signal was then selected for the next iteration.

The results of the scan of selection cuts is shown in Table 4.8. The average significance measured in the fits to the toy MC samples was plotted for each cut variable, with the other selection cuts held at their final value, and is shown in Figure 4.29. For the finally selected point, the distribution of $\sqrt{-2\ln(\mathcal{L}/\mathcal{L}_0)}$ and the distribution of the $Y(4260)$ yields returned by the fits to the toy MC samples is

[10] The $Y(4260)$ MC was generated over the range 3.86 GeV to 4.66 GeV. The $Y(4260)$ MC was fitted with a Breit-Wigner over its generated range and the fitted Breit-Wigner shape was used to generate events over the whole range of the toy MC (3.4 GeV to 6.0 GeV). Approximately 6% of the $Y(4260)$ yield was in the tails outside the range the $Y(4260)$ MC was generated over.

shown in Figure 4.30, in the left and right hand plots, respectively. The average significance of the $Y(4260)$ in toy MC for the selected cut values was ≈ 3.2, with a large spread. The average $Y(4260)$ yield in these toy MC samples was ≈ 7.8 events, again with a large spread, while the yield input into the these toy MC samples was 7.9 events. The yield input to the toy MC and the mean of the $Y(4260)$ yields from the fits show good agreement. These optimised values of the selection cuts were used in the remainder of this analysis.

Table 4.8: Results of the selection criteria optimisation scan. E and M are the energy and mass of the measured particle respectively. m_{π^0} and $m_{J/\psi}$ are the nominal masses of the π^0 and J/ψ particles respectively [1]. $P_{\perp}^{ISR}$ is the momentum of the $\pi^0\pi^0 J/\psi$ candidate with respect to the direction of the ISR photon. Rows are in the stated units, except for the number of points in each scan, which is unitless.

Selection	Scan points	Start	End	Result	Units
$E(\gamma)\ >$	12	25	80	35	MeV
$\lvert M(\gamma\gamma) - m_{\pi^0}\rvert\ <$	5	10	30	15	MeV
$P_{\perp}^{ISR}\ <$	4	50	200	50	MeV
$\lvert M(\mu^+\mu^-) - m_{J/\psi}\rvert\ <$	5	20	40	25	MeV
$\lvert M^2_{\text{recoil}}\rvert\ <$	16	1.0	2.5	1.2	GeV^2

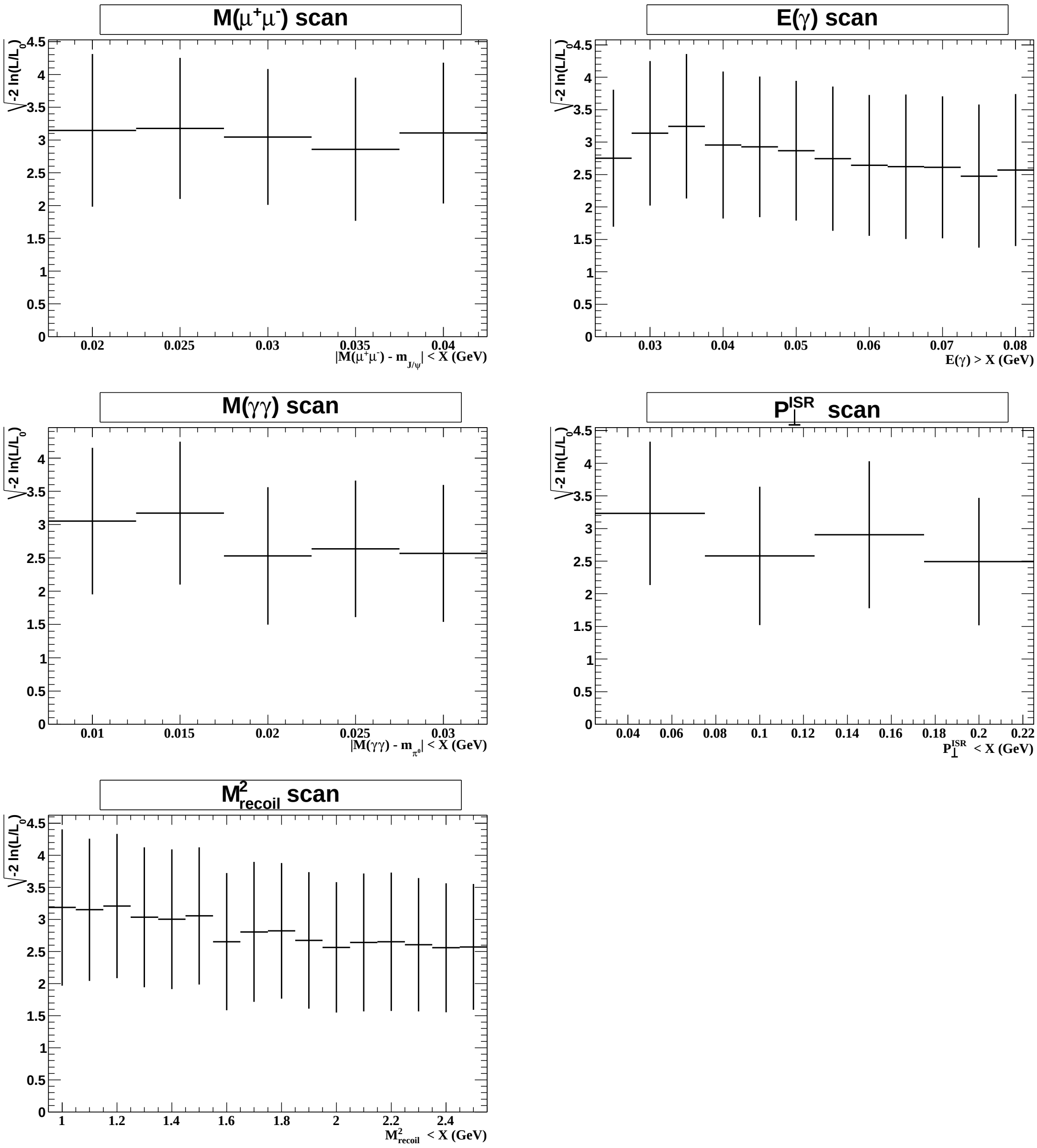

Figure 4.29: The average of the significance of the $Y(4260)$ in fits to toy MC (uncertainties are root mean square). Top row: $M(\mu^+\mu^-)$ cut, left, and π^0 photon energy cut, right. Middle row: $M(\gamma\gamma)$ cut, left, and $P_\perp^{ISR}$ cut, right. Bottom left: recoil mass squared cut.

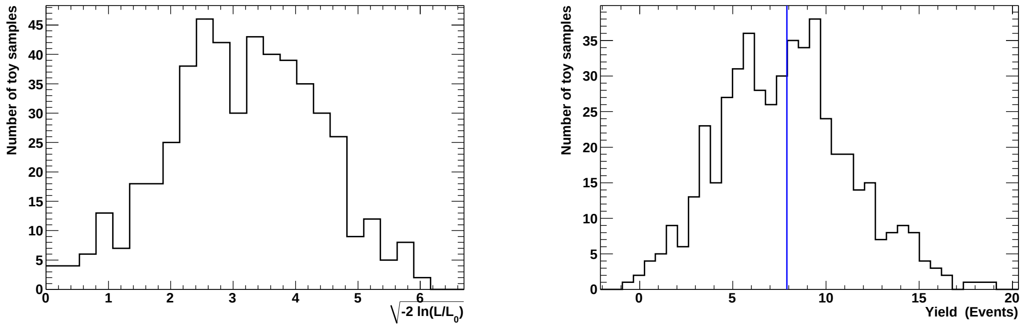

Figure 4.30: Left: distribution of the significance of the expected $Y(4260)$ signal for the final selected cut values. Right: distribution of the yields of the expected $Y(4260)$ signal in fits to toy MC for the final selected cut values. The vertical line indicates input yield used in the toy MC generation.

4.9 $\psi(2S)$ control sample with optimised cuts

Data in the $\psi(2S)$ control region was compared with MC after the selection criteria were optimised. The selection variables are shown in Figure 4.31, with the cut in each selection variable relaxed in its plot and the cuts in the other variables held at their final values. The data and MC distributions for $\psi(2S)$ events show good agreement, with few discrepancies in most plots. The greatest differences between data and MC occur in the $M(\mu^+\mu^-)$ and $M(\gamma\gamma)$ plots, in the top left and middle left positions in the figure, respectively. The $M(\mu^+\mu^-)$ distribution in MC appears to be slightly narrower than in data, with MC higher than data in the central bins and slightly lower than data in many of the bins forming the slope of the distribution. In the $M(\gamma\gamma)$ plot, the data has a small overabundance when compared to MC on the low energy slope of the distribution. These two differences between data and MC are not significant compared with the expected number of events above 4.0 GeV. The final selected cut values passed the majority of the correctly identified candidates and significantly reduced the number of broken candidates. With the optimised selection cuts, the simultaneous fit to the $\psi(2S)$ and high mass regions (shown previously in Figure 4.28 in Section 4.8.1) returned 629 ± 25 $\psi(2S)$ events, while MC predicted 635 ± 12 events (statistical uncertainty only). This yields a Γ_{ee} value of 2.33 ± 0.10 keV, *cf.* 2.35 ± 0.04 keV [1].

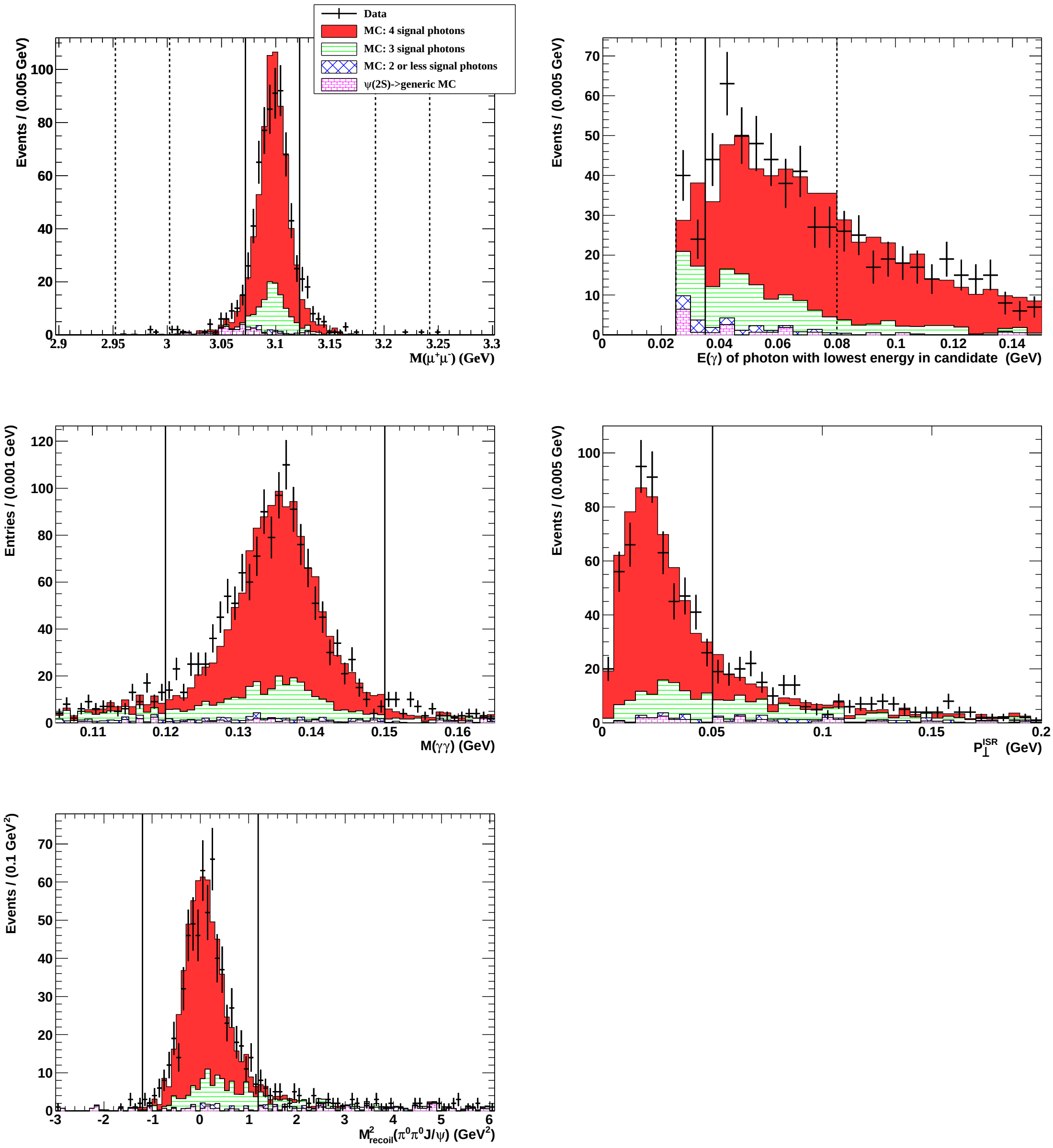

Figure 4.31: Distribution of selection variables for the $\psi(2S)$ control sample. Top row: $M(\mu^+\mu^-)$, left, and the π^0 photon with the lowest energy in each candidate, right. Middle row: $M(\gamma\gamma)$, left, and $P_{\perp}^{ISR}$, right. Bottom left: recoil mass squared. For events in data (data points) and MC. MC events are placed according to the number of correctly identified signal photons in the best candidate: all four photons correct (solid red histogram), three correct (green horizontally lined histogram), two or less correct (blue diagonally hatched histogram) and $\psi(2S) \rightarrow generic$ MC (magenta patterned histogram). Solid lines indicate the final selection cuts. Dashed lines indicate the J/ψ sidebands in the J/ψ mass plot and the range of the cut scan in the photon energy plot.

4.9.1 Sample without ISR photon reconstructed

To confirm that the sample without the ISR photon detected would not contribute to the final result, these events were re-investigated after the selection criteria were optimised and before the data in the $Y(4260)$ region was unblinded.

The invariant mass distribution of $\pi^0\pi^0 J/\psi$ candidates in this sample is shown in Figure 4.32. The expected number of $Y(4260)$ events in this sample was ≈ 3, which is consistent with the size of the statistical fluctuations on each bin in this data. The significance of a potential $Y(4260)$ peak in this sample was estimated using the procedure described in Section 4.8.1, using 200 toy MC samples. The distribution of $\sqrt{-2\ln(\mathcal{L}/\mathcal{L}_{0)}}$ for the $Y(4260)$ term in fits to the toy MC samples is shown in the left hand plot of Figure 4.33. The average value of $\sqrt{-2\ln(\mathcal{L}/\mathcal{L}_{0)}}$ produced by this method was 0.1, which can be compared to 3.2, the average significance of the $Y(4260)$ term in fits to toy MC samples from the fully reconstructed sample (Section 4.8.2). An example fit which returned the mean significance is shown in the right hand plot of Figure 4.33. In the example fit, the $Y(4260)$ yield returned by the fit is 1.0 ± 7.6 events. The addition of this sample was not expected to contribute to the expected result in the fully reconstructed sample and it was not included.

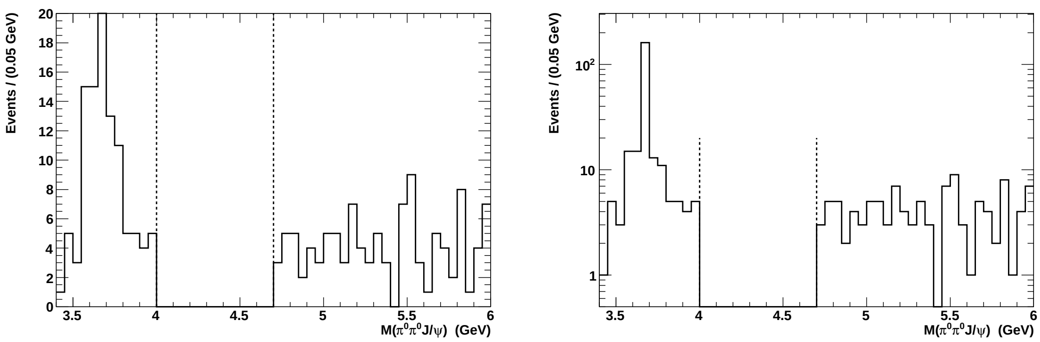

Figure 4.32: Di-muon $\pi^0\pi^0 J/\psi$ candidates without ISR photon detected. Left: cut-off linear scale. Right: log scale. Vertical lines indicate the blinded region.

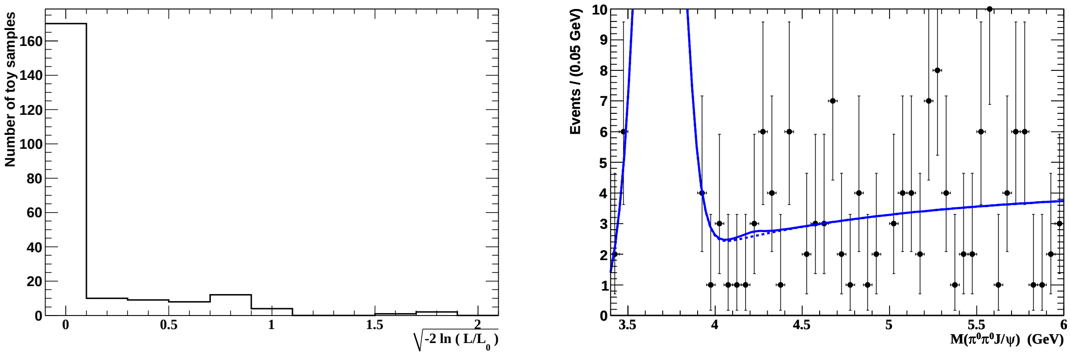

Figure 4.33: Left: $\sqrt{-2\ln(\mathcal{L}/\mathcal{L}_0)}$ of the $Y(4260)$ signal in fits to toy MC samples generated using the method of Section 4.8 for the sample without ISR photon reconstructed. Right: an example fit to a toy MC sample.

4.10 Systematic checks

The sources of systematic uncertainty on the efficiency and yield measurement were estimated, before the data in the blind region was analysed. MC predicted a small number of events and the uncertainty on the result was expected to be limited by statistical uncertainty. It is unknown which resonances may have decay modes that could affect the mass region of interest, therefore there was no generic ISR MC to study, however there were sidebands available; the J/ψ sidebands showed no obvious features. Because of the small size of the expected signal, the linearity of the fit function was checked (Section 4.10.1). The uncertainty on the J/ψ and π^0 branching fractions also contributes to the total uncertainty on these measurements (Section 4.10.2). There are several sources of systematic error that are well known and studied at Belle: these are discussed in Section 4.10.3. In addition to these sources of uncertainty, the effect of varying cuts was studied with the $\psi(2S)$ control sample (Section 4.10.4). The $Y(4260)$ yield was expected to be small, so the mass and width of the $Y(4260)$ fit function was fixed from MC in the final fit. Toy MC was generated with different shapes to check the effect that fitting with an incorrect mass and width would have on the $Y(4260)$ yield measurement (Section 4.10.5). At this time, the effect of varying the broken candidate ratios in $Y(4260)$ MC was also checked. These systematic uncertainties are summarised in Section 4.10.6.

4.10.1 Linearity of fit function

The linearity of the fit function was checked using the toy MC procedure used when optimising the selection criteria, which is described in Section 4.8. 2000 toy MC samples were generated for each of a range of input $Y(4260)$ yields and then fitted. The input yield was subtracted from the average of the fitted yields for each input and the results are shown in Figure 4.34. As can be seen in the figure, there is no bias on the fitted yield over the range near the expected yield of the $Y(4260)$ and the average of the fitted yields is near the expected $Y(4260)$ yield. At very small yields, there is a bias towards recording negative numbers, in this range the resultant size of a $Y(4260)$ peak would be too small to measure with any significance.

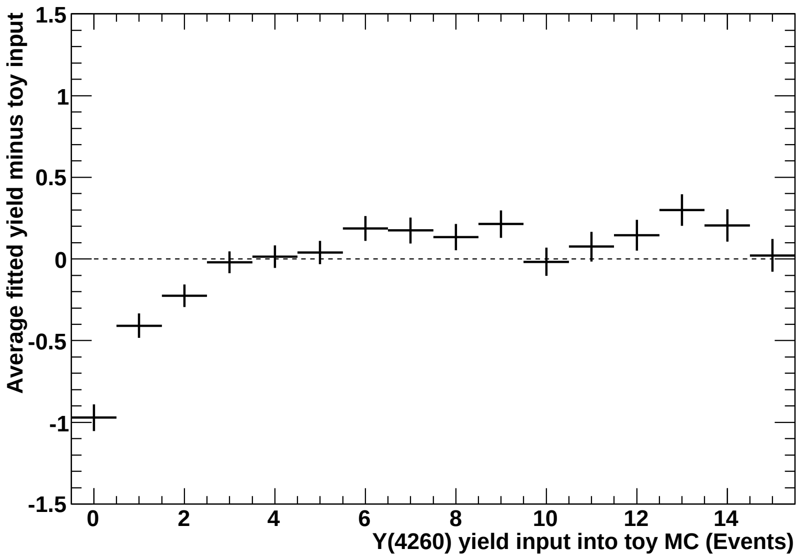

Figure 4.34: Average fitted $Y(4260)$ yield from toy MC fits minus input yield. Each point represents the average fitted yield in 2000 toy MC samples.

4.10.2 Uncertainty on branching fractions

From the PDG [1]: $\mathcal{B}(J/\psi \to \mu^+\mu^-) = (5.93 \pm 0.06) \times 10^{-2}$, therefore the uncertainty on this branching fraction is 1%. $\mathcal{B}(\pi^0 \to \gamma\gamma) = (98.823 \pm 0.034) \times 10^{-2}$, therefore the uncertainty on this branching fraction is 0.03% per π^0.

4.10.3 Well known systematics from Belle

There are several well known sources of systematic uncertainty that apply to many analyses at Belle. Because of this, they have been studied independently and the results have been made available to other collaborators. The systematics that are relevant to this analysis are: the uncertainty on the luminosity at Belle and the uncertainties from PID, tracking and the trigger at Belle.

Uncertainty of Belle Luminosity

The Belle collaboration has estimated the uncertainty on the luminosity to be 1.4% [111]. This was estimated by measuring the rate of Bhabha events in the detector and the main source of this uncertainty was from the accuracy of the MC generator simulating this process.

Uncertainty of the muon identification

The systematic error from the muon identification was estimated using collaboration software which was run over the $Y(4260)$ signal MC.[11] The result obtained was that the total efficiency correction applied to MC was: $(95.0 \pm 2.6)\%$, which provides a systematic uncertainty on the efficiency of 2.7%. (The MC used in this analysis has had this correction applied throughout this chapter.)

Uncertainty from tracking

The uncertainty on the efficiency of the tracking at Belle has been measured in previous studies (see Refs [113, 114], available to members of the Belle collaboration only). In these studies, the systematic uncertainty on the efficiency of the tracking was found to be 1% per track, which was added linearly for the two muon tracks in this analysis, giving a total uncertainty of 2%.

Uncertainty from the trigger

The trigger simulation software (`tsim`) was run over the same MC samples with two different settings: firstly, with inputs set manually, and secondly, with inputs set using the recommended package `tsimskin`, as discussed in Appendix B. The

[11] The software used was: `lid_syst_09.h`, which is described in Ref. [112].

largest differences between the trigger efficiency in each case was 2.8%, which was taken as the systematic uncertainty from the trigger.

4.10.4 The effect of varying cuts on the yield

The ratio of events in data and MC was produced for the $\psi(2S)$ control sample using the fitted yield from data and the event counts from MC, in order to test the effect of varying cuts on the predicted $Y(4260)$ yield. This ratio was made for the points scanned in the optimisation study and the difference from unity for each cut can be seen in Figure 4.35. As can be seen in the figure, the ratio of events measured in data and predicted by MC are consistent with unity. The largest positive and negative deviations are $+3.2\%$ in the plot made by varying the π^0 mass selection and -2.8% in the plot made by varying the M^2_{recoil} cut, respectively. These values were taken as the systematic errors on the cut selection.

4.10.5 Effect of varying $Y(4260)$ MC input shape on the yield

The $Y(4260)$ yield was expected to be small, so the mass and width of the $Y(4260)$ fit function was fixed to the shape predicted from MC. The fit function was shown to return the correct normalisation when measuring toy MC generated with the same input function (Section 4.10.1), however, if the underlying shape in data is different this procedure will not be correct.

Toy MC was generated with different underlying shapes for the $Y(4260)$ and fitted with the unchanged fit function, using a similar procedure to that described in Section 4.8.1. Three alterations to the input shape were attempted:

1. The mean of the input Breit-Wigner distribution was altered by the uncertainty on this value from the PDG: $+8$ MeV and -9 MeV [1].

2. The width of the input Breit-Wigner distribution was altered by the uncertainty on this value from the PDG: $+14$ MeV and -14 MeV [1].

3. The distribution was generated both with no broken candidates and with double the ratio of broken candidates.

50,000 toy MC samples were generated for each alteration to the input distribution, with an input of 7.9 $Y(4260)$ events (the prediction from MC). The difference between the averages from these toy samples and the unaltered sample can be seen in Table 4.9. The dominant effect was generated by varying the width of the underlying $Y(4260)$ peak. When the width was reduced, the peak was tightened and the fit overestimated the overall size of the peak. Correspondingly, when the peak was widened, the fit underestimated the overall size of the peak. The sum in quadrature of the positive and negative variations in the yield was taken as the systematic uncertainty from the fixing of the $Y(4260)$ shape parameters.

Table 4.9: Variation of the fitted $Y(4260)$ yield resulting from different input MC shapes. Left: the deviation from 7.9 events on the average of 50000 fitted yields, generated with a variation to the underlying $Y(4260)$ input shape. Right: the percentage uncertainty from this deviation. The error on the entries in this table are ± 0.03 ($\pm 0.3\%$) for the left (right) column.

Variation	Effect on yield		Percentage error	
Mean $+8$ MeV		-0.01	$+0.1$	
Mean -9 MeV		-0.08	$+1.0$	
Width $+14$ MeV		-0.42	$+5.4$	
Width -14 MeV	$+0.45$			-5.7
No broken candidates	$+0.03$			-0.4
Double the ratio of broken candidates		-0.04	$+0.4$	
Sum in quadrature	$+0.45$	-0.43	$+5.5$	-5.7

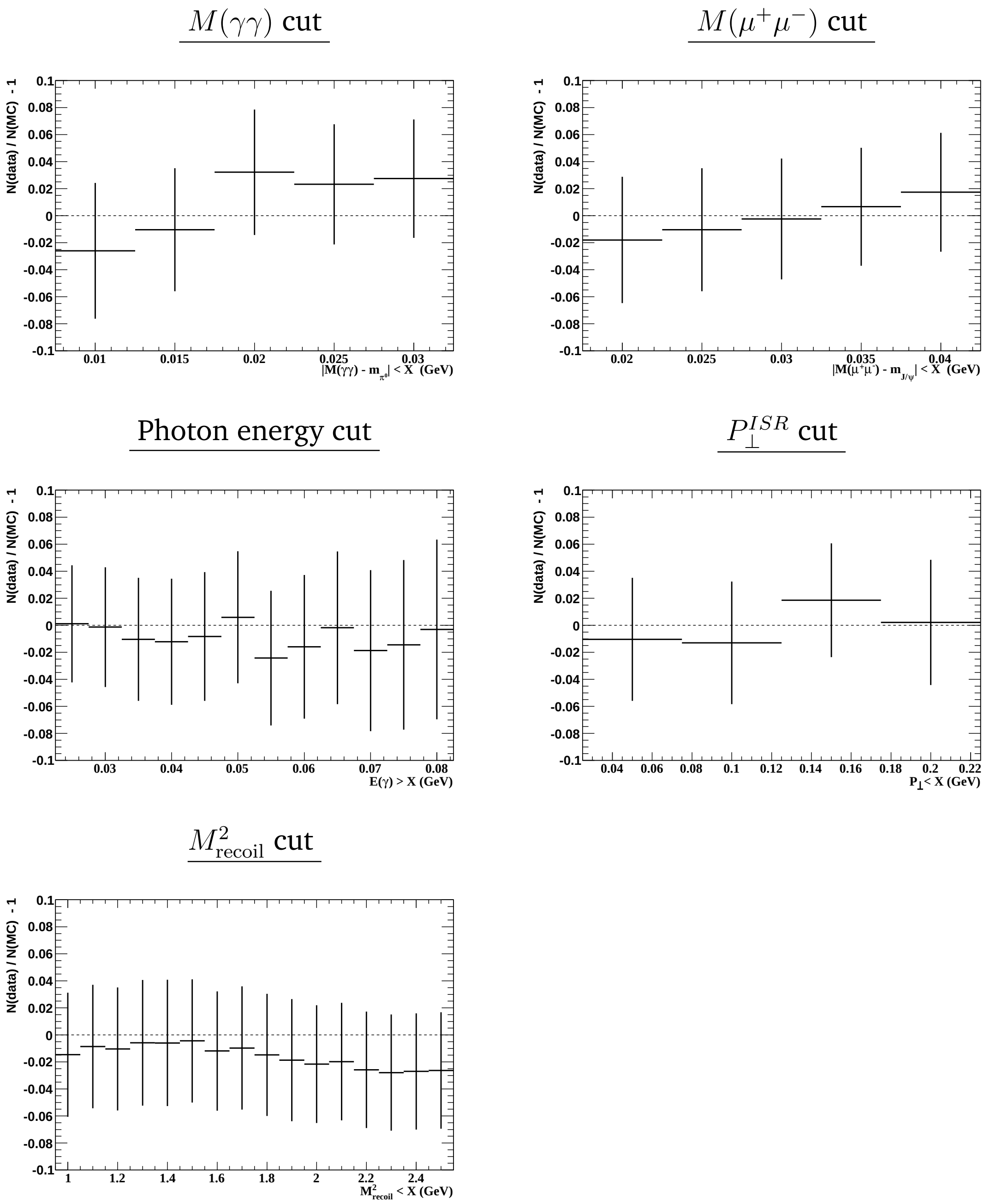

Figure 4.35: The ratio of events measured in data and predicted in MC for the $\psi(2S)$ control sample, subtracted from unity. Ratios are produced at selected points for the following selection criteria: Top left: π^0 mass cut. Top right: J/ψ cut. Middle left: minimum π^0 photon energy cut. Middle right: $P_\perp^{ISR}$ cut. Bottom left: M^2_{recoil} cut.

4.10.6 Summary of systematic uncertainties

A summary of the systematic uncertainties on the efficiency for $\gamma_{ISR}\pi^0\pi^0 J/\psi$ events and the expected $Y(4260)$ yield is shown in Table 4.10. The total expected systematic error is small when compared with the mean expected statistical error of 44%. In addition to these uncertainties, the effect on the $Y(4260)$ yield from fixing the shape of the fit function in the fit to data was measured and will be applied to the results in Section 5.3.

Table 4.10: Summary of systematic uncertainties.

Source	Error on yield (%)	
Luminosity	± 1.4	
Branching Fractions	± 1.0	
MuID	± 2.7	
Tracking	± 2.0	
Trigger	± 2.8	
Cut selection	$+3.2$	-2.8
$Y(4260)$ fit function	$+5.5$	-5.7
Sum in quadrature	$+7.9$	-7.9

4.11 Conclusion

Reconstruction techniques have been finalised in the $\pi^0\pi^0 J/\psi$ decay mode. The Belle datasets with the highest efficiency for signal were identified and studied. A $\pi^0\pi^0 J/\psi$ best candidate selection was implemented using the π^0 decay angle. Best candidates in the data and MC in the $\psi(2S)$ control sample were analysed and it was determined that events without the ISR photon reconstructed would not contribute significantly to the expected signal in the fully reconstructed di-muon subsample, which was chosen for the final result. Unfortunately, the fully reconstructed di-electron events did not pass data skim selection. In addition to the reconstruction of the ISR photon, the candidates were required to have a combined four-momentum consistent with production via ISR. The selection criteria were optimised for a potential $Y(4260)$ signal using a scan of selection cut values, before the consistency between the data and MC was checked in the $\psi(2S)$ control sample. From the MC it is expected that the fraction of mis-reconstructed events will be small. Finally, the systematic uncertainties were measured and found to be small compared to the expected statistical uncertainty on this result. After the analysis described in this chapter was finalised, the events in the $Y(4260)$ mass region were unblinded and studied, as will be discussed in the next chapter.

Chapter 5

$\pi^0\pi^0 J/\psi$ events near 4.26 GeV

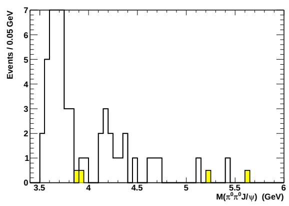

In this chapter, the $\pi^0\pi^0 J/\psi$ events in the $Y(4260)$ mass region are unblinded. An $e^+e^- \rightarrow \pi^0\pi^0 J/\psi$ cross-section as a function of mass is produced. The size of a possible $Y(4260)$ signal yield is measured and some properties of events in a cluster near 4260 MeV are presented.

THIS chapter relates the results of a search for $\pi^0\pi^0 J/\psi$ events produced via ISR, in Belle data. After the reconstruction and selection were finalised in the previous chapter, the events in the $Y(4260)$ mass region were unblinded. A small cluster of events near 4260 MeV was observed, with low background either side of the cluster. Section 5.1 details the $\pi^0\pi^0 J/\psi$ mass spectrum found, as well as the distributions of the selection variables for these events and the mass of the combinations of daughter particles. Using the events above 4.0 GeV, a cross-section as a function of mass was produced, which is presented in Section 5.2. The mass spectrum was fitted using shapes derived from the studies of the $\pi^+\pi^- J/\psi$ decay mode, which is detailed in Section 5.3, before this chapter is concluded. The results of this analysis were originally made public at the International Europhysics Conference on High Energy Physics EPS-HEP (Grenoble), during the Northern Hemisphere Summer of 2011.

5.1 Events in the unblinded region

The $M(\pi^0\pi^0 J/\psi)$ spectrum from events in the J/ψ signal region can be seen in Figure 5.1. In the top plot of the figure, in 10 MeV bins, the $\psi(2S)$ peak is clearly visible. The bottom plot of the figure shows this data in 50 MeV bins and also shows the data from the scaled J/ψ sidebands. A cluster of events near 4.26 GeV can be seen in these plots and the background is very low. This data was fitted, as will be discussed in Section 5.3. The selection variables for events in the region above 4.0 GeV are shown in Section 5.1.1 and the mass of the daughter combinations: $M(\pi^0\pi^0)$ and $M(\pi^0 J/\psi)$ are shown in Section 5.1.2, where the masses of these candidates and their daughter combinations are then tabulated.

5.1.1 Selection variables in events above 4.0 GeV

The distribution of each selection variable is shown in Figures 5.2 and 5.3, for events in data above 4.0 GeV. In these plots, the cut in the plot variable was loosened, while the other cuts were held at their final value.

In the top left plot of Figure 5.2, the $M(\mu^+\mu^-)$ plot is shown with the J/ψ signal and sideband regions indicated. In the remaining plots, the events from the J/ψ signal and scaled sideband regions are indicated by the unshaded and shaded histograms, respectively. The peak at the nominal J/ψ mass value indicates that these are events with a real J/ψ particle. In the top right plot, the value returned by the muon identification software (MuID) for the two J/ψ tracks per event is shown. Only one track was required to have MuID above 0.9 in each event and the majority of the tracks pass this cut, as can be seen in the plot. In the bottom left plot of the figure, the energies of the four π^0 photons per event can be seen. With the loosened selection, very few photons fall below the $E(\gamma) > 30$ MeV cut. The $M(\gamma\gamma)$ distribution is shown in the bottom right plot of the figure, where a clear peak at the nominal π^0 mass is seen.

In the top left plot of Figure 5.3, the energy of the photon with the largest energy in each event is shown, selected as the ISR photon. ISR photons have a range of energies, due to the changing mass of the $\pi^0\pi^0 J/\psi$ candidates; for a given $\pi^0\pi^0 J/\psi$ mass, the energy of the ISR photon is fixed in the CM frame as ISR production is a two-body process. In the top right of the figure, the recoil mass squared plot is shown. In these events M^2_{recoil} peaked near zero, consistent with the mass of the ISR photon recoiling against the $\pi^0\pi^0 J/\psi$ candidate. In the bottom left plot of the figure, the momentum of the $\pi^0\pi^0 J/\psi$ candidate perpendicular to the direction of the ISR photon is shown, which peaks close to zero, as the ISR photon and the $\pi^0\pi^0 J/\psi$ candidate decay back to back in the CM frame.

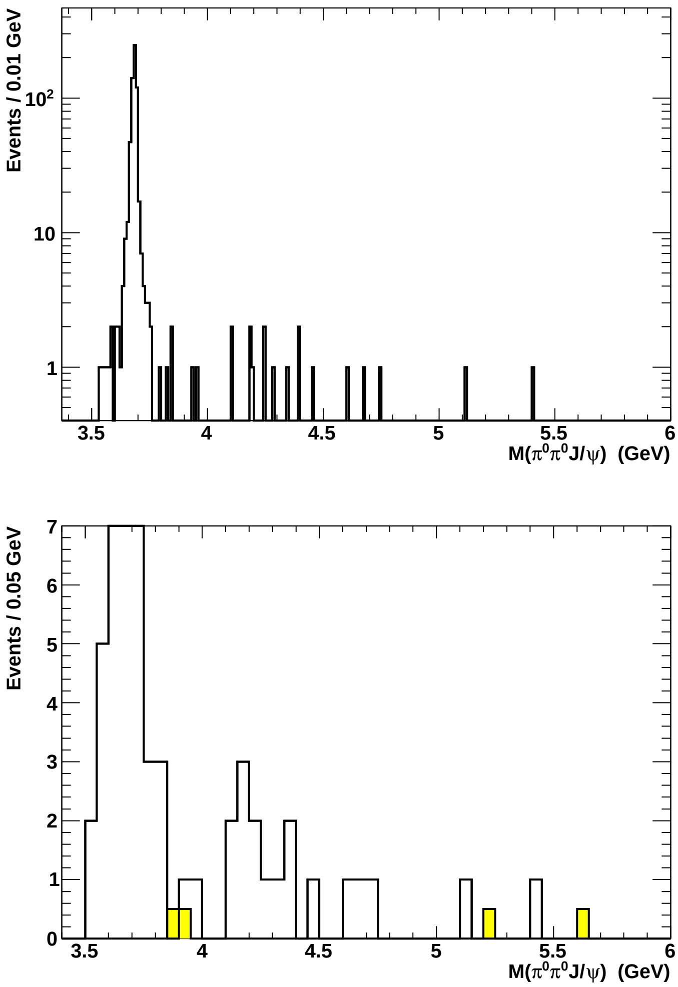

Figure 5.1: $M(\pi^0\pi^0 J/\psi)$ spectrum in data. Top: data from the J/ψ signal region in log scale with 10 MeV bins. Bottom: data from the J/ψ signal (unshaded histogram) and sideband (yellow shaded histogram) regions in cut-off linear scale with 50 MeV bins.

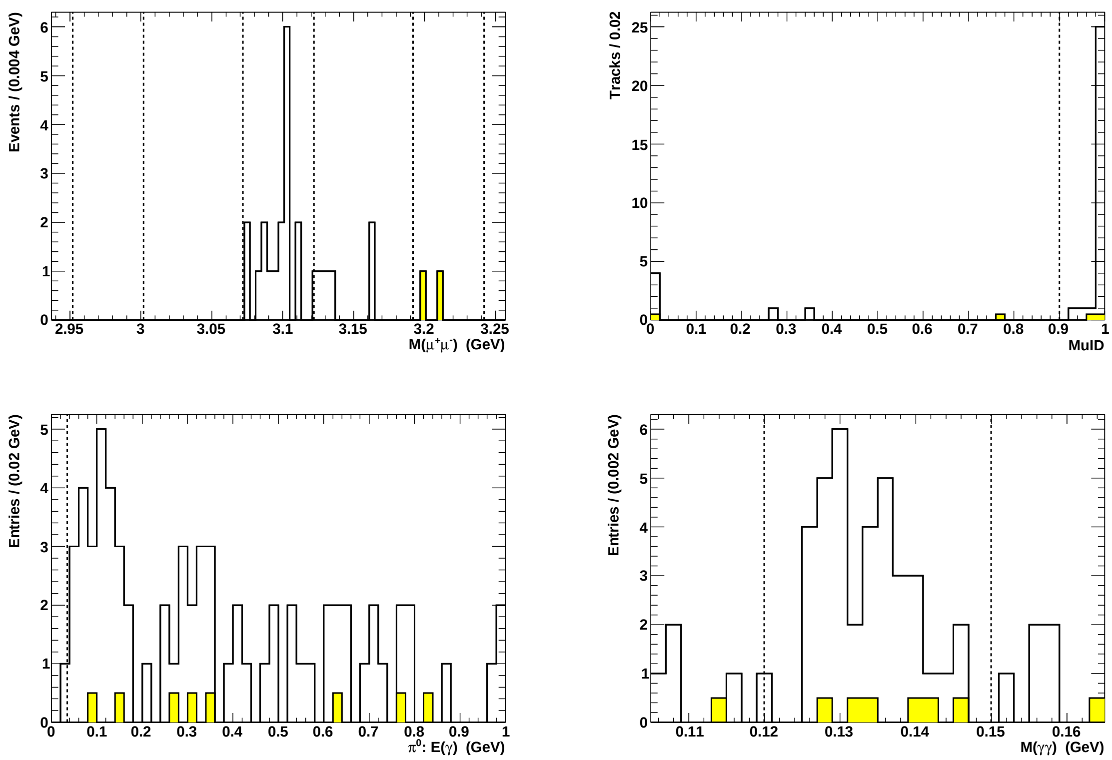

Figure 5.2: Selection variables in events above 4.0 GeV (set 1). Top left: $M(\mu^+\mu^-)$. Top right: MuID. Bottom left: energy of the π^0 photons. Bottom right: $M(\gamma\gamma)$. Events from the J/ψ sidebands are scaled and shaded yellow. The cuts for each selection are indicated by the vertical lines.

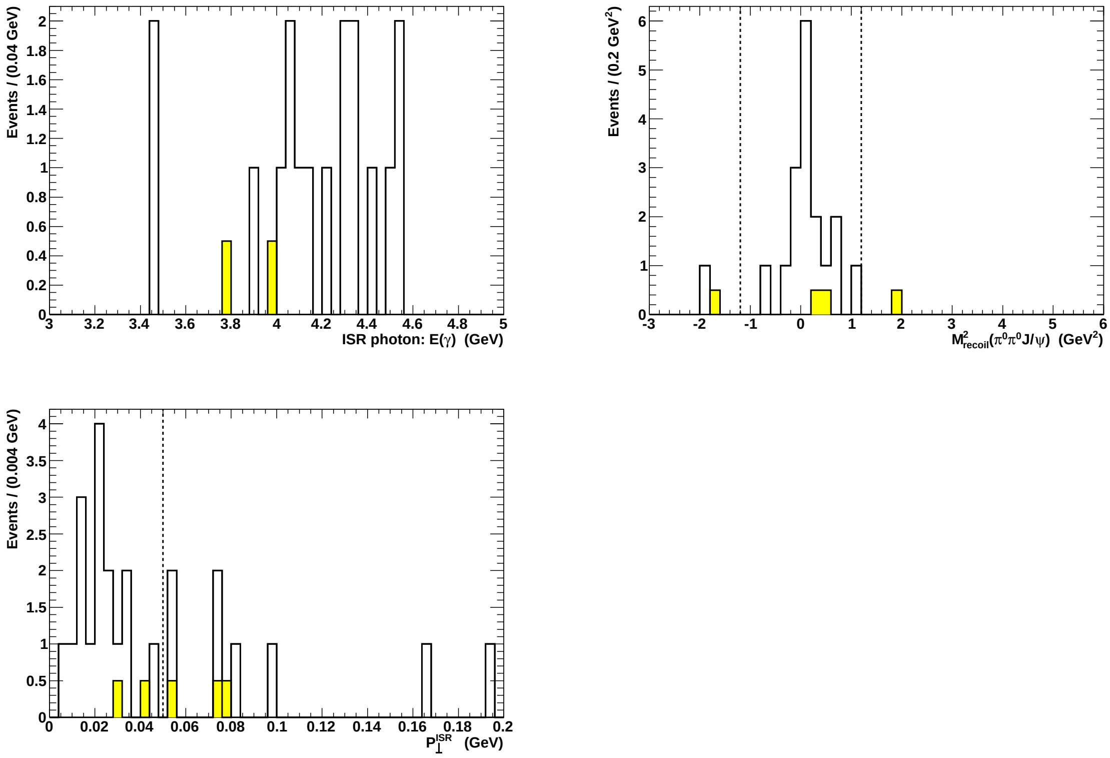

Figure 5.3: Selection variables in events above 4.0 GeV (set 2). Top left: energy of the ISR photon. Top right: recoil mass squared of the $\pi^0\pi^0 J/\psi$ candidate. Bottom left: $P_\perp^{ISR}$. Events from the J/ψ sidebands are scaled and shaded yellow. The selection cuts for the $P_\perp^{ISR}$ and M^2_{recoil} variables are indicated by the vertical lines.

5.1.2 Mass of daughter combinations

The invariant mass distribution of the combinations of daughter pairs of the $Y(4260)$ is not determined from the primary quantum numbers (J^{PC}) and hence is of theoretical interest. In this section, the distributions of $M(\pi^0\pi^0)$ and $M(\pi^0 J/\psi)$ are measured, for the cluster of events near 4.26 GeV.

In the $\pi^+\pi^- J/\psi$ mode, the di-pion distribution was shown to be inconsistent with phase space, as can be seen in the right hand plot of Figure 5.4, where the distribution of $M(\pi^+\pi^-)$ from the published Belle analysis [29] is shown. In the plot, the events with $M(\pi^+\pi^-\ell^+\ell^-) \in [4.2, 4.4]$ are compared with signal MC in which the π^+ and π^- were allowed to decay according to phase space. This distribution was checked to see if the $Y(4260)$ may be decaying to $\pi\pi J/\psi$ via intermediate resonances, for example: the authors of Ref. [64] proposed a $(\chi_c\rho^0)$ molecule structure for the $Y(4260)$. They suggest that the enhancement at high mass in $M(\pi^+\pi^-)$ seen by Belle and *BABAR* may be due to the $Y(4260)$ decaying via an intermediate ρ^0 resonance. The corresponding distribution in this case is the $M(\pi^0\pi^0)$ distribution, which was plotted and is shown in the left hand plot of Figure 5.4, for events in the J/ψ signal region, in the mass range $M(\pi^0\pi^0 J/\psi) \in [4.1, 4.4]$ GeV. This plots has six bins in the range between the two thresholds: $2m_{\pi^0} = 0.270$ GeV and $4.400 - m_{J/\psi} = 1.303$ GeV. The events from the J/ψ signal region are at face value consistent with the distribution observed in the charged pion mode, but there are very few events. No events from the J/ψ sidebands fall in the range $M(\pi^0\pi^0 J/\psi) \in [4.1, 4.4]$ GeV, in the plot, events from the J/ψ sidebands in the whole mass range ($M(\pi^0\pi^0 J/\psi) \in [3.4, 6.0]$ GeV) are displayed instead and show no structure.

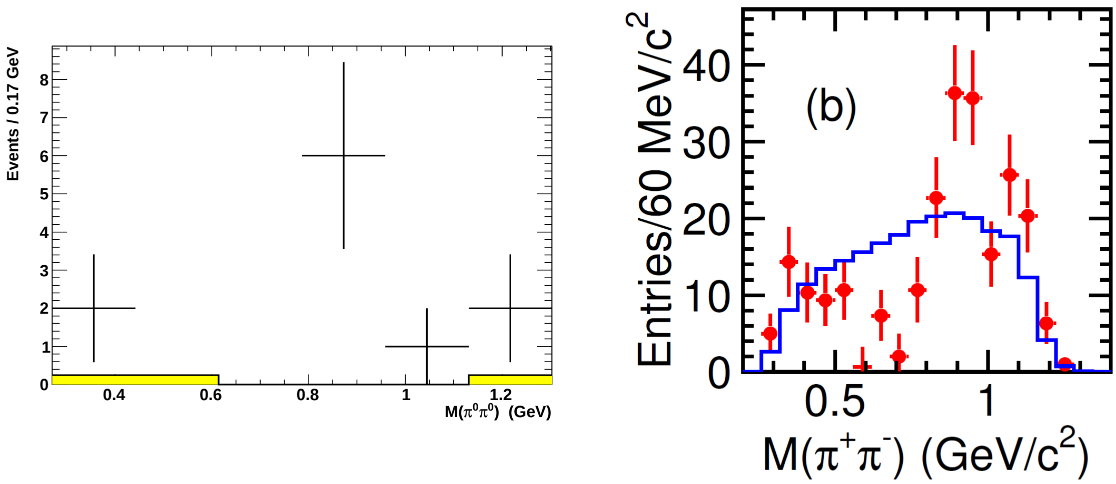

Figure 5.4: Left: $M(\pi^0\pi^0)$ distribution for events in the J/ψ signal region, with $M(\pi^0\pi^0 J/\psi) \in [4.1, 4.4]$ GeV (data points). The yellow shaded histogram is for scaled J/ψ sideband events from the whole $M(\pi^0\pi^0 J/\psi)$ mass range. Right: $M(\pi^+\pi^-)$ distribution for events in the range: $M(\pi^+\pi^-\ell^+\ell^-) \in [4.2, 4.4]$ GeV, shown with the prediction from MC allowed to decay according to phase space.

In addition to the di-pion mass, the other possible combination of $Y(4260)$ daughters is $\pi^0 J/\psi$. The $M(\pi^0 J/\psi)$ distribution was measured for the cluster of events between 4.1 and 4.4 GeV and was produced in a similar fashion to the

$M(\pi^0\pi^0)$ distribution. In each event the J/ψ candidate could be combined with one of two π^0 candidates; the π^0 candidate with the lower value of $|\cos(\theta_\gamma)|$ was chosen and the results are shown in Figure 5.5. Again, the data from the J/ψ sidebands are not from the same $M(\pi^0\pi^0 J/\psi)$ mass range. The data are shown in six bins from $m_{J/\psi} + m_{\pi^0} = 3.2$ GeV to $4.4 - m_{\pi^0} = 4.3$ GeV. No structure is observed, noting however that there are very few events.

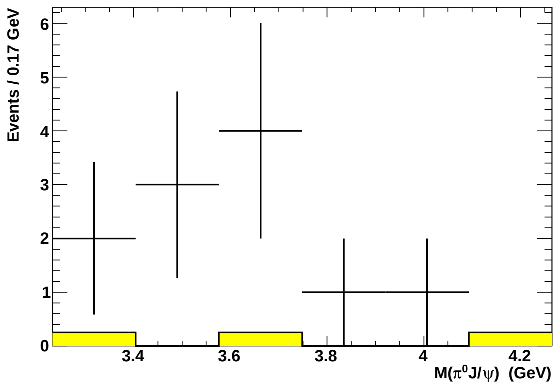

Figure 5.5: $M(\pi^0 J/\psi)$ distribution for events in the J/ψ signal region, with $M(\pi^0\pi^0 J/\psi) \in [4.1, 4.4]$ GeV (data points). No events from the J/ψ sideband region have $M(\pi^0\pi^0 J/\psi) \in [4.1, 4.4]$ GeV. The yellow shaded histogram is for scaled J/ψ sideband events from the whole $M(\pi^0\pi^0 J/\psi)$ region.

The $M(\pi^0\pi^0 J/\psi)$, $M(\pi^0\pi^0)$ and $M(\pi^0 J/\psi)$ masses were tabulated for events in the J/ψ signal region above $M(\pi^0\pi^0 J/\psi) = 4.0$ GeV and for the events from the J/ψ sidebands in the whole mass range: these are shown in Table 5.1.

Table 5.1: $M(\pi^0\pi^0 J/\psi)$, $M(\pi^0\pi^0)$ and $M(\pi^0 J/\psi)$ of events in data from the J/ψ signal region (with masses between 4.0 and 6.0 GeV), and events from the J/ψ sidebands (with masses between threshold and 6.0 GeV). For $M(\pi^0 J/\psi)$, the π^0 candidate with the lowest $|\cos(\theta_\gamma)|$ is chosen. All masses are in GeV.

Data from J/ψ signal region			Data from J/ψ sideband region		
For events $M(\pi^0\pi^0 J/\psi) \in [4.0,\ 6.0]$			For events $M(\pi^0\pi^0 J/\psi) \in [3.4,\ 6.0]$		
$M(\pi^0\pi^0 J/\psi)$	$M(\pi^0\pi^0)$	$M(\pi^0 J/\psi)$	$M(\pi^0\pi^0 J/\psi)$	$M(\pi^0\pi^0)$	$M(\pi^0 J/\psi)$
4.104	0.378	3.602	3.885	0.365	3.733
4.109	0.384	3.352	3.929	0.508	3.362
4.184	0.940	3.503	5.222	1.823	4.211
4.188	0.906	3.416	5.629	1.274	4.919
4.195	0.822	3.651			
4.240	0.920	3.369			
4.245	0.872	3.661			
4.287	1.068	3.722			
4.341	1.160	3.869			
4.393	0.837	3.481			
4.397	1.142	3.923			
4.456	0.833	3.842			
4.601	1.099	4.105			
4.676	1.443	3.865			
4.749	0.753	4.559			
5.111	1.913	3.976			
5.406	1.274	4.814			

5.2 Cross-section as a function of mass

These results were used to measure the $e^+e^- \to \pi^0\pi^0 J/\psi$ cross-section as a function of mass for events with $M(\pi^0\pi^0 J/\psi)$ above 4 GeV. This is the first measurement of this kind. In Ref. [38], the CLEO collaboration measured the cross-section of $e^+e^- \to \pi^0\pi^0 J/\psi$ at 4260 MeV in direct e^+e^- annihilation, however, because they were colliding at a fixed energy, they were unable to measure a line shape.

The method was as follows: Firstly, the efficiency as a function of mass was determined, as described in Section 5.2.1. Secondly, the effective luminosity produced via the ISR process was calculated, as detailed in Section 5.2.2. These functions were then combined with the $M(\pi^0\pi^0 J/\psi)$ results to produce the cross-section as a function of mass, as discussed in Section 5.2.3.

5.2.1 Efficiency as a function of mass

To measure the efficiency as a function of mass, 900,000 $\pi^0\pi^0 J/\psi$ MC events were produced at each of six mass points: 3.8 GeV, 4.0 GeV, 4.2 GeV, 4.5 GeV, 5.0 GeV and an additional point at the mass of the $\psi(2S)$.[1] These MC samples were generated with a width of 1 MeV and with $X \to \pi^0\pi^0 J/\psi$ decaying according to phase space. The efficiencies measured with these samples was fitted using the function:

$$\epsilon(m) = p_0 - e^{(p_1 - p_2 m)},$$

where p_0, p_1 and p_2 are parameters floated in the fit and $m = M(\pi^0\pi^0 J/\psi)$. These efficiencies and the fit results are shown in in Figure 5.6. The efficiency as a function of mass is slowly varying in the region of interest ($M(\pi^0\pi^0 J/\psi) \in [4.0,\ 6.0]$ GeV).

[1] The MC produced at the $\psi(2S)$ mass described here was only used to generate the efficiency as a function of mass. The $\psi(2S)$ signal MC was used to measure the efficiency of the $\psi(2S)$ itself and the efficiency generated by these two samples was found to be very similar.

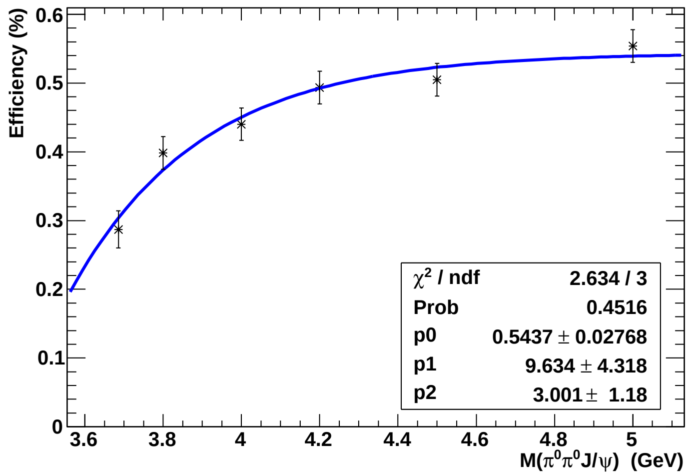

Figure 5.6: The efficiency for $\pi^0\pi^0 J/\psi$ MC produced at different masses. The solid line is the fit to these points described in the text.

5.2.2 Effective luminosity as a function of mass

The QED radiator was used to find the probability for an ISR event to occur with given energy (see Section 1.4). For each energy, this changing probability combined with the total luminosity measured by Belle produced an effective luminosity as a function of mass. The QED radiator, $W(s,x)$, is given by Equation 1.2 in Section 1.4. The effective luminosity in bin i is given by:

$$\mathcal{L}_i = \int \mathcal{L}dt \cdot W\left(s, \frac{x_i - x_{i+1}}{2}\right) \cdot (x_i - x_{i+1}),$$

where x_i is the fraction of the electron (or positron) energy taken by the ISR photon, when producing a state with the mass of the low edge of bin i; $\sqrt{s}$ is the total energy of the collision; and $\int \mathcal{L}dt$ is the total integrated luminosity collected by Belle. This function was plotted for 100 MeV bins and is shown in Figure 5.7.

In previous sections, the $Y(4260)$ MC was scaled according to the effective luminosity at the centre of the distribution, however, the effective luminosity changes across the peak. In order to check the effect of this change, the generated distribution of MC events was scaled using both methods and the resultant distributions are shown in Figure 5.8. As can be seen in the figure, the effect of this difference is small and the MC used for the remainder of this analysis was scaled using the bin by bin method.

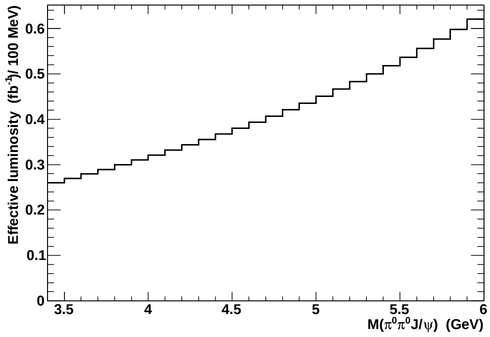

Figure 5.7: The effective luminosity as a function of mass in 100 MeV bins.

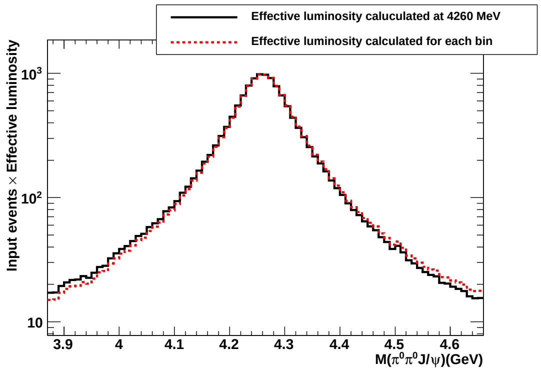

Figure 5.8: The generated distribution of $Y(4260)$ events in $Y(4260)$ MC. The distribution is scaled by the effective luminosity in the centre bin (solid line) and separately scaled by the effective luminosity in each bin (red dashed line). Shown on a log scale.

5.2.3 Cross-section as a function of mass result

The cross-section as a function of mass was calculated using:

$$\sigma_i = \frac{n_i^{sig} - n_i^{bkg}}{\epsilon_i \; \mathcal{L}_i \; \mathcal{B}(J/\psi \to \mu^+\mu^-) \; \mathcal{B}(\pi^0 \to \gamma\gamma) \; \mathcal{B}(\pi^0 \to \gamma\gamma)},$$

where n_i^{sig}, n_i^{bkg}, ϵ_i and $\mathcal{L}_i$ are the number of signal events, background events, the efficiency and the effective luminosity in the i-th $M(\pi^0\pi^0 J/\psi)$ bin, respectively; and the branching fractions, $\mathcal{B}$, were taken from the PDG [1]. The cross-section as a function of mass was calculated in 100 MeV bins in the mass region $M(\pi^0\pi^0 J/\psi) \in [4.0, 4.5]$ GeV, and 500 MeV bins in the mass region $M(\pi^0\pi^0 J/\psi) \in$

$[4.5, 6.0]$ GeV, because of the sparseness of the plot. The background level across the plot is assumed to be constant and the events from the J/ψ sidebands are shared across the whole range. The results are shown in Table 5.2 and plotted in Figure 5.9. The errors shown in the table are statistical only, from the error on n_i^{sig} and n_i^{bkg}. In addition to these errors, there are also the systematic errors from Table 4.10, with the exception of the uncertainty from the $Y(4260)$ fit function. The systematic uncertainty at each point is 6%. The average cross-section between 4.1 GeV and 4.4 GeV is $35 \pm 12 \pm 2$ pb, which is consistent, within large errors, with the cross-section for $\pi^0\pi^0 J/\psi$ production measured by the CLEO experiment in direct annihilation at $\sqrt{s} = 4260$ MeV: $\sigma = 23^{+12}_{-8} \pm 1$ pb [38].

Table 5.2: Values used to calculate the cross-section as a function of mass are shown with the final result. The error on the cross-section here is from the statistical error on n_i^{sig} and n_i^{bkg} only.

$M(\pi^0\pi^0 J/\psi)$ Bin (GeV)	n_i^{sig}	n_i^{bkg}	ϵ_i %	$\mathcal{L}_i$ pb^{-1}	σ_i pb
4.0, 4.1	0	0.15	0.47	321	-1.7 ± 12.3
4.1, 4.2	5	0.15	0.49	332	51.5 ± 24.5
4.2, 4.3	3	0.15	0.51	343	28.1 ± 17.8
4.3, 4.4	3	0.15	0.52	355	26.7 ± 17.0
4.4, 4.5	1	0.15	0.52	367	7.7 ± 9.7
4.5, 5.0	3	0.76	0.53	2034	3.6 ± 3.4
5.0, 5.5	2	0.76	0.54	2413	1.6 ± 2.4
5.5, 6.0	0	0.76	0.54	2882	-0.8 ± 1.5

In Ref. [38], CLEO measured the production of $\pi^0\pi^0 J/\psi$ at 4260 MeV in direct e^+e^- annihilation with better precision, however, because they were colliding at a fixed energy, they were unable to measure a line shape. The combined information from these two results indicates a peaking $\pi^0\pi^0 J/\psi$ distribution with approximately half the production rate of the charged mode. This contributes to the possible identification of the $Y(4260)$ in a decay mode other than the discovery mode, though more events are needed. $Y(4260)$ decaying to $\pi^0\pi^0 J/\psi$ with

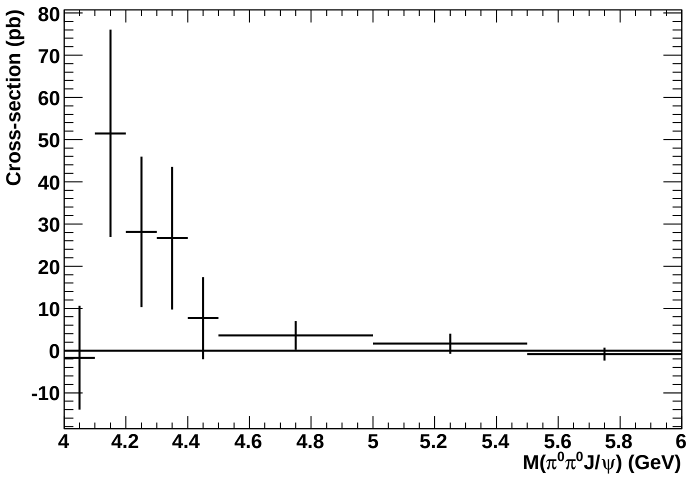

Figure 5.9: Cross-section as a function of mass. The error on the cross-section here is from the statistical error on the bin counts only.

approximately half the branching fraction of the charged mode would be consistent with the expectation from isospin and the majority of theoretical models for the structure of the $Y(4260)$. Though, as noted in Ref. [38], confirmation of $Y(4260) \to \pi^0\pi^0 J/\psi$ with this rate would disfavour the $(\chi_{cJ}\rho^0)$ molecule model discussed in Ref. [64], as ρ^0 does not decay to $\pi^0\pi^0$.[2]

5.3 Fits to $M(\pi^0\pi^0 J/\psi)$ spectrum

The interpretation of the excess of events around 4260 MeV is not yet fixed and there are many theoretical models for the production of these events that have been proposed (see Section 1.6). $\pi^+\pi^- J/\psi$ events produced via ISR in this mass range have been fitted using two different schemes: a single Breit-Wigner resonance with a floating polynomial background and two interfering Breit-Wigner resonances with the background fixed to the level of the J/ψ sidebands. Here, fits were performed to the $M(\pi^0\pi^0 J/\psi)$ spectrum using each method.[3]

[2] Historical note: The authors of Ref. [38] also noted that this would disfavour the baryonium interpretation of the $Y(4260)$ peak discussed in Ref. [70], as an early version of this paper predicted $\mathcal{B}(\pi^0\pi^0 J/\psi) \approx \mathcal{B}(\pi^+\pi^- J/\psi)$, which was updated after the CLEO paper to be $\mathcal{B}(\pi^0\pi^0 J/\psi) \approx \frac{1}{2}\mathcal{B}(\pi^+\pi^- J/\psi)$.

[3] Fits were performed using the `RooFit` software package (see Section 2.6.2).

BABAR in its discovery paper used a second-order polynomial to represent the background and a Breit-Wigner resonance to represent the peak at 4260 MeV [25]. Though they attempted a fit with two interfering resonances, they were unable to exclude or establish this hypothesis. Belle, *BABAR* and CLEO have all measured possible Breit-Wigner parameters with a single resonance fit to the $\pi^+\pi^- J/\psi$ spectrum, so this was chosen to be the primary fit to the $\pi^0\pi^0 J/\psi$ invariant mass spectrum for this study and is discussed in Section 5.3.1. Here, a single resonance fit including terms for a possible contribution from the $\psi(3770)$, $\psi(4040)$ and $\psi(4160)$ resonances was also performed: this is discussed in Section 5.3.2. This fit variation was included in the list of systematic uncertainties associated with the single resonance fit, which are detailed in Section 5.3.3. The primary fit used by Belle in its published $\pi^+\pi^- J/\psi$ analysis was a fit with two interfering Breit-Wigner terms. In this fit, the level of the background was fixed to the contribution from the J/ψ sidebands and all events above this were considered to be from resonant $\pi^+\pi^- J/\psi$ production. In the single resonance fit, the events in data above the level of the the J/ψ sidebands were interpreted as a possible non-resonant contribution. A two resonance fit using the style from the published Belle result is shown in Section 5.3.4.

5.3.1 Single resonance fit

An unbinned maximum likelihood fit was performed to the $M(\pi^0\pi^0 J/\psi)$ spectrum. There were three components to the fit: a $\psi(2S)$ term, a continuous term to account for possible non-resonant $\pi^0\pi^0 J/\psi$ production and a $Y(4260)$ signal term. The $\psi(2S)$ term consisted of a sum of Gaussians, which were fitted to the correctly identified and broken candidate $\psi(2S)$ shapes from the MC, which are described in Table 4.7 in Section 4.8.1. The shapes for each component were then fixed from MC and only the common mean of the Gaussians and the fractions of correctly identified and broken candidates allowed to float. The $\psi(2S)$ is narrow, meaning the fitted shape essentially parametrised the experimental resolution, therefore the $\psi(2S)$ peak was not adjusted for the change in effective luminosity or the value of the QED radiator across the peak. For the continuous term an exponential function with a threshold was chosen:

$$\frac{dN_{NR}}{dm} = \sqrt{m - m_{min}} \times e^{c_{exp}(m - m_{min})} \tag{5.1}$$

where $m = M(\pi^0\pi^0 J/\psi)$, $m_{min} = m_{J/\psi} + 2m_{\pi^0}$, and c_{exp} is the exponential shape parameter, which was floated in the fit.

The $Y(4260)$ signal was fitted as a single resonance over m, with fit function:

$$\frac{dN}{dm} = a \cdot F(m) \cdot \mathcal{L}_{eff}(m) \cdot \epsilon(m), \tag{5.2}$$

where a is a normalisation term; $\mathcal{L}_{eff}(m)$ is the effective luminosity as a function of mass:

$$\mathcal{L}_{eff}(m) = W(s, x(m)) \cdot 2m/s, \tag{5.3}$$

where $W(s, x)$ is the QED radiator (Section 5.2.2); $\epsilon(m)$ is the efficiency as a function of mass:

$$\epsilon(m) = 0.5437 - e^{9.634-3.001m}, \tag{5.4}$$

as is discussed in Section 5.2.1; and $F(m)$ is the formula for a Breit-Wigner:

$$F(m) = \frac{M^2}{m^2} \cdot \frac{12\pi\Gamma_{ee} \cdot \mathcal{B}(\pi^0\pi^0 J/\psi)\Gamma}{(m^2 - M^2)^2 + M^2\Gamma^2} \cdot \frac{\Phi(m)}{\Phi(M)}, \tag{5.5}$$

where, M and Γ are the Breit-Wigner mean and width parameters; and Γ_{ee} and $\mathcal{B}(\pi^0\pi^0 J/\psi)$ are the two-electron width and the branching fraction for $Y(4260) \to \pi^0\pi^0 J/\psi$, respectively; and $\Phi(m)$ is a phase space factor:

$$\Phi(m) = \sqrt{((m^2 + m^2_{J/\psi} - M^2_{\pi^0\pi^0})/2m)^2 - m^2_{J/\psi}}, \tag{5.6}$$

where $M_{\pi^0\pi^0}$ was fixed to a nominal value of 0.5 GeV in the fit.[4] The phase space factor had the effect of decreasing the low mass side and increasing the high mass side of the resonance.

Because of the small size of the yield, the Breit-Wigner mean and width parameters were fixed to the prediction from MC and only the normalisation allowed to vary. For this purpose, a fit was performed to $Y(4260)$ MC that had been generated using the world average values of the mean and width parameters ($M = 4263$ MeV and $\Gamma = 95$ MeV [1]). The events in this MC were then scaled according to the effective luminosity as a function of the MC truth mass before being fitted with the full $Y(4260)$ term.

The results of the fit to data are shown in Table 5.3, along with the results of a secondary fit, which included terms for the $\psi(3770)$, $\psi(4040)$ and $\psi(4160)$

[4] The results of the fit are not sensitive to the value of $M_{\pi^0\pi^0}$, variant fits were attempted with $M_{\pi^0\pi^0} = 0.25$ GeV and 1.0 GeV and there was no change in the value or error of any parameter floated in the fit at the quoted accuracy.

and will be discussed in Section 5.3.2. The number of measured $\psi(2S)$ events: 629^{+26}_{-25}, compares well with the predicted number of events from MC: 635 ± 12. The difference between the observed mean of the $\psi(2S)$ peak and the world average from the PDG (3686.09 ± 0.04 MeV [1]), is consistent with the observed differences between the input and fitted values of the $\psi(2S)$ mass in MC. As the mass of the $Y(4260)$ terms were fixed based on the values from the $\pi^+\pi^- J/\psi$ mode, the systematics on the mass measurements were not studied. From this fit we measure $\Gamma_{ee} \cdot \mathcal{B}(\pi^0\pi^0 J/\psi) = 3.19^{+1.82}_{-1.53}$ eV, which is consistent within large errors with $\frac{1}{2}\Gamma_{ee} \cdot \mathcal{B}(\pi^+\pi^- J/\psi) = \frac{1}{2} \times 5.9^{+1.2}_{-0.9} = 3.0^{+0.6}_{-0.5}$ eV [1], which is the expectation from isospin. This $\Gamma_{ee} \cdot \mathcal{B}$ corresponds to $8.6^{+4.9}_{-4.0}$ $Y(4260)$ events in the fit and the significance of the $Y(4260)$ term in the fit is $\sqrt{-2\ln \mathcal{L}/\mathcal{L}_0} = 2.4$, where $\mathcal{L}$ ($\mathcal{L}_0$) is the maximum likelihood returned by the fit with (without) the $Y(4260)$ term.

Table 5.3: Results of the single resonance fits to the $M(\pi^0\pi^0 J/\psi)$ spectrum. Left columns: primary fit. Right columns: Fit including terms for the $\psi(3770)$, $\psi(4040)$ and $\psi(4160)$. $\Gamma_{ee} \cdot \mathcal{B}(\pi^0\pi^0 J/\psi)$ is the production rate of $Y(4260) \to \pi^0\pi^0 J/\psi$ events. $N[\psi(2S)]$ is the number of $\psi(2S)$ events; and $N[3\gamma]/N[\psi(2S)]$ and $N[< 3\gamma]/N[\psi(2S)]$ are the fraction of events in the $\psi(2S)$ peak that fit the shape for broken candidates with three, or less than three, π^0 photons correctly identified. $N[NR]$ and c_{exp} are the number of events and the exponential shape parameter for the non-resonant term.

Parameter	Primary fit		Other ψ resonances		Units
$\Gamma_{ee} \cdot \mathcal{B}(\pi^0\pi^0 J/\psi)$	3.19	$^{+1.82}_{-1.53}$	2.86	$^{+1.76}_{-1.46}$	eV
$N[\psi(2S)]$	629	$^{+26}_{-25}$	629	$^{+26}_{-25}$	Events
$\psi(2S)$ mean	3684.2	± 0.5	3684.2	± 0.5	MeV
$N[3\gamma]/N[\psi(2S)]$	23	± 4	24	± 4	%
$N[< 3\gamma]/N[\psi(2S)]$	3.6	$^{+3.5}_{-3.4}$	3.7	$^{+3.4}_{-3.3}$	%
$N[NR]$	14	$^{+8}_{-7}$	12	$^{+8}_{-6}$	Events
c_{exp}	-1.4	$^{+0.7}_{-0.6}$	-1.3	$^{+0.7}_{-0.6}$	

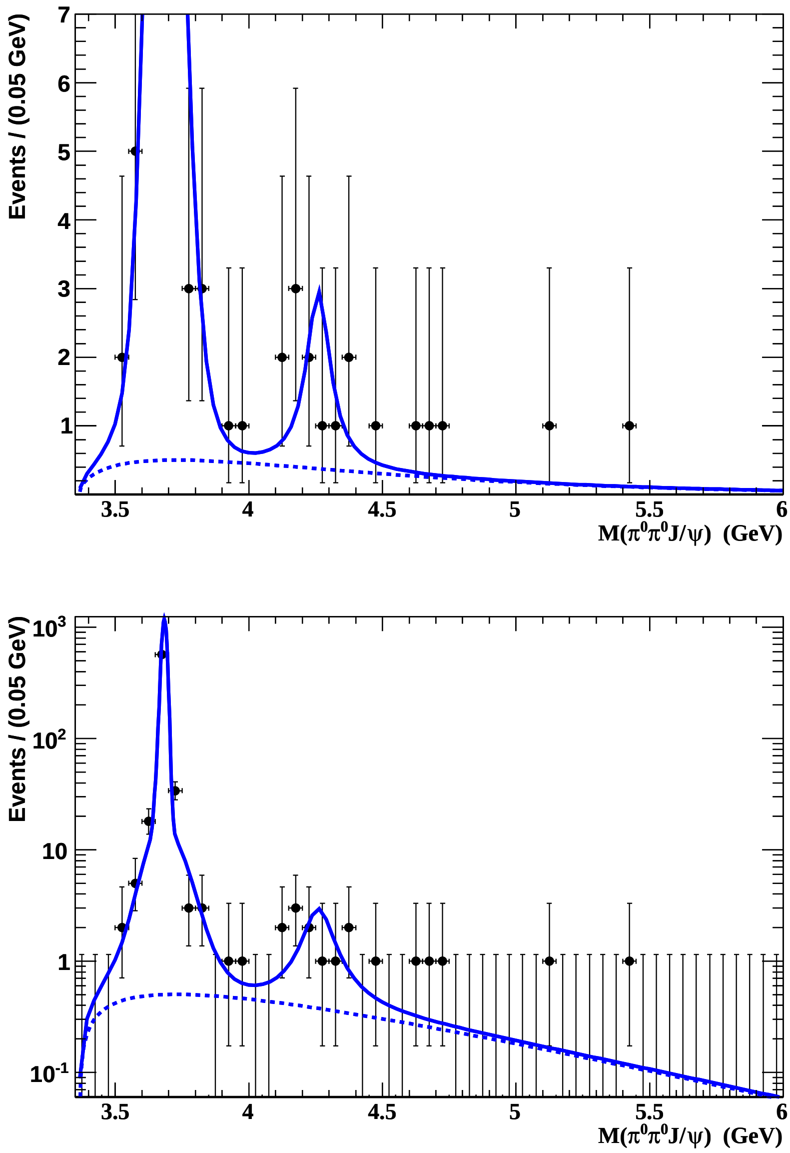

Figure 5.10: Single resonance fit to the $M(\pi^0\pi^0 J/\psi)$ spectrum. Top: cut-off linear scale. Bottom: log scale. The data from the J/ψ signal region is projected onto 50 MeV bins (data points) with the fit result (solid line) and the non-resonant component (dashed line).

5.3.2 Fit with other ψ resonances

Between the mass of the $\psi(2S)$ and the $Y(4260)$, there are three ψ resonances, at least one of which has a known decay to $\pi^0\pi^0 J/\psi$. A fit was performed using the fitting method described in the previous section, with the inclusion of three terms: one for the $\psi(3770)$ and two for a possible contribution from the $\psi(4040)$ and $\psi(4160)$ resonances.

In Ref. [38], the CLEO collaboration measured the $e^+e^- \rightarrow \pi^+\pi^- J/\psi$ and $e^+e^- \rightarrow \pi^0\pi^0 J/\psi$ cross-sections in direct production at values near the mass of the $\psi(4040)$, $\psi(4160)$ and $Y(4260)$. In that study, CLEO found the $\pi\pi J/\psi$ cross-section measured near the mass of the $\psi(4160)$ to be consistent with the tails of the $Y(4260)$. To check the maximum possible effect of these resonances on the $\Gamma_{ee} \cdot \mathcal{B}(Y(4260) \rightarrow \pi^0\pi^0 J/\psi)$ value, the whole $\pi^0\pi^0 J/\psi$ cross-section CLEO measured near 4160 MeV and half the $\pi^+\pi^- J/\psi$ cross-section measured near 4040 MeV (CLEO only measured an upper limit in $\pi^0\pi^0 J/\psi$ near 4040 MeV) was taken to be due to the $\psi(4160)$ and $\psi(4040)$ resonances, respectively, and fixed in the fit. The mass and width of these three states was fixed from the world average values, along with the branching fraction and Γ_{ee} of the $\psi(3770)$ [1]: these values are summarised in Table 5.4. The results of this fit are shown in Figure 5.11 and the right hand columns of Table 5.3. The deviation between the value of $\Gamma_{ee} \cdot \mathcal{B}$ measured by this fit and the fit in Section 5.3.1 was found to be small and taken as a systematic uncertainty.

Table 5.4: Parameters of the ψ resonances used in the fit to $\pi^0\pi^0 J/\psi$ spectrum. All values are taken from Ref. [1], except for σ near the $\psi(4040)$ and $\psi(4160)$ resonances, which are taken from Ref. [38]. For the $\psi(4040)$, the cross-section is taken as half that of the $\pi^+\pi^- J/\psi$ mode.

	Mass (MeV)	Width (MeV)	σ near state (pb)	$\Gamma_{ee} \cdot \mathcal{B}$ (eV)
$\psi(3770)$	3772.92 ± 0.35	27.3 ± 1.0		0.212 ± 0.09
$\psi(4040)$	4039 ± 1	80 ± 10	$\frac{1}{2} \times (9^{+5}_{-4} \pm 2)$	
$\psi(4160)$	4153 ± 3	103 ± 8	$5 \pm 2 \pm 1$	

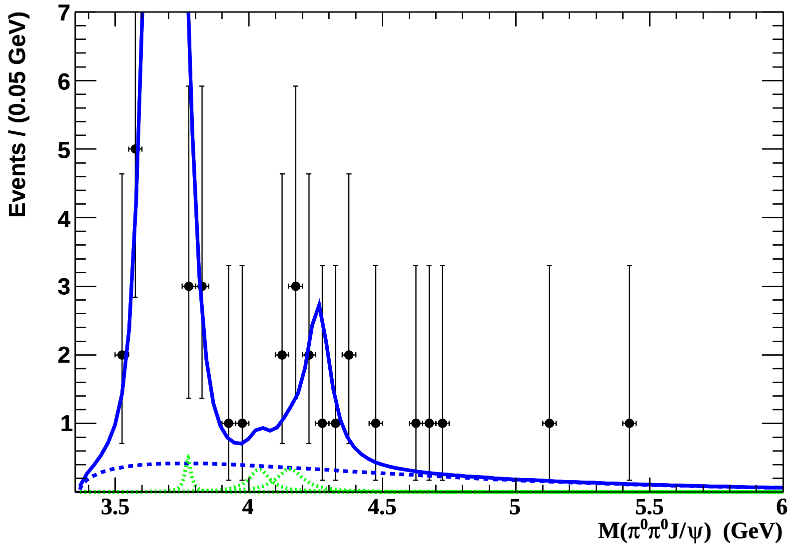

Figure 5.11: Single Breit-Wigner fit to the $M(\pi^0\pi^0 J/\psi)$ spectrum including terms for the $\psi(3770)$, $\psi(4040)$ and $\psi(4160)$. Data from the J/ψ signal region (data points) is projected onto 50 MeV bins with the fit result (solid line) and the maximum possible contribution from the $\psi(3770)$, $\psi(4040)$ and $\psi(4160)$ resonances (green dotted lines) and a possible non-resonant component (dashed line).

5.3.3 Fitting systematics of single resonance fit

In order to check the systematics associated with the choice of fit function, several variant fits were attempted. The maximum positive and negative deviations from the $\Gamma_{ee} \cdot \mathcal{B}$ value between these variant fits and the primary fit from Section 5.3.1 were taken as the positive and negative systematic errors for the choice of the fit function. The types of fits included were binned fits, with different binnings; the fit including possible contributions from other ψ resonances described in Section 5.3.2; fits with different fit ranges; and a fit with a $\psi(2S)$ term made from two Gaussians and a bifurcated Gaussian, with widths allowed to float in the fit. The variation in $\Gamma_{ee} \cdot \mathcal{B}$, $N[\psi(2S)]$ and $N[NR]$ between the primary fit and the variant fits are shown in Table 5.5.[5] The largest positive and negative deviation on $\Gamma_{ee} \cdot \mathcal{B}$ is $+18.3\%$ and -10.3%. Adding these terms in quadrature with the systematic uncertainties on the efficiency from Section 4.10 pro-

[5]Note that the large percentage errors in $N[NR]$ are with respect to a small number of events.

vides a total systematic error of $+20\%$ and -14%, which gives the final result $\Gamma_{ee} \cdot \mathcal{B}(Y(4260) \to \pi^0\pi^0 J/\psi) = 3.19^{+1.82+0.64}_{-1.53-0.45}$ eV.

Table 5.5: Systematics of the fit to the $M(\pi^0\pi^0 J/\psi)$ spectrum. The entries give the percentage difference between selected fitted values for the variant fits to $M(\pi^0\pi^0 J/\psi)$.

Variation (%)	$\Gamma_{ee} \cdot \mathcal{B}$	$N[\psi(2S)]$	$N[NR]$
Binned fit with 10 MeV bins	-4.5	-0.3	$+8.6$
Binned fit with 20 MeV bins	-6.4	-0.3	$+15.7$
Binned fit with 50 MeV bins	$+18.3$	$+0.6$	-40.0
With $\psi(4040)$ and $\psi(4160)$	-10.3	0.0	-14.3
Change of range 3.4 to 5.0 GeV	-2.4	$+0.2$	-21.0
Change range 3.4 to 5.5 GeV	$+2.0$	$+0.1$	-8.0
Change of $\psi(2S)$ shape	$+1.0$	$+0.1$	-6.6

5.3.4 Two resonance fit

The $M(\pi^0\pi^0 J/\psi)$ spectrum was fitted with two interfering Breit-Wigner resonances representing the $Y(4260)$ and $Y(4008)$, according to the fitting scheme used for the primary result of Ref. [29]. In the reference, the non-resonant contribution was fixed using a fit to the data from the J/ψ sidebands. In the reference, the J/ψ sidebands were fitted with a second order polynomial, here however, a first order polynomial was used because there were very few events. The $\psi(2S)$ term used in this section is the same as the $\psi(2S)$ term used for the single resonance fit in Section 5.3.1. A Breit-Wigner resonance term was used for each of the $Y(4008)$ and $Y(4260)$ terms (defined in Equation 5.5 from Section 5.3.1) with an interference term:

$$I(m) = 2\cos(\phi)\sqrt{F_{R1}F_{R2}},$$

where F_{R1} and F_{R2} are the Breit-Wigner terms for resonance 1 ($Y(4008)$) and resonance 2 ($Y(4260)$), respectively. In this fit, the masses and widths of the two resonances were fixed to the values found in the $\pi^+\pi^- J/\psi$ Belle result, as was the value of the parameter ϕ and the ratio of the number of events in each resonance. The values of these terms can be found in Table 3.18 ins Section 3.9. In the $\pi^+\pi^- J/\psi$ study, two fit results were found with the same mass and width parameters, one with constructive interference (Solution I) and one with destructive interference (Solution II). The results of these two fits to the $\pi^0\pi^0 J/\psi$ spectrum are summarised in Table 5.6 and the results of the fit with constructive interference is shown in Figure 5.12. From the fits, the value of $\Gamma_{ee} \cdot \mathcal{B}(\pi^0\pi^0 J/\psi)$ for each resonance (ratios fixed) is consistent, within large errors, with half the value found in the previous study of the charged mode by Belle [29], the expectation from isospin.

Table 5.6: Results of a two resonance fit to the $M(\pi^0\pi^0 J/\psi)$ spectrum. $\Gamma_{ee} \cdot \mathcal{B}(\pi^0\pi^0 J/\psi)$ is measured for the $Y(4008)$ ($R1$) and $Y(4260)$ ($R2$) resonances using two fits, Solution I and II, described in text. The ratio of these two terms is fixed in each fit. $N[\psi(2S)]$ is the number of $\psi(2S)$ events; and $N[3\gamma]/N[\psi(2S)]$ and $N[< 3\gamma]/N[\psi(2S)]$ are the fraction of events in the $\psi(2S)$ peak that fit the shape for broken candidates with three, or less than three, π^0 photons correctly identified.

Parameter		Value	Positive error	Negative error	Units
Solution I		(*ratio fixed)			
$\Gamma_{ee} \cdot \mathcal{B}(\pi^0\pi^0 J/\psi)$	$R1$	$^*1.9$	$+0.6$	-0.5	GeV
$\Gamma_{ee} \cdot \mathcal{B}(\pi^0\pi^0 J/\psi)$	$R2$	$^*2.3$	$+0.7$	-0.6	GeV
Solution II		(*ratio fixed)			
$\Gamma_{ee} \cdot \mathcal{B}(\pi^0\pi^0 J/\psi)$	$R1$	$^*5.2$	$+1.4$	-1.2	GeV
$\Gamma_{ee} \cdot \mathcal{B}(\pi^0\pi^0 J/\psi)$	$R2$	$^*8.7$	$+2.4$	-2.0	GeV
$N[\psi(2S)]$		631	$+26$	-25	
$\psi(2S)$ mean		3684.2	$+0.5$	-0.5	MeV
$N[3\gamma]/N[\psi(2S)]$		23	$+4$	-4	%
$N[< 3\gamma]/N[\psi(2S)]$		4.2	$+3.1$	-2.7	%

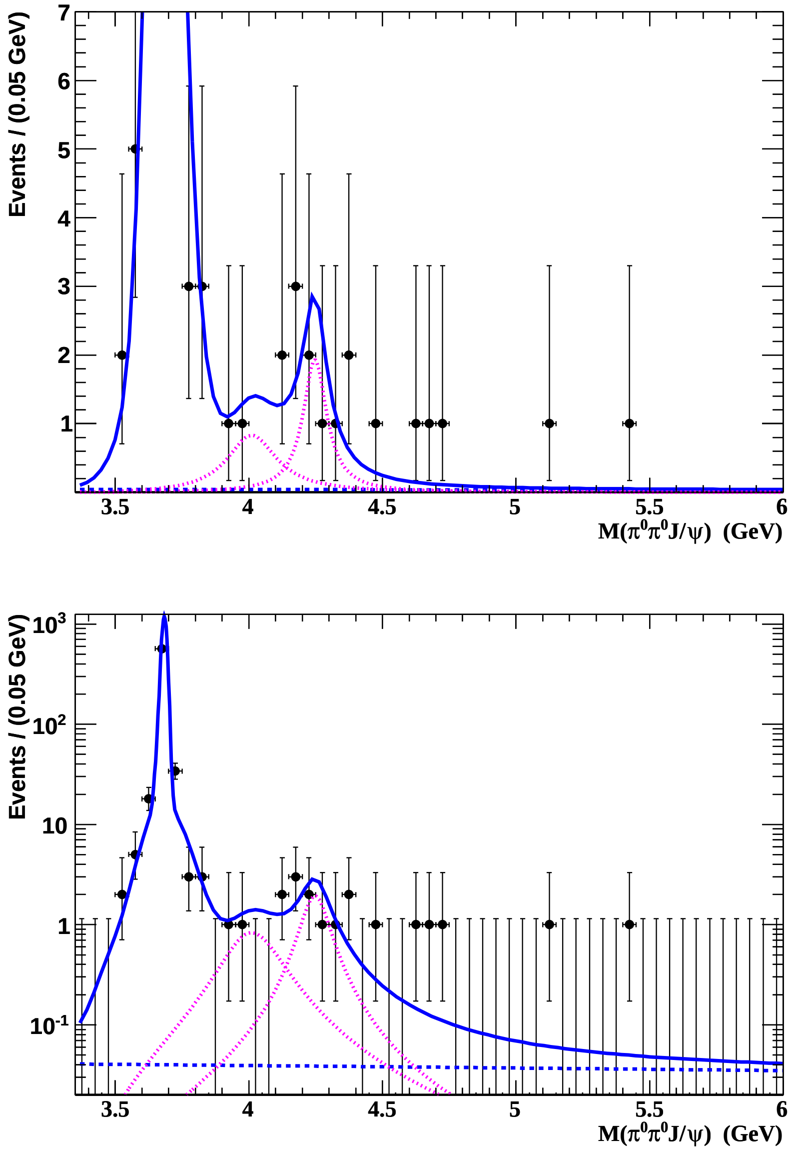

Figure 5.12: Two resonance fit to $M(\pi^0\pi^0 J/\psi)$ spectrum with constructive interference (referred to as Solution I). Top: cut-off linear scale. Bottom: log scale. Data from the J/ψ signal region (data points) are projected onto 50 MeV bins with the fit result (solid line) and the fit to the J/ψ sidebands (dashed line). The Breit-Wigner terms for the two resonances is shown with a dotted magenta line.

5.3.5 Summary of fit results

The results of the fits discussed in this section are summarised in Table 5.7, along with the relevant results from other studies. As can be seen in the table, the value of $\Gamma_{ee} \cdot \mathcal{B}$ measured in this study is consistent with half the value measured in the $\pi^+\pi^- J/\psi$ decay mode from both the single resonance fit and the two resonance fit, within large errors, corresponding to the expectation from isospin.

Table 5.7: Results of the measurements of the $Y(4260) \to \pi\pi J/\psi$ production rate using ISR events, arranged into two groups. Top group: the fits with a single Breit-Wigner resonance. Bottom group: the fits with two interfering Breit-Wigner resonances. The results in Belle (2006) were superseded by the results in Belle (2007). The results of *BaBar* (2005) were updated in *BaBar* (2008). Here the first errors are statistical and the second, where available, are systematic. The second column corresponds to half the measured production rate for $\pi^+\pi^- J/\psi$ events, for comparison with the whole $\pi^0\pi^0 J/\psi$ production rate.

		$\Gamma_{ee} \cdot \mathcal{B}$ (eV)	$\Gamma_{ee} \cdot \mathcal{B}$ (eV)
$\pi^+\pi^- J/\psi$ single resonance fit			$\times\frac{1}{2}$
BaBar (2005)	[25]	$5.5 \pm 1.0 ^{+0.8}_{-0.7}$	$2.8 \pm 0.5 ^{+0.4}_{-0.4}$
CLEO (2006)	[27]	$8.9 ^{+3.9}_{-3.1} \pm 1.8$	$4.5 ^{+2.0}_{-1.6} \pm 0.9$
Belle (2006)	[28]	$8.7 \pm 1.1 ^{+0.3}_{-0.9}$	$4.4 \pm 0.6 ^{+0.2}_{-0.5}$
Belle (2007)	[29]	9.7 ± 1.1	4.9 ± 0.6
BaBar (2008)	[30]	$7.5 \pm 0.9 \pm 0.8$	$3.8 \pm 0.5 \pm 0.4$
$\pi^0\pi^0 J/\psi$			$3.19 ^{+1.82}_{-1.53} ^{+0.64}_{-0.35}$
$\pi^+\pi^- J/\psi$ two resonance fit			$\times\frac{1}{2}$
Belle (2007) Sol. I	[29]	$6.0 \pm 1.2 ^{+4.7}_{-0.5}$	$3.0 \pm 0.6 ^{+2.4}_{-0.3}$
Belle (2007) Sol. II	[29]	$20.6 \pm 2.3 ^{+9.1}_{-1.7}$	$10.3 \pm 1.15 ^{+4.6}_{-0.9}$
$\pi^0\pi^0 J/\psi$ Sol. I			$2.3 ^{+0.7}_{-0.6}$
$\pi^0\pi^0 J/\psi$ Sol. II			$8.7 ^{+2.4}_{-2.0}$

5.4 Conclusion

$\pi^0\pi^0 J/\psi$ events have been observed in ISR events above 4.0 GeV. A cluster of events near the mass of the $Y(4260)$ has been observed in $M(\pi^0\pi^0 J/\psi)$, with a low level of background either side of the cluster. The distributions of the selection variables for these events were checked and are consistent with the expected distributions. In addition to this, the mass distribution of the daughter combinations, $\pi^0\pi^0$ and $\pi^0 J/\psi$, has also been measured. The $M(\pi^+\pi^-)$ distribution in the charged mode was found to be inconsistent with phase space and the measured $M(\pi^0\pi^0)$ distribution is consistent with $M(\pi^+\pi^-)$ result, at face value; though, there are too few events to draw a strong conclusion. A cross-section as a function of mass was produced using the $\pi^0\pi^0 J/\psi$ mass spectrum with large bins. The $\pi^0\pi^0 J/\psi$ cross-sections measured in this study were found to be consistent with the cross-section for $\pi^0\pi^0 J/\psi$ production measured by the CLEO collaboration. The combined information from these two results indicates a peaking $\pi^0\pi^0 J/\psi$ distribution with approximately half the production rate of the charged mode.

Unfortunately, there were too few events to measure the line shape in this data, so fits to the $M(\pi^0\pi^0 J/\psi)$ spectrum above 4.0 GeV were performed using fit shapes fixed from studies to the $\pi^+\pi^- J/\psi$ channel. An unbinned maximum likelihood fit was performed, consisting of a Breit-Wigner signal term for the $Y(4260)$ and a falling exponential function with a threshold to represent possible non-resonant $\pi^0\pi^0 J/\psi$ contributions. This fit found $\Gamma_{ee} \cdot \mathcal{B}(Y(4260) \to \pi^0\pi^0 J/\psi) = 3.19^{+1.82+0.64}_{-1.53-0.35}$ eV, which is consistent within large errors with half the production rate in the charged mode. The significance of this peak was found to be 2.4σ. A two resonance fit using the fit shape from the published Belle $\pi^+\pi^- J/\psi$ analysis [29] was also attempted. In this fit, the ratio of events in the two resonances and the interference between them was fixed to the results from that study and again, the results were found to be consistent with the $\pi^+\pi^- J/\psi$ result. This result contributes to the possible identification of the $Y(4260)$ in a decay mode other than the discovery mode, though more events are needed. A $\pi^0\pi^0 J/\psi$ decay mode with half the branching fraction of the charged pion mode would be consistent with the expectation from isospin and the majority of theoretical models for the structure of the $Y(4260)$.

Chapter 6

Conclusion

THIS thesis set out to confirm the existence of the $Y(4260)$ in the $\pi^+\pi^-J/\psi$ channel in ISR events in Belle data and, if possible, confirm its expected decay to $\pi^0\pi^0J/\psi$. The Belle detector, which sits on the KEKB asymmetric energy e^+e^- collider, was built to investigate CP violation in B-meson decays and was normally tuned to the energy of the $\Upsilon(4S)$ resonance. In addition to B-mesons, other types of particles were produced directly or indirectly in collisions with different rates of production. One class of events, ISR, allowed the study of particles produced in e^+e^- annihilation with a range of centre of mass energies lower than the normal energy of the collider. In 2005, *BABAR* discovered an enhancement in $\pi^+\pi^-J/\psi$ events produced via ISR, which they called the $Y(4260)$. From the production mechanism, it was known that this state had primary quantum numbers $J^{PC} = 1^{--}$. However, there were several properties that made the structure of this state difficult to determine, as discussed in Chapter 1. The first analysis conducted here was the confirmation of *BABAR*'s $Y(4260) \to \pi^+\pi^-J/\psi$ signal. The second analysis conducted was a search for $Y(4260)$ events in the $\pi^0\pi^0J/\psi$ channel.

In the first analysis, reconstruction techniques were developed and a $Y(4260) \to \pi^+\pi^-J/\psi$ signal was observed, as discussed in Chapter 3. The reconstruction of the ISR photon was not required, however, the four-momentum of each $\pi^+\pi^-J/\psi$ candidate was required to be consistent with ISR origin. The distribution of the production angle of the candidate with respect to the beam-line, $\cos(\theta)$, of the candidates was found to be consistent with the prediction from ISR MC. A peak was observed near the mass found by *BABAR*, which was fitted with a Breit-Wigner resonance term and found to have production rate $\Gamma_{ee} \cdot \mathcal{B}(Y(4260) \to \pi^+\pi^-J/\psi) = 8.7 \pm 1.1^{+0.3}_{-0.9}\,\text{eV}$ and a significance of 11σ. The mass $4295 \pm 10^{+11}_{-5}$ MeV and width

$\Gamma = 133 \pm 26^{+13}_{-6}$ MeV measured by the fit were found to be marginally consistent with other experiments. The mass of the $\pi^+\pi^-$ combination was found to be inconsistent with production via phase space and was found to be similar to the distribution observed by *BABAR*. This result was compared to another Belle result, in Section 3.9, which used a similar dataset and adopted different background and resonance assumptions to describe the peak.

As is presented in Chapter 4, reconstruction techniques were also developed to investigate the $\pi^0\pi^0 J/\psi$ decay mode. $\pi^0\pi^0 J/\psi$ events were more difficult to reconstruct experimentally than $\pi^+\pi^- J/\psi$ events and additionally they had a lower efficiency for the detection of all the daughter particles by the detector. In the $\pi^+\pi^- J/\psi$ analysis, events without the ISR photon reconstructed contributed the majority of the signal. These events tended to be closely aligned with the beam direction, which meant that the ISR photon was lost down the beampipe. The $Y(4260)$ decay however, often imparted enough momentum transverse to the $Y(4260)$ flight direction[1] that all of the daughters passed through the detector acceptance. In the case of the $\pi^0\pi^0 J/\psi$ decay mode, while this same process occurred, the additional decay of the $\pi^0 \to \gamma\gamma$ meant that the majority of these events lost at least one of the four π^0 photons. The sample without the ISR photon reconstructed contained the majority of the background in both decay modes. In the analysis of the $\pi^0\pi^0 J/\psi$, with the lower expected signal yield and larger background, the sample without the ISR photon reconstructed did not contribute significantly to the larger and cleaner signal in the fully reconstructed mode and was not included in the final result. J/ψ particles decay to e^+e^- and $\mu^+\mu^-$ with nearly identical branching fractions and ideally in these events, both decay modes would contribute equally. Unfortunately, while di-electron and di-muon $\pi^0\pi^0 J/\psi$ events passed trigger conditions with approximately the same rate, the fully reconstructed di-electron sample failed the selection cuts in each data skim designed to remove Bhabha events. Whereas in the $\pi^+\pi^- J/\psi$ channel, the additional two charged tracks were enough to prevent the di-electron sample being lost.

The analysis of the unblinded $\pi^0\pi^0 J/\psi$ events with mass near 4.26 GeV is discussed in Chapter 5. Using the fully reconstructed di-muon sample, a cluster of events near the mass of the $Y(4260)$ was observed in $M(\pi^0\pi^0 J/\psi)$, with a low level of background on either side of the cluster. The significance of the cluster was measured to be 2.4σ, using a fit with a single Breit-Wigner resonance with mass and width parameters fixed using the world average values from the $\pi^+\pi^- J/\psi$ mode.

[1] The ISR photon and the $\psi(2S)$ or $Y(4260)$ particle are produced back to back in the CM frame.

This fit found $\Gamma_{ee} \cdot \mathcal{B}(Y(4260) \to \pi^0\pi^0 J/\psi) = 3.2^{+1.8+0.6}_{-1.5-0.4}$ eV, which is consistent with half the production rate in the charged mode within large errors, the expectation from isospin. A cross-section as a function of mass was produced using the $\pi^0\pi^0 J/\psi$ mass spectrum with large bins. In Ref. [38], CLEO measured the cross-section of $\pi^0\pi^0 J/\psi$ at 4260 MeV in direct e^+e^- annihilation with better precision, however, they only measured fixed energy points and were unable to measure the line shape. Taken together, these two measurements contribute to the possible identification of the $Y(4260)$ in a second decay mode, however, more events will be needed to provide an unambiguous measurement of the $Y(4260)$ and its line shape parameters in the $\pi^0\pi^0 J/\psi$ decay mode.

The interpretation of $\pi\pi J/\psi$ events produced via ISR, with a mass above 4.0 GeV, is not fixed. There are many possible and conflicting theoretical models available and in addition to this, there is still the question of how to measure and interpret the peak experimentally. In the charged mode, two interpretations of both the number of resonances and the possible non-resonant contribution and background have been presented. In the published Belle analysis, a second broad resonance with a central mass of $4008 \pm 40^{+114}_{-28}$ was observed, however, its existence has yet to be confirmed by other experiments. The $\pi^0\pi^0 J/\psi$ mode does not yet have the statistics to independently measure the line shape parameters of the cluster near 4260 MeV, but the peak measured here is consistent with the expectation from isospin, within large errors. Looking ahead, with the recent groundbreaking ceremony for the SuperKEKB collider; the Belle II experiment is hoping to study collisions at and near the $\Upsilon(4S)$ resonance with a luminosity of 8×10^{35} cm^{-1}s^{-1}, which is around 50 times as large as the peak luminosity achieved by the KEKB collider. With the anticipated dataset, the Belle II collaboration expects to greatly improve the precision of the $\pi\pi J/\psi$, and J/ψ with other light hadron, cross-sections; as well as those for various D meson combinations, see Sections 5.13.3 and 5.13.4 of Ref. [115]. However, as a consequence of the increased luminosity, Belle II also anticipates a greater rate of beam background events and non-signal photons in each event, which could provide difficulties in any future analysis of the $\pi^0\pi^0 J/\psi$ decay mode. In the near future, as Belle II develops its analysis strategies, it is suggested that a dedicated data skim for the study of ISR events be produced, to provide an improved dataset for spectroscopy. At Belle II, with more precise measurements, these cross-sections across multiple channels will provide information for a greater theoretical understanding of charmonium and potential charmonium-like systems.

Appendix A

Data skim selection criteria

Here, the selection criteria for selected Belle skims are described. The skims used in this thesis were the HadronA, Psi, HadronB(J), Low Multiplicity and Tau Skims. The first three of these were designed to identify $\Upsilon(4S) \rightarrow B\overline{B}$ events, while the Low Multiplicity and Tau Skims were designed to identify two-photon processes and $e^+e^- \rightarrow \tau^+\tau^-$ events, respectively. The quantities used by the skimming software in the selection of events are defined in Table A.1.

HadronA Skim

The HadronA Skim was the basic selection used by Belle to select hadronic $B\overline{B}$ meson events. The hadronic skims that were available to users, such as the Psi and HadronB Skims, were then selected from the HadronA dataset. The HadronA Skim selected events that passed:

- $N_{trk} \geq 3$,
- $N_{ECL} > 1$ within $-0.7 < \cos(\theta) < 0.9$,
- $|V_r| < 1.5$ cm, $|V_z| < 3.5$ cm,
- $\Sigma|P_z|/E_{CM} < 0.5$,
- $0.1 < E_{sum}/E_{CM} < 0.8$ and
- $E_{vis}/E_{CM} \geq 0.2$.

Psi Skim

Psi Skim was designed to select hadronic events that contained a J/ψ particle. Psi Skim events were selected from events that had passed the HadronA Skim selection, using the following procedure [116]:

1. Select pairs of oppositely charged tracks and
2. combine track pairs with the following mass hypotheses:
   - μ^+ with μ^-;
   - e^+ with e^-;
   - the electron track hypotheses were also combined with nearby photons in order to recover bremsstrahlung losses in the following manner:
     - $e^+ + \gamma$ with e^-,
     - e^+ with $e^- + \gamma$ and
     - $e^+ + \gamma$ with $e^- + \gamma$.
3. Events with at least one candidate in the range:
   2.48 GeV $\leq M_{\ell^+\ell^-} \leq 4.02$ GeV, pass selection.

HadronB(J) Skim

The HadronB Skim was the main hadronic skim used for Belle analysis until experiment 19, when it was combined with events that passed the Psi Skim (described above) to form the HadronB(J) Skim. HadronB Skim events were selected from HadronA Skim events with the following additional criteria:

- events that passed either $E_{sum}/E_{CM} > 0.18$ or $M_{HJ} > 1.8$ GeV and
- passed either $M_{HJ}/E_{vis} > 0.25$ or $M_{HJ} > 1.8$ GeV and
- passed $E_{sum}/N_{ECL} < 1$ GeV.

Low Multiplicity (LM) Skim

The LM Skim was designed to identify a variety of two-photon processes which had a low track multiplicity. The LM Skim selected events that passed one of three sets of selection criteria, described below as A, B or C.

A. Low track multiplicity events passed:

  - $P_{sum} < 6$ GeV,
  - $E_{sum} < 6$ GeV and
  - the number of level-3 tracks $\in [2,\, 4]$.

B. Low visible energy events were:

  - Events that failed selection A and passed
  - $E_{vis} < 4$ GeV and
  - the number of level-3 tracks ≥ 2.

C. Four track exclusive events were:

  - Events that failed selection A and passed
  - $P_{sum} < 6$ GeV,
  - $E_{sum} < 6$ GeV,
  - 4 level-1 tracks and
  - $Q_{sum} = 0$.

Tau Skim

The Tau Skim was designed to identify $e^+e^- \rightarrow \tau^+\tau^-$ events, with the following selection criteria:

- The number of "good tracks" $\in [2,\, 8]$,
- $Q_{sum} \leq 2$,
- $|V_r| < 1$ cm, $|V_z| < 3$ cm,
- $P_t^{max} > 0.5$ GeV,
- $E_{vis} > 3$ GeV or $P_t^{max} > 1.0$ GeV and
- for 2 track events:
  - $E_{sum} < 11$ GeV and
  - the direction of the missing momentum is in the range: $5° < \theta < 175°$;

- and for events with 2-4 charged tracks:
  - $N_{barrel} >= 2$ or $E_{trk} < 5.3$ GeV and
  - passed at least one of:
    * $E^{\star}_{sum} + |P^{\star}_{miss}| < 9$ GeV (CM frame) or
    * the maximum opening angle between track pairs $< 175°$ or
    * 2 GeV $< E_{sum} < 10$ GeV.

Table A.1: Definitions of quantities used in skim cuts. All quantities are in the laboratory frame except where indicated by $\star$, which indicates a quantity in the centre of mass frame.

E, P, P_t, P_z, M	Energy, momentum, transverse and z momentum and mass
P_t^{max}	The maximum P_t for tracks in the event
$dr\,(dz)$	The radial (z) distance to the interaction point (IP) for tracks
$V_r\,(V_z)$	The radial (z) distance from the IP to the event vertex
"Good track"	Tracks passing: $P_t > 0.1$ GeV, $\lvert dr\rvert < 2$ cm, $\lvert dz\rvert < 4$ cm
level-1 track	Tracks passing: $P_t > 0.1$ GeV, $\lvert dr\rvert < 5$ cm, $\lvert dz\rvert < 5$ cm
level-3 track	Tracks passing: $P_t > 0.3$ GeV, $\lvert dr\rvert < 1$ cm, $\lvert dz\rvert < 5$ cm, $17^\circ < \theta < 150^\circ$
N_{trk}	Number of "good tracks"
E_{trk}	Energy sum of tracks in the ECL
P_{sum}	The scalar sum of "good track" momenta
P_{miss}	The missing momentum in the event
$\lvert\Sigma P_t^*\rvert$	Absolute value of the vector sum of the transverse-momenta for level-1 tracks in the CM frame
"Good cluster"	Clusters in the ECL with $E > 0.1$ GeV
N_{ECL}	The number of "good clusters" in an event
E_{sum}	The scalar sum of the cluster energies
E_{vis}	$P_{sum} + E_{sum}$
E_{CM}	The total energy of the event
Q_{sum}	Sum of the electric charges of the tracks
M_{HJ}	The Heavy jet mass is the larger mass of the sum of tracks in the forward or backward direction with respect to the thrust axis of the event

Appendix B

Trigger simulation

At Belle, the response of the Level 1 trigger was simulated during MC production using software called `tsim`. `Tsim` was designed to run immediately after the GSIM detector simulation (see Section 2.6.4). Initially, the MC used in Chapter 4 was produced with `tsim` using the conditions specified below. This MC was used for that analysis up to Section 4.3. Later, the same input files were reprocessed with `tsimskin`, a wrapper for the `tsim` software which sets the `tsim` conditions to the values used by the trigger for the majority of each experiment. The output files from each set of conditions used for `tsim` were compared and the difference between them was found to be small. The MC generated with `tsimskin` was used in the analysis of Chapter 4 from Section 4.4 onwards. The code used to set the options for `tsim` initially was:

```
path add_module main tsim rectrg

### tsim
module put_parameter tsim debug\0

module put_parameter tsim gdl_algfile\/belle/belle/b20090127_0910/share/
data-files/tsim/ftdlv7_02.alg.dat

module put_parameter tsim gdl_psnmfile\/belle/belle/b20090127_0910/share/
data-files/tsim/20050117_col18c.psnm.dat

module put_parameter tsim tecl_Etot3\3.0
module put_parameter tsim tecl_overlap\0.
module put_parameter tsim tecl_eth\0.100
```

```
module put_parameter tsim tecl_eth2\0.100
module put_parameter tsim tecl_Bhabha1\5.0
module put_parameter tsim tecl_Bhabha2\5.5
module put_parameter tsim tecl_Bhabha3\5.0
module put_parameter tsim tecl_Bhabha4\5.0
module put_parameter tsim tecl_Bhabha5\5.0
module put_parameter tsim tecl_Bhabha6\5.0
module put_parameter tsim tecl_Bhabha7\5.0
module put_parameter tsim tecl_Bhabha8\5.0
module put_parameter tsim tecl_Bhabha9\5.0
module put_parameter tsim tecl_Bhabha10\5.0
module put_parameter tsim tecl_Bhabha11\3.0
# before exp 11
#module put_parameter tsim cosmic_mode\0

module put_parameter rectrg Time_window_lo\-1.0
module put_parameter rectrg Time_window_hi\1.0
```

Appendix C

$\pi^0\pi^0 J/\psi$ best candidate plots

The best candidate selection variables: $M(\gamma\gamma)$ and $|\cos(\theta_\gamma)|$, for di-electron best candidates in $\psi(2S)$ signal MC in can be seen in Figure C.1 and for di-electron and di-muon best candidates in $Y(4260)$ signal MC, in Figures C.2 and C.3, respectively. These distributions are divided into fractions according to how many of the selected π^0 photons corresponded to generated signal photons and how many corresponded to non-signal photons in the event. The $M^2_{recoil}(\pi^0\pi^0 J/\psi)$ and $M(\pi^0\pi^0 J/\psi)$ distributions of the selected candidates are shown in Figure C.4, for di-electron best candidates in $\psi(2S)$ signal MC and Figures C.5 and C.6, for di-electron and di-muon events from $Y(4260) \rightarrow \pi^0\pi^0 J/\psi$ signal MC, respectively. The distribution of these variables for di-muon candidates in the $\psi(2S)$ signal MC are shown in Section 4.3, where these plots are discussed in more detail.

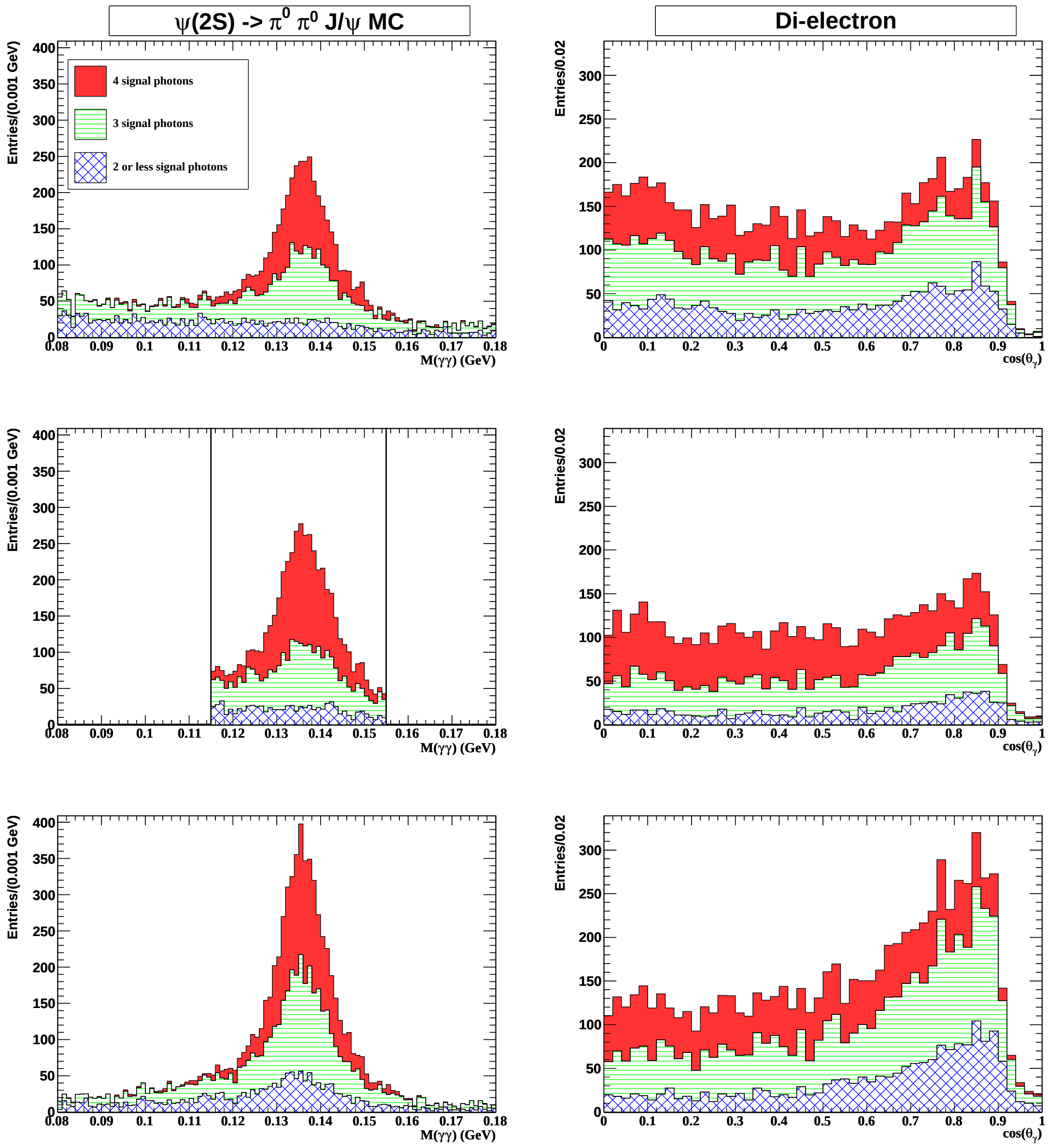

Figure C.1: Best candidate selection variables for di-electron $\psi(2S)$ signal MC events: Left column: π^0 mass. Right column: $|\cos(\theta_\gamma)|$. Top row: best candidates from the $\cos(\theta_\gamma)$-based selection, with a precut $0.08\,\mathrm{GeV} < M(\gamma\gamma) < 0.18\,\mathrm{GeV}$. Middle row: Best candidates from the $\cos(\theta_\gamma)$-based selection, with a precut $|M(\gamma\gamma) - m_{\pi^0}| < 0.02\,\mathrm{GeV}$ (vertical lines). Bottom row: best candidates from the $M(\gamma\gamma)$-based selection. Events are divided according to the number of correctly identified signal π^0 photons in the selected $\pi^0\pi^0 J/\psi$ candidate: all four photons correct (solid red histogram), three correct (green horizontally lined histogram) and two or less correct (blue diagonally hatched histogram).

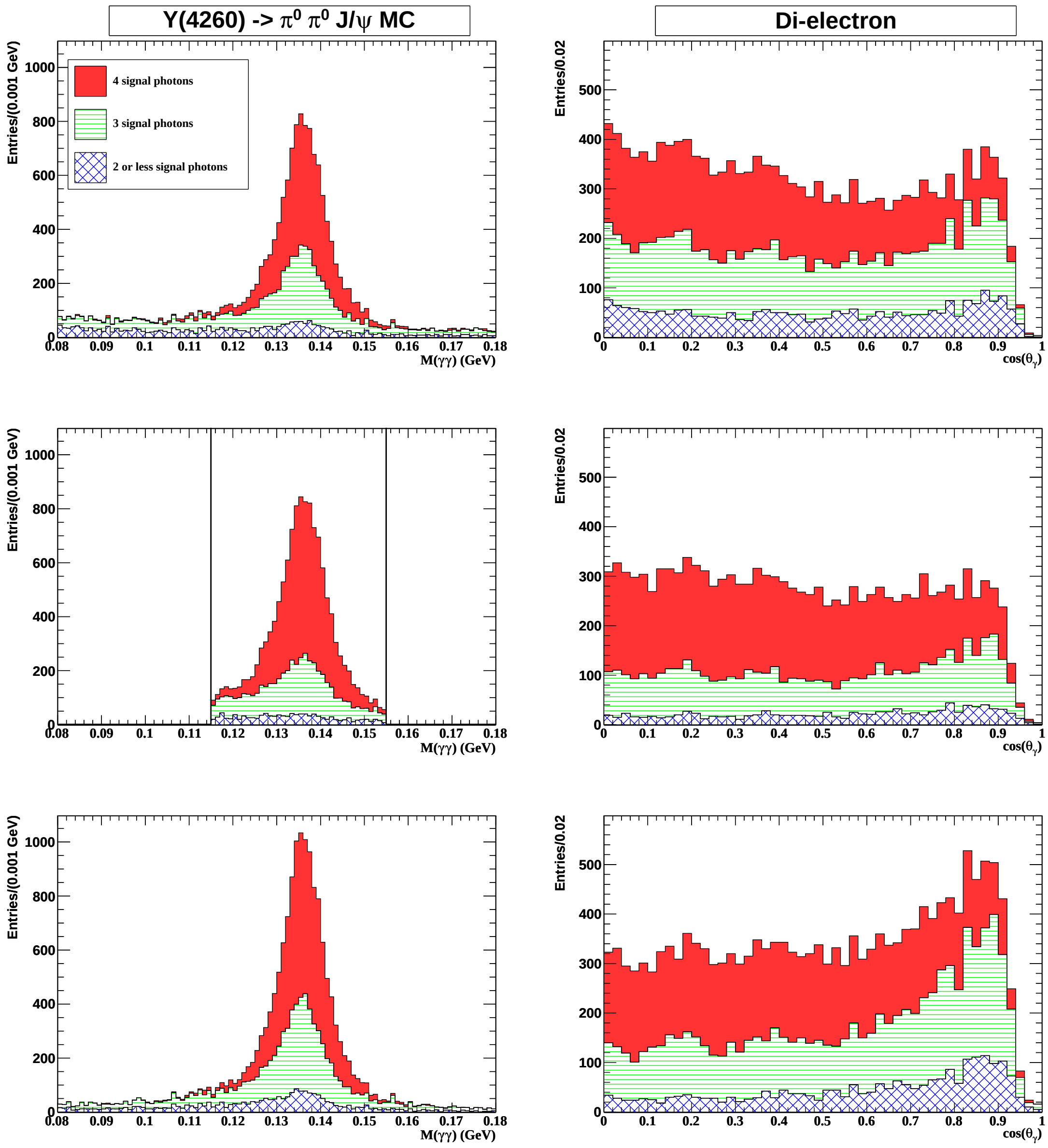

Figure C.2: Best candidate selection variables for di-electron $Y(4260)$ signal MC events: Left column: π^0 mass. Right column: $|\cos(\theta_\gamma)|$. Top row: best candidates from the $\cos(\theta_\gamma)$-based selection, with a precut $0.08\,\mathrm{GeV} < M(\gamma\gamma) < 0.18\,\mathrm{GeV}$. Middle row: Best candidates from the $\cos(\theta_\gamma)$-based selection, with a precut $|M(\gamma\gamma) - m_{\pi^0}| < 0.02\,\mathrm{GeV}$ (vertical lines). Bottom row: best candidates from the $M(\gamma\gamma)$-based selection. Events are divided according to the number of correctly identified signal π^0 photons in the selected $\pi^0\pi^0 J/\psi$ candidate: all four photons correct (solid red histogram), three correct (green horizontally lined histogram) and two or less correct (blue diagonally hatched histogram).

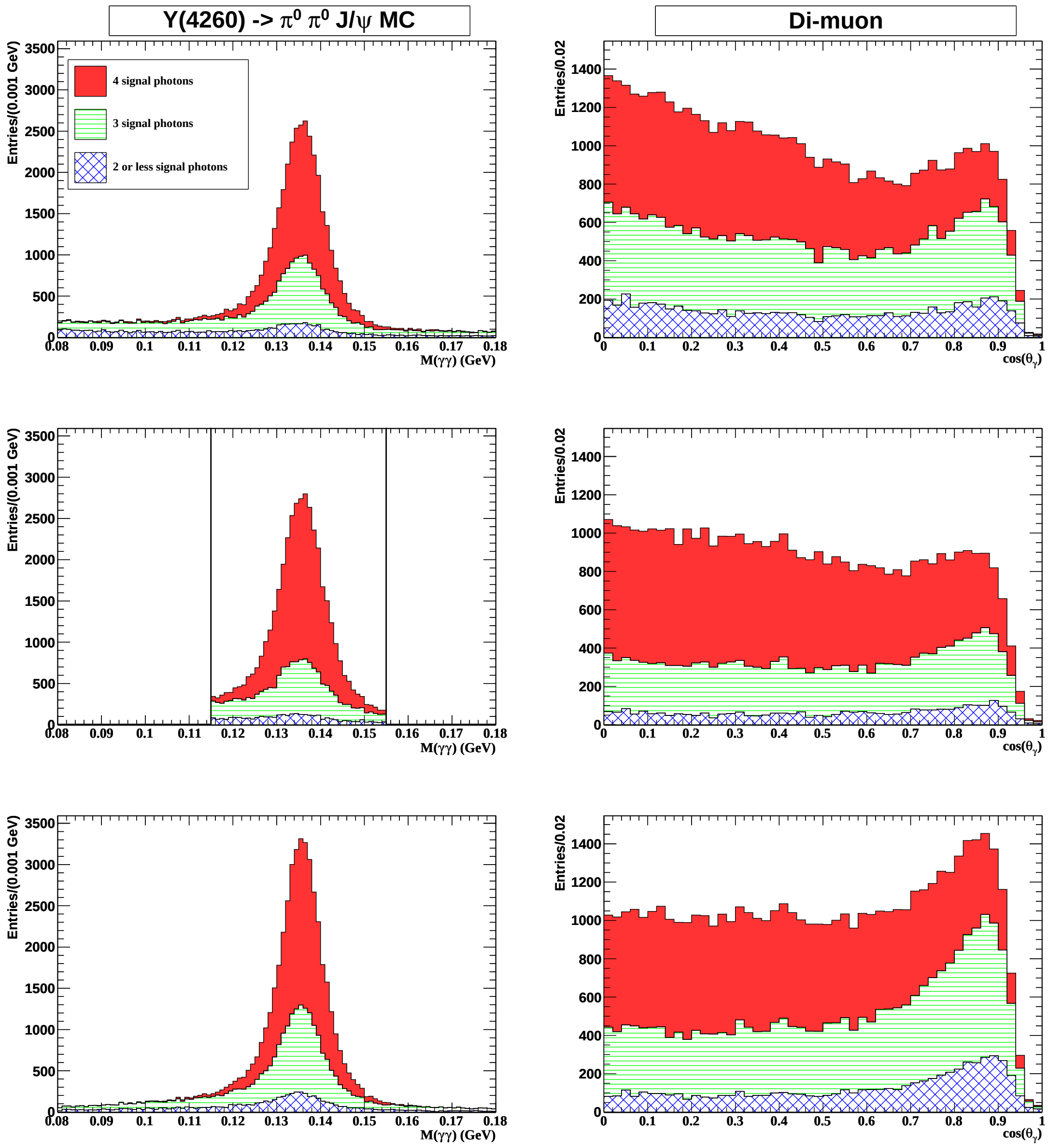

Figure C.3: Best candidate selection variables for di-muon $Y(4260)$ signal MC events: Left column: π^0 mass. Right column: $|\cos(\theta_\gamma)|$. Top row: best candidates from the $\cos(\theta_\gamma)$-based selection, with a precut $0.08\,\mathrm{GeV} < M(\gamma\gamma) < 0.18\,\mathrm{GeV}$. Middle row: Best candidates from the $\cos(\theta_\gamma)$-based selection, with a precut $|M(\gamma\gamma) - m_{\pi^0}| < 0.02\,\mathrm{GeV}$ (vertical lines). Bottom row: best candidates from the $M(\gamma\gamma)$-based selection. Events are divided according to the number of correctly identified signal π^0 photons in the selected $\pi^0\pi^0 J/\psi$ candidate: all four photons correct (solid red histogram), three correct (green horizontally lined histogram) and two or less correct (blue diagonally hatched histogram).

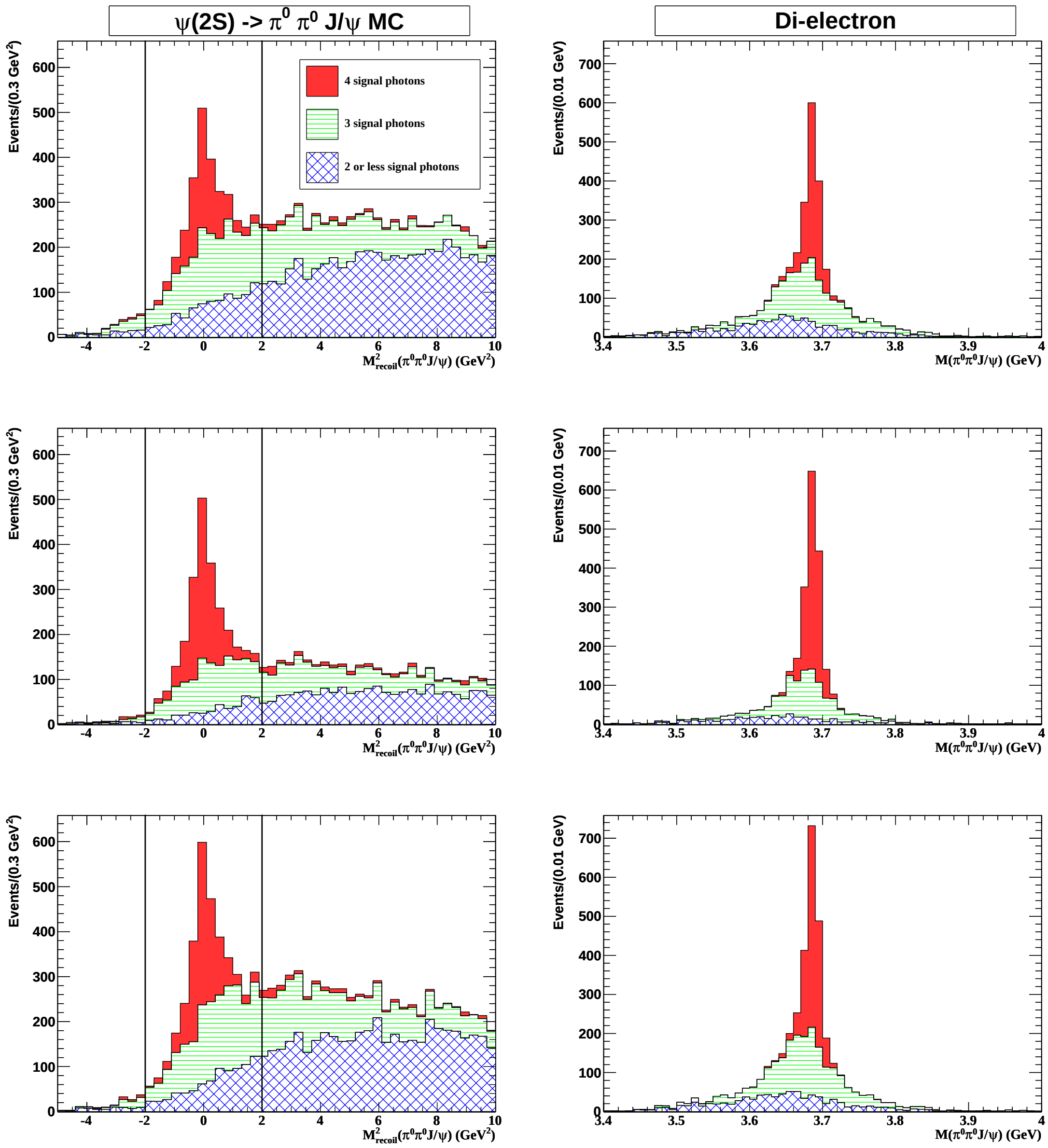

Figure C.4: Selected best candidates in di-electron $\psi(2S)$ signal MC events. Left column: $M^2_{\text{recoil}}(\pi^0\pi^0 J/\psi)$. Right column: $M(\pi^0\pi^0 J/\psi)$ of candidates passing cut: $|M^2_{\text{recoil}}(\pi^0\pi^0 J/\psi)| < \text{GeV}^2$ (indicated by vertical lines in left column). Top row: best candidates from the $\cos(\theta_\gamma)$-based selection, passing $0.08\,\text{GeV} < M(\gamma\gamma) < 0.18\,\text{GeV}$. Middle row: best candidates from the $\cos(\theta_\gamma)$-based selection, passing $|M(\gamma\gamma) - m_{\pi^0}| < 0.02\,\text{GeV}$. Bottom row: best candidates from the $M(\gamma\gamma)$-based selection. Events are divided according to the number of correctly identified signal π^0 photons in the selected $\pi^0\pi^0 J/\psi$ candidate: all four photons correct (solid red histogram), three correct (green horizontally lined histogram) and two or less correct (blue diagonally hatched histogram).

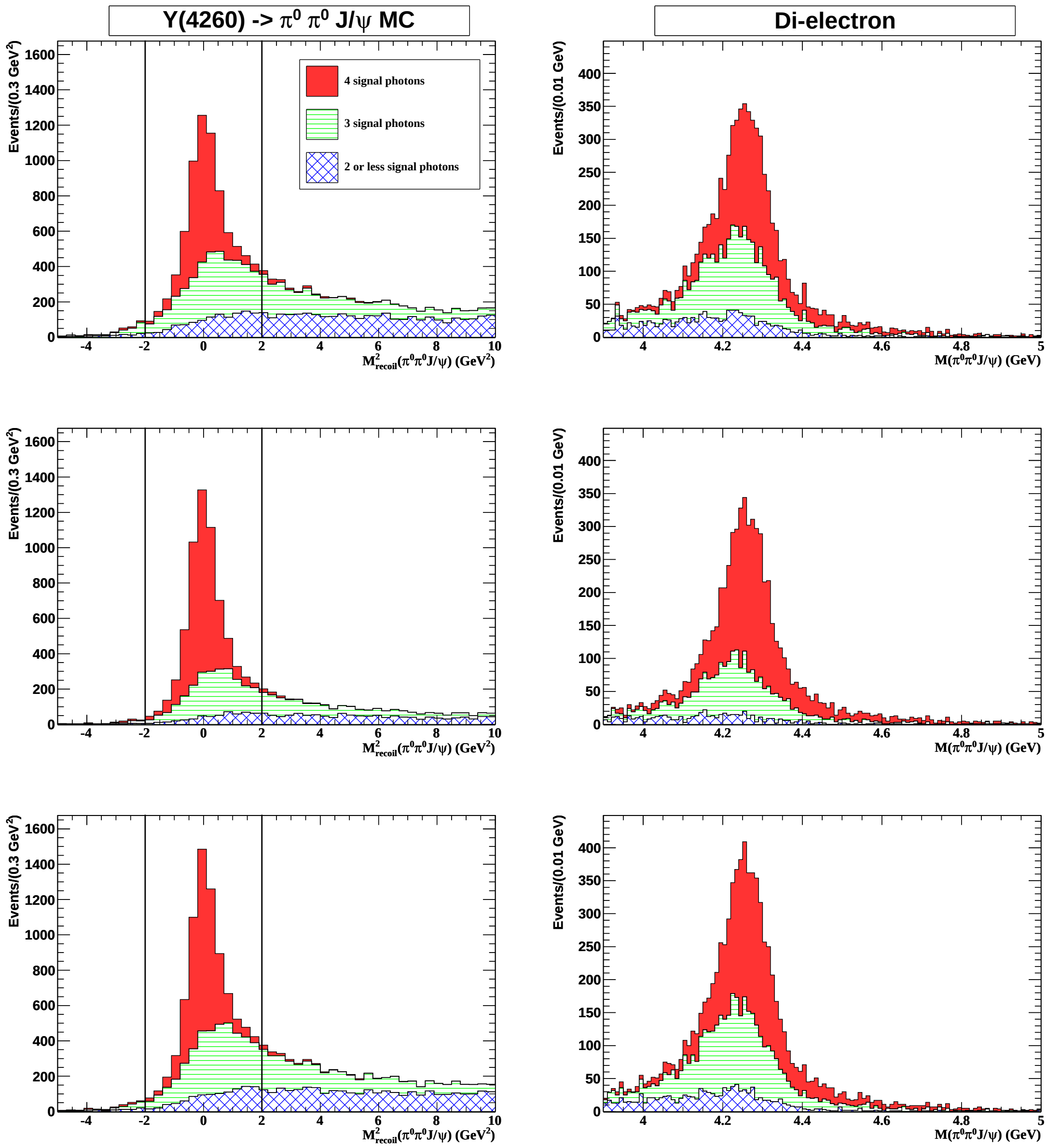

Figure C.5: Selected best candidates in di-electron $Y(4260)$ signal MC events. Left column: $M^2_{\text{recoil}}(\pi^0\pi^0 J/\psi)$. Right column: $M(\pi^0\pi^0 J/\psi)$ of candidates passing cut: $|M^2_{\text{recoil}}(\pi^0\pi^0 J/\psi)| < \text{GeV}^2$ (indicated by vertical lines in left column). Top row: best candidates from the $\cos(\theta_\gamma)$-based selection, passing $0.08\,\text{GeV} < M(\gamma\gamma) < 0.18\,\text{GeV}$. Middle row: best candidates from the $\cos(\theta_\gamma)$-based selection, passing $|M(\gamma\gamma) - m_{\pi^0}| < 0.02\,\text{GeV}$. Bottom row: best candidates from the $M(\gamma\gamma)$-based selection. Events are divided according to the number of correctly identified signal π^0 photons in the selected $\pi^0\pi^0 J/\psi$ candidate: all four photons correct (solid red histogram), three correct (green horizontally lined histogram) and two or less correct (blue diagonally hatched histogram).

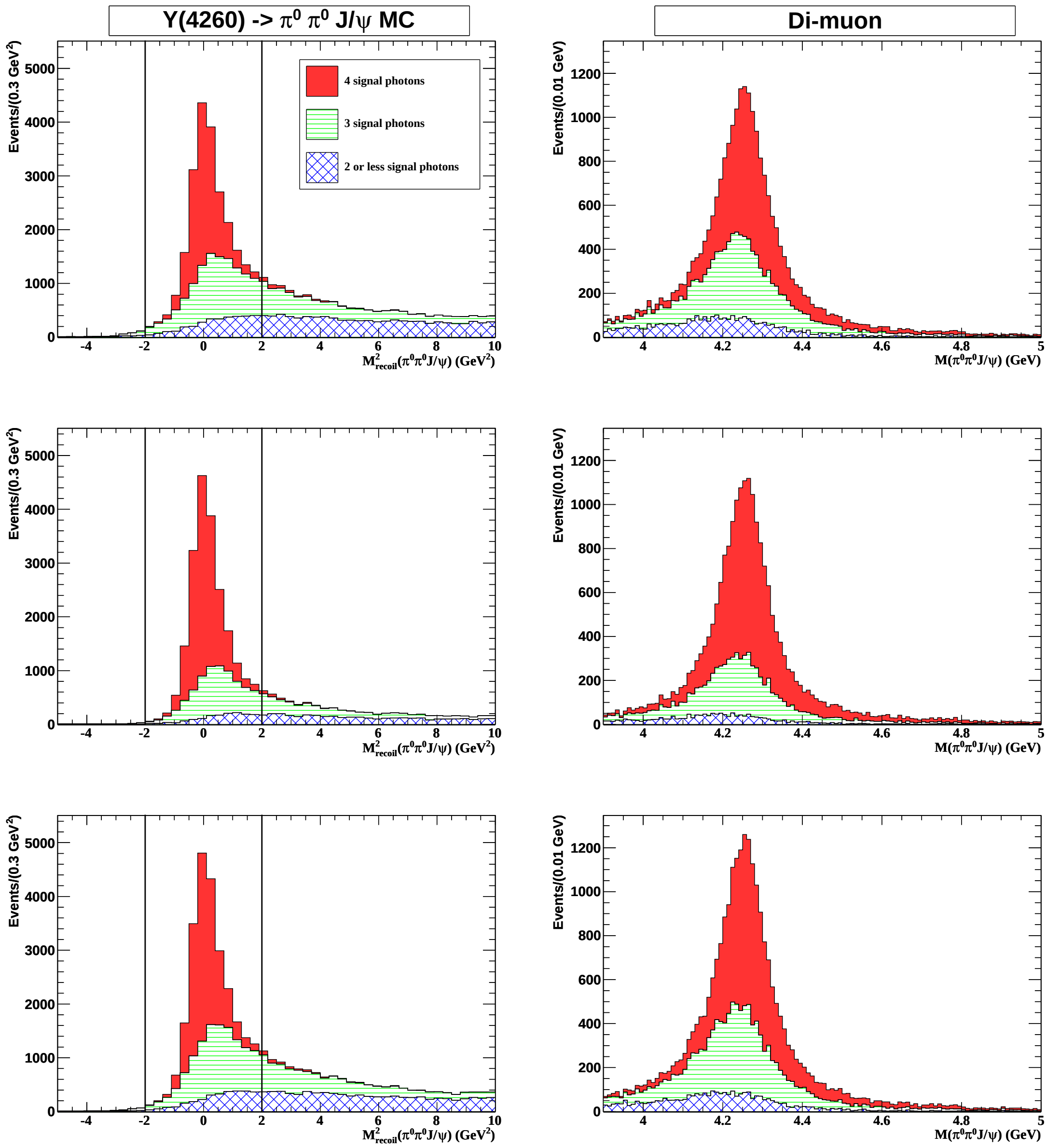

Figure C.6: Selected best candidates in di-muon $Y(4260)$ signal MC events. Left column: $M^2_{\text{recoil}}(\pi^0\pi^0 J/\psi)$. Right column: $M(\pi^0\pi^0 J/\psi)$ of candidates passing cut: $|M^2_{\text{recoil}}(\pi^0\pi^0 J/\psi)| < \text{GeV}^2$ (indicated by vertical lines in left column). Top row: best candidates from the $\cos(\theta_\gamma)$-based selection, passing $0.08\,\text{GeV} < M(\gamma\gamma) < 0.18\,\text{GeV}$. Middle row: best candidates from the $\cos(\theta_\gamma)$-based selection, passing $|M(\gamma\gamma) - m_{\pi^0}| < 0.02\,\text{GeV}$. Bottom row: best candidates from the $M(\gamma\gamma)$-based selection. Events are divided according to the number of correctly identified signal π^0 photons in the selected $\pi^0\pi^0 J/\psi$ candidate: all four photons correct (solid red histogram), three correct (green horizontally lined histogram) and two or less correct (blue diagonally hatched histogram).

Appendix D

Effect of $P_{\perp}^{ISR}$selection

The $P_{\perp}^{ISR}$ selection is discussed in Section 4.3.1. The best candidate selection variables: π^0 mass and $|\cos(\theta_\gamma)|$, are shown for candidates selected with and without the $P_{\perp}^{ISR}$ precut in Figures D.1 and D.2, for the $\psi(2S)$ and $Y(4260)$ signal MC, respectively. The recoil mass squared and candidate mass for best candidates with and without the $P_{\perp}^{ISR}$ selection are shown in Figures D.3 and D.4, for the $\psi(2S)$ and $Y(4260)$ signal MC, respectively.

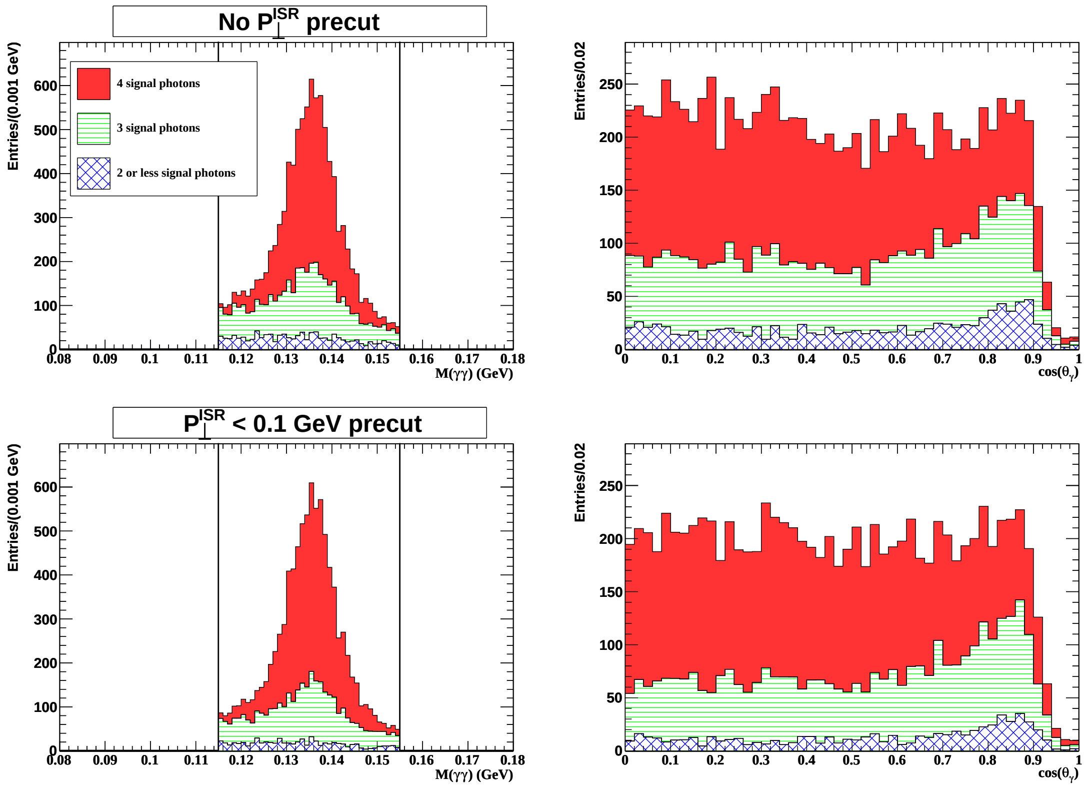

Figure D.1: Effect of $P_{\perp}^{ISR}$ cut on best candidates in $\psi(2S)$ signal MC. Left column: π^0 mass. Right column: $|\cos(\theta_\gamma)|$. Top row: best candidates without the $P_{\perp}^{ISR}$ selection. Bottom row: best candidates with the $P_{\perp}^{ISR}$ selection. Events are divided according to the number of correctly identified signal π^0 photons in the selected $\pi^0\pi^0 J/\psi$ candidate: all four photons correct (solid red histogram), three correct (green horizontally lined histogram) and two or less correct (blue diagonally hatched histogram).

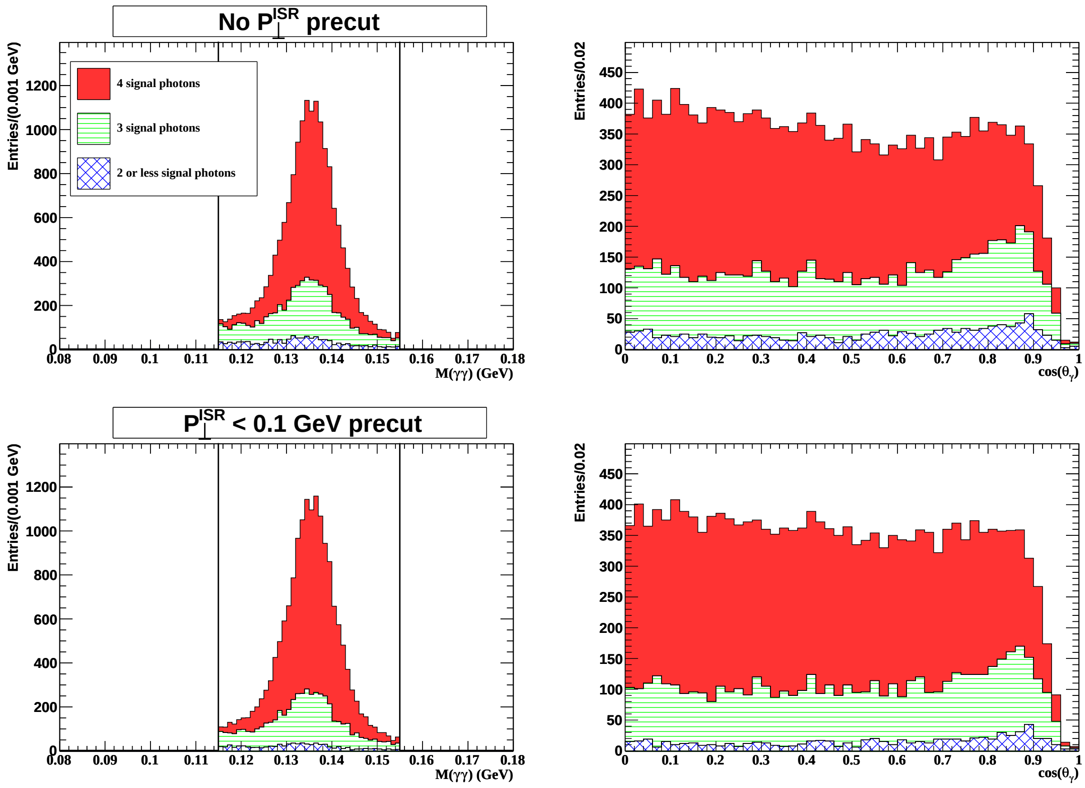

Figure D.2: Effect of $P_\perp^{ISR}$ cut on best candidates in $Y(4260)$ signal MC. Left column: π^0 mass. Right column: $|\cos(\theta_\gamma)|$. Top row: best candidates without the $P_\perp^{ISR}$ selection. Bottom row: best candidates with the $P_\perp^{ISR}$ selection. Events are divided according to the number of correctly identified signal π^0 photons in the selected $\pi^0\pi^0 J/\psi$ candidate: all four photons correct (solid red histogram), three correct (green horizontally lined histogram) and two or less correct (blue diagonally hatched histogram).

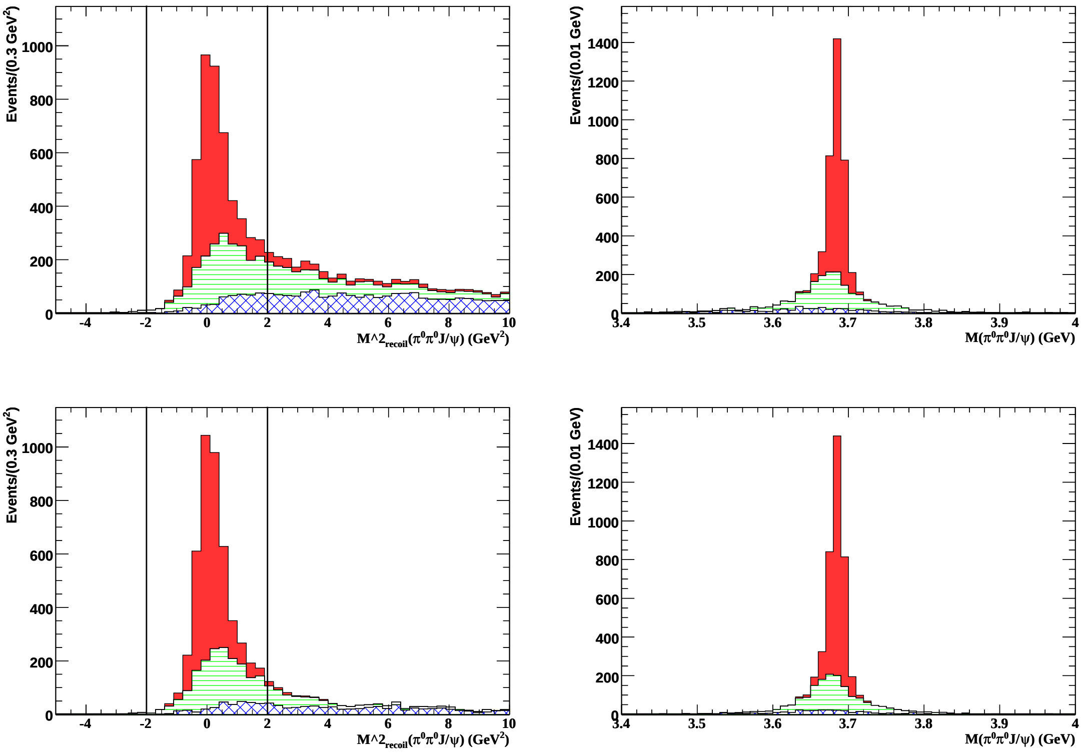

Figure D.3: Effect of $P_{\perp}^{ISR}$ cut on the best candidates in $\psi(2S)$ signal MC. Left column: M^2_{recoil}. Right column: best candidate mass. Top row: best candidates without the $P_{\perp}^{ISR}$ selection. Bottom row: best candidates with the $P_{\perp}^{ISR}$ selection. Events are divided according to the number of correctly identified signal photons in the selected $\pi^0\pi^0 J/\psi$ candidate: all four photons correct (solid red histogram), three correct (green horizontally lined histogram) and two or less correct (blue diagonally hatched histogram).

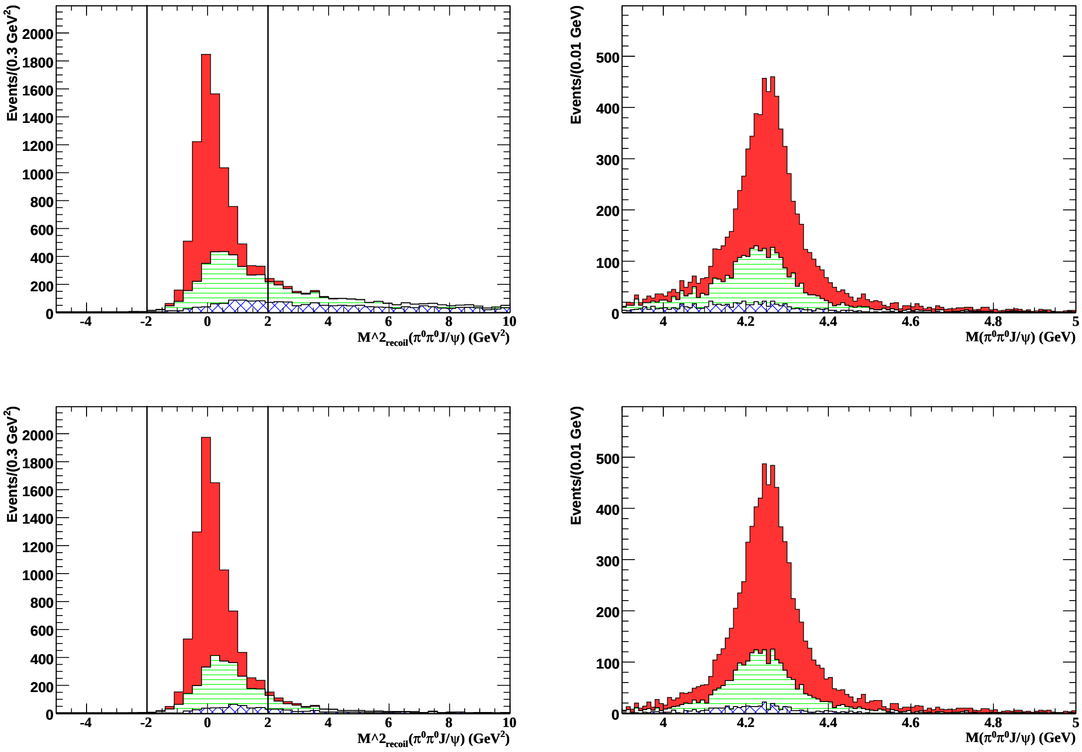

Figure D.4: Effect of $P_{\perp}^{ISR}$ cut on the best candidates in $Y(4260)$ signal MC. Left column: M^2_{recoil}. Right column: best candidate mass. Top row: best candidates without the $P_{\perp}^{ISR}$ selection. Bottom row: best candidates with the $P_{\perp}^{ISR}$ selection. Events are divided according to the number of correctly identified signal photons in the selected $\pi^0\pi^0 J/\psi$ candidate: all four photons correct (solid red histogram), three correct (green horizontally lined histogram) and two or less correct (blue diagonally hatched histogram).

Bibliography

[1] K. Nakamura et al. (Particle Data Group). Review of Particle Physics. *Journal of Physics G*, 37:075021, 2010.

[2] D.H. Perkins. *Introduction to High Energy Physics*. Cambridge University Press, fourth edition, 2000.

[3] B. R. Martin and G. Shaw. *Particle Physics*. John Wiley & Sons, third edition, 2008.

[4] E. Laermann and O. Philipsen. Lattice QCD at Finite Temperature. *Annual Review of Nuclear and Particle Science*, 53:163, 2003.

[5] S. Godfrey and N. Isgur. Mesons in a relativized quark model with chromodynamics. *Physical Review D*, 32:189, 1985.

[6] S. Capstick and N. Isgur. Baryons in a relativized quark model with chromodynamics. *Physical Review D*, 34:2809, 1986.

[7] J. J. Aubert et al. Experimental Observation of a Heavy Particle J. *Physical Review Letters*, 33:1404, 1974.

[8] J. E. Augustin et al. Discovery of a Narrow Resonance in e^+e^- Annihilation. *Physical Review Letters*, 33:1406, 1974.

[9] M.B. Voloshin. Charmonium. *Progress in Particle and Nuclear Physics*, 61:455, 2008.

[10] G. S. Abrams et al. Discovery of a Second Narrow Resonance in e^+e^- Annihilation. *Physical Review Letters*, 33:1453, 1974.

[11] E. Eichten et al. Spectrum of Charmed Quark-Antiquark Bound States. *Physical Review Letters*, 34:369, 1975.

[12] S.-L. Zhu. Pentaquarks. *International Journal of Modern Physics A*, 19:3439, 2004.

[13] T.H. Burnett and S.R.Sharpe. Non-Quark Model Mesons. *Annual Review of Nuclear and Particle Science*, 40:327, 1990.

[14] J.-P. Ader et al. Do narrow heavy multiquark states exist? *Physical Review D*, 25:2370, 1982.

[15] D. Janc and M. Rosina. Phenomenological Estimate of the Binding Energy of Heavy Dimesons. *Few-Body Systems*, 31:1, 2001.

[16] M.B. Voloshin and L.B. Okun. Hydronic molecules and the charmonium atom. *JETP Letters*, 23:333, 1976.

[17] N.A. Törnqvist. From the deuteron to deusons, an analysis of deuteronlike meson-meson bound states. *Zeitschrift Für Physik C*, 61:525, 1993.

[18] D. Horn and J. Mandula. Model of mesons with constituent gluons. *Physical Review D*, 17:898, 1978.

[19] T. Barnes et al. Hybrid and conventional mesons in the flux tube model: Numerical studies and their phenomenological implications. *Physical Review D*, 52:5242, 1995.

[20] F. Iddir et al. Do 1^{-} $c\bar{c}g$ hybrids exist, do they mix with charmonium? *Physics Letters B*, 433:125, 1998.

[21] F. Close. Gluonic hadrons. *Reports on Progress in Physics*, 51:833, 1988.

[22] E. Klempt. Glueballs, Hybrids, Pentaquarks : Introduction to Hadron Spectroscopy and Review of Selected Topics. *arXiv*:hep-ph/0404270v1, 2004.

[23] C.J. Morningstar and M. Peardon. Glueball spectrum from an anisotropic lattice study. *Physical Review D*, 60:034509, 1999.

[24] M. Benayoun et al. Spectroscopy at B-Factories Using Hard Photon Emission. *Modern Physics Letters A*, 14:2605, 1999.

[25] B. Aubert et al. (*BABAR* Collaboration). Observation of a Broad Structure in the $\pi^+\pi^- J/\psi$ Mass Spectrum around 4.26 GeV/c^2. *Physical Review Letters*, 95:142001, 2005.

[26] B. Aubert et al. (*BABAR* Collaboration). The BABAR detector. *Nuclear Instruments and Methods A*, 479:1, 2002.

[27] Q. He et al. (CLEO Collaboration). Confirmation of the $Y(4260)$ resonance production in initial state radiation. *Physical Review D*, 74:091104(R), 2006.

[28] K. Abe et al. (S. McOnie corresponding for the Belle Collaboration). Study of the $Y(4260)$ resonance in e^+e^- collisions with initial state radiation at Belle. *arXiv*:hep-ex/0612006v1, 2006.

[29] C.-Z. Yuan, C.-P. Shen, P. Wang, S. McOnie, et al. (Belle Collaboration). Measurement of $e^+e^- \to \pi^+\pi^- J/\psi$ cross-section via Initial State Radiation at Belle. *Physical Review Letters*, 99:182004, 2007.

[30] B. Aubert et al. (*BABAR* Collaboration). Study of the $\pi^+\pi^- J/\psi$ Mass Spectrum via Initial-State Radiation at BABAR. *arXiv*:0808.1543v2 [hep-ex], 2008.

[31] Y. Kubota et al. (CLEO Collaboration). The CLEO II detector. *Nuclear Instruments and Methods A*, 320:66, 1992.

[32] M. Artuso et al. (CLEO Collaboration). The CLEO RICH detector. *Nuclear Instruments and Methods A*, 554:147, 2005.

[33] D. Peterson et al. (CLEO Collaboration). The CLEO III drift chamber. *Nuclear Instruments and Methods A*, 478:142, 2002.

[34] B. Aubert et al. (*BABAR* Collaboration). Study of the $X(3872)$ and $Y(4260)$ in $B^0 \to J/\psi\pi^+\pi^-K^0$ and $B^- \to J/\psi\pi^+\pi^-K^-$ decays. *Physical Review D*, 73:011101(R), 2006.

[35] C. Z. Yuan et al. (Belle Collaboration). Observation of $e^+e^- \to K^+K^-J/\psi$ via initial-state radiation at Belle. *Physical Review D*, 77:011105(R), 2008.

[36] B. Aubert et al. (*BABAR* Collaboration). Evidence of a Broad Structure at an Invariant Mass of 4.32 GeV/c^2 in the Reaction $e^+e^- \to \pi^+\pi^-\psi(2S)$ Measured at BABAR. *Physical Review Letters*, 98:212001, 2007.

[37] X.L. Wang et al. (Belle Collaboration). Observation of Two Resonant Structures in $e^+e^- \to \pi^+\pi^-\psi(2S)$ via Initial State Radiation at Belle. *Physical Review Letters*, 99:142002, 2007.

[38] T.E. Coan et al. (CLEO Collaboration). Charmonium Decays of the $Y(4260)$, $\psi(4160)$, and $\psi(4040)$. *Physical Review Letters*, 96:162003, 2006.

[39] E. Eichten et al. Quarkonia and their transitions. *Reviews of Modern Physics*, 80:1161, 2008.

[40] G. Pakhlova et al. (Belle Collaboration). Measurement of the Near-Threshold $e^+e^- \to D^{(*)\pm}D^{(*)\mp}$ Cross Section using Initial-State Radiation. *Physical Review Letters*, 98:092001, 2007.

[41] B. Aubert et al. (*BABAR* Collaboration). Exclusive initial-state-radiation production of the $D\bar{D}$, $D^\star\bar{D}$, and $D^\star\bar{D}^\star$ systems. *Physical Review D*, 79:092001, 2009.

[42] G. Pakhlova et al. (Belle Collaboration). Measurement of $e^+e^- \to D_s^{(\star)+}D_s^{(\star)-}$ cross sections near threshold using initial-state radiation. *Physical Review D*, 83:011101(R), 2011.

[43] G. Pakhlova et al. (Belle Collaboration). Measurement of the near-threshold $e^+e^- \to D\bar{D}$ cross section using initial-state radiation. *Physical Review D*, 77:011103(R), 2008.

[44] B. Aubert et al. (*BABAR* Collaboration). Study of the exclusive initial-state-radiation production of the $D\overline{D}$ system. *Physical Review D*, 76:111105(R), 2007.

[45] D. Cronin-Hennessy et al. (CLEO Collaboration). Measurement of Charm Production Cross Section in e^+e^- Annihilation at Energies between 3.97 and 4.26 GeV. *Physical Review D*, 80:072001, 2009.

[46] P. del Amo Sanchez et al. (*BABAR* Collaboration). Exclusive production of $D_s^+D_s^-$, $D_s^{\star+}D_s^-$, and $D_s^{\star+}D_s^{\star-}$ via e^+e^- annihilation with initial-state-radiation . *Physical Review D*, 82:052004, 2010.

[47] G. Pakhlova et al. (Belle Collaboration). Observation of the $\psi(4415) \to D\overline{D}_2^\star(2460)$ Decay Using Initial-State Radiation. *Physical Review Letters*, 100:062001, 2008.

[48] G. Pakhlova et al. (Belle Collaboration). Measurement of the $e^+e^- \to D^0D^{\star-}\pi^+$ cross section using initial-state radiation. *Physical Review D*, 80:091101(R), 2009.

[49] J.Z. Bai et al. Measurements of the Cross Section for $e^+e^- \rightarrow$ Hadrons at Center-of-Mass Energies from 2 to 5 GeV. *Physical Review Letters*, 88:101802, 2002.

[50] X. H. Mo et al. Determining the upper limit of Γ_{ee} for the $Y(4260)$. *Physics Letters B*, 640:182, 2006.

[51] J. Segovia et al. $J^{PC} = 1^{--}$ hidden charm resonances. *Physical Review D*, 78(11):114033, 2008.

[52] S.-L. Zhu. The possible interpretations of Y(4260). *Physics Letters B*, 625:212, 2005.

[53] Frank E. Close and Philip R. Page. Gluonic charmonium resonances at BaBar and Belle? *Physics Letters B*, 628:215, 2005.

[54] Bai-Qing Li and Kuang-Ta Chao. Higher charmonia and x, y, z states with screened potential. *Physical Review D*, 79(9):094004, 2009.

[55] Felipe J. Llanes-Estrada. $Y(4260)$ and possible charmonium assignment. *Physical Review D*, 72:031503(R), 2005.

[56] E. J. Eichten et al. New states above charm threshold. *Physical Review D*, 73(1):014014, 2006.

[57] D.-Y. Chen et al. A non-resonant explanation to the $Y(4260)$ structure observed in the $e^+e^- \rightarrow J/\psi\pi^+\pi^-$ process. *arXiv*:1012.5362v2 [hep-ph], 2011.

[58] Eef van Beveren and George Rupp. The $X(4260)$ and possible confirmation of $\psi(3D)$, $\psi(5S)$, $\psi(4D)$, $\psi(6S)$ and $\psi(5D)$ in $J/\psi\pi\pi$. *arXiv*:0904.4351v1 [hep-ph], 2009.

[59] Eef van Beveren and George Rupp. Interference effects in the $X(4260)$ signal. *Physical Review D*, 79(11):111501(R), 2009.

[60] Eef van Beveren et al. Very Broad $X(4260)$ and the Resonance Parameters of the $\psi(3D)$ Vector Charmonium State. *Physical Review Letters*, 105(10):102001, 2010.

[61] Eef van Beveren and George Rupp. Is the $Y(4260)$ just a coupled-channel signal? *arXiv*:hep-ph/0605317v1 , 2006.

[62] E. Kou and O. Pene. Suppressed decay into open charm for the $Y(4260)$ being an hybrid. *Physics Letters B*, 631:164, 2005.

[63] Y. S. Kalashnikova and A. V. Nefediev. Spectra and decays of hybrid charmonia. *Physical Review D*, 77:054025, 2008.

[64] Xiang Liu et al. Possible molecular structure of the newly observed Y(4260). *Physical Review D*, 72:054023, 2005.

[65] C. Z. Yuan et al. The $Y(4260)$ as an $\omega\chi_{c1}$ molecular state. *Physics Letters B*, 634:399, 2006.

[66] G.-J. Ding. Are $Y(4260)$ and $Z_2^+(4250)$ D_1D or $D^0D^\star$ hadronic molecules? . *Physical Review D*, 79:014001, 2009.

[67] F. Close and C. Downum. Possibility of Deeply Bound Hadronic Molecules from Single Pion Exchange. *Physical Review Letters*, 102:242003, 2009.

[68] F. Close et al. Novel charmonium and bottomonium spectroscopies due to deeply bound hadronic molecules from single pion exchange. *Physical Review D*, 81:074033, 2010.

[69] J.L. Rosner. Effects of S-wave thresholds. *Physical Review D*, 74:076006, 2006.

[70] C.-F. Qiao. One explanation for the exotic state Y(4260). *Physics Letters B*, 639:263, 2006.

[71] A. Martínez Torres et al. $Y(4260)$ as a $J/\psi K\bar{K}$ system. *Physical Review D*, 80:094012, 2009.

[72] L. Maiani et al. Four quark interpretation of Y(4260). *Physical Review D*, 72:031502, 2005.

[73] D. Ebert et al. Masses of heavy tetraquarks in the relativistic quark model. *Physics Letters B*, 634:214, 2006.

[74] D. Ebert et al. Excited heavy tetraquarks with hidden charm. *European Physical Journal C*, 58:399, 2008.

[75] KEKB B-Factory Design Report. *KEK Technical Report*, 95-7, 1995.

[76] S. Kurokawa and E. Kikutani. Overview of the KEKB accelerators. *Nuclear Instruments and Methods A*, 499:1, 2003, and other papers included in this volume.

[77] http://www-acc.kek.jp/KEKB/Commissioning/Record/Total/integrated_luminosity.gif.

[78] A. Abashian et al. (Belle Collaboration). The Belle detector. *Nuclear Instruments and Methods A*, 479:117, 2002.

[79] S. Hashimoto et al., editors. *Letter of Intent for KEK Super B Factory*. KEK Report 2004-4. High Energy Accelerator Research Organization, Tsukuba, Japan, 2004.

[80] G. Taylor. The Belle silicon vertex detector: present performance and upgrade plan. *Nuclear Instruments and Methods A*, 501:22, 2003.

[81] H. Aihara et al. Status and upgrade plans of the Belle silicon vertex detector. *Nuclear Instruments and Methods A*, 582:709, 2007.

[82] R. Abe et al. The new beampipe for the Belle experiment. *Nuclear Instruments and Methods A*, 535:558, 2004.

[83] P. A. Čerenkov. Visible Radiation Produced by Electrons Moving in a Medium with Velocities Exceeding that of Light. *Physical Review*, 52(4):378–379, 1937.

[84] K. Miyabayashi. Belle electromagnetic calorimeter. *Nuclear Instruments and Methods A*, 494:298, 2002.

[85] J. G. Wang. RPC performance at KLM/BELLE. *Nuclear Instruments and Methods A*, 508:133, 2003.

[86] A. Abashian et al. The K_L^0/μ detector subsystem for the Belle experiment at the KEK B-factory. *Nuclear Instruments and Methods A*, 449:112, 2000.

[87] K. Hanagaki et al. Electron identification in Belle. *Nuclear Instruments and Methods A*, 485:490, 2002.

[88] A. Abashian et al. Muon Identification in the Belle Experiment at KEKB. *Nuclear Instruments and Methods A*, 491:69, 2002.

[89] E. Nakano. Belle PID. *Nuclear Instruments and Methods A*, 494:402, 2002.

[90] (Internal) http://belle.kek.jp/group/software/newdst/How2UseNewData.html.

[91] Y. Ushiroda et al. Development of the central trigger system for the BELLE detector at the KEK B-factory. *Nuclear Instruments and Methods A*, 438:460, 1999.

[92] T. Hojo et al. Level 3 trigger at Belle. *Belle Note Draft* (Internal), 2002.

[93] K. Hanagaki et al. The Level 4 Software Trigger at BELLE. *Belle Note 299* (Internal), 2000.

[94] R. Itoh. BASF User's Manual. *Belle Note 161* (Internal), 1996.

[95] R. Brun and F. Rademakers. ROOT – An Object Oriented Data Analysis Framework. *Proceedings AIHENP'96 Workshop, Lausanne*, 1996, *Nuclear Instruments and Methods A*, 389:81-86, 1997. See also http://root.cern.ch/.

[96] W. Verkerke and D. Kirkby. RooFit Users Manual v2.91, 2008. See also http://roofit.sourceforge.net/.

[97] H. Czyz et al. Electron positron annihilation into three pions and the radiative return. *European Physics Journal C*, 47:617, 2006.

[98] http://www.lns.cornell.edu/public/CLEO/soft/QQ/.

[99] D. J. Lange. The EvtGen particle decay simulation package. *Nuclear Instruments and Methods A*, 462:152, 2001.

[100] R. Brun et al. GEANT 3.21. *CERN Report*, DD/EE/84–1:1, 1984.

[101] https://www.bnl.gov/hqworkshop/.

[102] C. Amsler et al. (Particle Data Group). The Review of Particle Physics. *Physics Letters B*, 667:1, 2008.

[103] S. Nishida. Study of Kaon and Pion Identification Using Inclusive D^* Sample. *Belle Note 779* (Internal), 2005.

[104] W.-M. Yao et al. (Particle Data Group). Review of Particle Physics. *Journal of Physics G*, 33:1, 2006.

[105] T. Skwarnick. Ph.D. Thesis, Institute for Nuclear Physics, Krakow 1986; DESY Internal Report, DESY F31-86-02., 1986.

[106] S.-K. Choi et al. (Belle Collaboration). Observation of a Resonancelike Structure in the $\pi^{+-}\psi'$ Mass Distribution in Exclusive $B \to K\pi^{+-}\psi'$ Decays. *Physical Review Letters*, 100:142001, 2008.

[107] A. Abulencia et al. (CDF Collaboration). Analysis of the Quantum Numbers J^{PC} of the $X(3872)$ Particle. *Physical Review Letters*, 98:132002, 2007.

[108] S. Godfrey. The XYZ's of $c\bar{c}$: Hints of Exotic New Mesons. *arXiv*:hep-ph/0605152v1, 2006.

[109] A. Roodman. Blind Analysis in Particle Physics. *Proceedings of PHYSTAT2003 (California, USA)*, page 166, 2003.

[110] J. Tanaka. KFitter Usage and Effect. *Belle Note 193* (Internal), 1998.

[111] (Internal) http://belle.kek.jp/group/ecl/private/lum/lum6.html.

[112] L. Hinz. Lepton ID efficiency correction and systematic error. *Belle Note 954* (Internal), 2006.

[113] P. Koppenburg. A Measurement of the Track Finding Efficiency Using Partially Reconstructed D^* Decays. *Belle Note 621* (Internal), 2003.

[114] K. Inami et al. Track finding efficiency in τ decay with π^0. *Belle Note 976* (Internal), 2007.

[115] A. G. Akeroyd. Physics at Super B Factory. *arXiv*:1002.5012v1 [hep-ex], 2010. See also http://belle2.kek.jp/physics.html.

[116] From the source code for psi_skim in BELLE_LEVEL b20050311_0738.